Turbulent coarse-particle non-Newtonian suspension flow

Enzu Zheng

Department of Mechanical and Aerospace Engineering

Monash University

This dissertation is submitted for the degree of

Doctor of Philosophy

Nov 2020

Copyright notice

I certify that I have made all reasonable efforts to secure copyright permissions for third-party content included in this thesis and have not knowingly added copyright content to my work without the owner's permission.

Declaration

I hereby declare that this thesis contains no material which has been accepted for the award of any other degree or diploma at any university or equivalent institution and that, to the best of my knowledge and belief, this thesis contains no material previously published or written by another person, except where due reference is made in the text of the thesis.

This thesis includes *two* original papers published in peer reviewed journals. The core theme of the thesis is *Turbulent coarse-particle non-Newtonian suspension flow*. The ideas, development and writing up of all the papers in the thesis were the principal responsibility of myself, the student, working within the *Department of Mechanical & Aerospace Engineering* under the primary supervision of *Prof. Murray Rudman* with co-supervisors *Dr Shibo Kuang (Dept. Chemical Engineering)* and *Dr Andrew Chryss (CSIRO).*

In the case of *Chapter 3* my contribution and co-authors' contribution to the work involved the following:

Thesis Chapter	Publication Title	Status	Nature and % of student contribution	Co-author name(s) Nature and % of Co-author's contribution*	Co-author(s), Monash student Y/N*
3	Direct numerical simulation of turbulent non-Newtonian flow using OpenFOAM	published	Conducting all simulation and data analysis, manuscript writing and editing. 63%.	Prof. Murray Rudman. Conception, direction, manuscript writing and revision. 20%.	N
				Dr. Jagmohan Singh. Postprocessing results, manuscript writing and revision. 11%.	N
				Dr. Shibo Kuang. Direction, manuscript revision. 6%.	N

In the case of *Chapter 5: Section 5.1* my contribution and co-authors' contribution to the work involved the following:

Thesis Chapter	Publication Title	Status	Nature and % of student contribution	Co-author name(s) Nature and % of Co-author's contribution*	Co-author(s), Monash student Y/N*
5.1	Turbulent coarse-particle suspension flow: Measurement and modelling	published	Conducting experiment & simulation, manuscript writing, editing, data analysis. 60%.	Prof. Murray Rudman. Conception,direction, manuscript writing and revision. 18%.	N
				Dr. Shibo Kuang. Assistance with method development (CFD-DEM), manuscript revision. 12%.	N
				Dr. Andrew Chryss. Experimental direction, manuscript revision. 10%.	N

The authors are also thankful for the funding and support from CSIRO Mineral Resources, particularly *Kosta Simic* for his help on setting up the pipe loop and *Keri Constanti-Carey* for her rheological characterisation of the carrier fluids.

I have not renumbered sections of published papers in order to generate a consistent presentation within the thesis.

Student signature: **Date: 11 March 2021**

The undersigned hereby certify that the above declaration correctly reflects the nature and extent of the student's and co-authors' contributions to this work. In instances where I am not the responsible author I have consulted with the responsible author to agree on the respective contributions of the authors.

Main Supervisor signature: **Date: 11 March 2021**

Acknowledgements

The past three and half years have been a wonderful and challenging experience. The thesis would not have been made possible without the support of many wonderful individuals. First and foremost, I would like to extend my sincere gratitude to my principal supervisor Prof. Murray Rudman for his unending guidance and support throughout my candidature. His expertise and enthusiasm provided me with the continual inspirations and confidence when things did not go as expected. I feel extremely lucky to have such an excellent supervisor who always offers invaluable feedback on my work.

I would like to thank my associate supervisors Dr. Shibo Kuang and Dr. Andrew Chryss, for their unending support. Shibo′s expertise in CFD-DEM provided invaluable guidance on developing the methodology in this project. He always pointed me in the right direction and provided help whenever I had problems. I would like to thank Andrew for his patient guidance and continual support in conducting the experiments. I am thankful for Commonwealth Scientific and Industrial Research Organisation (CSIRO) colleagues Kosta Simic on setting up the pipe loop, Keri Constanti-Carey for her rheological characterisation, Dr. Lachlan Graham for his help on Electronic Resistance Tomography postprocessing and Bon Nguyen for his help on improving the mixer performance.

My special gratitude goes to Dr. Jagmohan Singh for his great help during my PhD. Thanks for his detailed guidance on using the *Semtex* code and explanation on all my non-Newtonian questions. I am also thankful to Bev Pearce, Nancy Hawe, Fiona Pyrczak, Jacelyn Tan and Stelios Konstantinidis from the departmental office for their administrative support.

My thanks also go out to the Laboratory for Simulation and Modelling of Particulate Systems (SIMPAS) group and other Monash colleagues for their encouragement, assistance, and suggestions during my research. Thanks Dr. Tony Vo, Dr. Tzekih Tsai, Dr. Farah Houdroge, Dr. Shibo Wang, Dr. Zhi Ng and many others for the time together both as tutors and friends to provide an escape from the PhD work. Thanks Mohammad

Fazli for checking the literature review chapter and tolerating my weekly presentation during the last year.

I am grateful for the financial support from Monash University, as well as funding and support from CSIRO Minerals. I also acknowledge support from the ARC Research Hub for Computational Particle Technology (IH1401001035) in undertaking this research and National Computational Infrastructure (NCI), D77 in proving the computational resources. Particularly, I would like to thank Alexis Espinosa from Pawsey Supercomputing Centre for his patient guidance and continual support in installing OpenFOAM and CFDEM containers on Magnus.

I would like to thank my family for their unconditional love and encouragement over the years. Thanks for being supportive of my decision to pursue a PhD. Last, but not least, a special thanks to my wife, Liangchi Chen. Without you standing by me, the PhD would be incredibly difficult and stressful. Thanks for your constant support, particularly during the downs of my PhD. This thesis is dedicated to you.

Abstract

Currently there is a need to move towards higher concentration tailings suspensions due to their environmental and economic benefits. With increasing solids concentration, the rheologically active fine particles combine with the water to form a non-Newtonian carrier, which typically exhibits shear-thinning behaviour along with the presence of a yield stress. All coarser solids are conveyed as coarse burden. The interaction between non-Newtonian carrier and coarse particles is still poorly understood, particularly in the transitional and turbulent flow regimes.

This project presents a DNS-DEM model for investigating weakly turbulent coarse-particle non-Newtonian suspension flows in a horizontal pipe. Direct Numerical Simulation (DNS) is applied to capture the unsteady turbulent flow structure, and the Discrete Element Method (DEM) is used for modelling the detailed coarse particle-particle interaction. Turbulent Newtonian and non-Newtonian suspension experiments in a pipe are conducted for model validation. Suspension data including pressure drop, mixture flow rates and concentration profiles are obtained. The validated DNS-DEM model is subsequently applied for investigations on the effects of carrier fluid rheology (yield stress τ_y & flow index n), solids properties (particle size d_p & in-line concentration C_v) and pipe size on the flow regime, pressure drop, velocity and concentration distribution in turbulent non-Newtonian suspension flows.

Heterogeneous flow and a sliding bed are present in a weakly turbulent non-Newtonian suspension. Turbulence in the lower portion of the pipe is damped with the presence of concentrated particles thus becomes ineffective in re-suspending the particles. Nevertheless, the degree of packing in the stratified bed reduces compared to a Newtonian equivalent with the same mean wall viscosity. A stronger coupling between the fluid and particles is found for the flow with a higher yield stress as revealed by the larger magnitude of drag in the central region. However, higher yield stress simultaneously leads to further damping of the turbulence. The combined effect contributes to only slightly improved solids suspension in the flow with a higher yield

stress. Meanwhile, this beneficial effect is at the cost of a higher pressure drop. The modelling predicts an increase in pressure drop with increasing yield stress, flow index or in-line solids concentration, and a decrease in pressure drop with increasing pipe diameter or particle diameter. The velocity profiles are generally asymmetrical about the centreline due to particle settling in the lower portion and there is a gradual flattening of the velocity profile with increasing $\boldsymbol{\tau}_y$ or lower n.

The developed DNS-DEM model provides an extended understanding of the complex interaction between the non-Newtonian rheology and particle transport in high concentration suspensions occurring in a weakly turbulent regime. Compared to an experimental approach, the DNS-DEM model is able to quantify the effect of different flow parameters on the suspension flow behaviour under a wide range of operating conditions. This project is a first step by investigating weakly turbulent non-Newtonian suspensions and will provide guidance for coupling Large Eddy Simulation with DEM for investigating turbulent non-Newtonian suspensions with higher Reynolds number in the future.

Table of contents

List of figures

List of tables

List of principal symbols

Greek Symbols

ε_f fluid volume fraction

ε_p particle volume fraction

ρ_f fluid density

ρ_p particle density

η dynamic viscosity

η_w mean wall viscosity

α diffusion coefficient

$\boldsymbol{\tau}$ fluid stress tensor

$\boldsymbol{\tau}_w$ mean wall shear stress

$\boldsymbol{\tau}_y$ yield stress

δ the overlap of a colliding pair of particles

$\dot{\gamma}$ second invariant of the rate-of-strain tensor

γ damping coefficient

$\boldsymbol{\omega}$ particle angular velocity

Roman Symbols

Bi Bingham number

C_D drag coefficient

C_r the Courant-Friedrich-Levy (CFL) number

D pipe diameter

d_p particle diameter

e coefficient of restitution

$\boldsymbol{F}$ volumetric force

$\boldsymbol{f}$ particle scale force

$\boldsymbol{g}$	gravitational acceleration
G	shear modulus
I	moment of inertial of particle
k	consistency
$k_{f/p}$	turbulent kinetic energy of fluid and particle phase
K_{fp}	fluid-particle exchange coefficient
L	pipe length
$\boldsymbol{M}$	torque
n	flow index
P	pressure
R	pipe radius
r	radial distance from the pipe centre
Re	Newtonian Reynolds number
Re_τ	friction Reynolds number
Re_G	generalised Reynolds number
Re_p	particle Reynolds number
Δt	time step
t	time
$\boldsymbol{U}$	mean axial velocity
$\boldsymbol{u}$	velocity
$\boldsymbol{U}_b$	bulk velocity
$\boldsymbol{U}_\tau$	friction velocity
$\boldsymbol{v}$	particle translational velocity
V_p	volume of a particle
Δx	CFD cell size
X_n	deviation factor
Y	Young's modulus
y	distance from the wall $(R - r)$
z	axial direction

1

Introduction

Mining and mineral extraction process produce enormous amount of waste material known as tailings that require disposal. According to recent production figures, more than 14 billion metric tons of tailings are produced every year [63, 83]. Traditionally, mine tailings have been conveyed with water at a relatively low solids concentration (less than 15% by volume) [132]. The solids and carrier fluid are regarded as two separate phases, with an aim of allowing the solids to settle in a dam and water to be recovered [14]. Therefore, large storage facilities are required in conventional tailings for solids settling, consolidation and water recovery processes. However, large storage sites are subject to failure due to leakage, instability and liquefaction, the mobility of conventional tailings inevitably results in inundation around impoundment during a dam breach [96]. More than 35 tailings dam failures have occurred since 2000 worldwide and have caused over 315 deaths [145]. These dam failures result in inundation of more than 55×10^6 m^3 of tailings and cause severe damage to the surrounding environment. In addition, significant volume of water used in conventional tailings has been an environmental and financial concern that it is necessary to reduce the water consumption and conserve limited water resources.

With advances of dewatering technologies (thickeners), there has been a consideration towards higher concentration tailings suspension. Thickeners use flocculants

to aggregate fine particles. Modern thickeners can produce higher solids concentration tailings that allow a large amount of water removal before deposition. It has been demonstrated that water volume discharge into the storage facility can be reduced by 60% when increasing solids (sand) volume concentration from 15% to 30% [132]. Besides reduced water usage, higher concentration transport brings about other benefits including reduced land use for tailings disposal, improved deposit stability and lower tailings mobility. Therefore, moving to higher concentration transport is a promising trend for various safety, environmental and financial considerations.

Tailings suspensions typically involve a broad size distribution. With increasing solids concentration, inter-particle interaction becomes significant and the fine particles combining with the water form a non-Newtonian carrier fluid, which exhibits completely different behaviour to conventional tailings. Coarser solids contribute to the conveyed coarse burden. A general criteria in distinguishing the fine and coarse particle is $d_p = 50\mu m$ [117]. In this thesis, coarse particle represents particle with d_p in the mm range and is able to settle. The complex interaction between the carrier fluid and coarse particles is directly related to the pumping energy requirement and transport stability. Pipeline design for transport of thickened slurries requires a good understanding of both the non-Newtonian carrier rheology and behaviour of conveyed coarse particles. Although numerous research has been conducted on the suspension flow, most of these studies work on Newtonian carrier fluid suspensions [119], such comprehensive analyses are lacking for non-Newtonian carrier fluid based suspensions.

Practically, a wide variety of non-Newtonian carrier fluid in the mineral industry exhibits visco-plastic behaviour, which can be represented using a relation between the apparent viscosity and shear rate. In addition, the relation includes a yield stress, namely the critical shear stress which needs to be exceeded before any flow can occur [56]. A number of non-Newtonian rheology models have been developed for description of the mineral carrier fluid and the generally used power-law and Herschel-Bulkley model are selected in this project,

Power-law

$$\eta = k\dot{\gamma}^{(n-1)} \tag{1.1}$$

Herschel-Bulkley

$$\eta = \frac{\boldsymbol{\tau}_y}{\dot{\gamma}} + k\dot{\gamma}^{(n-1)} \tag{1.2}$$

where η is the apparent viscosity, $\dot{\gamma}$ is the shear rate, k is the consistency, n is the flow index, and $\boldsymbol{\tau}_y$ is the fluid yield stress. As can be seen from the equations, the carrier fluid viscosity decreases with increased shear rate or strain, therefore, they are also called shear-thinning or pseudo-plastic carrier fluid [20]. Different from the Newtonian counterparts, the local carrier viscosity is constantly changing with shear rate or velocity profile, which significantly complicates the physics of the non-Newtonian suspension system. The apparent viscosity of a shear-thinning fluid reaches its maximum at the pipe centre and minimum at the pipe wall for laminar and on average for turbulent flows [20]. The advantage associated with this is it may require lower power consumption for transportation compared to an equivalent Newtonian flow at the same Re. In addition, these carriers often exhibit a yield stress that if sufficiently strong, can be beneficial in supporting coarse particles near the pipe centre and prevent them settling [20, 70]. However, once the carrier is sheared, yield stress is no longer available to support coarse particles, where the local viscosity around the particle is reduced and coarse particles can freely move relative to the carrier [6, 95]. The effect of yield stress on non-Newtonian suspension behaviour is still unclear and requires further investigation.

The complex interaction between the non-Newtonian carrier rheology and coarse particle transport in high concentration suspension is still poorly understood, particularly under transitional or turbulent flow regimes. Although effective viscosity of thickened tailings can be very high, they can be irreversibly broken down in pumps [96]. Because of flow rates and large pipe sizes, these flows in a pipe can occur in transitional or turbulent regimes. However, currently used Newtonian models fail to work properly in predicting the non-Newtonian suspension because the lack of fundamental understanding of the fluid dynamics and coarse particle interactions. Currently there is no clear understanding on the flow regime in a turbulent non-Newtonian suspension. Investigation is needed to understand how flow regime changes under different flow conditions (e.g., solids concentration and particle size) in order to develop appropriate correlation for predicting the flow behaviour. It is also necessary to understand and predict the

pressure drop changes for transportation energy requirements. Flow characteristics of tailings suspensions can vary significantly between small and large pipes. General approaches for scale-up from lab-scale to industry scale is lacking and current suspension models are mostly for the conventional Newtonian carrier suspensions. Understanding of the underpinning non-Newtonian suspension science is a necessity for successful application of high concentration suspensions.

The main aim of this thesis is to achieve a fundamental understanding of the complex interaction between non-Newtonian carrier rheology and coarse particle transport in a turbulent suspension flow. The specific aims of this project are to:

- Identify the flow regime in a turbulent non-Newtonian suspension and determine how the carrier fluid rheology (yield stress τ_y and flow index n), solids properties (in-line concentration C_v and solids size d_p) and pipe size D affect the flow regime;
- Understand how the pressure drop changes under different operating conditions by varying the carrier fluid rheology and solids properties in a turbulent non-Newtonian suspension;
- Determine how the carrier fluid rheology, particularly the yield stress τ_y could support particle suspension and compare the difference with an equivalent Newtonian suspension;
- Determine how concentration distribution across the pipe can be affected by the carrier fluid and solid properties;
- Investigate how the interaction of turbulent eddies, yield stress and coarse particles act together to produce different phenomenon.

As pipelines are commonly used for tailings transportation, the project focuses on simulation and experimentation of turbulent non-Newtonian suspension flow in a pipe. The project is divided into

- Developing a Direct Numerical Simulation (DNS) - Discrete Element Method (DEM) coupling methodology for non-Newtonian suspensions and validate the methodology against coarse solid suspension experimental data;

- Using the validated methodology for investigations on the effect of carrier fluid rheology, solids properties and pipe size on flow regime, pressure drop and concentration distribution in a non-Newtonian suspension flow.

The DNS-DEM model developed in the project can be used to quantitatively determine the influence of different flow parameters on pipeline performance under a wide range of operating conditions compared to an experimental approach. Such knowledge can be used to provide guidance on modifying existing Newtonian empirical correlations & stratified layer models and enable predicting the non-Newtonian suspension behaviour with improved certainty and accuracy.

The structure of the thesis is as follows. Chapter 2 summarises previous studies on non-Newtonian suspensions including experimental work, empirical correlations and CFD modelling. Chapter 3 presents the development of a general-purpose DNS approach for shear-thinning non-Newtonian turbulence. Chapter 4 introduces the DNS-DEM coupling methodology and development of a DNS-DEM coupling framework via the open-source package OpenFOAM-CFDEM-LIGGGHTS [52]. Chapter 5 summarises experimental work of turbulent Newtonian and non-Newtonian suspension flow, as well as the DNS-DEM model validation. Chapter 6 presents a DNS-DEM investigation of how carrier fluid rheology, solids properties and pipe diameter affect flow regime, pressure drop, velocity and concentration profiles. Chapter 7 concludes the work in this project and recommends the future way forward in studies of non-Newtonian suspension flows.

2

Literature Review

Solid-liquid suspension flows are widely encountered in industrial applications including oil & gas well drilling [3], pipeline transport [50, 96, 119], biomedical [131] and food industries [25]. This chapter introduces the general background of solid-liquid suspension flows in a pipe, followed by an overview of previous studies on non-Newtonian suspension flows, the modelling approaches available for coupled particle-fluid flow and turbulence in shear-thinning non-Newtonian fluids. On this basis, several research questions requiring further investigation in turbulent non-Newtonian suspension flows are raised.

2.1 Solid-liquid suspension flows in a pipe

Pipe flows of solid-liquid suspensions are typically classified into two categories: homogeneous and heterogeneous flow [115]. This is not a clearly cut classification because solid-liquid suspension flows are complex and influenced by many parameters such as mixture flow rates and solids concentration. However this binary classification indicates the degree of solids distribution over the pipe cross-section and provides an initial basis for selecting appropriate correlations when describing flow behaviour. A general criteria for classification [117] states that for a pipe flow with mean solids size $d_{50} > 50\,\mu m$ and a low viscosity carrier fluid, the flow will be heterogeneous. However this will depend

on the slurry flow parameters such as solids concentration, carrier viscosity, flow rate and pipe size.

Homogeneous slurries are those in which the solids are uniformly distributed. They are commonly found in fine particles ($d_{50} \leq 50\,\mu m$) suspension flows where the two distinct phases do not separate to a significant extent. The behaviour of homogeneous slurries can be reasonably described using a single-phase approximation [24] where the slurry is regarded as a continuum with a viscosity and density of the mixture. In practice, fine particles suspensions such as concentrated flocculated kaolin and coal slurries would exhibit a shear-thinning non-Newtonian behaviour, which deviates from the conventional Newtonian tailings suspension. Various continuum models (e.g., Power-Law, Herschel-Bulkley, Casson, Bingham plastic) have been proposed for describing their shear-thinning behaviour. Generally for a yield-plastic shear-thinning flow, the Buckingham equation (for a Bingham plastic fluid) [15] is applied to estimate the pressure gradient in a laminar flow and the Wilson & Thomas correlation [130, 144] is used in a turbulent flow. A systematic overview of homogeneous slurry flow in a pipe can be found in [56].

With the presence of coarse particles ($d_{50} > 50\,\mu m$), the flow displays a heterogeneous concentration as coarse particles tend to settle down under gravity. In this thesis, coarse particle represents particle with d_p in the mm range and is able to settle. The carrier and coarse particles behave differently and the single-phase flow approximation is no longer applicable to the stratified heterogeneous flows. Study of heterogeneous slurry flow is more complex, and its design and the prediction of pressure drop has been based on empirical correlations and layer models. It should proceed with caution to ensure reliable operation without pipe blockage. In practice, solid-liquid suspension flows can occur in horizontal, vertical or inclined pipes. The flow characteristics of coarse particle suspensions are affected by various flow parameters including pipe size, inclination angle, solids size distribution, carrier fluid rheology and mixture flow rates. The major variables influencing pipe flows of coarse-particle suspensions are summarised in Table 2.1.

Table 2.1 Major variables in pipe flows of solid-liquid suspensions

Element	Flow Parameters
Carrier fluid	Rheology (Newtonian, Non-Newtonian), density
Solids	Concentration, size (PSD), density, shape
Pipe	Diameter, length, geometry (e.g., bend, fittings), materials
Operating conditions	Conveying velocity, pump type

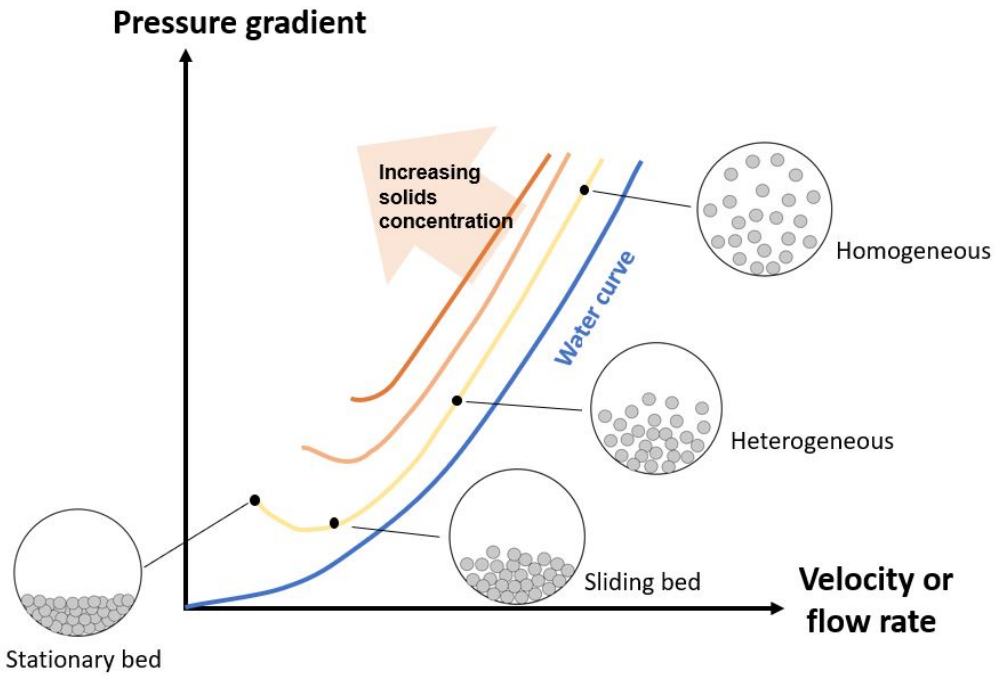

Fig. 2.1 Flow characteristics and regime transition of conventional tailings (reproduced from Pullum et al. [96])

Identifying the flow regime is important in order to select the appropriate correlation for predicting the flow behaviour. Despite homogeneous and heterogeneous slurries displaying distinct flow behaviour, they may exhibit characteristics similar to each other in some flow conditions. The criteria in delineating these patterns are generally subjective based on the extent of solids settling [45]. The flow characteristics and flow regime in conventional tailings suspensions are shown in Fig 2.1. Providing the velocity is sufficiently high, solids are continually being lifted and form a pseudo-homogeneous distribution over the pipe cross-section. At lower velocity, turbulence intensity decreases and gravity accelerates the settling of particles, forming a heterogeneous distribution

that is partially suspended. Further reduction of conveying velocity leads to more solids settling at the bottom of the pipe. A sliding bed with solids saltation at the top of the bed is formed. This also results in increased particle-wall friction. A higher pressure gradient relative to the water curve is therefore required to maintain transport. The pressure gradient also increases with increasing solids concentration. Sliding bed is commonly found in slurry transportation due to the capacity limit of the centrifugal pump. When the velocity is below the critical conveying velocity [92], a stationary bed forms at the bottom and because new solids are continually being fed into the system, this consequently leads to pipe blockage when the increased pressure drop (due to bed formation) exceeds the available pump head.

In addition to the flow regime transition, flow characteristics such as pressure drop, minimum conveying velocity, velocity and concentration distribution of heterogeneous slurries carried with a Newtonian fluid have also been comprehensively studied. There are many suspension models and empirical correlations available for predicting the conventional Newtonian suspension flow ([47, 50, 79, 111, 117, 118, 143]). However, with the advances of thickeners and dewatering technology, there is an increasing attention to high concentration tailings suspension. As introduced in Chapter 1, at high concentrations, the fine particles will combine with the water to form a non-Newtonian carrier, with larger solids conveyed as a coarse burden. These non-Newtonian slurries exhibit more complex behaviour compared to conventional Newtonian suspensions. Currently used suspension models fail to accurately predict the flow behaviour in these scenarios.

2.2 Non-Newtonian suspension flows

For non-Newtonian suspension flows, due to the presence of the more viscous carrier fluid, the flow will potentially have relatively lower Reynolds number compared to a Newtonian equivalent at the same flow rate [108]. The flow may be weakly turbulent or laminar for thickened tailings at flow rates in the order of meters per second [96]. There is no general agreement on the flow regime transition for a non-Newtonian suspension flow. Traditionally, turbulent non-Newtonian suspensions have been treated as if they are homogeneous when pipeline design has been undertaken [96]. The relatively stronger coupling between carrier and suspended particles will help to reduce the particle settling

rate and aid suspension [20, 70]. However, later studies [6, 95] reveal that once the carrier is sheared, yield stress is no longer available to support coarse particles, where the local viscosity around the particle is reduced and coarse particles can freely move relative to the carrier.

Coarse particle settling has been found in laminar non-Newtonian suspension flows, such as in the study by Cooke [22] and Thomas et al. [129]. They presented a review of thickened slurry flows with coarse particle settling in both laboratory scale and large scale pipes. Coarse particles were found suspended and stable in a static settling test, however, settling occurred once the mixture was transported in the pipe. Wilson et al. [142], Wilson and Horsley [141] investigated particle settling in a sheared non-Newtonian flow. The particle terminal velocity was found to be greater compared to the unsheared case. In a laminar non-Newtonian flow, a coaxial unsheared plug region (as shown in Fig 2.2) existed where the applied shear stress $\tau_{(r)}$ was less than the yield stress τ_y ($\tau_y/\tau_{(r)} > 1$) [96]. Particle settling occurred in the annular sheared region outside the plug and once settled, particles were not able to be re-suspended as they could be in a turbulent flow. With the formation of a settled particle bed, the area of the unsheared plug reduced and moved upward. Particles initially in the unsheared plug were thus exposed to shear and could settle.

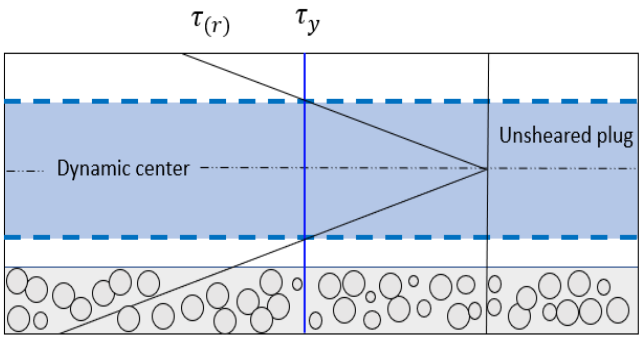

Fig. 2.2 Schematic of the unsheared plug in a laminar non-Newtonian suspension flow

Consensus has been reached in the literature that for laminar non-Newtonian suspension flows, coarse particle settling can occur and unsheared settling tests are not appropriate for describing settling in suspension transport. However, less is known for coarse particle settling in a transitional & turbulent non-Newtonian flow. Predicting the

flow in a turbulent regime is more difficult due to the inherent stochastic nature of fluid turbulence and its interaction with coarse particles. How and to what degree the carrier fluid rheology, particularly the yield stress τ_y, would support particle suspension in a turbulent flow regime remains unclear. Instead of a homogeneous flow, it is assumed that heterogeneous flow and possibly with a sliding bed can be present in a turbulent regime similarly to a Newtonian suspension, but the details and extent of the flow will be different and require further investigation.

The complex behaviour of non-Newtonian suspension flows is affected by a variety of factors, as shown in Table 2.1. A wide variety of techniques including experimental and modelling approaches have been applied for investigations of non-Newtonian suspension flows. A review of these studies is provided below.

2.2.1 Experimental work

Experiments have investigated non-Newtonian solid-liquid flows in a pipe. Charles et al. [17] compared the head loss for conveying $216\ \mu m$ sand particles in both water and shear-thinning clay suspensions ($n = 0.24 \sim 0.35$). The head loss of the clay suspensions was about one sixth of a water-sand slurry. Chhabra and Richardson [19] conducted an extensive experimental study of transporting coarse particles (up to $8.1\ mm$) in both highly viscous Newtonian fluid and non-Newtonian fluids (Carboxymethyl cellulose solution and kaolin suspension) in a $42\ mm$ horizontal pipe. Duckworth et al. [31] carried out a pipe flow of coarse coal particles (up to $19\ mm$) with a Bingham fluid. It was observed in these studies that most coarse particles settled and formed a sliding bed in both laminar and turbulent flow regimes. Ghosh and Shook [43] observed reduced pressure drop in a pipe flow of $600\ \mu m$ sand particles conveyed with shear-thinning carboxymethyl cellulose solution compared to a water-based slurry, while the other test conducted by them using $2.7mm$ pea gravel particles exhibited no reduction in pressure drop, mostly due to the coarse solids that formed a sliding bed at the bottom. Hill and Shook [57] carried out experimental flows of $1.7\ mm$ and $4\ mm$ particles conveyed by water and clay slurries in a $52\ mm$ pipe. The clay slurries exhibited yield stress in the range of $3 \sim 25\ Pa$. The clay slurry flows showed no pressure drop reduction and flows were all highly stratified. The predicted pressure gradient was in good agreement with

measurements for both laminar and turbulent flows by incorporating the additional kinetic wall friction term for coarse particles in the suspension model.

Fairhurst et al. [38] and Barigou et al. [9] investigated coarse ($d_p = 5 \sim 10$ mm) nearly-neutrally buoyant particles ($\rho_s = 1020\ kg/m^3$) flow carried with a non-Newtonian CMC fluid. The solid phase velocity profile was captured using Positron Emission Particle Tracking (PEPT). It was found the degree of asymmetry of the solid velocity profile depended on the mixture flow rates, carrier fluid viscosity, solids size and concentration. Increasing the carrier fluid viscosity reduced the degree of asymmetry. Benslimane et al. [12] conducted experimental measurements of 3.5, 5 and 8 $\%wt$ bentonite suspensions in both laminar and turbulent pipe flow. The velocity profile of the bentonite suspensions was found to be accurately represented with flow parameters fitted using the Herschel-Bulkley model. Penik et al. [89] carried out pipe flow of coarse glass-bead particles ($0.57 \sim 1.5\ mm$) in a pseudoplastic carrying fluid and proposed an experimental approach in determining the local particle diffusivity.

In terms of particle settling in a non-Newtonian fluid, Gillies et al. [48] examined laminar non-Newtonian flow of coarse particles ($d_{50} = 0.1, 0.2$ and $0.4\ mm$) in pipe loops of diameter $50 \sim 250\ mm$. In contrast to the 'rule of thumb' criteria of minimum frictional pressure gradient ($1.5 \sim 2\ KPa/m$) for effective transport of sand in viscous Newtonian oils, they proposed a criteria based on the ratio of the mean wall shear stress τ_w to the mean surficial particle stress τ_p to ensure no settling would occur in a laminar non-Newtonian flow. The mean surficial particle shear stress τ_p was a parameter defined by Wilson and co-workers [142] as

$$\tau_p = \frac{(\rho_s - \rho_f) g d_p}{6} \tag{2.1}$$

It was demonstrated in [142] that the τ_p was a significant parameter in determining the terminal velocity of particles settling in a non-Newtonian fluid. Based on their experimental tests of kaolin clay slurry with a Bingham yield stress ($0 \sim 130Pa$), the potential for settling was significantly reduced when $\tau_w/\tau_p > 60$ and almost eliminated when $\tau_w/\tau_p > 100$.

In summary, these studies covered a particle diameter range from $0.1 \sim 19\ mm$. For the coarse-particles of interest here (d_p in the mm range), coarse-particle settling and formation of a sliding bed was observed in the majority of studies. Reduced pressure drop was found in flows with a smaller particle size ($200\mu m \sim 600\mu m$) compared to a water-based slurry, while no reduction in pressure drop was found in flows with a coarser particle size ($1.7 \sim 19mm$). However, comprehensive understanding on the effect of carrier rheology and solids properties on the non-Newtonian suspension flows is not yet available. The degradation of the carrier in model laboratory suspension using CMC/Carbopol with time makes it difficult to keep the non-Newtonian system uniform. In addition at high concentration, it is challenging to measure both fluid and particle velocities reliably due to loss of measuring signal integrity caused by particle induced diffraction, refraction and obscuration. Detailed measurements of velocity and concentration distribution in high concentration suspensions are lacking.

2.2.2 Empirical correlations and layer models

Many empirical and semi-empirical correlations have been established for predicting pressure drop in non-Newtonian suspension flows. Chhabra and Richardson [19] presented a correlation to predict the pressure drop for non-Newtonian solid-liquid pipe flows with the sliding bed regime based on their extensive experimental study. However, they declared this correlation to be unsuitable in other flow regimes and pressure drop obtained were in significant error.

As opposed to simple correlations such as [19], layer models have been proposed that attempt to include additional physics. For Newtonian suspensions, the two-layer and three-layer models have been proposed [30, 47, 102, 140]. These models vary in details such as the criteria in distinguishing the layers, number of layers and bed formation, but they are all derived based on a force balance between different layers, as shown in Fig 2.3.

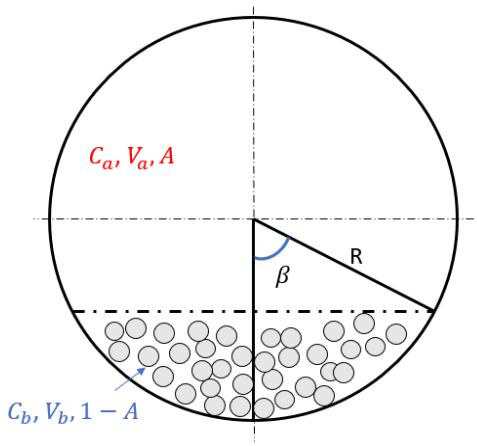

Fig. 2.3 Schematic of the conceptual basis of a two-layer model with a uniformly suspended upper layer and a concentrated bed layer (C - concentration; V - bulk flow and A - area)

In calculating the pressure drop of turbulent heterogeneous solid-liquid flows, the model assumes that the suspension of solid particles results from the dynamic balance between the gravity induced settling and turbulence induced dispersion. Pressure drop is estimated for each layer according to the established correlation. Afterwards, the local layer pressure drops are integrated to obtain the total pressure drop. The layer model is able to predict most flow characteristics such as minimum conveying velocity, bed height, delivered concentration and pressure drop. Currently they are widely used in the design and operation of conventional tailing suspensions where the carrier is a Newtonian fluid.

Based on similar ideas, a modified non-Newtonian two-layer model [98, 107] was developed using experimental results from non-Newtonian suspensions under various operating conditions in both laminar and turbulent flow regimes. The non-Newtonian suspension was decomposed into a pseudo-homogeneous layer comprising the carrier fluid and fine particles (less than $38\ \mu m$) and a settled coarse particle layer. Subsequently a more advanced multi-component model was developed accounting for the non-Newtonian rheology [97]. The solids were split into three components including a settled bed of coarse particles, a heterogeneous layer and a fine component. The fine component included the very fine fraction contributing to the viscosity and the homogeneously suspended fine fraction.

For a low viscosity carrier fluid such as water, Shook et al.[117] proposed the maximum size of particles that could be considered as fraction of the carrier was 74 μm. For a non-Newtonian suspension, a larger value of 200 μm was justified to be a reasonable cut-off based on the higher viscosity in a non-Newtonian fluid, therefore the fluid would be capable to homogeneously support larger particles. The total pressure gradient comprised of the contribution from the three components and was calculated as

$$\frac{dp}{dx}|_{tot} = k_1 \frac{dp}{dx}|_e + k_2 \frac{dp}{dx}|_h + k_3 \frac{dp}{dx}|_s \tag{2.2}$$

Details of the pressure drop calculation can be found in [97]. Each of these components was scaled by empirically determined constants k_1, k_2 and k_3 accounting for enhanced non-Newtonian effects. The values of k_1, k_2 and k_3 were 1.65, 1 and 1, respectively. The model was compared with the pressure drop from a bimodal suspension of glass ballotini, a sand suspension conveyed in carbopol and tailings suspension in pipes of 100 and 150 mm, and was found to predict the pressure drop well for these flows. However, the limitations of the above correlations and layer models are they all adopt empirical constants in the model and are overly simplified compared to more sophisticated approaches based on elemental volumes. To make the multi-component model more accurate for pressure drop analysis, general trends for the empirical constants k_1, k_2 and k_3 with varied carrier rheology and solids properties need to be established.

2.2.3 CFD modelling

Computational fluid dynamics (CFD) is increasingly being applied to modelling multiphase flows. The presence of multi-scale phenomena in the particle-fluid flow requires modelling approaches capable of working at different length and time scales. In a particle-fluid system, motion of discrete particles is governed by Newton's second law while the continuum fluid behaviour is captured by the Navier-Stokes equations. However, enormous numbers of particles occur in industry-scale problems and solving particle motion individually can take a huge computational effort. In addition, resolving fluid between closely spaced particles requires very fine resolution. These factors result in the computation being too intensive to be conducted. Therefore, simplications on analysis of

fluid and particle motion are needed based on the time and length scale to be captured [41, 72, 153].

Generally CFD codes for multiphase flow, particularly for solid-liquid settling suspension flows, can be categorised as continuum or discrete approaches [119, 153]. The categories of modelling approaches for coupled particle-fluid flow are shown in Figure 2.4.

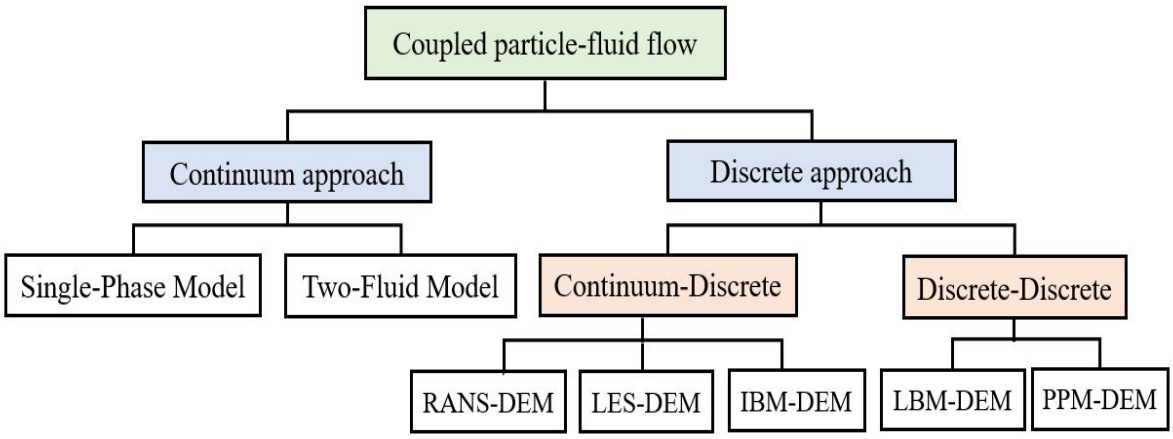

Fig. 2.4 Modelling approaches for coupled particle-fluid flow

2.2.3.1 Single-Phase Model

The single-phase model is suitable for modelling pseudo-homogeneous suspension flow or flow with low solids concentration that the presence of the solids phase has little impact on the fluid phase, namely one-way coupling is considered [24]. Gradeck et al. [54] calculated the pressure drop of a $30\ mm$ diameter pipe flow with fairly low concentration suspensions and treated the solid-liquid suspension as a single homogeneous fluid phase. Both water, Newtonian glucose solutions and non-Newtonian CMC solutions were used as carrier fluid to convey the coarse ($4.4\ mm$) nearly-neutrally buoyant alginate particles. For settling suspension flows, studies proposed a turbulence model based on the mixture properties [106] and later the two-equation single phase turbulence models were applied for highly concentrated suspension flows with turbulence modulation [10, 11]. The presence of particles affects the turbulence intensity, turbulence kinetic energy and dissipation rate, these alternations in turbulence can be categorized as turbulence augmentation and attenuation. Previous studies quantitatively

described these phenomenon and introduced additional parameters into the single-phase model to incorporate the influence of dispersed phase on the carrier fluid [59, 62].

The single-phase model is computationally convenient and inexpensive in describing a suspension flow. However, this approach is not suitable in concentrated suspensions, where the inter-particle force increases significantly with solids concentration. It has relatively large deviation from experimental measurements in stratified suspension flows, particularly with the presence of coarse particles. With more complex and sophisticated approaches available, the application of the single-phase model is relatively limited and is mostly used as an initial estimate of the flow behaviour which can be used as initial conditions in other models.

2.2.3.2 Two Fluid Model

Compared to single-phase model, the Two Fluid Model (TFM)[44], which is usually framed as the Eulerian-Eulerian approach, is more commonly used for modelling the solid-liquid flow. The TFM treats solid and liquid phases in the computational domain as two interpenetrating and interactive continuum, with the computational cell size typically much larger than the particle size [44]. The continuum method models the particle-fluid flow following the conservation law of mass, momentum and energy at a macroscopic level. Constitutive relations, initial and boundary conditions are required for closure. The computational convenience and effectiveness of TFM makes it popular among researchers and has been widely used in the past decades for particle-fluids flow [34, 61, 82].

Smith et al. [122] carried out CFD simulation of neutrally-buoyant solid particle ($d_p = 6.25\ mm$) mixing in a tank using TFM. Good agreement in solids mixing was achieved when compared with their experimental results. Krampa-Morlu et al. [67] conducted CFD studies of turbulent solid-liquid flow in an upward pipe with solids concentration up to 30% v/v. The solids density was $2650\ kg/m^3$ and diameters were in the range of $0.47 \sim 1.7\ mm$. The velocity profile was generally in good agreement for small size particles compared to experimental results from Sumner et al. [124], while results deteriorated for particles with $d_p = 1.7\ mm$. Ekambara et al. [34] investigated the effect of solids volume concentration ($8 \sim 45\%$), particle size ($90 \sim 500\mu m$), mixture

flow rate ($1.5 \sim 5.5m/s$) and pipe size ($50 \sim 500mm$) in horizontal slurry flows using ANSYS-CFX. The degree of asymmetry in particle distribution was found to increase with increasing particle size and depended only on solids concentration when particle size was sufficiently large. TFM had been found to be valid in predicting the pressure drop and concentration profile for suspension flows in most of these studies, however, it was not promising for predicting coarse particle ($dp > 0.5\ mm$) suspensions and the predicted concentration profile displayed large deviation compared to experiments [53]. Eesa & Barigou [32, 33] numerically simulated the laminar pipe flow of coarse particle suspensions in non-Newtonian carrier fluids. The effect of solids concentration and carrier fluid rheology on the pressure drop, concentration and velocity distribution were investigated. As solids concentration increased, solids distributions were found to be radially more uniform and solid & liquid velocity profile became flatter. The mean flow velocity and consistency index were found to have little impact on the normalized solids concentration profile, the normalized velocity profile or the pressure drop compared to fluid only flow.

The TFM model, despite its computational convenience and efficiency, requires defining the complex constitutive relationships for the frictional, collisional and kinetic stresses of the solid phase in a continuum framework [76]. These relationships can be difficult to model especially with the presence of different types of particles in the flow [28]. Theories and correlations have been proposed for different particle types and flow regimes based on phenomenological assumption [153]. However, currently there is no generally accepted continuum theory suitable for all flow conditions and it is a challenging area requiring further investigation.

2.2.3.3 CFD-DEM

Compared to the Eulerian-Eulerian approach, the Eulerian-Lagrangian approach models the fluid as a continuum and describes the particle motions and interactions at a particle-scale level. Many models have been developed for dealing with individual particle motion and among them, the Discrete Element Method (DEM) [26] is widely used. CFD-DEM was initially developed by Tsuji et al. [134] with subsequent rationalization by Xu and Yu [147]. In DEM, particle motion is predicted with Newton's second law that

captures particle interactions via contact/non-contact forces [153]. At each time step, DEM calculates the location and velocity of individual particles. The particle position and velocity information is then used for evaluation of the volume fraction and the volumetric interaction force in a CFD cell. With the porosity and the volumetric interaction force information, fluid flow is then solved using the CFD solver. The interaction force on an individual particle is subsequently calculated from the fluid solution and DEM starts to solve the particle flow for the next coupling cycle.

Compared with TFM, CFD-DEM is capable of modelling a wide range of flow systems as the requirement of specifying complex constitutive relations between stress and strain tensors for the particle phase can be eliminated [69]. Depending on the length and time scales used for modelling fluid flow, the CFD-DEM approach can be classified into several categories varying from discrete Lattice-Boltzmann Method (LBM), pseudo-particle method (PPM) to continuum Reynolds averaged Navier-Stokes (RANS), large eddy simulation (LES) and Immersed Boundary Method (IBM). They are all promising in coupling with DEM for modelling particle-fluid flow [153]. Some examples of particle-fluids flow using these approaches can be found in LBM-DEM [100, 138], PPM-DEM [40, 72], RANS-DEM [3], LES-DEM [150] and IBM-DEM [4].

CFD-DEM has been applied in recent studies of solid-liquid suspension flows. For conventional suspensions where the carrier is a Newtonian fluid, Uzi and Levy [136] conducted RANS-DEM to investigate how pipe flow characteristics (e.g., pressure drop, velocity and concentration profile) were modified by operating conditions such as solids concentration and pipe diameter. A robust LES-DEM solver called *Sedifoam* was developed for the simulation of sediment transport with implementing the lubrication and added mass force on the particles in [125]. This solver was found to be parallelly efficient in solving large-scale sediment transport. Zhou et al. [150] presented a LES-DEM model on hydraulic conveying of coarse solid particles in a vertical pipe. A more dispersed distribution of particles occurred with increasing conveying speed and feed solid concentration.

Based on a similar coupling framework as in a Newtonian suspension, Smuts [123] first attempted a RANS-DEM approach to model non-Newtonian suspension rheology. The model predicted a correct shear-thinning trend by varying the range of

rheological parameters including particle surface charge and solids fraction. Akhshik et al. [3] developed a RANS-DEM model to simulate cuttings transport in well drilling by taking into account the particle dynamic collision process. The Herschel-Bulkley (*HB*) model was applied to describe the non-Newtonian rheology. Simulations results were validated and found to reasonably match with measurements from laboratory-scale experiments. A dam collapse comprising of a mixture of an *HB* type non-Newtonian fluid and particles was also studied using RANS-DEM [73]. Compared to water-particle mixture, the non-Newtonian fluid showed a better mixing with granular particles during the collapse due to its high viscosity. However, the RANS-DEM studies mentioned above all adopt same empirical constants and wall-damping functions as in a single-phase Newtonian flow. A lack of understanding of the transition and turbulence in non-Newtonian fluid has limited the applicability of RANS/LES-DEM in non-Newtonian suspension flows. Despite a few studies exist on investigating transition and turbulence in shear-thinning fluid, which will be briefly covered in section 2.3, general RANS and LES models are still unavailable for shear-thinning fluids.

Compared to RANS/LES-DEM, DNS-DEM solves coupled particle-fluid flow without relying on any turbulence models, the DNS attempts to model all time & length scales in the fluid flow. Although being more computationally intensive, DNS-DEM contributes significantly to fundamental understanding of the coupled particle-fluid flow [55]. Particle resolved DNS-DEM is based on the IBM [116] or LBM [100]. In IBM-DEM, the fluid-particle interaction is fully resolved via the immersed boundary method, thus this approach is sometimes called resolved CFD-DEM. This is in contrast to unresolved CFD-DEM (e.g. RANS-DEM) where the particles are smaller than the cell size and empirical correlation (e.g. drag force) is needed for closure of the momentum exchange. IBM-DEM requires the cell size to be much smaller than the particles and directly derives the drag force from the resolved flow field. The drag force is calculated from the pressure and viscous forces acting on the solid surface [116]. A few IBM-DEM studies of suspension flows can be found in [4, 7, 39, 71, 90]. Among them, Alghalibi et al., [4] investigated non-colloidal spherical and rigid particles suspension in Newtonian, shear-thinning and shear-thickening fluids using IBM and proposed a closure model for the suspension shear stress in Newtonian and power-law fluids.

Another type of particle resolved DNS-DEM is the LBM-DEM. The Lattice Boltzmann method has become an established CFD approach for modelling fluid flow in the last two decades. Unlike traditional CFD approach which discretises the macroscopic continuum equations based on finite-difference, finite-volume or finite-element methods, LBM solves the fluid flow as fictive particles that propagate and collide over a discrete lattice mesh. Due to its particulate nature, simple implementation and parallel scalability, LBM has several advantages over traditional CFD approach, particularly in modelling flow applications with complex boundaries and interfacial dynamics [2, 137, 148]. Nie and Lin [85] used three 2D particles as representation of cylinders in a power-law fluid and carried out LBM simulations on particle-fluid interaction. Qi et al. [100] carried out LBM study of non-Newtonian fluid flow through a packed bed of porosity 0.366. The study was conducted with different power-law index ($0.6 < n < 1.4$) and particle Reynolds number from $0.1 \sim 500$. Effects of bed porosity and particle size on the flow of power-law fluids through packed beds were evaluated and a modified drag correlation was proposed [99]. In particle resolved DNS-DEM, the fluid-particle interaction is fully resolved and thus is computationally expensive. Current IBM/LBM-DEM studies are mostly limited to flow systems of $O(10^3)$ particles [64] and are practically confined to the laminar flow regime and specific applications.

Summary

Solid-liquid suspension flows are widely encountered in industrial applications. Many empirical correlations and layer models are available for predicting conventional Newtonian suspension flows, however such comprehensive analysis are lacking for non-Newtonian suspensions. Techniques including experimental and modelling approaches have been applied for investigations of non-Newtonian suspension flows. Experimental techniques can reproduce the actual flow behaviour of non-Newtonian suspensions but can be difficult to implement and are limited to specific applications. CFD codes for coupled particle-fluid flow can be categorised as continuum and discrete approaches based on the modelling length and time scales. Among them, the TFM and CFD-DEM are widely used in modelling suspension flows. Effective use of TFM requires defining the complex constitutive equations for the solid phases, while a lack of understanding of the transition and turbulence in non-Newtonian fluid has limited the applicability of RANS/LES-DEM in non-Newtonian suspension flows. DNS-DEM solves coupled particle-

fluid flow without relying on any turbulence models and contributes significantly to its ability to provide fundamental understanding of the underlying physics. However, particle resolved DNS-DEM (e.g., LBM/IBM-DEM) are computationally intensive and are limited to systems of $O(10^3)$ particles. For laminar non-Newtonian suspension flows, a consensus has been reached that coarse particles settling can occur. However, less is known for coarse particle settling in a turbulent non-Newtonian flow. Predicting the flow in a turbulent regime is more difficult due to the inherent stochastic nature of fluid turbulence and its interaction with coarse particles. How and to what degree the carrier fluid rheology, particularly the yield stress $\boldsymbol{\tau}_y$, would support particle suspension in a turbulent flow regime remains unclear. A comprehensive parametric study on how carrier rheology and solids properties affect the turbulent non-Newtonian suspension flows is needed.

2.3 Turbulence in shear-thinning fluids

Transition and turbulence in shear-thinning fluids is still poorly understood. This has limited the applicability of RANS/LES-DEM in non-Newtonian suspension flows. There have been a number of experimental studies on the transition and turbulence for shear-thinning flow in a pipe [36, 37, 91]. However, the experimental degradation of the model carrier with time makes it difficult to keep the non-Newtonian system uniform in obtaining the desired flow. Additionally, some polymer additives [37] used in the experiment bring a certain degree of visco-elasticity to the carrier thus it can not represent the shear-thinning properties as found in actual concentrated suspensions.

Compared to experiment, computational modelling is more effective in understanding transition and turbulence in shear-thinning fluids. There have been a few RANS and LES studies on non-Newtonian turbulence. Wu [146] tested the performance of different Reynolds-averaged turbulence models in simulating mechanical agitation of power-law fluids in a anaerobic digestion tank. Among them, the standard $k-\omega$ models and realizable $k-\epsilon$ were found to have better prediction than the other RANS models. Malin [78] extended a low Reynolds number $k-\epsilon$ model to a turbulent pipe flow of power-law fluids. The wall damping function was modified and results were found to match relatively well with experiments. Kyoungchul and Honsun [105] developed a high Reynolds number $k-\epsilon$ model for shear-thinning fluids. The effect of drag reduction was

included in the wall and damping functions. A major concern in high Reynolds number RANS model is that they still adopt same empirical constants valid for Newtonian fluid. Sawko [113] and Mehta et al. [80] derived rheology dependent wall functions to make up this limitation but these correlations were theoretically derived with approximations and were not applicable to real application.

Gnambode et al. [51] carried out LES of power law ($n = 0.5 \sim 1.4$) fluids in a turbulent pipe flow with $Re = 4000 \sim 12,000$. They investigated the effect of flow index n and Reynolds number on the higher-order turbulence statistics and found the features of the power-law fluids could be well reproduced with the conventional Lilly [74] and Germano et al. [42] subgrid-scale (SGS) model. Based on the Newtonian Smagorinsky model, Ohta and Miyashita [87] incorporated the effect of non-Newtonian rheology and developed an extended SGS model for shear-thinning fluids. A correction for the filter width of the locally varying viscosity for shear-thinning fluids was proposed. The predictions using the extended SGS model were more consistent with the DNS results in their study. However, a universal criteria for the filter width correction for different type of non-Newtonian fluid was lacking. Further investigation into suitable SGS models are still required before LES of shear-thinning flows could be undertaken reliably.

Direct numerical simulation (DNS) is promising in understanding transition and turbulence in shear-thinning fluids. Despite not being applicable to high Re turbulent flow, it attempts to simulate the turbulence exactly without relying on any turbulence model, thus the uncertainty in RANS/LES model can be eliminated. DNS of turbulent visco-elastic flow [27, 103, 135] has been used to investigate the causes of drag reduction. Ohta and Miyashita [87] conducted DNS of various shear-thinning fluids via a high-order finite-difference code. The DNS code adopted a time-explicit finite difference method with a structured mesh, thus is valid only for simple geometries [128]. Based on a high order Spectral element-Fourier code *Semtex*, Rudman et al., [108, 109] and Singh et al., [120] carried out DNS of turbulent shear-thinning flow in a pipe. The shear-thinning turbulence structures were found to be more transitional compared to an equivalent Newtonian flow. Despite the high order accuracy of the spectral element method, its successful implementation required a homogeneous direction in the Fourier (axial) direction. This set constrains on the spectral element method and could only be applied to limited flow conditions.

Summary

Transition and turbulence in shear-thinning fluids is still not well understood and general RANS and LES models are unavailable. Suitable wall functions for RANS and SGS model for LES require further investigation. DNS is promising in understanding transition and turbulence in shear-thinning fluids, but current DNS studies of turbulent non-Newtonian fluids are constrained to simple geometries and limited flow conditions. A more general-purpose DNS approach is needed in applications where more complex geometries are involved such as pipe bends, mixing vessels and other process equipment.

2.4 Literature review summary

A wide variety of techniques including experiments and modelling approaches ranging from continuum to discrete methods have been applied for investigations of non-Newtonian suspension flows. However, general approaches and theoretical models for predicting non-Newtonian suspension behaviour are still lacking because of their complexity.

Experimental measurement can capture most aspects of a suspension flow but the degradation of the model carriers used in typical lab experiments with time makes it difficult to keep the non-Newtonian system uniform in time. In addition, experiments are generally expensive and time-consuming. Importantly, detailed measurements such as velocity and concentration distributions are difficult, particularly for dense suspension flows. In contrast to experiments, the TFM and CFD-DEM are two widely used modelling approaches for suspension flows. However, defining the complex constitutive equations for the solid phases can be difficult in TFM and a lack of understanding of the transition and turbulence in non-Newtonian fluid has limited the applicability of RANS/LES-DEM in non-Newtonian suspension flows. DNS-DEM solves the non-Newtonian suspension flow without relying on any turbulence models but particle resolved DNS-DEM (e.g. LBM/IBM-DEM) are computationally intensive and are limited to systems of $O(10^3)$ particles. Thus, such a method cannot be used to directly handle the practical applications of hydraulic conveying that are the focus of this project where particle numbers are of $O(10^5)$ (e.g., a coarse-particle suspension flow with $d_p/D = 1/22$ and $C_v = 0.2$ in a $100\ mm$ pipe).

Despite the presence of previous studies, fundamental understanding of the interaction between non-Newtonian rheology and coarse particles is still unresolved, particularly in the transitional and turbulent flow regimes. Behaviour such as flow regime transition and solids distribution in a turbulent non-Newtonian suspension remains substantially unknown. The effect of carrier fluid rheology, solids properties and pipe size on the pressure drop, velocity and concentration distribution in these flows needs to be investigated.

The above uncertainty motivates this project to investigate the underpinning fundamentals of these flows. This project presents a DNS-DEM model for investigating weakly turbulent coarse-particle non-Newtonian suspension flows in a horizontal pipe. The following questions will be answered:

1. How can non-Newtonian turbulence be reliably modelled, particularly in applications where more complex geometries are involved such as pipe bends?

2. Particle-particle collisions are significant in high concentration suspensions. How can the detailed particle-particle interaction be correctly captured? How can the particle interaction with non-Newtonian rheology be reliably modelled?

3. Suspension flows of interest in this project have particle numbers of $O(10^5)$, how can DNS be made computationally feasible for the non-Newtonian turbulence?

4. Despite a few experimental studies available, most of these flows are with high $Re >> 15,000$ (where DNS is not feasible) and detailed measurements of velocity and concentration distributions in dense suspension flow are lacking. How can the DNS-DEM model be validated for weakly turbulent flow regime?

5. What is the effect of carrier fluid rheology on non-Newtonian suspension flows? Will yield stress help to suspend the particles during a turbulent suspension flow?

6. What is the effect of solids properties and pipe size on the turbulent non-Newtonian suspension flows? What's the similarity and difference compared to an equivalent Newtonian suspension flow?

To answer these questions, a suitable modelling framework will be developed & validated in the following chapters.

3

DNS of Shear-Thinning Non-Newtonian Turbulence

The desirability of developing a general CFD framework for simulating transition & turbulence in non-Newtonian fluids is discussed in Chapter 3. The ideal model is expected to accurately capture the non-Newtonian turbulence and work efficiently in flow situations where complex geometries are involved. Many bespoke codes are available for modelling the non-Newtonian turbulence but are limited to applications in simple geometries. In this chapter, a flexible DNS approach for modelling the turbulence in shear-thinning fluids is presented utilising the open source CFD library OpenFOAM. OpenFOAM is selected as it has been widely used in modelling turbulent flow and complex geometries can reliably be accommodated by the adopted finite volume approach together with unstructured meshes [66]. In addition, the modularly-structured feature in OpenFOAM makes it feasible to couple with DEM [52] for describing coarse-particle non-Newtonian suspension flow. To assess OpenFOAM for its accuracy and efficiency in DNS of shear-thinning fluids, DNS results of turbulent Newtonian and shear-thinning flow in a periodic pipe using OpenFOAM are compared to those from *Semtex* - a validated spectral element DNS code [13]. Although pipe flow is a simple geometry, this approach can be easily extended to more complex flow domains by changing the mesh.

This chapter is presented by publication. A paper summary is provided and details of the study are covered in the paper.

3.1 Paper summary

DNS of turbulent Newtonian and shear-thinning non-Newtonian flow in a periodic pipe using OpenFOAM are conducted. DNS results of Newtonian fluids predicted by OpenFOAM correspond very well with the *Semtex* and experimental data. DNS quality is obtained for both the mean velocity and turbulence intensities profiles. The maximum error observed is 4.1% when predicting the radial turbulence intensity. DNS predictions of shear-thinning fluids are being more transitional with lower radial and azimuthal but higher axial turbulence intensities. Despite this, the first and second order turbulence statistics differ by at most 16%, and usually much less. The discrepancy between the codes decreases as the Reynolds number increases, with a maximum difference of 10% for $Re_G = 7,500$. OpenFOAM is severely memory bandwidth bound that scaling within the node (from 1 to 8 CPUs) is quite poor, while it appears very differently when scaling out to multiple nodes and OpenFOAM scales very well from 8 to 512 CPUs. The number of grid nodes per CPU to achieve optimum parallel efficiency is found to be $32,000$.

Overall, despite the comparatively low order spatial discretisation schemes used in OpenFOAM, the predicted first and second order turbulence statistics for turbulent shear-thinning flows are in good agreement with the DNS reference, particularly with mean viscosity profiles being predicted to be almost the same. On this basis, this modelling approach can be recommended and will form the basis of future work that aims to couple OpenFOAM with DEM for describing coarse-particle non-Newtonian suspension flow, an application that has significant interest in the disposal of mining waste streams.

3.2 Publication

The article Zheng, E.Z., Rudman, M., Singh, J. and Kuang, S.B., Direct numerical simulation of turbulent non-Newtonian flow using OpenFOAM. *Appl. Math.*72:50-67(2019) is reproduced with permission Elsevier Publishing, Copyright 2019.

Applied Mathematical Modelling 72 (2019) 50–67

Contents lists available at ScienceDirect

Applied Mathematical Modelling

journal homepage: www.elsevier.com/locate/apm

Direct numerical simulation of turbulent non-Newtonian flow using OpenFOAM

E.Z. Zheng[a,*], M. Rudman[a], J. Singh[a], S.B. Kuang[b]

[a] Department of Mechanical and Aerospace Engineering, Monash University, VIC 3800, Australia
[b] ARC Hub for Computational Particle Technology, Department of Chemical Engineering, Monash University, Clayton, VIC 3800, Australia

ARTICLE INFO

Article history:
Received 17 September 2018
Revised 31 January 2019
Accepted 5 March 2019
Available online 11 March 2019

Keywords:
Turbulent pipe flow
Shear-thinning fluid
Generalized Newtonian fluid
Direct numerical simulation (DNS)
OpenFOAM

ABSTRACT

Understanding transition and turbulence in the flow of shear-thinning non-Newtonian fluids remains substantially unresolved and additional research is required to develop better computational methods for wall-bounded turbulent flows of these fluids. Previous DNS studies of shear-thinning fluids mainly use purpose-built codes and simple geometries such as pipes and channels. However in practical application, the geometry of mixing vessels, pumps and other process equipment is far more complex, and more flexible computational methods are required. In this paper a general-purpose DNS approach for shear-thinning fluids is undertaken using the OpenFOAM CFD library. DNS of turbulent Newtonian and non-Newtonian flow in a pipe flow are conducted and the accuracy and efficiency of OpenFOAM are assessed against a validated high-order spectral element-Fourier DNS code – *Semtex*. The results show that OpenFOAM predicts the flow of shear-thinning fluids to be a little more transitional than the predictions from *Semtex*, with lower radial and azimuthal turbulence intensities and higher axial intensity. Despite this, the first and second order turbulence statistics differ by at most 16%, and usually much less. An assessment of the parallel scaling of OpenFOAM indicates that OpenFOAM scales very well for the CPUs from 8 to 512, but the intranode scalability is poor for less than 8CPUs. The present work shows that OpenFOAM can be used for DNS of shear-thinning fluids in the simple case of pipe flow, and suggests that more complex flows, where flow separation is often important, are likely to be simulated with accuracies that are acceptably good for engineering application.

1. Introduction

Many fluids in industrial applications including pipeline transport, polymer processing and biological applications exhibit complex non-Newtonian behaviour i.e. they show a non-uniform viscosity. For a special class of non-Newtonian fluids called generalised Newtonian (GN) fluids, the viscosity is well-approximated by a function of shear rate alone. Under conditions in which the flow is laminar due to significant yield stress or high effective viscosity, models and simulations can be reliably used to predict GN fluid flows. Practically, a wide variety of non-Newtonian fluids show generalised Newtonian behaviour, in particular shear-thinning behaviour for which the fluid viscosity decreases with increasing shear rate. For some lower viscosity non-Newtonian fluids, the flow can be transitional or become turbulent under expected operating conditions. For

* Corresponding author.
E-mail address: enzu.zheng@monash.edu (E.Z. Zheng).

https://doi.org/10.1016/j.apm.2019.03.003
0307-904X/

suspension transport in a pipe for example, it is advantageous to operate in a transitional regime because this results in the lowest energy consumption [1]. Despite their practical importance, the understanding of transition and turbulence in shear-thinning fluids is still significantly unresolved. Additional research is required to develop better computational methods for wall-bounded turbulence in shear-thinning fluids.

There have been a number of experimental investigations on the transitional and turbulent pipe flow of GN fluids [2–4]. Experiments can provide an accurate description of non-Newtonian flow behaviour but it can be difficult to design appropriate laboratory fluids in which the rheological properties can be adjusted as needed. In addition, certain degree of visco-elasticity can be present in some polymer additives [5] (especially at higher shear rates typical of turbulent flow), which complicates the physics and which results in fluids that are not representative of the industrial fluids (e.g. fine particle suspensions) they are attempting to model.

Considering the difficulty of the experiments, computational modelling is an effective means to understand transition and turbulence in shear-thinning fluids. Based on a low Reynolds number k–ε model, Malin [6] extended it to power-law fluids in a turbulent pipe flow. Results corresponded reasonably well with experiments after modifying the wall damping functions. A more generally used high Reynolds number k–ε model for GN fluids was developed by Kyoungchul and Honsun [7] with wall and damping functions considering the drag reduction. Mean velocity profiles and friction factors predicted for power-law fluids ($0.4 \leq n \leq 1$) were found to correspond well with experimental results. A major concern in the high-*Re* Reynolds-averaged Navier-Stokes (RANS) model is that the standard wall functions are not strictly valid for GN fluids. Although rheology dependent wall functions have been investigated by Sawko [8] and Mehta et al. [9], they are theoretically derived with necessary approximations and pose serious difficulty in practical application. Wu [10] evaluated six Reynolds-averaged turbulence models for mechanical agitation of power-law fluids in a lab-scale anaerobic digestion tank. The realizable k–ε and the standard k-ω models were suggested to be more reliable than the other turbulence models. Overall, Reynolds-averaged approach requires partially empirical parameters and suitable wall functions that are not yet available for GN fluids. Additionally, the Reynolds-averaged approach does not provide an insight into the turbulent flow structure. Large Eddy Simulation (LES) has also been performed to study the transition-to-turbulent non-Newtonian blood flow through a 3D model of arterial stenosis by using five different blood viscosity models including power-law and Casson models [11]. Gnambode et al. [12] conducted LES of turbulent pipe flow of power-law fluids ($0.5 \leq n \leq 1.4$) at Reynolds number 4000, 8000 and 12,000, most features of the GN fluids could be reproduced with the conventional Germano et al. [13] and Lilly [14] subgrid-scale (SGS) turbulence model. Ohta and Miyashita [15] evaluated the capability of an extended SGS model with a correction for the filter width of the locally varying viscosity for various GN fluids. The mean velocity profiles predicted by the extended model rather than the standard model were more consistent with the DNS results. However, further investigation on suitable SGS models is still required for additional improvement to LES of GN fluid flows.

Direct numerical simulation (DNS) is a promising approach to understand transition and turbulence in GN fluids. We acknowledge that DNS is not feasible for higher Reynolds numbers where other techniques such as LES or RANS would be better suited, provided validated closure models can be developed. However there is significant scope of utilisation of DNS in practical application and a validated DNS can be reliably applied to model flow behaviour and capture the details of turbulent structure that are difficult to obtain experimentally. In addition, the effect of varying rheological parameters of a selected rheology model can be unambiguously studied using DNS. DNS has been used to investigate the causes of drag reduction in the turbulent flow of visco-elastic fluids [16–18]. Ohta and Miyashita [15] performed high-order finite-difference DNS of various GN fluids. That DNS code used a time-explicit finite difference method in combination with a structured mesh, which worked well only for simple geometries like boxes or squares [19,20]. Rudman et al. [21,22] and Singh et al. [23] conducted DNS of the turbulent flow of GN fluids using the validated Spectral element—Fourier code *Semtex*. The turbulence structures were found to be larger and weaker for shear-thinning fluids compared to equivalent Newtonian fluids. Adding yield stress to the fluid gave rise to a flow that, at the same Reynolds number, was predicted to be more transitional [24]. The *Semtex* code achieves spectral accuracy on unstructured meshes but requires a homogeneous direction in the Fourier direction (axial), which limits its applicability to a rather limited set of flow domains. This latter limitation is apparent in the majority of previous DNS studies of turbulent non-Newtonian fluids and suggests the need for more general-purpose DNS approach for practical applications such as mixing vessels, pumps, eccentric annulus in drill pipe and other process equipment, where the geometries can be complex and even time-dependent. This is the motivation for the current study.

Complex geometries can be reliably represented using an unstructured finite volume mesh. The open source CFD library OpenFOAM, which based on finite volume method, has been widely used in modelling turbulent flow. Although the finite volume method in combination with unstructured meshes limits the order of spatial discretization compared to other DNS approaches, OpenFOAM has demonstrated its DNS capability in a variety of applications including chemically reacting flow [25], non-premixed syngas combustion [26], turbulent channel and pipe flow [27,28] and drag reduction of a turbulent duct flow [18]. These simulation results agree very well with the reference data. However, most of these studies work on Newtonian fluids or visco-elastic fluids, and very few have investigated OpenFOAM for DNS of turbulent shear-thinning Generalised Newtonian fluids. There are some studies of shear-thinning fluids using OpenFOAM, but most of them are for laminar flow [29] or adopt the RANS model for turbulent flow [30]. In addition, OpenFOAM is open-source and modularly-structured, making it feasible to couple with a discrete element method (DEM) for describing coarse-particle non-Newtonian suspension flow, an application that has significant interest in the disposal of mining waste streams. This is currently being undertaken using the open source LIGGGHTS package [31] and the CFDEM coupling library [32].

Given the limitations of many DNS approaches for shear-thinning fluids, this paper applies a more general-purpose approach by using OpenFOAM. Predictions of DNS using OpenFOAM and *Semtex* [33] are compared for a turbulent pipe flow of both Newtonian and shear-thinning fluids. The parallel performance of OpenFOAM is also assessed. Our aim is to understand the accuracy and efficiency of OpenFOAM in DNS simulation of turbulent shear-thinning fluids and to attempt to quantify the magnitude of errors that may arise. We will demonstrate that OpenFOAM is a viable option for such flows, and provide some quantification on the levels of error that might be expected in practice.

2. Non-Newtonian rheology

2.1. Rheology model

A generalised Newtonian model is used to describe the rheology of the fluids considered in this study. The fluid stress tensor is expressed as the product of an isotropic viscosity η and the rate-of-strain tensor $\boldsymbol{S} = \frac{1}{2}(\nabla \boldsymbol{U} + (\nabla \boldsymbol{U})^{\mathrm{T}})$, where $\boldsymbol{U}$ is the velocity vector and T represents the matrix transpose.

$$\boldsymbol{\tau} = 2\eta(\dot{\gamma})\boldsymbol{S} \tag{1}$$

The viscosity η is a function of shear rate, $\dot{\gamma}$ defined as the second invariant of the rate-of-strain tensor

$$\dot{\gamma} = (2\boldsymbol{S} : \boldsymbol{S})^{1/2} \tag{2}$$

In the present work, Herschel-Bulkley (HB) model is used, which is expressed as

$$\eta = \frac{\tau_Y}{\dot{\gamma}} + K\dot{\gamma}^{n-1} \tag{3}$$

where K is the consistency, n is the flow index, and τ_Y is the fluid yield stress. HB model shows shear-thinning behaviour for $n < 1$ and with $\tau_Y = 0$, it reduces to a power-law rheology model.

2.2. Generalized Reynolds number

Owing to the non-uniform viscosity, it is difficult to define a Reynolds number for non-Newtonian fluids. Although different viscosity scales can be selected, the option of mean wall viscosity, η_w is used here based on a discussion of various options for wall-bounded flows in [22]. For HB fluid, the mean wall viscosity is given as:

$$\eta_w = \frac{K^{1/n}\tau_w}{(\tau_w - \tau_Y)^{1/n}} \tag{4}$$

where τ_w is the mean wall shear stress which for a given pressure gradient $\partial p/\partial z$ can be calculated from:

$$\tau_w = \frac{D}{4}\frac{\partial P}{\partial Z} \tag{5}$$

Here D is the pipe diameter. Similar to a Newtonian flow, the generalized Reynolds number is defined with the constant Newtonian viscosity being replaced by the mean wall viscosity as:

$$Re_G = \frac{\rho U D}{\eta_w} \tag{6}$$

Details of the near wall flow are significant in understanding transition and the turbulence in wall-bounded flows of shear-thinning fluids. Although it is difficult to completely establish the validity of the GN rheology model, past studies of GN fluids have been found to agree reasonably well with the experiments [21].

3. Numerical methods

3.1. Non-dimensionalisation

Similar to the Newtonian flow, wall units are used to present results with the mean wall viscosity replacing the constant Newtonian viscosity. The formula for friction velocity is expressed as

$$U_\tau = \sqrt{\frac{\tau_w}{\rho}} \tag{7}$$

The non-dimensional velocity is defined as

$$U^+ = \frac{U}{U_\tau} \tag{8}$$

and the non-dimensional distance from the wall in a pipe is defined as

$$y^+ = \frac{\rho U_\tau}{\eta_w}(R - r) \tag{9}$$

where R is the pipe radius, r is the radial distance from the pipe center.

Table 1
Details of mesh size and spacing for different meshes used with OpenFOAM. The periodic pipe length is fixed at $L = 4\pi D$ in all meshes.

Mesh Resolution	Coarse	Medium	Fine
Number of cells (million)	1.4	4.1	8.0
r^+, $(R\theta)^+$ and z^+	1.0, 9.4, 14.1	0.5, 5.7, 9.4	0.5, 4.7, 5.7

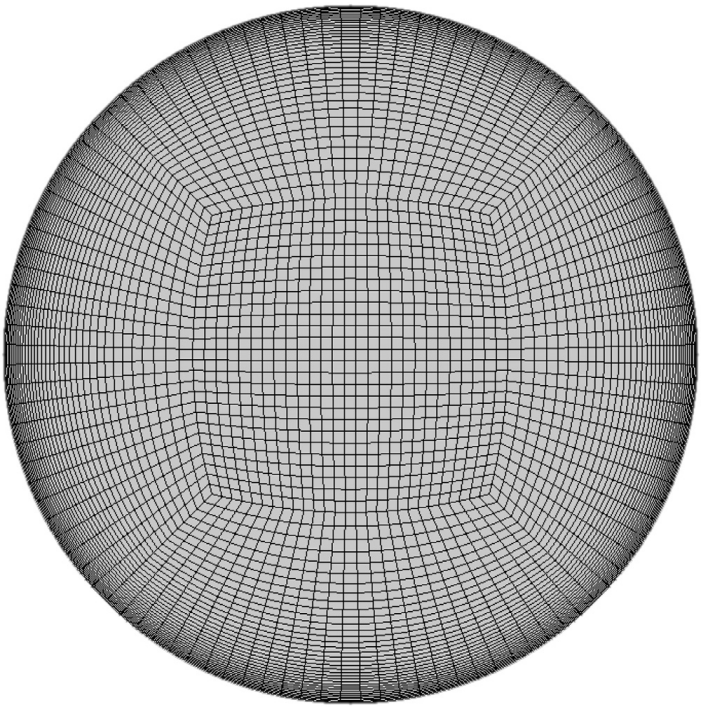

Fig. 1. Cross-sectional view of the 4.1 million cell OpenFOAM mesh.

3.2. Governing equations

The general conservation equations of mass and momentum for both Newtonian and non-Newtonian constant-density flow without gravity are as follows,

$$\nabla \cdot \boldsymbol{U} = 0 \tag{10}$$

$$\partial \mathrm{U}/\partial \mathrm{t} + \nabla \cdot (\mathrm{UU}) = -\nabla \mathrm{P} + \nabla \cdot \left\{ \nu \left(\nabla \mathrm{U} + (\nabla \mathrm{U})^{\mathrm{T}} \right) \right\} \tag{11}$$

Here the pressure has been divided by the uniform density and a non-uniform kinematic viscosity $\nu = \eta/\rho$ is used. Viscosity is modelled via a HB rheology model as described in Section 2.1.

3.3. Implementation in OpenFOAM

3.3.1. Domain discretization

The domain considered here is periodic in the axial direction with length $L = 4\pi D$ and is the same as used in earlier DNS studies at similar Reynolds numbers [21–23]. Although a pipe geometry lends itself to a cylindrical polar coordinate system, OpenFOAM does not support cylindrical coordinates by default. Of equal importance, because we are ultimately interested in simulation in non-uniform geometries, hexahedral meshes are used and simulations undertaken in Cartesian coordinates. Hexahedral meshes are generated using ICEM-CFD and results are transformed to present them in cylindrical coordinates. Understanding the mesh requirements for these flows is one focus of this work and three different mesh resolutions are considered (details given in Table 1). In the near-wall region ($r/R > 0.55$) the mesh-spacing follows a geometric progression to generate 36 layers in the radial direction giving finer mesh elements near the wall. In the axial direction, meshes are uniformly distributed**.** Fig. 1 displays the cross-section of a structured hexahedral mesh of size 4.1 million, and the other two meshes are qualitatively similar.

3.3.2. Initial and boundary conditions

Following the approach developed by De Villiers [34], the Newtonian simulations are initialized with a perturbed laminar velocity distribution to get a fully developed flow field. To achieve this, a laminar background velocity profile is initially

Table 2
Specification of the DNS solver.

Term	Description
Solver names	icoFoam nonNewtonianIcoFoam (non-Newtonian)
Solver type	Pressure-based, segregated solver
Time dependence	Transient
Pressure-velocity coupling	PISO
nCorrectors (pressure corrector loops)	2; 4 (non-Newtonian)
nNonOrthogonalCorrectors	1
transportModel	Newtonian; HerschelBulkley (non-Newtonian)

Table 3
Discretization schemes for the DNS solver.

Term	Type	Scheme Description
ddtSchemes	backward	Second order, implicit, potentially unbounded
gradSchemes	Gauss linear	Second order, unbounded
divSchemes	Gauss linear	Second order, unbounded
LaplacianSchemes	Gauss linear limited 1	Second order, bounded, with nonorthogonal corrections.
interpolationSchemes	linear	Second order, unbounded
snGradSchemes	limited 1	Second order

assumed, the base parabolic flow is then modified to produce parallel near-wall streaks of slow and faster moving fluid. Afterwards, a spanwise velocity component normal to the streaks is introduced to give them the wavy character that in turn produces streamwise vortices. Detailed equations for adding the superimposed streamwise and spanwise streaks can be found in [34]. For the non-Newtonian simulations, the fully developed Newtonian flow is used as the initial field. Standard no-slip boundary condition is applied at the pipe wall. Following the approach proposed by Patankar et al. [35], the pressure field in the pipe is split into a fluctuating periodic part and a non-periodic part, where the non-periodic part can be introduced into the source term in the momentum equation. A body force per unit mass equivalent to the pressure gradient estimated in Section 3.5 is applied to the z-momentum equation throughout the entire run for periodic pressure implementation to drive the flow in this direction.

3.3.3. Averaging procedure

Once the flow has become randomly unsteady, typically, 10 Flow Through Times (FTT $= L/\bar{U}$ where $\bar{U}$ is the bulk flow mean velocity) are required for the flow to develop into a statistically steady state after initialization. Afterwards, 30 FTTs are applied for accumulating statistics and an additional averaging in both the axial and azimuthal directions is done before extracting profiles that are only a function of radius. Mean bulk flow velocity and wall shear stress are established as indicators for sensitivity analysis in order to assure the flow is statistically developed before accumulating the turbulence statistics. The choice of 30FTTs is found to reduce statistical uncertainties of the mean and root mean square (RMS) velocity profiles to within 0.5% and 1%, respectively.

3.3.4. Solver and solution scheme settings

The IcoFoam and nonNewtonianIcoFoam [36] solvers are used for the DNS of Newtonian and shear-thinning fluids, respectively. The default pressure-velocity coupling algorithm PISO in OpenFOAM is selected. The specification of the DNS solver can be found in Table 2. IcoFoam and nonnewtonianIcoFoam stand for transient solvers for incompressible laminar flow of Newtonian fluids and non-Newtonian fluids, respectively. The appropriate discretization schemes and linear solvers are selected according to previous DNS studies of Newtonian fluids using OpenFOAM [27,28]. The discretization schemes are shown in Table 3 and all the schemes used are of second-order accuracy. The “Gauss” entry specifies the standard finite volume discretisation of Gaussian integration and “linear” entry means linear interpolation or central differencing. The snGradSchemes stands for surface normal gradient schemes. Gauss Linear scheme is unstable and can give unphysical results. The solution can be stabilised by applying the limited scheme to the non-orthogonal correction which requires a coefficient between 0 and 1. More details regarding numerical schemes in OpenFOAM can be found in [36]. For the linear solvers, p is solved with the Pre-conditioned Conjugate Gradient (PCG) solver with the Diagonal Incomplete-Cholesky (DIC) pre-conditioning. The velocity $\boldsymbol{U}$ is solved with a smoothSolver with a corresponding symGaussSeidel smoother. Solver tolerances of 10^{-6} are set for both p and $\boldsymbol{U}$ to assure the variable have been solved with adequate accuracy. Due to the higher core viscosity in non-Newtonian fluid, two extra corrector loops are applied to add stability in the simulation [30]. A smaller time step of 1e-4 s is initially used to maintain solver stability and gradually increased to 1e-3 s. The maximum Courant–Friedrichs–Lewy (CFL) number is 0.6. For each simulation, it generally takes 48 h for flow to develop into a statistically steady-state when running on 64 CPUs, and another 144 h for accumulating statistics.

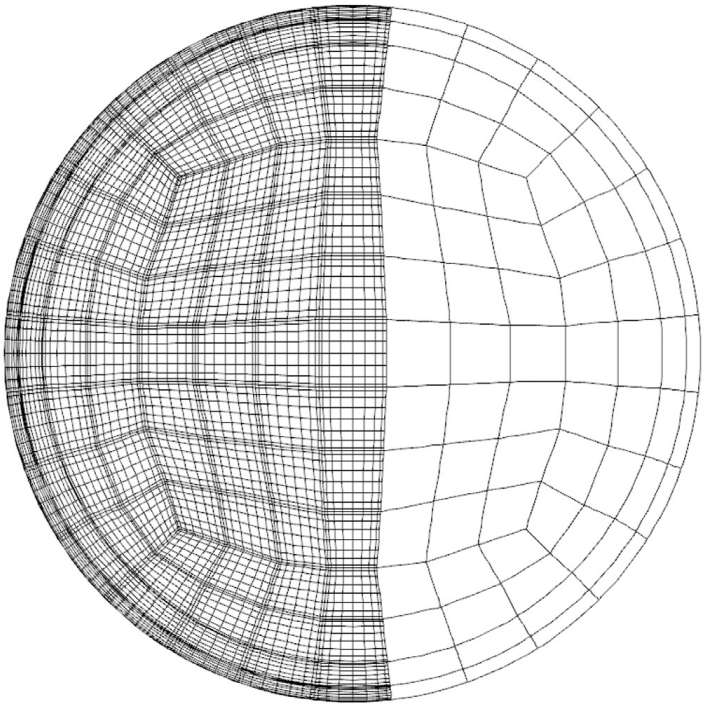

Fig. 2. Cross-sectional view of the *Semtex* mesh. (Right: elemental mesh, left: basis function nodal points).

3.4. Implementation in Semtex

Semtex is a validated spectral element simulation code primarily used for DNS of an incompressible flow [33]. The 3D spatial discretization of the computational domain is subdivided into two dimensions of isoparametrically mapped quadrilateral spectral elements, with Fourier expansions in the third orthogonal direction in which the flow is periodic [37]. Importantly for this study, the code is spectrally convergent meaning that results converge faster than any power of the mesh spacing provided sufficient mesh resolution is used. More details of the *semtex* code can be found in [21,33]. Validation of the code for application in turbulent flow has been undertaken for both Newtonian fluids [23] and, less completely, for non-Newtonian fluids [21,22].

As in OpenFOAM, a body force equal to the pressure gradient is applied in *Semtex* for periodic pressure implementation to drive the flow in the axial direction. The computational domain is made up of 161 9th-order elements in the pipe cross-section and 96 Fourier modes (i.e. 192 data planes) in the axial direction, with a domain length of $4\pi D$. The cross-section view of a *Semtex* mesh is shown in Fig. 2. The total number of grid nodes is 2.6 million and the near-wall mesh resolution in non-dimensional wall units is $r^+ \approx 0.85$, $(r\theta)^+ \approx 4.8$ and $z^+ \approx 22.4$. The current mesh resolution has been demonstrated to be sufficiently well-resolved at comparable Reynolds number [22]. Statistics are accumulated over 30 FTTs after reaching statistically steady state. A step size of 1e-3 s is used and the maximum CFL number is 0.023. For each simulation, it generally takes 18 h for flow to develop into a statistically steady-state when running on 64 CPUs, and another 54 h for accumulating statistics.

3.5. Computational parameters for pipe flow simulations

Because we consider numerical simulations of shear-thinning fluids that can be categorised as undergoing weak turbulence, a Reynolds number of 5000 is used as a DNS benchmark test for the Newtonian fluid. For the non-Newtonian fluid, flow at Re_G=5000 is only marginally turbulent and we consider bulk flow Reynolds number of both 5000 and 7500. The simulation parameters in *Semtex* and OpenFOAM are shown in Table 4. Blasius correlation [38] is used to calculate the pressure gradient for Newtonian fluid and the Wilson and Thomas correlation [39] is used for HB fluids for given rheological parameters. Since the pressure gradient is estimated from empirical correlations and remains uniform throughout the entire run, the actual Re_G is slightly different from the target Re_G. In addition, because the HB model has a singular viscosity at zero shear rate, a "cut-off" value equal to 10^{-5} times the mean shear rate is implemented. Experience has demonstrated that this is rarely (if ever) switched on during a simulation, and thus does not appear to introduce any significant errors or stability problems [22]. The "cut-off" shear rate is 0.01/s in this study and value below this is assumed to be constant for calculating the viscosity.

Table 4
Dimensional parameters for the pipe flow simulations (Note: the pipe diameter is 0.1 m; fluid density is 1000 kg m^{-3}; expected superficial flow velocity is 1m s^{-1}; $n = 0.65$).

Sim.	$\partial p/\partial z$	τ_Y	K	*Semtex*		OpenFOAM	
	$kg \bullet m^{-2} \bullet s^{-2}$	$kg \bullet m^{-1} \bullet s^{-2}$	$kg \bullet m^{-1} \bullet s^{n-2}$	Actual $\boldsymbol{U}$	Re_G	Actual $\boldsymbol{U}$	Re_G
Newt	1.88e+02	N/A	N/A	0.999	4992	1.002	5011
HB1	1.48e+02	6.62e-02	1.22e-01	0.951	4757	1.003	5018
HB2	1.34e+02	4.28e-02	9.09e-02	0.928	6980	0.981	7277

The actual $\boldsymbol{U}$ defines the predicted Re_G.

Table 5
The Re_{MR} and generalized Hedstrom number for HB fluids.

Sim	*Semtex*				OpenFOAM			
	Re_G	Re_{MR}	He	f	Re_G	Re_{MR}	He	f
Newt	4992	4995	N/A	9.4e-03	5011	5010	N/A	9.4e-03
HB1	4757	4162	23	8.2e-03	5018	4389	23	7.4e-03
HB2	6980	6115	23	7.8e-03	7277	6464	23	7.0e-03

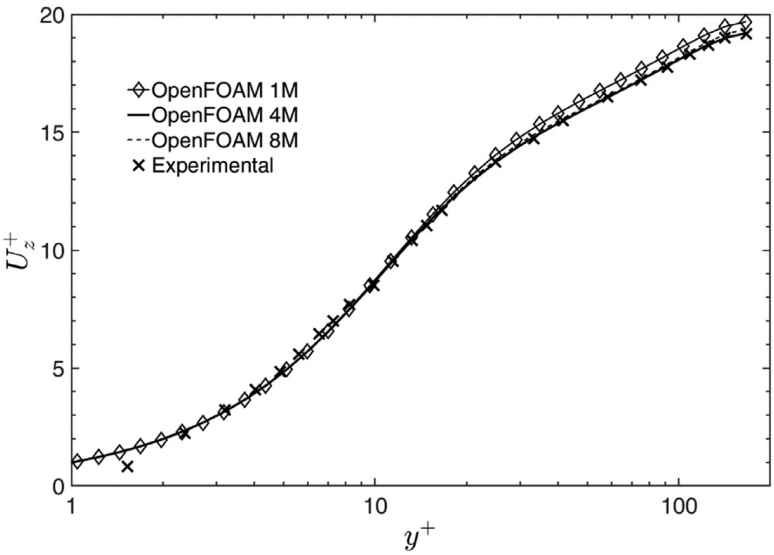

Fig. 3. The mean velocity profiles predicted for different grids (See Table 1) and experimental results [42].

Since it is common to use Metzner-Reed Reynolds number (Re_{MR}) for power-law fluids, a similar Reynolds number for HB fluids can be defined according to [40]. The Re_{MR} and generalized Hedstrom number (He) [41] for HB fluids as well as the fanning friction factor $f = 2\tau_w/(\rho \bar{U}^2)$ are quoted in Table 5 as a reference for readers.

4. Results

4.1. Mesh resolution & requirements for DNS in OpenFOAM

The mesh-resolution requirements for DNS in OpenFOAM are evaluated by comparing mean velocity and turbulence intensities profiles of Newtonian fluids (Re=5000) based on three different number of grid nodes, which are 1.4, 4.1 and 8.0 million, respectively. The near-wall mesh resolution for these meshes is given in Table 1. We also compare the first and second order turbulence statistics with the time-step size 1e-3 s and 1e-4 s. Despite very slight improvements of the results at a smaller time-step 1e-4 s (not shown), we have chosen 1e-3 s as the time step size in our future simulations considering the computation time and efficiency. Fig. 3 shows that the mean velocity profiles predicted using 4.1 M and 8.0 M grids are in reasonable agreement with each other and with the data available in the literature, while the results based on the 1.4 M resolution show the highest (although still acceptable) discrepancies, with the error at the peak being 2.7%.

The turbulent intensities predicted with different mesh-resolutions are shown in Fig. 4. Results indicate the difference between 4.1 M and 8.0 M cases is negligible and the resolution of 4.1 M is adequate for the current simulations. Note that experimental measurements near the wall are difficult and are stated as being inaccurate there [43]. This is clearly seen in Fig. 4b by the large discrepancies in radial turbulence intensity for $y^+ < 20$. The 1.4 M simulation underestimates the radial and azimuthal turbulence intensities. In terms of the axial intensity, the resolution of 1.4 M gives more transitional

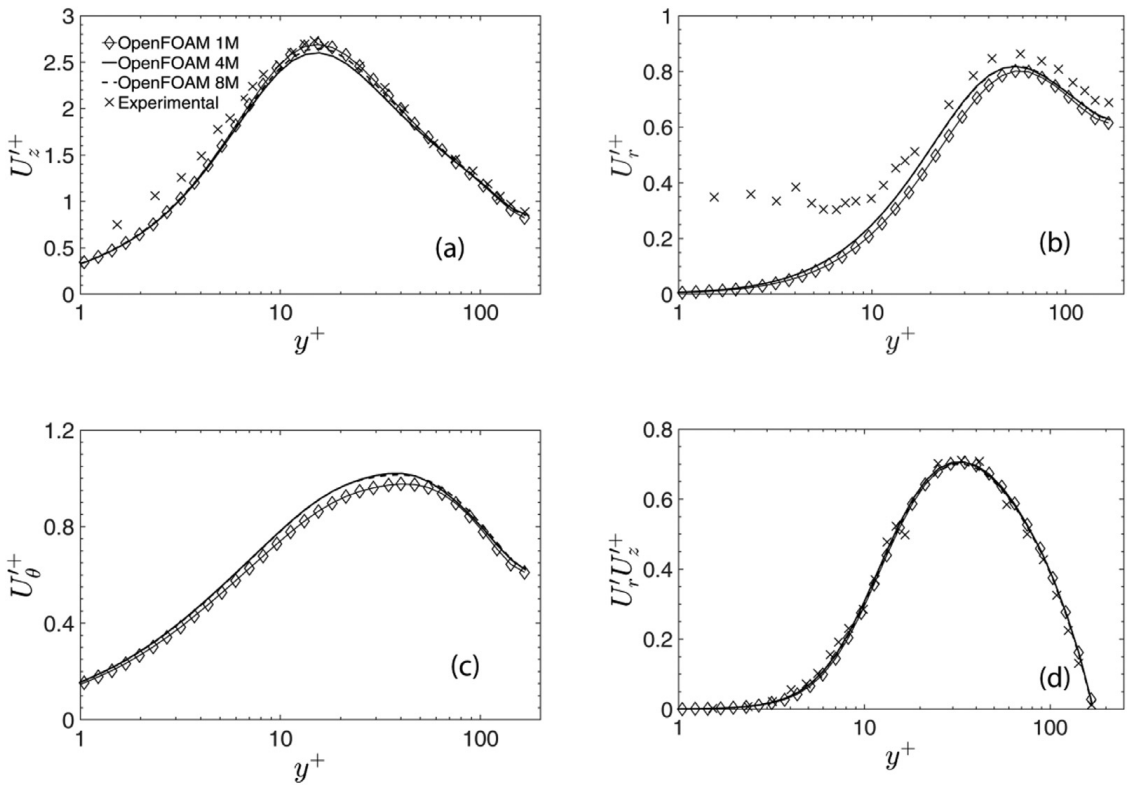

Fig. 4. The turbulence intensities and Reynolds shear stress profiles predicted for different grids and experimental results [42] (a) axial, (b) radial, (c) azimuthal and (d) Reynolds shear stress.

results with higher axial intensity, and results based on the resolution of 4.1 M and 8.0 M deviate from experimental results of Den Toonder and Nieuwstadt [42] by approximately 4.8% and 3.1%, respectively. The Reynolds shear stress profiles of all meshes agree well with each other and the experimental data. These results suggest that the turbulence intensities are more difficult to resolve than the Reynolds shear stress. Despite the relatively lower order of discretisation schemes applied in OpenFOAM, the DNS study shows all the profiles appear to be well represented and the flow well resolved. Overall, simulations with the resolution of 4.1 M provide predictions with adequate accuracy. In terms of the wall units, the resolution of 4.1 M corresponds to a near wall mesh spacing of $r^+ \approx 0.5$, $(r\theta)^+ \approx 5.7$ and $z^+ \approx 9.4$, with relatively coarser resolution being applied close to the pipe centerline in the pipe cross-section.

4.2. Mean flow profiles for the Newtonian case

The DNS results predicted by OpenFOAM and *Semtex* for a Newtonian fluid are compared in this section to the experimental data of Den Toonder and Nieuwstadt [42]. The mean flow profiles are shown in Fig. 5 and turbulence intensities profiles in Fig. 6.

As seen in Fig. 5, the mean velocity profile predicted by OpenFOAM is very close to the experimental data. Results also correspond very well with the difference between OpenFOAM and *Semtex* within 0.6% difference at the peak. The conventional 'Law of the wall' non-dimensionalisation is plotted for comparison of the mean velocity profiles. Both OpenFOAM and *Semtex* results display a linear relationship between U^+ and y^+ in the near wall region and a log profile $U^+ = A + B \ln y^+$ in the logarithmic region, with the values of A and B being 5.5 and 2.5, respectively. These values are more suitable to use for low Reynolds number such as considered here [42].

In terms of the turbulence intensities and Reynolds shear stress, the profiles correspond well but OpenFOAM results show slight underestimations, especially at the peaks for the radial and azimuthal turbulence intensities. The difference for the axial intensity at the peak is 1.1%, while the differences for the radial and azimuthal intensities at the peak are higher at 4.1% and 3.0% respectively. *Semtex* seems to display a better prediction when compared to the experimental data (although experimental measurements near the wall are difficult and stated as being inaccurate there by Durst et al. [43]). The Reynolds shear stress profiles are also similar and are within 3% of each other. Fig. 7 shows the mean non-dimensionalised shear rate profiles for a Newtonian fluid, which are included here to compare with non-Newtonian results in Section 4.3. It can be seen that OpenFOAM slightly underpredicts the shear rate compared to *Semtex*, however, as seen earlier in Figs. 5 and 6, it does not affect the mean velocity, turbulence intensity and Reynolds stress predictions to a significant extent. Overall, DNS predictions using OpenFOAM are in a good agreement with experiments and *Semtex*. The maximum difference with OpenFOAM is 4.1% in predicting the peak radial turbulence intensity compared to *Semtex*.

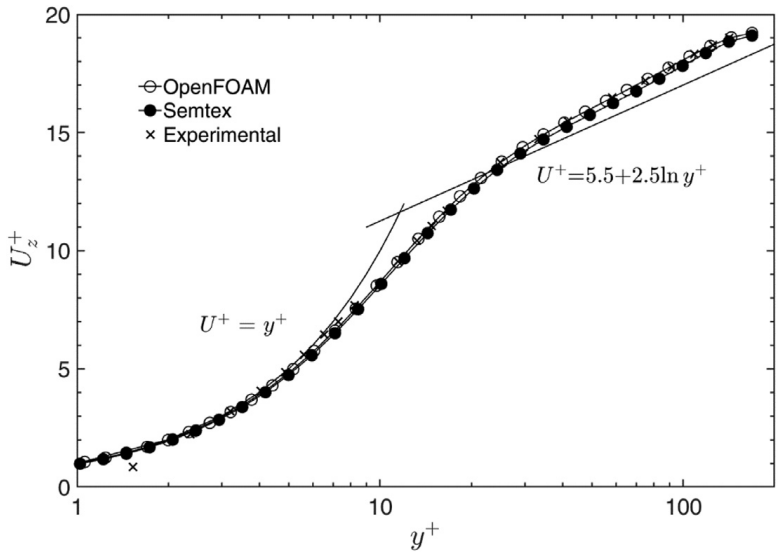

Fig. 5. Mean velocity profiles for the turbulent pipe flow and experimental results [42] (Newtonian, $Re = 5000$).

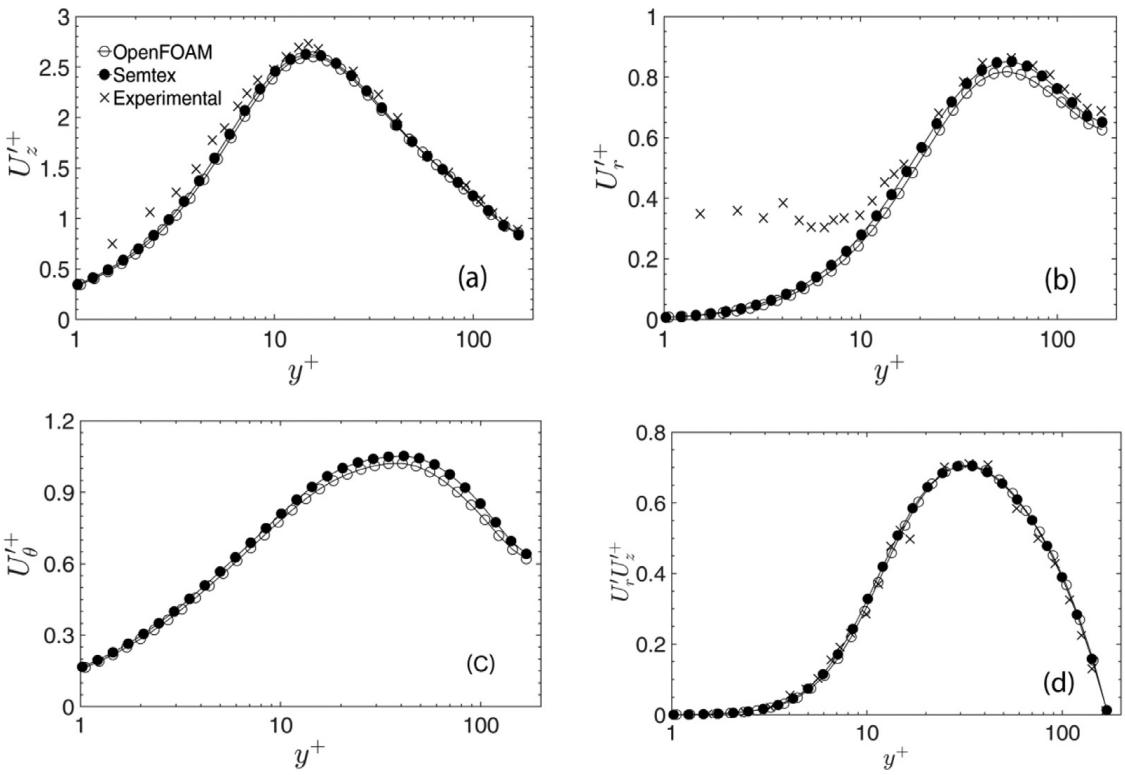

Fig. 6. Turbulence intensities and Reynolds shear stress profiles and experimental results [42] (Newtonian, Re=5000) (a) axial, (b) radial, (c) azimuthal and (d) Reynolds shear stress.

4.3. Results for shear-thinning fluids

4.3.1. Velocity and viscosity contours

Instantaneous velocity contours for both Newtonian and HB fluids are shown in Fig. 8. These contours indicate the level of unsteadiness and turbulence development in the flow. The contours predicted by OpenFOAM and *Semtex* display a qualitatively similar pattern. An apparent difference is observed between the results for the Newtonian and HB fluids as well as between the two HB fluids with different Re_G. As demonstrated in previous work at similar Reynolds number [21], the Newtonian fluid is predicted to display flow behavior close to fully developed turbulence, generating random and small-scale fluctuations in every direction. The HB fluid with Re_G of 7500 shows a similar random, unsteady flow behavior but larger scale turbulent structure compared to the Newtonian fluid. For the HB fluid with a lower Re_G of 5000, the unsteady structure is significantly larger with decreased unsteadiness predicted. The high-speed core appears more like

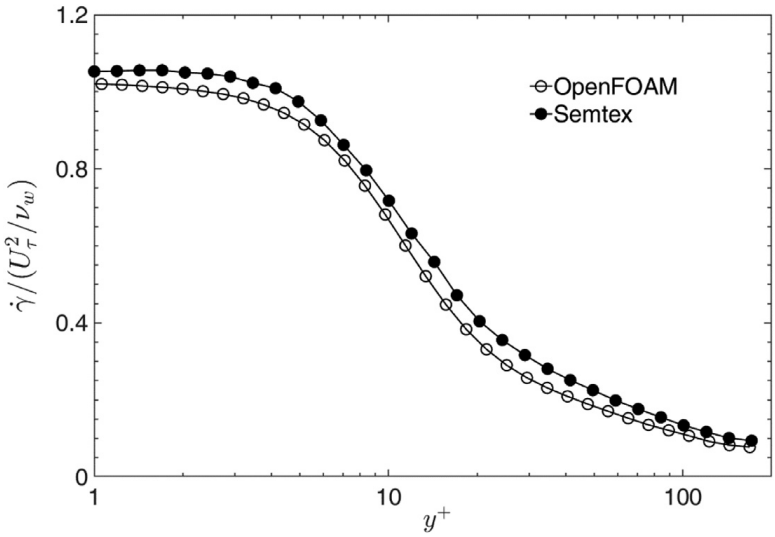

Fig. 7. Mean shear rate profiles in a Newtonian fluid.

a spiral structure that spreads along the entire domain, suggesting that the flow is predicted to be transitional, and not well-developed turbulence. Viscosity contours of the HB fluids are shown in Fig. 9, and the contour scales for each plot are identical and non-dimensionalised with the mean wall viscosity. As can be seen, the near wall viscosity is significantly lower than that predicted in the core of the flow.

4.3.2. Mean flow profiles of shear-thinning fluids

The mean velocity profiles of the HB fluids with Re_G of 5000 and 7500 are shown in Fig. 10a. All the non-Newtonian velocity profiles lie slightly above the low Reynolds number Newtonian profile, revealing the flow is predicted to be less fully developed compared to a Newtonian fluid at the same Reynolds number. The non-Newtonian law of the wall for GN fluids has been investigated by Clapp [44], Sawko [8] and Anbarlooei et al. [45]. The proposed law of the wall for both power-law and HB fluids by Anbarlooei et al. [45] (dashed line in Fig. 10a) is also plotted for comparison, which suggests a better agreement with the mean velocity profiles compared to the Newtonian law of the wall. The OpenFOAM predictions show generally acceptable agreement in terms of shape and magnitude compared to the profiles simulated with *Semtex*, although the profiles predicted with OpenFOAM lie slightly higher, again suggesting OpenFOAM predicts the flow to be more transitional. For fluids with the same Re_G, velocity profiles correspond very well in the near-wall sub-layer and all display a linear behaviour. However, in the log-law and core region, the relative differences between OpenFOAM and *Semtex* velocity profiles for shear-thinning fluids are higher than in the Newtonian case. The differences at the peak for Re_G of 5000 and 7500 are 2.7% and 5.7%, respectively.

Fig. 10b shows that the mean viscosity predictions from OpenFOAM also agree very well with those from *Semtex*. More puzzling is that the mean shear rate predictions from the two codes are different, especially in the near wall region (shown in Fig. 11, compare open and closed triangles for Re_G=5000 and squares for Re_G=7500). The difference in predicted wall shear rate is approximately 12%, which is three to four times larger than the shear rate difference predicted for the Newtonian fluid in Fig. 7. Despite this difference, it appears that the discrepancy in shear rate has a negligible effect on the predicted viscosity from the HB rheology model. If the mean shear profile is used to calculate a viscosity profile (not shown), the 12% difference in the shear rate at the wall corresponds to around a 4% difference in viscosity for this model and shear rate range, primarily because the model is dominated by the power law term. For different rheology with higher shear rate, the discrepancy would be different. Nevertheless, the discrepancy in viscosity predicted by the two codes (and shown in Fig. 10b) is less than 1% at the wall indicating that the fluctuating viscosity must also be playing a significant role in viscosity prediction. Details of why this result occurs have not been uncovered.

As can be seen in Fig. 12, OpenFOAM predicts lower radial and azimuthal turbulence intensities whose peaks are further from the wall, especially for $Re_G = 5000$, corresponding to weaker wall streaks. Axial turbulence intensities are predicted to be higher using OpenFOAM, and collectively these results are consistent with OpenFOAM predicting a flow that is more transitional than that predicted by *Semtex*.

For Re_G of 5000, the relative differences in axial, radial and azimuthal turbulence intensities at the peak are 10.0%, 5.9% and 15.7%, respectively. For the higher Re_G of 7500, the profiles correspond better, with relative differences decreasing to 6.3%, 2.0% and 7.7%, respectively. In addition, Reynolds shear stress profiles as shown in Fig. 12 also indicate the results with higher Re_G correspond much better than the flow with lower Re_G.

In summary, the results suggest that the discrepancy between the OpenFOAM and *Semtex* results is likely to be worst for flows that are close to transition, and that better agreement might be reduced for still higher Re_G, although this is currently supposition.

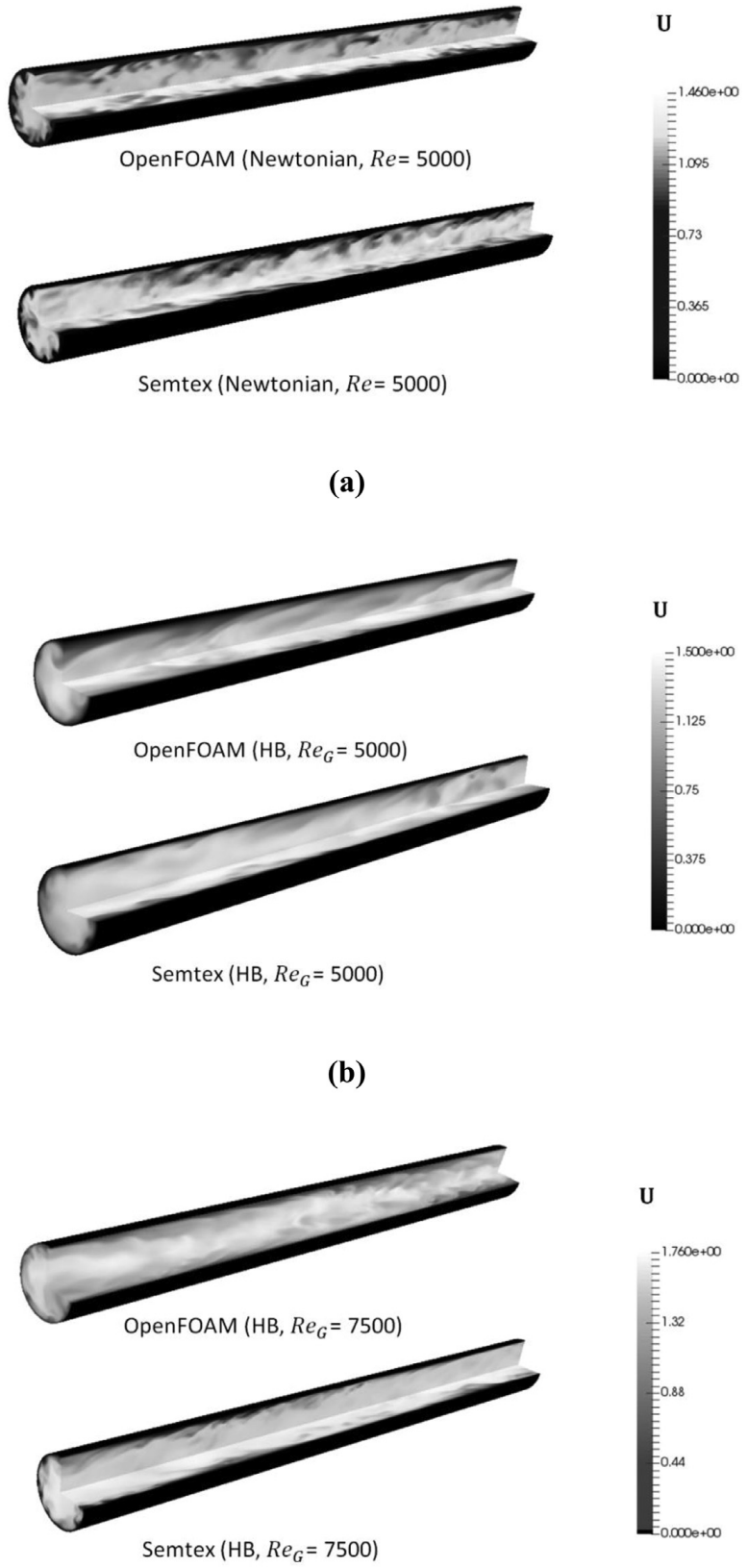

Fig. 8. Instantaneous velocity contours for simulations (a) Newtonian, (b) HB ($Re_G = 5000$) and (c) HB ($Re_G = 7500$).

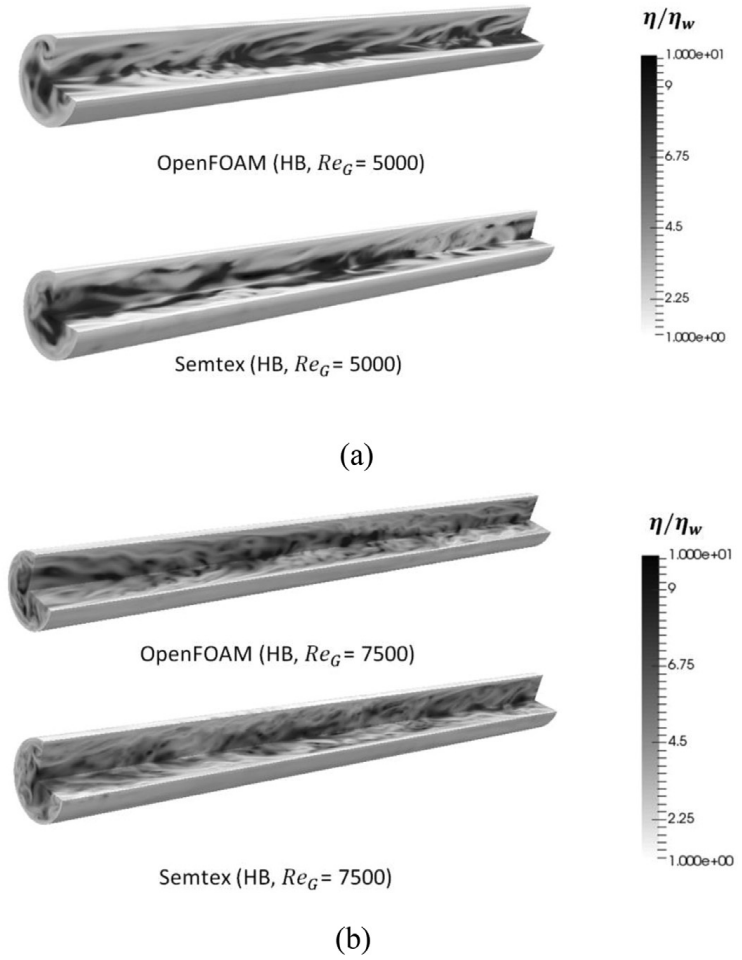

Fig. 9. Instantaneous viscosity contours of shear-thinning fluids at (a) $Re_G = 5000$ and (b) $Re_G = 7500$.

These differences in results for the non-Newtonian fluid were unexpected given that good agreement between OpenFOAM and *Semtex* was obtained for a Newtonian fluid on the 4 M node mesh. Although that agreement was good, it is still possible that the lower order spatial discretization schemes used in OpenFOAM are impacting the results for the non-Newtonian fluids. In addition to the low order schemes, the collocated grid pressure correction used in OpenFOAM is known to give erroneous velocity divergence [46]. Even though we found that the OpenFOAM predictions of mean flow and turbulence intensity profiles for the non-Newtonian fluid at Re_G of 5000 did not significantly change between an 8 M cell mesh compared to 4 M (results not shown), it is possible that further refining the mesh (especially in the azimuthal direction where the worst agreement in turbulence intensity occurs) may help to reduce the effect of these issues, and is now considered.

Consequently, an additional simulation was run for Re_G of 5000 using a 14 million mesh with a near-wall mesh resolution of $r^+ \approx 0.5$, $(r\theta)^+ \approx 3.2$ and $z^+ \approx 4.7$. Compared to the 4 M mesh, this mesh has more than 1.5 times finer mesh-resolution in the azimuthal and axial direction. Fig. 11 shows refining the mesh improves the accuracy of the mean shear rate predictions in the near wall region (compare open diamonds ◊ and open triangles △). Although some slight improvements in mean flow, turbulence intensities and Reynolds stresses were observed (see Figs. 13 and 14), these are not large.

The largest improvement is seen in the Reynolds shear stress predictions with the profile shifted closer to the *Semtex* profile. Although the radial and azimuthal turbulence intensity profiles shift slightly closer to the *Semtex* profiles, these improvements are seen away from the wall for $y^+ > 15$, and do not change in the near wall region. In summary, it is not believed that insufficient mesh resolution causes the difference between OpenFOAM and *Semtex*.

Overall, OpenFOAM predicts most of the mean flow profiles of non-Newtonian fluids to within a few percents of the *Semtex* predictions. Larger errors are seen in the predicted turbulence intensities with the maximum difference up to 15.7% in predicting the peak turbulence intensities for $Re_G = 5000$, although these errors diminish with increasing Reynolds number. Despite the comparatively low order spatial discretisation schemes used in OpenFOAM, it is still capable of providing reasonably good DNS results in modelling turbulent canonical flow for engineering grade simulations. For flows in which turbulence is triggered by geometry and flow separation, rather than flow instability, we might expect this agreement to improve. One factor that could modify this assessment (which is not addressed here) is the use of non-hexahedral meshes

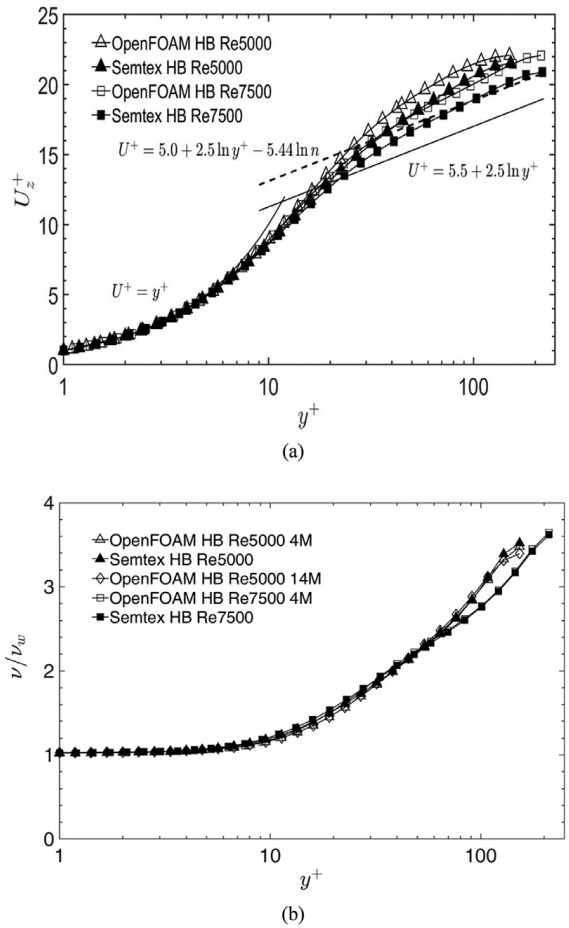

Fig. 10. (a) The mean velocity profiles of shear-thinning fluids – the dashed line is the law of the wall proposed by Anbarlooei et al. [45] (b) mean viscosity profiles of shear-thinning fluids.

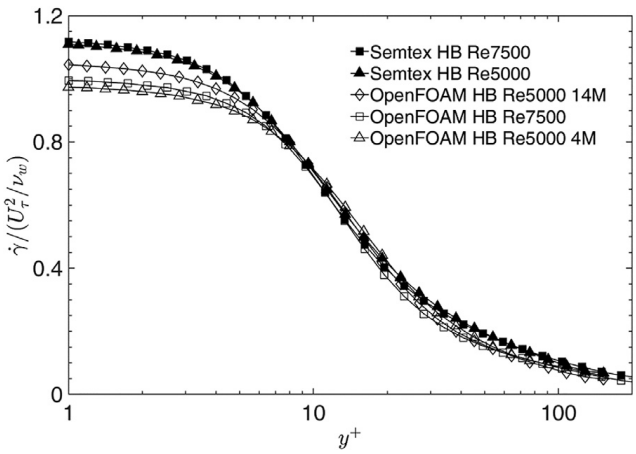

Fig. 11. Mean shear rate profiles of shear-thinning fluids.

in OpenFOAM that could reduce the accuracy of OpenFOAM predictions. Such a study would be a very useful adjunct to the results presented here.

4.4. Performance and parallel scalability

Having seen that OpenFOAM provided acceptable results for turbulent flow of shear-thinning fluids, an assessment of efficiency in these flows is required. Two factors are important, the total execution time and the parallel scalability of the code. Parallel execution of OpenFOAM was performed using MPI (Message Passing Interface). The adopted master-slave configuration and encapsulated bindings in one functional library of OpenFOAM allow easy optimization. However, such flexibility

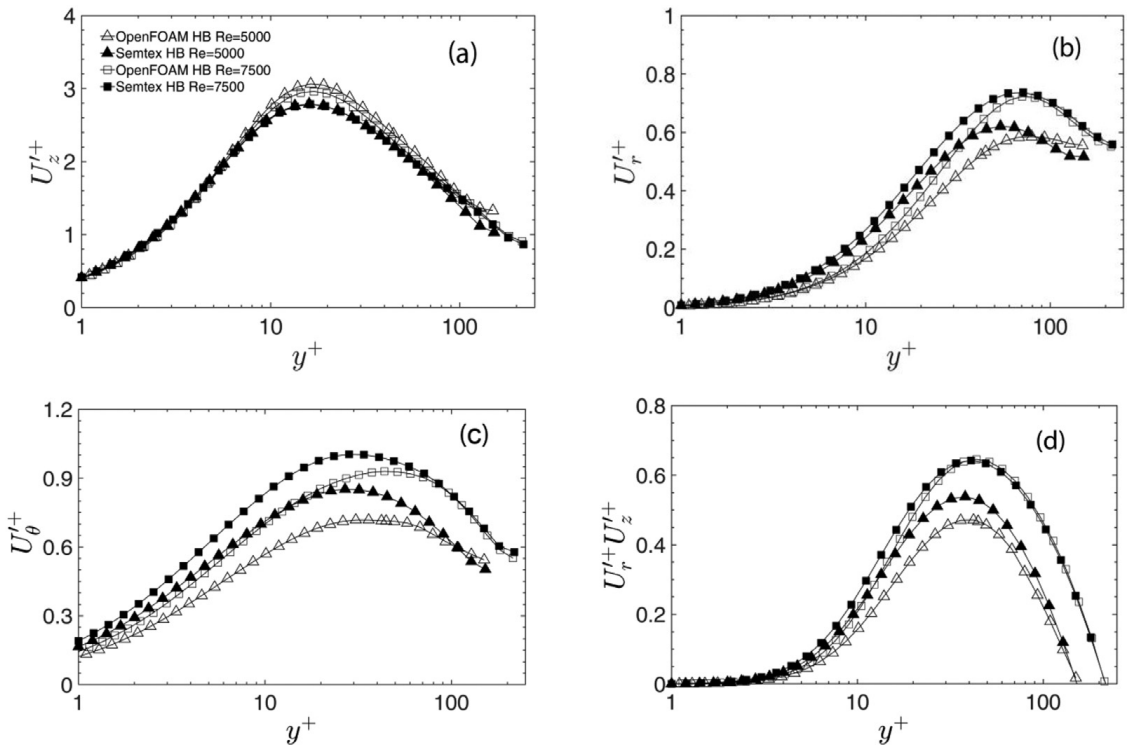

Fig. 12. The turbulence intensities and Reynolds shear stress profiles of shear-thinning fluids (a) axial, (b) radial, (c) azimuthal and (d) Reynolds shear stress.

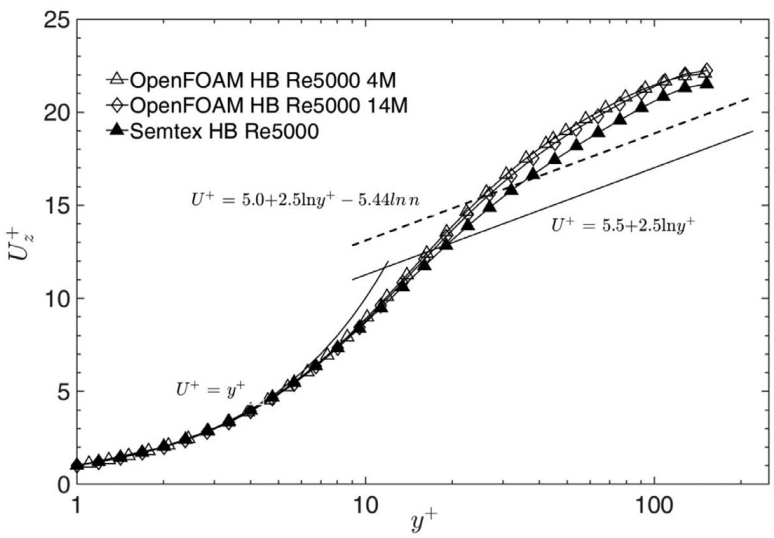

Fig. 13. The mean velocity profiles of shear-thinning fluids predicted for different grids (Re_G=5000).

results in a more complex behavior when running on massively parallel systems [47]. Some studies have been presented recently on the parallel performance and scalability of OpenFOAM. Super linear scalability up to 1024 CPUs [48] and even up to 2048 CPUs [49] has been reported. Parallel performance of OpenFOAM strongly depends on the number of mesh cells on each core, with the optimum number reported to be between 15,000 and 20,000 [47]. For *Semtex*, memory exchanges are also implemented using MPI, the memory exchanges for the parallel solution and method of exchange has been illustrated schematically in [21].

Simulation with OpenFOAM contains 4.1 million grid nodes. The test is done on the number of CPUs from 1 to 512. While for the *Semtex* simulation, the computational domain is made up of 161 9th-order elements in the pipe cross-section and 192 Fourier modes (i.e. 384 data planes) in the axial direction. The simulation contains 3.9 million grid nodes. The test is done on the number of CPUs from 1 to 192, where the maximum number of CPUs can be used for *Semtex* is half the number of Fourier modes. Both simulations are run for 1000 time-steps to calculate the efficiency and minimize the contribution of start-up. All computations are run on the hybrid Fujitsu Primergy and Lenovo NeXtScale high-performance,

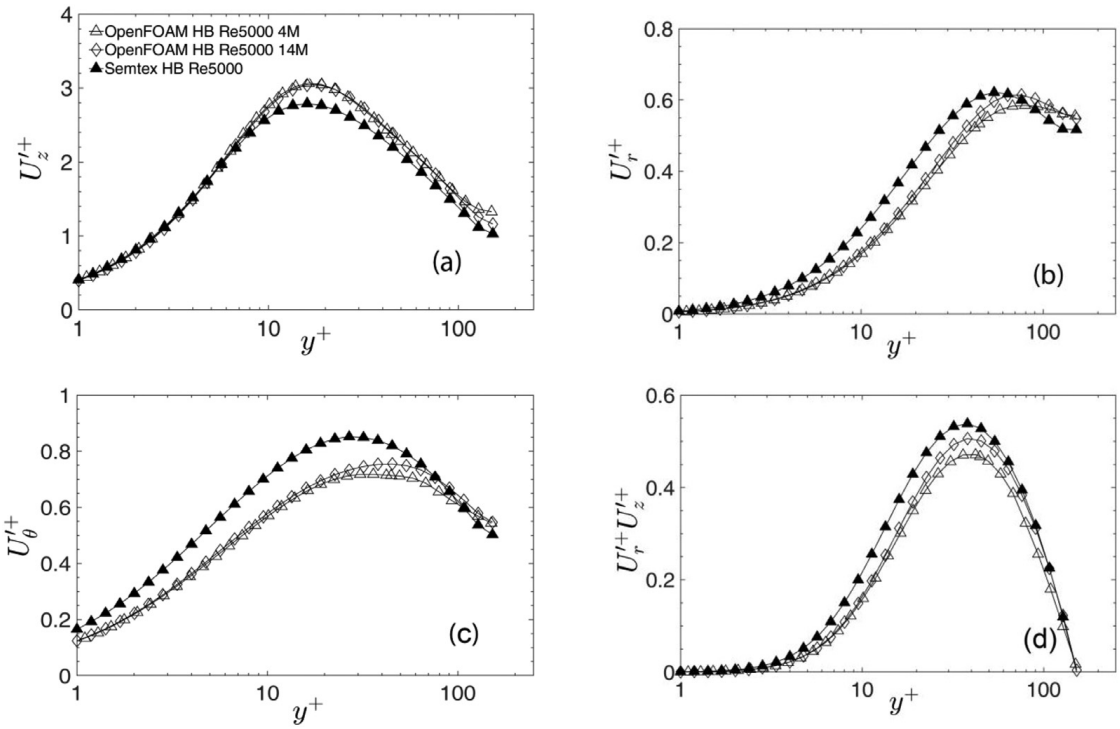

Fig. 14. The turbulence intensities and Reynolds shear stress profiles of shear-thinning fluids predicted for different grids (Re_G=5000) (a) axial, (b) radial, (c) azimuthal and (d) Reynolds shear stress.

Table 6
Parallel performance of the OpenFOAM implementation.

No. CPUs	Total CPU time per time step per million grid nodes (s)	Parallel Efficiency (%)	Total CPU time per 1000 time steps (h)	Wall time per 1000 time steps (h)	Speedup
1	19.4	100.0	22.2	22.156	1
8	63.5	30.6	72.5	9.059	2.4
16	64.2	30.2	73.4	4.585	4.8
32	59.5	32.6	68.0	2.125	10.4
64	49.7	39.0	56.8	0.887	25.0
128	41.4	46.8	47.3	0.370	59.9
256	51.8	37.5	59.1	0.231	95.9
512	80.9	24.0	92.4	0.180	122.8

Table 7
Parallel performance of the *Semtex* implementation.

No. CPU s	Total CPU time per time step per million grid nodes (s)	Parallel Efficiency (%)	Total CPU time per 1000 time steps (h)	Wall time per 1000time steps (h)	Speedup
1	1.6	100.0	1.70	1.703	1
8	2.8	55.4	3.07	0.386	4.4
16	2.7	58.4	2.91	0.183	9.4
32	2.7	58.0	2.93	0.100	18.6
64	3.3	47.0	3.63	0.057	30.0
96	4.0	39.8	4.28	0.045	38.2
192	9.1	17.3	9.87	0.050	33.1

distributed-memory cluster *NCI-Raijin*, which currently comprises of 84,656 cores in 4416 compute nodes. The normal queue of *Raijin* is used and each node has 2×8 core Intel Xeon E5-2670 (Sandy Bridge) 2.6 GHz processors.

The parallel performances of the OpenFOAM and *Semtex* implementation are shown in Table 6 and Table 7, respectively. The parallel efficiency is defined as the total CPU time for 1 CPU divided by the total CPU time for N CPUs. The CPU time per time-step per million grid nodes is used as an indicator to compare the parallel performance of OpenFOAM and *Semtex*. The speedup S_p is defined as the wall time for 1 CPU divided by the wall time for N CPUs.

The execution time (CPU time per time-step per million grid nodes) for *Semtex* computation is significantly less than that of OpenFOAM for any number of CPUs, see Fig. 15. The superior efficiency of *Semtex* is not surprising given the Fourier

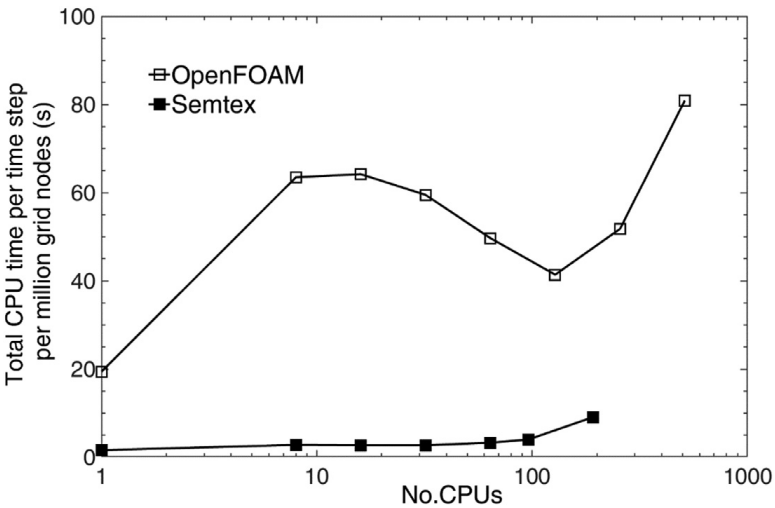

Fig. 15. Comparison of parallel running between *Semtex* and OpenFOAM.

parallelization requires very little inter-CPU communication and the implicit viscous and pressure solves are decoupled across Fourier modes. The efficient parallel running of *Semtex* has been previously demonstrated in [21].

In terms of parallel scalability, OpenFOAM, scales very well from 8 to 512 CPUs, but the intranode scalability from 1 to 8 CPUs is quite poor (interestingly, this is also the case for *Semtex*, although it is a little better, 4.4 vs 2.4 see Tables 6 and 7). An optimum parallel efficiency of 46.8% is achieved with OpenFOAM when using 128 CPUs and the optimum number of grid nodes per CPU is found to be 32,000. The wall time for turning a simulation around using 128 CPUs is 60 times less than 1 CPU. OpenFOAM depends heavily on the iterative solution of sparse linear algebra kernels [50], which is severely memory bandwidth bound. Intranode scaling is very different compared to scaling out to multiple nodes. When scaling to multiple nodes, in addition to the additional CPU resource, there is also additional memory bandwidth available. The saturation of the bandwidth to memory leads to the scalability inside the node being far from optimal [51]. Regardless, the intranode scalability that deviates from linear requires further investigation.

5. Conclusion

In this paper, a flexible DNS approach for modelling the turbulent flow of shear-thinning non-Newtonian fluids was presented that utilises the widely used open source CFD library OpenFOAM. DNS of turbulent flow in a periodic pipe demonstrated that the quality of predictions of both the mean velocity and turbulence intensities profiles in Newtonian fluids compared very well with the DNS reference (computed using a SEM-Fourier code, *Semtex*) and experimental data.

For a shear thinning fluid, OpenFOAM predicts the flow to be a little more transitional than the equivalent results from *Semtex*. The mean flow profiles predicted by OpenFOAM are within a few percents of the references. Profiles of the turbulent intensities and Reynolds stresses are in larger disagreement, with the maximum difference being around 16% when comparing the peak value of turbulence intensities for the shear-thinning fluid at $Re_G = 5000$. The discrepancy between the codes decreased as the Reynolds number increased, with a maximum difference of 10% for $Re_G = 7500$. This suggests that the difficulty associated with accurately predicting transitional flow may be a causal factor in the difference.

Quite reasonable results were obtained here with OpenFOAM on the 4 M node mesh which had near wall grid spacing of $r^+ \approx 0.5$, $(r\theta)^+ \approx 5.7$ and $z^+ \approx 9.4$. Increasing the mesh size from 4 M to 14 M did not show significant improvement in the results for the shear-thinning fluid except providing a slightly better fit for the Reynolds shear stress and a closer y^+ value for the peak in radial and azimuthal turbulence intensities compared to the *Semtex* results. Thus the causes of the differences between OpenFOAM and *Semtex* do not appear related to issues of resolution. They might be in part related to the relatively lower second-order spatial discretisation schemes. This suggestion is not definitive because the turbulent flow of a Newtonian fluid was calculated by OpenFOAM to be within a few percents of the reference data. A related point is that because structured hexahedral meshes were used in this study, additional work that considers more complex geometries with different cell types is recommended as this will potentially impact on the quality of the OpenFOAM predictions.

OpenFOAM scales very well from 8 to 512 CPUs, but the intranode scalability for from 1 to 8 CPUs is poor. OpenFOAM is severely memory bandwidth bound, scaling within the node appear very differently when compare scaling out to multiple nodes. Parallel efficiency of 46.8% is achieved when using 128 CPUs and the wall time for turning a simulation around is 60 times less than for 1 CPU on a 4 M node mesh.

In summary, the results presented here demonstrate that while OpenFOAM does not provide identical results to a high accuracy SEM-Fourier code for DNS of a non-Newtonian shear thinning fluid, the results are quite reasonable with mean flow velocity and viscosity profiles being predicted to be almost the same. Even though there are discrepancies in the second order turbulence statistics, these are not large and will likely not affect predictions where engineering accuracy is

the desired outcome. On this basis, this modelling approach can be recommended and will form the basis of our future work that aims to couple OpenFOAM with a discrete element method (DEM) for describing coarse-particle non-Newtonian suspension flow, an application that has a significant interest in the disposal of mining waste streams.

Acknowledgements

The research was supported by Monash International Postgraduate Research Scholarship and Monash Graduate Scholarship, Monash University, Australia. Computations in this study were carried out with the assistance of resources and services from the National Computational Infrastructure (NCI), which is supported by the Australian Government via merit allocation scheme grant number D77. We gratefully acknowledge the resources and their support. The authors EZ, MR and SK also acknowledge support from the ARC Research Hub for Computational Particle Technology (IH1401001035) in undertaking this research.

References

[1] L. Pullum, D.V. Boger, F. Sofra, Hydraulic mineral waste transport and storage, Annu. Rev. Fluid Mech. 58 (2018) 157–185, doi:10.1146/annurev-fluid-122316-045027.
[2] F. Pinho, J. Whitelaw, Flow of non-Newtonian fluids in a pipe, J. Non-Newton. Fluid Mech. 34 (1990) 129–144, doi:10.1016/0377-0257(90)80015-R.
[3] M. Escudier, F. Presti, Pipe flow of a thixotropic liquid, J. Non-Newton. Fluid Mech. 62 (1996) 291–306, doi:10.1016/0377-0257(96)01417-6.
[4] M. Escudier, F. Presti, S. Smith, Drag reduction in the turbulent pipe flow of polymers, J. Non-Newton. Fluid Mech. 81 (1999) 197–213, doi:10.1016/S0377-0257(98)00098-6.
[5] R. Sureshkumar, A.N. Beris, R.A. Handler, Direct numerical simulation of the turbulent channel flow of a polymer solution, Phys. Fluids. 9 (1997) 743–755, doi:10.1063/1.869229.
[6] M. Malin, Turbulent pipe flow of power-law fluids, Int. Commun. Heat Mass Transf. 24 (1997) 977–988, doi:10.1016/S0735-1933(97)00083-3.
[7] R.O. Kyoungchul, R. HongSun, Development of the modified k-ε turbulence model of power-law fluid for engineering applications, Sci. China 55 (2012) 276–284.
[8] R. Sawko, Mathematical and computational methods of non-Newtonian, multiphase flows, Ph.D. Thesis, Cranfield University, Cranfield, UK, 2012.
[9] D. Mehta, A.K.T. Radhakrishnan, J. van Lier, F. Clemens, A wall boundary condition for the simulation of a turbulent non-Newtonian domestic slurry in pipes, Water 10 (2018) 124, doi:10.3390/w10020124.
[10] B. Wu, CFD investigation of turbulence models for mechanical agitation of non-Newtonian fluids in anaerobic digesters, Water Res. 45 (2011) 2082–2094, doi:10.1016/j.watres.2010.12.020.
[11] M.M. Molla, M. Paul, LES of non-Newtonian physiological blood flow in a model of arterial stenosis, Med. Eng. Phys. 34 (2012) 1079–1087, doi:10.1016/j.medengphy.2011.11.013.
[12] P.S. Gnambode, P. Orlandi, M. Ould-Rouiss, X. Nicolas, Large-Eddy simulation of turbulent pipe flow of power-law fluids, Int. J. Heat. Fluid Flow 54 (2015) 196–210, doi:10.1016/j.ijheatfluidflow.2015.05.004.
[13] M. Germano, U. Piomelli, P. Moin, W.H. Cabot, A dynamic subgrid-scale eddy viscosity model, Phys. Fluids. A Fluid Dyn. 3 (1991) 1760–1765, doi:10.1063/1.857955.
[14] D.K. Lilly, A proposed modification of the Germano subgrid-scale closure method, Phys. Fluids. A Fluid Dyn. 4 (1992) 633–635, doi:10.1063/1.858280.
[15] T. Ohta, M. Miyashita, DNS and LES with an extended Smagorinsky model for wall turbulence in non-Newtonian viscous fluids, J. Non-Newton. Fluid Mech. 206 (2014) 29–39, doi:10.1016/j.jnnfm.2014.02.003.
[16] E. De Angelis, C. Casciola, R. Piva, DNS of wall turbulence: dilute polymers and self-sustaining mechanisms, Comput. Fluids 31 (2002) 495–507, doi:10.1016/S0045-7930(01)00069-X.
[17] T. Tsukahara, T. Ishigami, B. Yu, Y. Kawaguchi, DNS study on viscoelastic effect in drag-reduced turbulent channel flow, J. Turbul. 12 (2011) N13, doi:10.1080/14685248.2010.544657.
[18] E. Rasti, F. Talebi, K. Mazaheri, A DNS investigation of drag reduction phenomenon in turbulent flow of a viscoelastic fluid, J. Solid Fluid Mech. 7 (2017) 255–274.
[19] D. Thévenin, F. Behrendt, U. Maas, B. Przywara, J. Warnatz, Development of a parallel direct simulation code to investigate reactive flows, Comput. Fluids. 25 (1996) 485–496, doi:10.1016/0045-7930(96)00009-6.
[20] N. Babkovskaia, N. Haugen, A. Brandenburg, A high-order public domain code for direct numerical simulations of turbulent combustion, J. Comput. Phys. 230 (2011) 1–12, doi:10.1016/j.jcp.2010.08.028.
[21] M. Rudman, H.M. Blackburn, Direct numerical simulation of turbulent non-Newtonian flow using a spectral element method, Appl. Math Model. 30 (2006) 1229–1248, doi:10.1016/j.apm.2006.03.005.
[22] M. Rudman, H.M. Blackburn, L.J.W. Graham, L. Pullum, Turbulent pipe flow of shear-thinning fluids, J. Non-Newton. Fluid Mech. 118 (2004) 33–48, doi:10.1016/j.jnnfm.2004.02.006.
[23] J. Singh, M. Rudman, H.M. Blackburn, The influence of shear-dependent rheology on turbulent pipe flow, J. Fluid Mech. 822 (2017) 848–879, doi:10.1017/jfm.2017.296.
[24] J. Singh, M. Rudman, H.M. Blackburn, A. Chryss, L. Pullum, L.J.W. Graham, The importance of rheology characterization in predicting turbulent pipe flow of generalized Newtonian fluids, J. Non-Newton. Fluid Mech. 232 (2016) 11–21, doi:10.1016/j.jnnfm.2016.03.013.
[25] F. Zhang, H. Bonart, T. Zirwes, P. Habisreuther, H. Bockhorn, N. Zarzalis, Direct numerical simulation of chemically reacting flows with the public domain code OpenFOAM, High Performance Computing in Science and Engineering '14, Springer, Cham, 2015, pp. 221–236.
[26] S. Vo, A. Kronenburg, O.T. Stein, E.R. Hawkes, Direct numerical simulation of non-premixed syngas combustion using OpenFOAM, High Performance Computing in Science and Engineering´16, Springer, Cham, 2016, pp. 245–257.
[27] S.W. Van Haren, Testing DNS Capability of OpenFOAM and STAR-CCM+, Master's thesis, Delft University of Technology, Delft, The Netherlands, 2011.
[28] E. Komen, A. Shams, L. Camilo, B. Koren, Quasi-DNS capabilities of OpenFOAM for different mesh types, Comput. Fluids 96 (2014) 87–104, doi:10.1016/j.compfluid.2014.02.013.
[29] P. Ternik, New contributions on laminar flow of inelastic non-Newtonian fluid in the two-dimensional symmetric expansion: creeping and slowly moving flow conditions, J. Non-Newton. Fluid Mech. 165 (2010) 1400–1411, doi:10.1016/j.jnnfm.2010.07.007.
[30] E.M. Smuts, A Methodology For Coupled CFD-DEM Modeling of Particulate Suspension Rheology, Doctoral dissertation, University of Cape Town, 2015.
[31] C. Kloss, C. Goniva, A. Hager, S. Amberger, S. Pirker, Models, algorithms and validation for opensource DEM and CFD–DEM, Prog. Comput. Fluid Dyn. Int. J. 12 (2012) 140–152.
[32] C. Goniva, C. Kloss, N.G. Deen, J.A. Kuipers, S. Pirker, Influence of rolling friction on single spout fluidized bed simulation, Particuology 10 (2012) 582–591, doi:10.1016/j.partic.2012.05.002.
[33] H.M. Blackburn, S.J. Sherwin, Formulation of a Galerkin spectral element–Fourier method for three-dimensional incompressible flows in cylindrical geometries, J. Comput. Phys. 197 (2004) 759–778, doi:10.1016/j.jcp.2004.02.013.
[34] E. De Villiers, The Potential of Large Eddy Simulation For the Modelling of Wall Bounded Flows, Doctoral dissertation, University of London, 2007.

[35] S.V. Patankar, C.H. Liu, E.M. Sparrow, Fully developed flow and heat transfer in ducts having streamwise-periodic variations of cross-sectional area, J. Heat. Trans. 99 (1977) 180–186.
[36] C.J. Greenshields, Openfoam User Guide, OpenFOAM Foundation Ltd, version 3.1, 2015.
[37] G. Karniadakis, Spectral element-Fourier methods for incompressible turbulent flows, Comput. Methods Appl. Mech. Eng. 80 (1990) 367–380, doi:10.1016/0045-7825(90)90041-J.
[38] K.T. Trinh, On the Blasius correlation for friction factors (PDF), arXiv:1007.2466, Bibcode:2010 arXiv1007.2466T.
[39] A. Thomas, K. Wilson, New analysis of non-Newtonian turbulent flowndashyield-power-law fluids, Can. J. Chem. Eng. 65 (1987) 335–338, doi:10.1002/cjce.5450650221.
[40] R.A. Chilton, R. Stainsby, Pressure loss equations for laminar and turbulent non-Newtonian pipe flow, J. Hydraul. Eng. 124 (1998) 522–529, doi:10.1061/(ASCE)0733-9429(1998)124:5(522).
[41] M.R. Malin, Turbulent pipe flow of Herschel–Bulkley fluids, Int. Comm. Heat Mass Transf. 25 (1998) 321–330.
[42] J. Den Toonder, F. Nieuwstadt, Reynolds number effects in a turbulent pipe flow for low to moderate Re, Phys. Fluids. 9 (1997) 3398–3409, doi:10.1063/1.869451.
[43] F. Durst, J. Jovanović, J. Sender, LDA measurements in the near-wall region of a turbulent pipe flow, J. Fluid Mech. 295 (1995) 305–335, doi:10.1017/S0022112095001984.
[44] R.M. Clapp, Turbulent heat transfer in pseudoplastic non-Newtonian fluids, Int. Dev. Heat transfer, Part III (1961) 652–661.
[45] H.R. Anbarlooei, D.O.A. Cruz, A.P. Silva Freire, Fully turbulent mean velocity profile for purely viscous non-Newtonian fluids, in: Proceedings of the 15th European Turbulence Conference, Delft, The Netherlands, 2015, pp. 25–28.
[46] F.N. Felten, T.S. Lund, Kinetic energy conservation issues associated with the collocated mesh scheme for incompressible flow, J. Comput. Phys. 215 (2006) 465–484, doi:10.1016/j.jcp.2005.11.009.
[47] G. Axtmann, U. Rist, Scalability of OpenFOAM with large eddy simulations and DNS on high-performance systems, High Performance Computing in Science and Engineering´16, Springer, Cham, 2016, pp. 413–424.
[48] G.J. Pringle, Porting OpenFOAM to HECToR: A dCSE Project, EPCC, The University of Edinburgh, Report, 2010.
[49] A. Duran, M.S. Celebi, S. Piskin, M. Tuncel, Scalability of OpenFOAM for bio-medical flow simulations, J Supercomput. 71 (2015) (2015) 938–951.
[50] K. Asanovic, R. Bodik, B.C. Catanzaro, J.J. Gebis, P. Husbands, K. Keutzer, D.A. Patterson, W.L. Plishker, J. Shalf, S.W. Williams, K.A. Yelick, Technical Report UCB/EECS-2006-183, EECS Department, University of California, Berkeley, 2006.
[51] M. Culpo, Current bottlenecks in the scalability of OpenFOAM on massively parallel clusters, PRACE white paper to appear on http://www.prace-ri.eu 2011.

4

DNS-DEM Coupling Methodology

In Chapter 3, the OpenFOAM platform was demonstrated to be suitable for accurately & reliably simulating turbulence in non-Newtonian fluid. In this chapter, the coupling of OpenFOAM for DNS to a DEM method (LIGGGHTS [65]) via the CFDEM® [52] interface is described. The DNS-DEM governing equations and coupling algorithm between particle and fluid phase are firstly introduced, followed by a discussion of the DNS-DEM coupling procedure implemented in the CFDEM® package. The computational parameters, implementations and mesh resolution requirements are also presented.

4.1 Governing equations

4.1.1 Governing equations for the particle phase

In LIGGGHTS, the governing equations for the particle phase are

$$m_i \frac{d\boldsymbol{v}_i}{dt} = \sum_j \boldsymbol{f}_{ij}^c + \boldsymbol{f}_i^{fp} + \boldsymbol{f}_i^g \tag{4.1}$$

$$I_i \frac{d\boldsymbol{w}_i}{dt} = \sum_j \boldsymbol{M}_{ij} \tag{4.2}$$

For particle i, $\boldsymbol{v}_i$ and $\boldsymbol{w}_i$ represent translational and angular velocity, $\boldsymbol{f}_{ij}^c$ and $\boldsymbol{M}_{ij}$ represent the contact force and torque arising from its interaction with particle j or pipe wall, $\boldsymbol{f}_i^g$ is the gravitational force, and $\boldsymbol{f}_i^{fp}$ represents the particle-fluid interaction force. The calculation of $\boldsymbol{f}_i^{fp}$ will be discussed in Section 4.1.2. The contact force on particle i exerted by particle j is calculated using the soft-sphere contact model [26] as shown below:

$$\boldsymbol{f}_{ij}^c = \boldsymbol{f}_{ij}^{cn} + \boldsymbol{f}_{ij}^{ct} \tag{4.3}$$

$$\boldsymbol{f}_{ij}^{cn} = -k_{ij}^n \delta_{ij}^n \boldsymbol{n}_i - \gamma_{ij}^n (\boldsymbol{v}_r \cdot \boldsymbol{n}_i) \boldsymbol{n}_i \tag{4.4}$$

$$\boldsymbol{f}_{ij}^{ct} = -k_{ij}^t \delta_{ij}^t \boldsymbol{t}_i - \gamma_{ij}^t [(\boldsymbol{v}_r \cdot \boldsymbol{t}_i) \boldsymbol{t}_i + (\boldsymbol{w}_i \times \boldsymbol{r}_i - \boldsymbol{w}_j \times \boldsymbol{r}_j)] \tag{4.5}$$

Here n and t represent the normal and tangential direction, respectively. The distance vector from particle mass centroid to the contact point is written as $\boldsymbol{r}$, $\boldsymbol{v}_r$ is the relative velocity between the two paired particles i and j, k is the spring constant, γ is the damping coefficient and δ represents the overlap of a colliding pair. The calculation of spring constant k and damping coefficient γ is shown in Table 4.1.

Table 4.1 Calculation of spring constant k and damping coefficient γ from the material properties

Spring constant and damping coefficients	Symbol	Equations
Elastic constant for normal contact	k_{ij}^n	$\frac{4}{3}Y^*\sqrt{R^*\delta_{ij}^n}$
Viscoelastic damping constant for normal contact	γ_{ij}^n	$2\sqrt{\frac{5}{6}}\beta\sqrt{S_{ij}^n m^*}$
Elastic constant for tangential contact	k_{ij}^t	$8G^*\sqrt{R^*\delta_{ij}^n}$
Viscoelastic damping constant for tangential contact	γ_{ij}^t	$2\sqrt{\frac{5}{6}}\beta\sqrt{S_{ij}^t m^*}$

where $\frac{1}{Y^*} = \frac{(1-\nu_i^2)}{Y_i} + \frac{(1-\nu_j^2)}{Y_j}$, $\frac{1}{R^*} = \frac{1}{R_i} + \frac{1}{R_j}$, $\frac{1}{m^*} = \frac{1}{m_i} + \frac{1}{m_j}$, $\beta = \frac{\ln(e)}{\sqrt{\ln^2(e)+\pi^2}}$,

$\frac{1}{G^*} = \frac{2(2+\nu_i)(1-\nu_i)}{Y_i} - \frac{2(2+\nu_j)(1-\nu_j)}{Y_j}$, $S_{ij}^n = 2Y^*\sqrt{R^*\delta_{ij}^n}$ and $S_{ij}^t = 8G^*\sqrt{R^*\delta_{ij}^t}$

Here Y is the Young's modulus, G is the shear modulus, ν is the Poisson ratio and e is the coefficient of restitution. These parameters are chosen based on the materials used in the simulation. Further details can be found in [65].

4.1.2 Governing equations for the fluid phase

Governing equations for the carrier fluid follow the conservation laws of mass and momentum [5]. The general 'model A' formulation [151] in CFD-DEM is adopted and pressure is shared between the particle and fluid phase:

$$\frac{\partial \varepsilon_f}{\partial t} + \nabla \cdot (\varepsilon_f \boldsymbol{u}_f) = 0 \tag{4.6}$$

$$\frac{\partial(\rho_f \varepsilon_f \boldsymbol{u}_f)}{\partial t} + \nabla \cdot (\rho_f \varepsilon_f \boldsymbol{u}_f \boldsymbol{u}_f) = -\varepsilon_f \nabla p - \boldsymbol{F}_{fp} + \nabla \cdot (\varepsilon_f \boldsymbol{\tau}) + \rho_f \varepsilon_f \boldsymbol{g} \tag{4.7}$$

Here $\boldsymbol{u}_f$, p, $\boldsymbol{\tau}$ and ε represent the fluid velocity, fluid pressure, fluid stress tensor and fluid volume fraction, respectively. In a non-Newtonian suspension, the Herschel-Bulkley model is used to describe the non-Newtonian rheology of the carrier fluid,

$$\eta = \frac{\boldsymbol{\tau}_y}{\dot{\gamma}} + k\dot{\gamma}^{(n-1)} \tag{4.8}$$

Here $\boldsymbol{\tau}_y$ is the yield stress, n is the flow index, k is the consistency and $\dot{\gamma}$ is the shear rate. The volumetric particle-fluid interaction force $\boldsymbol{F}_{fp}$ is expressed as

$$\boldsymbol{F}_{fp} = \frac{1}{\Delta V}\sum_{i=1}^{m}(\boldsymbol{f}_i^{drag} + \boldsymbol{f}_i^{lift} + \boldsymbol{f}_i^{vm}) \tag{4.9}$$

Here ΔV is the volume of a computational cell and m represents the number of particles in a CFD cell. The $\boldsymbol{f}_i^{drag}$, $\boldsymbol{f}_i^{lift}$ and $\boldsymbol{f}_i^{vm}$ represent the particle-fluid drag force, lift force and virtual mass force on an individual particle i, respectively. The particle-fluid interaction force on an individual particle $\boldsymbol{f}_i^{fp}$ also includes the pressure gradient force $\boldsymbol{f}^p$ and the viscous force $\boldsymbol{f}^{vis}$ and is expressed as

$$\boldsymbol{f}_i^{fp} = \boldsymbol{f}_i^{drag} + \boldsymbol{f}_i^{lift} + \boldsymbol{f}_i^{vm} + \boldsymbol{f}^p + \boldsymbol{f}^{vis} \tag{4.10}$$

Note that in 'model A' the pressure gradient $\boldsymbol{f}^p$ and viscous force $\boldsymbol{f}^{vis}$ are excluded in calculating the volumetric particle-fluid interaction force $\boldsymbol{F}_{fp}$. The drag force on an individual particle is represented by the Gidaspow model [44], which is a combination of the Wen and Yu model [139] and the Ergun equation [35].

$$\boldsymbol{f}^{drag} = \frac{V_p}{\varepsilon_p}K_{fp}(\boldsymbol{u}_f - \boldsymbol{u}_p) \tag{4.11}$$

When $\varepsilon_f > 0.8$, the fluid-solid exchange coefficient K_{fp} is of the following form

$$K_{fp} = \frac{3}{4}C_D\frac{\varepsilon_p\varepsilon_f\rho_f|\boldsymbol{u}_f - \boldsymbol{u}_p|}{d_p}\varepsilon_f^{-2.65} \tag{4.12}$$

with the drag coefficient given by

$$C_D = \frac{24}{\varepsilon_f Re_p}[1 + 0.15(\varepsilon_f Re_p)^{0.687}] \tag{4.13}$$

$$Re_p = \frac{\rho_f d_p |\boldsymbol{u}_p - \boldsymbol{u}_f|}{\eta_f} \tag{4.14}$$

When $\varepsilon_f \leq 0.8$

$$K_{fp} = 150\frac{\varepsilon_p(1-\varepsilon_f)\eta_f}{\varepsilon_f d_p^2} + 1.75\frac{\rho_f \varepsilon_p |\boldsymbol{u}_p - \boldsymbol{u}_f|}{d_p} \tag{4.15}$$

In a non-Newtonian suspension, the Gidaspow model [44] is extended to Herschel-Bulkley (*HB*) fluid with the drag coefficient replaced by correlations developed for spheres settling in an unsheared *HB* fluid [8, 126], while the effect of fluid volume fraction related to the contribution by neighbouring particles remains the same:

$$C_D = \frac{24X_n}{\varepsilon_f Re_{HB}}[1 + 0.15(\varepsilon_f Re_{HB})^{0.687}] \tag{4.16}$$

$$Re_{HB} = \frac{Re_{PL}}{1 + 0.6143 Bi_{HB}} \tag{4.17}$$

Here Re_{PL} is the Reynolds number defined for a power-law fluid, X_n is the deviation factor and Bi_{HB} is the Bingham number. These are of the following forms

$$Re_{PL} = \frac{\rho_f d_p^n |\boldsymbol{u}_f - \boldsymbol{u}_p|^{(2-n)}}{k} \tag{4.18}$$

$$Bi_{HB} = \frac{\boldsymbol{\tau}_y / k}{(|\boldsymbol{u}_f - \boldsymbol{u}_p|/d_p)^n} \tag{4.19}$$

$$X_n = 6^{(n-1)/2}(\frac{3}{(n^2+n+1)})^{(n+1)} \tag{4.20}$$

Here $\boldsymbol{\tau}_y$ is the yield stress, n is the flow index and k is the consistency.

The lift force on a spherical particle is computed based on the Loth and Dorgan model [77], which is an extended formulation of Saffman lift [110] and includes the influence of particle rotation:

$$\boldsymbol{f}^{lift} = 0.125\pi d_p^2 \rho_f C_L(\boldsymbol{u}_f - \boldsymbol{u}_p)[|\boldsymbol{u}_f - \boldsymbol{u}_p| \times \frac{\boldsymbol{\omega}_f}{|\boldsymbol{\omega}_f|}] \tag{4.21}$$

$$C_L = J^* \frac{12.92}{\pi}\sqrt{\frac{\boldsymbol{\omega}^*}{Re_P}} + \boldsymbol{\Omega}^*_{p,eq} C^*_{L,\boldsymbol{\Omega}} \tag{4.22}$$

In a non-Newtonian suspension, Eq. 4.22 is modified with Re_p replaced by Re_{HB}. Here J^* is a function proposed by Mei [81], $\boldsymbol{\omega}^*$ and $\boldsymbol{\Omega}^*$ are magnitude of the vorticity and particle angular velocity. Full details of the Loth and Dorgan lift model can be found in [77] and are not shown here for brevity.

The virtual mass force generated by the acceleration of fluid phase surrounding a particle is expressed as

$$\boldsymbol{f}^{vm} = 0.5\rho_f V_p(\frac{D\boldsymbol{u}_f}{Dt} - \frac{D\boldsymbol{u}_p}{Dt}) \tag{4.23}$$

The pressure gradient force on an individual particle is expressed as

$$\boldsymbol{f}^{p} = -V_p \nabla(p) \tag{4.24}$$

and the viscous force on an individual particle is expressed as

$$\boldsymbol{f}^{vis} = -V_p(\nabla \cdot \boldsymbol{\tau}) \tag{4.25}$$

4.2 Coupling between fluid and particle phase

4.2.1 Conventional CFD-DEM *vs* DNS-DEM

In CFD-DEM, the DEM solves the particle flow at an individual particle level, while CFD solves the carrier fluid at a computational cell level. The CFD-DEM coupling procedure and information exchange is shown in Figure 4.1. For every time step, DEM calculates the location $\boldsymbol{x}_i$ and velocity $\boldsymbol{v}_i$ of individual particles and this information is used to evaluate the fluid volume fraction ε_f and the volumetric interaction force $\boldsymbol{F}^{fp}$ in a fluid computational cell. The CFD solver then solves the fluid equations to update the

fluid velocity $\boldsymbol{u}_f$ and pressure P. The interaction force on an individual particle $\boldsymbol{f}^{fp}$ is subsequently updated and incorporated into the DEM calculation to obtain motion of particles to start next coupling cycle.

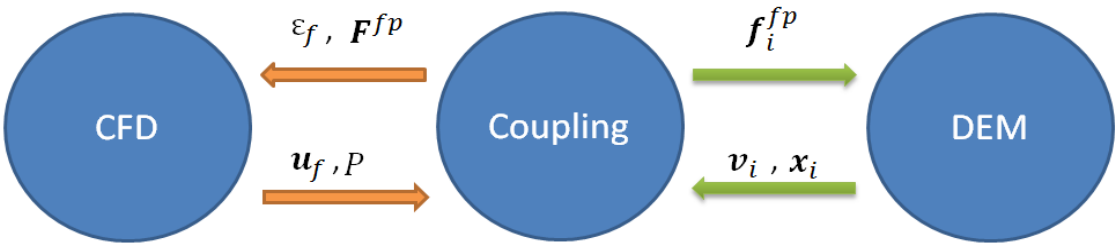

Fig. 4.1 CFD-DEM coupling procedure and information exchange

Conventional CFD-DEM such as RANS-DEM [3] requires that the Eulerian mesh size is bigger than the particle size, as shown in Figure 4.2 (a). The fluid volume fraction in a cell is calculated as

$$\varepsilon_f = 1 - \frac{\sum_{i=1}^{n} \alpha_i V_{p,i}}{\Delta V} \tag{4.26}$$

Here ΔV is the fluid cell volume, $V_{p,i}$ is the volume of particle i, n is the number of particles that overlap with the cell and α_i is the fractional volume of particle i inside the cell. Similarly, the volumetric particle-fluid interaction force in a CFD cell is computed as

$$F_{fp} = \frac{\sum_{i=1}^{n} \alpha_i f_i^{fp}}{\Delta V} \tag{4.27}$$

Compared to RANS-DEM, DNS-DEM solves the Navier-Stokes equations without using any turbulence models. Fine meshes are required to fully resolve the whole range of spatial and temporal scales of turbulence, thus the mesh scale is typically smaller than the particle diameter for the coarse particle suspensions of interest here, as shown in Figure 4.2 (b). When the whole cell is occupied by a particle, the fluid volume fraction becomes zero in the cell, and it would be meaningless to solve the two governing equations and estimate the drag on an individual particle. The $\varepsilon_f = 0$ also causes problems of singularity in numerical calculation. Several approaches have

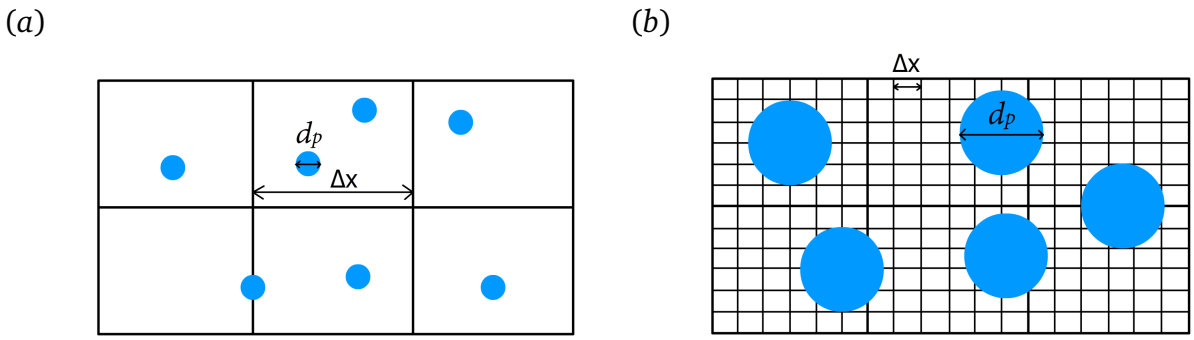

Fig. 4.2 Scenarios of fine and coarse particles in CFD-DEM

been proposed to deal with the presence of coarse particles in fine meshes such as the statistical kernel method [152], the porous cube method [75], the big sphere method [68] and the diffusion approach [101]. The diffusion approach is selected here because of its easy parallelization and implementation in CFD solvers for arbitrary meshes. Grid-based quantities (e.g., volume fraction and coupling force) are smoothed over a length scale l_{smooth} by solving a pseudo-transient, homogeneous diffusion equation with pseudo-time t :

$$\frac{\partial \gamma}{\partial t} = \alpha \nabla^2 \gamma \tag{4.28}$$

In eqn 4.28, γ is the transferred quantity (e.g., volume fraction or the coupling force), α is the diffusion coefficient chosen to be as $\alpha = l_{smooth}^2/\Delta t$, Δt is the CFD time step and l_{smooth} is the smoothing length scale, which is typically chosen to be $2{\sim}3d_p$. The diffusion approach is based on the theory that each particle will influence the surrounding fluid over a small but non-zero distance. Large values or gradients of volume fraction and coupling force can therefore be avoided to ensure computational stability. Previous work has proved the conservation of the smoothing operation [16, 93]. More details on the diffusion approach can be found in [101].

4.2.2 DNS-DEM implementation in CFDEM®

An open source package CFDEM® [52], which couples OpenFOAM and LIGGGHTS [65] is adopted for the DNS-DEM coupling. LIGGGHTS is an open source package that applies the soft-sphere approach in describing particle motions. LIGGGHTS is short for LAMMPS Improved for General Granular and Granular Heat Transfer Simulations, where LAMMPS

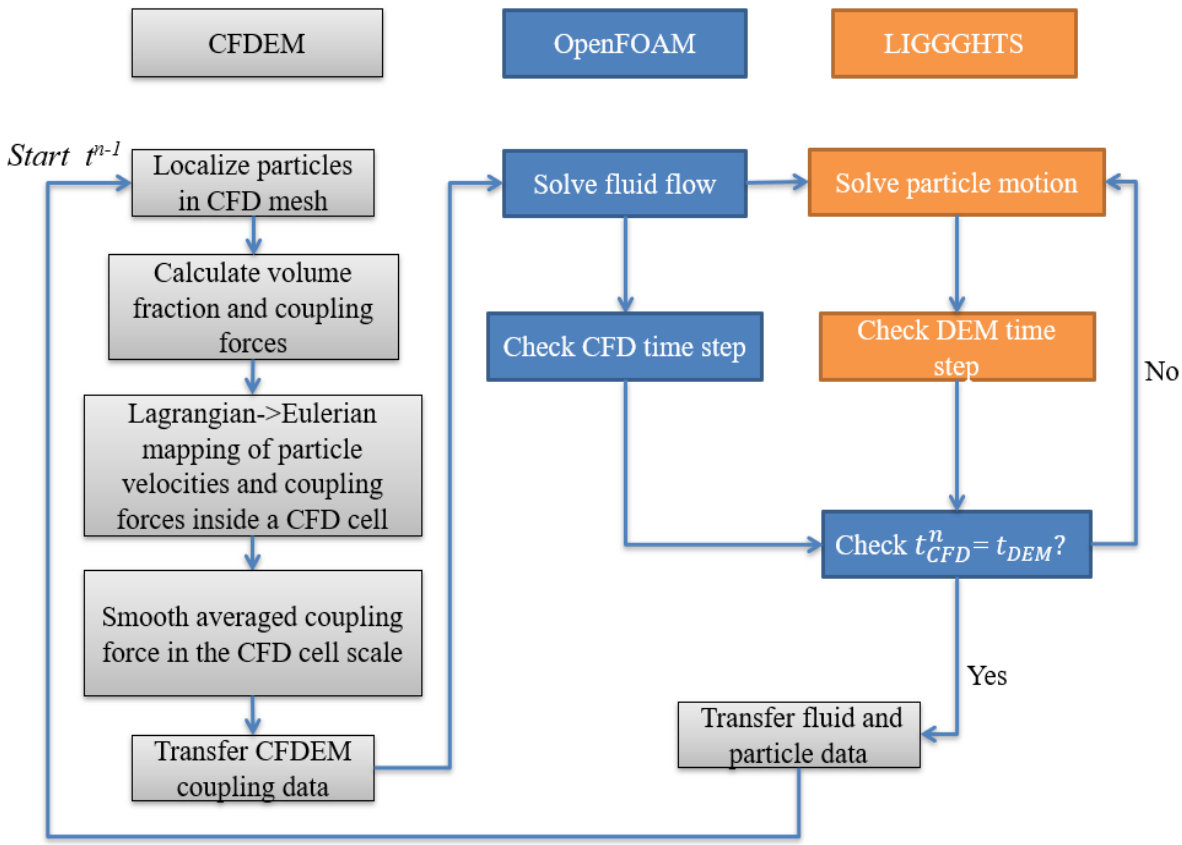

Fig. 4.3 DNS-DEM coupling procedure in OpenFOAM-CFDEM®-LIGGGHTS

[94] is a classical molecular dynamics simulator providing basic functionalities for DEM calculations. CFDEM® is essentially an OpenFOAM based solver, with LIGGGHTS called as a C++ function library. It supports four-way coupling including particle-particle interactions and particle-fluid interactions.

A schematic of the DNS-DEM coupling procedure implemented in OpenFOAM-CFDEM®-LIGGGHTS is shown in Figure 4.3. It follows a regular CFD-DEM coupling procedure. The diffusion of volume fraction and coupling forces is implemented using the "Smoothing" model in CFDEM®. The smoothed quantities in the CFD cell scale are then transferred from coupling library to the CFD solver to update the fluid flow field. From time t^{n-1} to t^n, the particle properties (i.e., velocity and position) are updated with sub-time stepping in DEM calculation. With known fluid velocity $\boldsymbol{u}_f$ and particle velocities $\boldsymbol{v}_i$ at t^n, the next coupling cycle will start.

4.3 Computational parameters and implementation in CFDEM®

4.3.1 Computational domain and parameters

This study simulates a horizontal periodic pipe with length $L = 4\pi D$ (D is the pipe diameter) and is the same domain as in Chapter 3 and earlier DNS studies at similar Reynolds number [108]. Meshes are symmetric in the pipe cross-section and Fig 4.4 shows a quarter of the structured hexahedral mesh.

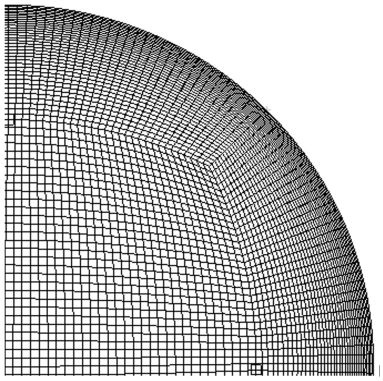

Fig. 4.4 A quarter of the structured hexahedral mesh in the pipe cross-section used in DNS-DEM simulation

For the weakly turbulent range ($5000 < Re < 15,000$) in this study, the Kolmogorov length η and time scales τ_η for turbulent pipe flows are estimated to be in the range of $140 \sim 390\ \mu m$ and $0.0021 \sim 0.0055\ s$. The Kolmogorov length η and time scale τ_η are estimated according to [60]. Mesh independency study ($1.4 \sim 8$ million) for DNS of turbulent pipe flow have been conducted in Chapter 3 paper section 3.1. The structured hexahedral mesh here is of size 6.1 million. The non-dimensional wall units r^+, $(R\theta)^+$ and z^+ (as defined in Chapter 3 paper section 3.1) in the near-wall region are approximately 0.6, 5.7 and 9.5 respectively, with the first layer thickness in the radial direction being $150\ \mu m$. Grid points in the axial direction (540 layers) are uniformly distributed. These mesh sizes have previously been shown in Chapter 3 paper section 4.1 and in [108] to provide acceptable DNS results of wall-bounded flows. Particles are generated in the DEM package LIGGGHTS and computational parameters used in validation of Newtonian and non-Newtonian suspension flows in Chapter 5 are shown

in Table 4.2. Particles are spherical as to eliminate the uncertainty from other factors such as irregularity of the particle shape. The particle Reynolds number Re_p is in the range of $25 \sim 70$.

The regular Young's modulus of glass beads is in the range of $60 \sim 70\ GPa$. The Young's modulus is related to the critical DEM time step size (as in sec 4.3.2) and using a lower Young's modulus than its true value (E_0) is commonly adopted in DEM studies [86]. This helps to reduce the computational costs. Simulation results are found to be insensitive to the Young's modulus in the range of $0.001 \sim 1\ E_0$ [18]. A value of $0.003E_0$ (2×10^8) is used in this study to ensure numerical efficiency. The coefficient of restitution and particle-particle friction is adopted from the glass beads supplier. The coefficient of particle-wall friction is adopted according to the empirical value in the non-Newtonian two-layer model [98]. Sensitivity analysis for the particle-particle friction coefficient ($0.1 \sim 0.4$) and particle-wall friction coefficient ($0.2 \sim 0.5$) has also been carried out, but the difference is minor in the predicted suspension velocity and concentration distribution (although particle behaviour is found different in cases without the presence of carriers).

Table 4.2 Computational parameters in validation of Newtonian and non-Newtonian suspension flows

Property	Value
Particle density, $\rho_s(kg/m^3)$	2600
Particle size, $d_p(mm)$	2
Young's modulus (Pa)	2×10^8
Coefficient of restitution	0.9
Coefficient of friction (particle-wall)	0.3
Coefficient of friction (particle-particle)	0.1
Newtonian fluid (Glycerol) density, $\rho_f(kg/m^3)$	$1163 \sim 1172$
Non-Newtonian fluid (Carbopol) density, $\rho_f(kg/m^3)$	1000
Newtonian fluid (Glycerol) viscosity, $\eta_f(mpa \cdot s)$	$13.9 \sim 14.2$
Non-Newtonian fluid (Carbopol) viscosity, $\eta_w(mpa \cdot s)$	$9.3 \sim 19.8$

4.3.2 Determination of time step and coupling interval

In a dense particle-fluid flow, the particle movement is not only affected by its neighbouring particles and surrounding fluid, but also from interaction with far away fluid and particles due to the propagation of disturbance waves [147]. The DEM is a framework for explicit time integration of particle motions and necessitates a numerical time step during which the disturbance wave can not propagate farther than its direct neighbouring particles [26]. In LIGGGHTS, the Rayleigh criteria [86] is adopted for determining the critical DEM time step size Δt_{crit}, which is

$$\Delta t_{crit} = \frac{\pi R_p}{0.1631\nu + 0.8766}\sqrt{\frac{\rho}{G}} \tag{4.29}$$

Here G is the shear modulus, ρ is particle density, ν is Poisson's ratio and R_p is particle radius. A fraction of the Rayleigh criteria should be used as the DEM time step to ensure numerical stability. The DEM time step depends on particle properties and generally falls into the range of 1e-7∼1e-5. The DEM time step in this study is 1e-6, which is approximately $1/10$ of the Rayleigh criteria.

In CFD-DEM, a coupling interval is required to determine the time during which the information is exchanged between the two solvers. It is also important that the CFD time step be small enough to ensure particles don't move too far away before the fluid-particle interaction is updated. Ideally, the information is exchanged after every single time step, that is one DEM time step for every CFD time step. However this can be extremely computational expensive and inefficient. Typically, a coupling interval in the range of $50 \sim 100$ is used to achieve both numerical accuracy and efficiency [52]. The coupling interval is set to 100 in this study. The Courant-Friedrich-Levy (CFL) number [23], C_r is also adopted to set the upper limit of the CFD time step, which is defined as

$$C_r = \frac{|\boldsymbol{u}|\Delta t}{\Delta x} \tag{4.30}$$

Here Δt is the CFD time step, Δx is the CFD cell size in the flow direction and $|\boldsymbol{u}|$ is the magnitude of flow velocity. The CFD time step is 1e-4 in this study and the maximum CFL number is 0.83.

4.3.3 Initial and boundary conditions

Simulations are initialized with a fully developed turbulent velocity profile obtained from a previous fluid only DNS. A no-slip boundary condition is applied at the wall. The flow is driven by including a body force per unit mass to the momentum equations throughout the run. The body force added is equivalent to the pressure gradient obtained from experiment as shown in Table 5.3, Chapter 5.

4.3.4 Averaging procedure

Typically 10 Flow Through Times ($FTT = L/\overline{U}$ where $\overline{U}$ is the bulk flow mean velocity) are required for the flow to develop into a stochastically steady state after initialization. Afterwards, $30\ FTTs$ are applied for accumulating statistics and an additional averaging in the axial direction is done before extracting profiles. Mean bulk flow velocity and wall shear stress are established as indicators for sensitivity analysis in order to assure the flow is stochastically developed before accumulating the turbulence statistics. The choice of $30\ FTTs$ is found to reduce statistical uncertainties of the mean and root mean square velocity profiles to within 0.5% and 1%, respectively.

4.3.5 Solver and solution scheme settings

The *cfdemSolverPiso* solver, which is the transient solver for incompressible flow in CFDEM®, is used for DNS of fluid flow. The specification of the DNS solver can be found in Table 4.3. The PISO algorithm is used for pressure-velocity coupling.

Table 4.3 Specification of the CFDEM® solver

Term	Description
Solver Name	cfdemSolverPiso
Solver Type	Pressure-based, segregated solver
Time Dependence	Transient
Pressure-velocity coupling	PISO
nCorrectors	2
transportModel	Newtonian; Herschel-Bulkley

Table 4.4 Discretization schemes for the CFDEM® solver

Term	Type	Scheme Description
ddtSchemes	backward	Second order, implicit, potentially unbounded
gradSchemes	Gauss linear	Second order, unbounded
divSchemes	Gauss linear	Second order, unbounded
LaplacianSchemes	Gauss linear limited 1	Second order, bounded, with nonorthogonal corrections
interpolationSchemes	linear	Second order, unbounded
snGradSchemes	limited 1	Second order, unbounded

The discretization schemes for the CFDEM® solver are shown in Table 4.4. Convection and diffusion terms are discretized using second-order central schemes and time integrations are based on second-order implicit scheme. The selection of schemes and linear solvers are according to DNS studies in Chapter 3. For the linear solvers, P is solved with the Pre-conditioned Conjugate Gradient (PCG) solver with the Diagonal Incomplete-Cholesky (DIC) pre-conditioning. The velocity $\boldsymbol{U}$ is solved with a smooth-Solver with a corresponding symGaussSeidel smoother. Solver tolerances of 1e-6 are set for both P and $\boldsymbol{U}$ to assure the variable have been solved with adequate accuracy. All computations are run on the high-performance cluster National Computational Infrastructure (NCI) - Gadi, which currently comprises of $3,024$ nodes each containing two 24-core Intel Xeon Scalable 'Cascade Lake' processors and 192 Gigabytes of memory. Each simulation generally takes 10 hours for the flow to develop into a stochastically steady-state when run on 240 CPUs and another 30 hours for accumulating statistics.

5

Coarse-Particle Suspension Experiments and Model Validation

To validate the DNS-DEM model, pipe flow suspension data with $Re < 15,000$ is required, where DNS is feasible. Considering the limited experimental data available for dense suspensions in a weakly turbulent ($4,000 < Re < 15,000$) flow regime, turbulent Newtonian and non-Newtonian suspension experiments have been designed & undertaken for validation. For a non-Newtonian suspension, discrepancy between experiment and simulation could result from either the approximations in the DNS-DEM coupling or the unknown particle-fluid drag correlation. To remove the uncertainty in the particle-fluid interaction forces and quantify the discrepancy arising from only the DNS-DEM coupling, the aim is to firstly develop a validated model that works well in Newtonian suspensions. Once confidence in Newtonian suspension flows is achieved, the DNS-DEM model is subsequently validated with non-Newtonian suspension flows.

5.1 Validation with Newtonian Suspension Flows

Section 5.1 is presented with publication. A paper summary of the validation with Newtonian suspension flows is provided and details of the study are covered in the paper. A detailed description of the experimental procedure is also provided in Appendix A.

5.1.1 Paper summary

A DNS-DEM model for weakly turbulent ($4,000 < Re < 15,000$) coarse-particle Newtonian suspension flow is presented. Suspension experiments with glass beads conveyed in a Glycerol solution are carried out for validation. Data obtained includes mixture flow rates, pressure drop and concentration distribution from Electrical Resistance Tomography (ERT), as well as the qualitative view revealing the flow regime transition.

The predicted flows are in both good qualitative & quantitative agreement with the experiments. A formation of the sliding bed (e.g., $Re = 6100$, $C_v = 0.18$) and transition from sliding bed to partial suspension (e.g., $Re = 10200$, $C_v = 0.15$) are observed. The predicted mixture flow rates and concentration profiles are mostly within 10% difference, particularly for the flow cases where particles are mostly suspended with only a small bed at the bottom (e.g., $Re = 10200$ and $C_v = 0.15$). Good agreement in the concentration profiles are always obtained at both the top and bottom in the pipe and maximum deviation is observed near the pipe centre. The relatively higher discrepancy in the central region may result from a fairly coarse ERT resolution in the experiment, the diffusion approach in the DNS-DEM coupling or a combination of both. Compared to a fluid-only flow, the predicted mean flow profiles are significantly damped by the presence of coarse particles, particularly in the stream-wise direction. The particle fluctuations resemble the fluid phase fluctuation but usually with a higher fluctuation level in the cross-stream direction.

The DNS-DEM model provides good quantitative results and predicts the trends well in the flow as parameters change. The results demonstrate that the DNS-DEM model is a promising approach for investigating weakly turbulent coarse-particle suspension flow. On this basis, this DNS-DEM modelling approach can be recommended and will form the basis of the remaining work on coarse-particle non-Newtonian suspension flow in this thesis.

5.1.2 Publication

The article E. Zheng, M. Rudman, S. Kuang, A. Chryss, Turbulent coarse-particle suspension flow: measurement and modelling. *Powder Technol* 373:647-659(2020) is reproduced with permission Elsevier Publishing, Copyright 2020.

Powder Technology 373 (2020) 647–659

Contents lists available at ScienceDirect

Powder Technology

journal homepage: www.elsevier.com/locate/powtec

Turbulent coarse-particle suspension flow: Measurement and modelling

Enzu Zheng [a,*], Murray Rudman [a], Shibo Kuang [b], Andrew Chryss [c]

[a] Department of Mechanical & Aerospace Engineering, Monash Univeristy, VIC 3800, Australia
[b] ARC Research Hub for Computational Particle Technology, Department of Chemical Engineering, Monash University, Clayton, VIC 3800, Australia
[c] CSIRO Mineral Resources, Clayton, VIC 3168, Australia

ARTICLE INFO

Article history:
Received 24 December 2019
Received in revised form 16 May 2020
Accepted 28 June 2020
Available online 05 July 2020

Keywords:
CFD-DEM
DNS
Turbulent
Suspension coarse-particle

ABSTRACT

Solid-liquid suspension flows are widely encountered in industrial applications. In many of these flows, the carrier fluid exhibits shear-thinning behaviour and the solids have a broad size distribution. Shear-thinning suspensions can occur in laminar or weakly turbulent regimes due to their high viscosity. This paper presents a DNS-DEM model for weakly turbulent coarse-particle suspension flows. Although our interest is in shear-thinning suspensions, we aim firstly to develop a liquid-solid model in a Newtonian fluid to remove the uncertainty in particle-fluid interaction in non-Newtonian suspensions. Matching experiments were conducted for validation. The predicted mixture velocity and concentration profiles are in good agreement with experiments, and discrepancies are mostly less than 10%. The mean velocity profiles are significantly damped by coarse particles and particle phase generally exhibits a higher fluctuation. This DNS-DEM modelling approach is viable for simulating these flows and will form the basis of future work on shear-thinning suspension flow.

1. Introduction

Solid-liquid suspension flows are widely encountered in industrial applications including oil & gas well drilling [1], pipeline transport [2–4] and food industries [5]. The flow behaviour of these suspensions is affected by a number of factors such as carrier fluid rheology, particle concentration, particle size, density and shear-induced migration. Such flows are yet to be fully understood due to their inherent complexity. Suspension flows can occur in either laminar or turbulent flow regimes and predicting their flow in a turbulent regime is more difficult due to the interaction between particles and turbulent eddies of different sizes. Previous studies in the turbulent regime mainly consider dilute or very dilute flow [6], and it remains unclear how the presence of dense particles affects the turbulence. At high solid concentration, the coupling between particles and fluid phase becomes stronger and particle-particle collisions need to be considered. In addition, dense suspension flows often occur with a broad size distribution [7], and the coarse particles may form a settled slurry and significantly alter the turbulence. A good understanding of the complex interaction between the carrier fluid and coarse particles is a necessity for efficient transportation of these flows.

Many studies have been conducted on solid-liquid suspension flows in recent years [2–4]. However, general approaches and theoretical models for predicting their flow behaviour are still lacking because of their complexity. There have been a wide variety of techniques developed for investigating suspension flows. Based on experimental data, Durand and Condolios [8] presented the first correlation for predicting the pressure drop of solid-liquid flow. The pressure drop was correlated as a function of mean flow velocity, solid volume fraction, solids density and size distribution. The limitations of empirical correlations are that they only apply to the specific flow regime for which they are developed and are, thus not generally applicable to other flow regimes [4,9].

Mechanistic models have later been proposed to offset the shortcomings of experimental approaches. A semi-theoretical correlation was derived by Rasteiro et al. [10] for calculating the pressure drop of turbulent heterogeneous solid-liquid flow. The model presumed the suspension of solid particles resulted from the dynamic balance between the gravity induced settling and turbulence induced dispersion. The pipe cross-section was decomposed into two layers to compute the pressure drop. A similar three-layer model was later proposed by Doron and Barnea [11]. Despite these mechanistic approaches being computationally convenient, they all adopt empirical constants and are overly simplified compared to more sophisticated approaches based on elemental volume.

Recently, computational fluid dynamics (CFD) is increasingly applied for modelling multiphase flows. Two numerical approaches are normally used for modelling solid-liquid flow: the Eulerian-Eulerian and Eulerian-Lagrangian approaches. In the Eulerian-Eulerian approach, both the fluid and solid phases are treated as continuous media, giving rise to the name Two Fluid Model (TFM) [12]. TFM has been applied in many studies of solid-liquid suspension flows [13–16] and has been found to be valid in predicting the pressure

* Corresponding author.
E-mail address: enzu.zheng@monash.edu (E. Zheng).

https://doi.org/10.1016/j.powtec.2020.06.080
0032-5910/

drop and concentration profile for suspenison flows. However, Gopaliya et al. [16] declared it was not promising for predicting coarse particle ($d_p > 0.5mm$) suspension and the predicted concentration profile displayed large deviation compared to experiments. In addition, it is a necessity to define complex constitutive relationships for the frictional, collisional and kinetic stresses of the solid phase in the granular kinetic theory in TFM [17], and such relationships are not well understood. Compared to the Eulerian-Eulerian approach, the Eulerian-Lagrangian approach describes the particle motions at a particle-scale level. Many models have been developed for dealing with individual particle motion and among them, the Discrete Element Method (DEM) is one of the most popular ones. In DEM, particle motion is predicted with Newton's second law that captures particle interactions via contact/non-contact forces [18]. Traditional CFD approach including Reynolds averaged Navier-Stokes (RANS), large eddy simulation (LES) and Direct Numerical Simulation (DNS) can all be coupled with DEM for modelling solid-liquid flows. CFD-DEM was initially developed by Tsuji et al. [19] with subsequent rationalization by Xu and Yu [20]. Compared with TFM, CFD-DEM is capable of modelling a wide range of flow systems as the requirement of specifying complex constitutive relations between stress and strain tensors for the particle phase can be eliminated [21].

CFD-DEM has been applied in recent studies of solid-liquid suspension flows. Akhshik et al. [1] developed a coupled RANS-DEM solver to simulate cuttings transport in oil & gas well drilling by taking into account the particle dynamic collision process. Simulation results were found reasonably matched with measurements from laboratory-scale experiments. Uzi and Levy [22] conducted RANS-DEM to investigate how pipe flow characteristics were modified by operating conditions such as solids concentration and pipe diameter. A robust LES-DEM solver called *Sedi foam* was developed for the simulation of sediment transport with implementing the lubrication and added mass force on the particles in [23]. This solver was found to be parallelly efficient in solving large-scale sediment transport. Zhou et al. [24] presented a LES-DEM model on hydraulic conveying of coarse solid particles in a vertical pipe. A more dispersed distribution of particles occurred with increasing conveying speed and feed solid concentration. Compared to RANS/LES-DEM, DNS-DEM solves the Navier-Stokes equations without using any turbulence models. With the development of increasingly powerful computational resources, DNS-DEM is gaining more attention for fundamental study of coupled fluid-particle flow [25]. Current DNS-DEM studies on solid-liquid suspension flows are mainly based on the Lattice Boltzmann Method (LBM) [26–28] and Immersed Boundary Method (IBM) [6,29–31]. These studies identify three regimes in particle-laden channel flow, i.e. the laminar, turbulent and inertial shear-thickening regimes. Each regime is dominated by different components of the total stress such as viscous, turbulent and particle-induced stresses depending on the solid volume fraction and the Reynolds number in the flow. However, the particle-fluid interaction in these DNS-DEM studies is treated at a sub-particle scale and the interface between particle-fluid phases needs to be fully resolved. This is computationally expensive and is mostly limited to systems of $O(10^3)$ particles [32].

In practice, a wide variety of suspension flows in the mineral industries exhibit shear-thinning behaviour in which the viscosity decreases with increasing shear rate [2]. Shear-thinning suspensions can occur in laminar or weakly turbulent regimes due to their high viscosity. In addition, the turbulence behaviour in shear-thinning fluids is not well understood and currently there are no general RANS and LES models available for shear-thinning fluids [33,34]. Thus DNS is a suitable approach for modelling non-Newtonian turbulence. Although our ultimate interest is in shear-thinning suspension, we aim to firstly develop a validated liquid-solid model for flows of interest that provides good results in Newtonian suspensions, in order to remove the uncertainty in particle-fluid interaction forces in non-Newtonian fluids. This paper presents a DNS-DEM model for investigating weakly turbulent coarse-particle suspension flow. DNS is applied to capture the unsteady turbulent flow structure, and the DEM is used for modelling the detailed particle-particle interaction. The interface between the solid-liquid phases is not fully resolved as in IBM/LBM, therefore it is much less computational expensive and can apply to large-scale particle systems but solid-liquid interaction correlations are still needed. The developed DNS-DEM approach will form the basis of our future work on coarse-particle shear-thinning suspension flow.

In order to validate the DNS-DEM coupling, suspension data with $Re < 10{,}000$ is required. Experimental studies are available for coarse particle transport in horizontal pipes [7,35,36], however, detailed velocity and concentration measurements at high concentrations is rare. The *Re* considered in those studies is several orders greater than 10,000, where DNS is not feasible. Considering the limited experimental data available for dense suspension in weakly turbulent ($4000 < Re < 10{,}000$) flow, suspension experiments were designed & undertaken to obtain data for validation of the DNS-DEM model. Data including pressure drop, flow rate and concentration profile, as well as the visual observations of the flow were obtained at different flow regimes ranging from the settled bed regime to partially suspended flow.

The structure of this paper is as follows. First, a description of the DNS-DEM methodology that introduces the governing equations and coupling algorithm between particle and fluid phase is presented, followed by the experimental set up and measurement. For the results section, the validation of the DNS-DEM model is presented. Once confidence in the results is demonstrated, a comparison of the mean velocity and fluctuation profiles of both fluid and particle phases is presented to show how the presence of particles affects the flow. The distribution of forces acting on particles in both axial and vertical direction are also obtained from DEM to demonstrate which force is dominating and supporting the particles in dense suspension flow.

2. Methodology

2.1. Governing equations

In DNS-DEM, the governing equations for the particle phases are

$$m_i \frac{d\boldsymbol{v}_i}{dt} = \sum_j \boldsymbol{F}_{ij}^c + \boldsymbol{F}_i^f + \boldsymbol{F}_i^g \tag{1}$$

$$I_i \frac{d\boldsymbol{w}_i}{dt} = \sum_j \boldsymbol{M}_{ij} \tag{2}$$

For particle *i*, $\boldsymbol{v}_i$ and $\boldsymbol{w}_i$ represent translational and angular velocity, $\boldsymbol{F}_{ij}^c$ and $\boldsymbol{M}_{ij}$ represent the contact force and torque arising from its interaction with particle j or pipe wall, $\boldsymbol{F}_i^f$ represents the particle-fluid interaction force, and $\boldsymbol{F}_i^g$ is the gravitational force. The contact force on particle *i* exerted by particle *j* is calculated using the soft-sphere contact model [37] as shown below:

$$\boldsymbol{F}_{ij}^c = \boldsymbol{F}_{ij}^{cn} + \boldsymbol{F}_{ij}^{ct} \tag{3}$$

$$\boldsymbol{F}_{ij}^{cn} = -k_{ij}^n \delta_{ij}^n \boldsymbol{n}_i - \gamma_{ij}^n (\boldsymbol{v}_r \cdot \boldsymbol{n}_i) \boldsymbol{n}_i \tag{4}$$

$$\boldsymbol{F}_{ij}^{ct} = -k_{ij}^t \delta_{ij}^t \boldsymbol{t}_i - \gamma_{ij}^t \left[(\boldsymbol{v}_r \cdot \boldsymbol{t}_i) \boldsymbol{t}_i + (\boldsymbol{w}_i \times \boldsymbol{r}_i - \boldsymbol{w}_j \times \boldsymbol{r}_j) \right] \tag{5}$$

Here *n* and *t* represent the normal and tangential direction, respectively. The distance vector from particle mass centroid to the contact point is written as $\boldsymbol{r}$, $\boldsymbol{v}_r$ is the relative velocity between the two paired particles *i* and *j*, *k* is the spring constant, γ is the damping coefficient and δ represents the overlap of a colliding pair. Further details can be found in [38].

Governing equations for the carrier fluid follow the conservation laws of mass and momentum [39]:

$$\frac{\partial \varepsilon_f}{\partial t} + \nabla\cdot(\varepsilon_f \boldsymbol{u}_f) = 0 \tag{6}$$

$$\frac{\partial\left(\rho_f \varepsilon_f \boldsymbol{u}_f\right)}{\partial t} + \nabla\cdot\left(\rho_f \varepsilon_f \boldsymbol{u}_f \boldsymbol{u}_f\right) = -\varepsilon_f \nabla p - \boldsymbol{F}_{fp} + \nabla\cdot(\varepsilon_f \boldsymbol{\tau}) + \rho_f \varepsilon_f \boldsymbol{g} \tag{7}$$

Here $\boldsymbol{u}_f$, p, $\boldsymbol{\tau}$ and ε represent the fluid velocity, fluid pressure, fluid stress tensor and fluid volume fraction, respectively. The volumetric particle-fluid interaction force $\boldsymbol{F}_{fp}$ is expressed as

$$\boldsymbol{F}_{fp} = \frac{1}{\Delta V}\sum_{i=1}^{n}\left(\boldsymbol{f}_i^{drag} + \boldsymbol{f}_i^{lift} + \boldsymbol{f}_i^{vm}\right) \tag{8}$$

Here ΔV is the volume of a computational cell. The $\boldsymbol{f}_i^{drag}$, $\boldsymbol{f}_i^{lift}$ and $\boldsymbol{f}_i^{vm}$ are the particle-fluid drag force, lift force and virtual mass force on an individual particle i, respectively. Interaction force on an individual particle also includes the pressure gradient force $\boldsymbol{f}^p$ and the viscous force $\boldsymbol{f}^{vis}$. The drag force on an individual particle is represented by the Gidaspow model [40], which is a combination of the Wen and Yu model [41] and the Ergun equation [42].

$$\boldsymbol{f}^{drag} = \frac{V_p}{\varepsilon_p} K_{fp}(\boldsymbol{u}_f - \boldsymbol{u}_p) \tag{9}$$

The volume of an individual particle is V_p. When $\varepsilon_f > 0.8$, the fluid-solid exchange coefficient K_{fp} is of the following form

$$K_{fp} = \frac{3}{4} C_D \frac{\varepsilon_p \varepsilon_f \rho_f |\boldsymbol{u}_f - \boldsymbol{u}_p|}{d_p} \varepsilon_f^{-2.65} \tag{10}$$

with

$$C_D = \frac{24}{\varepsilon_f Re_p}\left[1 + 0.15(\varepsilon_f Re_p)^{0.687}\right] \tag{11}$$

$$Re_p = \frac{\rho_f d_p |\boldsymbol{u}_p - \boldsymbol{u}_f|}{\eta_f} \tag{12}$$

When $\varepsilon_f \le 0.8$

$$K_{fp} = 150\frac{\varepsilon_p(1-\varepsilon_f)\eta_f}{\varepsilon_f d_p^2} + 1.75\frac{\rho_f \varepsilon_p |\boldsymbol{u}_p - \boldsymbol{u}_f|}{d_p} \tag{13}$$

The lift force on a spherical particle due to velocity gradients in the fluid phase is computed from [43].

$$\boldsymbol{f}^{lift} = 0.5\rho_f V_p(\boldsymbol{u}_f - \boldsymbol{u}_p)(\nabla \times \boldsymbol{u}_f) \tag{14}$$

The study also implements the Loth and Dorgan model [44] to calculate the lift force, which is an extended formulation of Saffman lift [45] and includes the influence of particle rotation:

$$\boldsymbol{f}^{lift} = 0.125\pi d_p^2 \rho_f C_L(\boldsymbol{u}_f - \boldsymbol{u}_p)\left[|\boldsymbol{u}_f - \boldsymbol{u}_p| \times \frac{\boldsymbol{\omega}_f}{|\boldsymbol{\omega}_f|}\right] \tag{15}$$

$$C_L = J^* \frac{12.92}{\pi}\sqrt{\frac{\boldsymbol{\omega}^*}{Re_P}} + \Omega_{p,eq}^* C_{L,\Omega}^* \tag{16}$$

Here J^* is an approximated function proposed by Mei [46], $\boldsymbol{\omega}^*$ and Ω^* are magnitude of the vorticity and particle angular velocity. Full details of the Loth and Dorgan lift model can be found in [44] and are not shown here for brevity.

The virtual mass force generated by the acceleration of fluid phase surrounding a particle is expressed as

$$\boldsymbol{f}^{vm} = 0.5\rho_f V_p\left(\frac{D\boldsymbol{u}_f}{Dt} - \frac{D\boldsymbol{u}_p}{Dt}\right) \tag{17}$$

The buoyance term is implicitly included in the model formulation in the pressure gradient force [47] and the pressure gradient force on individual particles is expressed as

$$\boldsymbol{f}^p = -V_p \nabla(p) \tag{18}$$

and the viscous force on individual particles is expressed as

$$\boldsymbol{f}^{vis} = -V_p \nabla(\boldsymbol{\tau}) \tag{19}$$

2.2. Coupling between fluid and particle phase

In CFD-DEM, DEM solves the particle flow at an individual particle level, while CFD solves the carrier fluid at a computational cell level. For every time step, DEM calculates the location and velocity of individual particles and these information will be used to evaluate the volume fraction and the volumetric interaction force in a computational cell. The CFD solver then solves the fluid equations to update the fluid velocity. The interaction force on an individual particle is subsequently updated and incorporated into the DEM calculation to obtain motion of particles to start next coupling cycle.

Conventional CFD-DEM such as RANS-DEM [1,22] requires that the Eulerian mesh size to be bigger than the particle size and calculates the fluid volume fraction in a cell as

$$\varepsilon_f = 1 - \frac{\sum_{i=1}^{n} V_{i,part}}{V_{cell}} \tag{20}$$

Here V_{cell} is the cell volume, n is the number of particles that overlapped with the cell and $V_{i,part}$ is the volume of each overlapped particle. A detailed description of the calculation of solid volume fraction and its influence on the fidelity of CFD-DEM simulation based on particle centroid method and analytical approach in conventional CFD-DEM can be found in [48]. Compared to RANS-DEM, DNS-DEM solves the Navier-Stokes equations without using any turbulence models. Fine meshes are required to fully resolve the whole range of spatial and temporal scales of turbulence, thus the mesh scale will be smaller than the particle diameter for the coarse particle suspension of interest here. When the whole cell is occupied by a particle, the fluid volume fraction becomes zero in the cell, and it would be meaningless to solve the two governing equations and the drag on an individual particle. Several approaches have been proposed to deal with the presence of coarse particles in fine meshes such as the statistical kernel method [49], the porous cube method [50], the big sphere method [51] and the diffusion approach [52]. The diffusion approach is selected here because of its easy parallelization and implementation in CFD solvers for arbitrary meshes. Grid-based quantities (e.g., volume fraction and coupling force) are smoothed over a length scale l_{smooth} by solving a pseudo-transient, homogeneous diffusion equation with pseudo-time τ:

$$\frac{\partial \gamma}{\partial \tau} = \alpha \nabla^2 \gamma \tag{21}$$

In Eq. (21), γ is the transferred quantity (e.g., volume fraction or the coupling force), α is the diffusion coefficient as $\alpha = l_{smooth}^2/\Delta t$ and l_{smooth} is the smoothing length scale, which is typically 2~3d_p. The diffusion approach is based on the theory that each particle will influence the surrounding fluid over a small but non-zero distance. Abnormally large values or gradients of volume fraction and coupling force can therefore be avoided to ensure computational stability. Previous work has proved the conservation of the smoothing operation [53,54]. More details on the diffusion approach can also be found in [23].

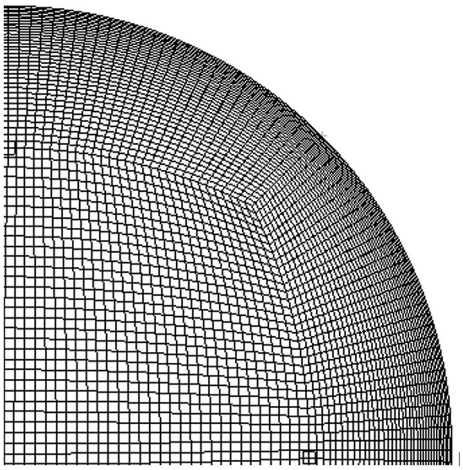

Fig. 1. A quarter of the structured hexahedral mesh in the pipe cross-section.

2.3. Computational parameters and implementation

This study simulates a horizontal periodic pipe with length $L = 4\pi D$ (D is the pipe diameter) and is the same as used in earlier DNS studies at similar Reynolds number [55,56]. Meshes are symmetric in the pipe cross-section and Fig. 1 shows a quarter of the structured hexahedral mesh. The non-dimensional wall units $y^+ = \rho_f u_\tau y/\eta_f$, where u_τ is the friction velocity as $u_\tau = \sqrt{\tau_w/\rho_f}$, and τ_w is the mean wall shear stress determined from the axial pressure gradient. The r^+, $(R\theta)^+$ and z^+ are wall units in the radial, azimuthal and axial direction in the near-wall region and are approximately 0.6, 5.7 and 9.5 respectively. Grid points in the axial direction are uniformly distributed. These mesh sizes have previously been shown [55,56] to provide accurate and reliable DNS results of wall-bounded flows. Despite the comparatively lower second order spatial discretisation schemes used in OpenFOAM, DNS results of Newtonian fluids predicted by OpenFOAM correspond very well with the DNS reference (computed using a spectral element code, Semtex [57]) and experimental data. The maximum error observed is 4.1% when predicting the mean velocity and turbulence intensities [56], and is usually less than 2% for turbulence statistics. Particles are generated in the DEM package LIGGGHTS [38] and the computational parameters are shown in Table 1.

Simulations are initialized with a fully developed turbulent velocity profile obtained from previous DNS work. A no-slip boundary condition is applied at the wall. The flow is driven by including a body force per unit mass to the momentum equations throughout the run. The body force added is equivalent to the pressure gradient obtained from experiment as shown in Table 3. Statistics are accumulated after the flow develops into a stochastically steady state. An Open Source package CFDEM [58], which couples OpenFOAM and LIGGGHTS is adopted for realizing the DNS-DEM coupling. The cfdemSolverPiso solver, which is the transient solver for incompressible flow in CFDEM, is used for DNS of fluid flow. The PISO algorithm is used for pressure-velocity coupling. The capability of OpenFOAM for DNS of turbulent Newtonian flow has been previously demonstrated in [56,59,60]. Convection and diffusion terms are discretized using a second-order central schemes and time integrations are based on a second-order implicit scheme. The selection of schemes and linear solvers are selected according to previous DNS studies mentioned above. The CFD time step is 1e-4 and the maximum Courant-Friedrichs-Lewy (CFL) number is 0.73. The DEM time step is 1e-06 and satisfies the Rayleigh time step requirement for DEM [61]. Each simulation generally takes 10 Flow Transit Times ($FTT = L/U_m$, where U_m is the bulk flow mean velocity) for the flow to develop into a stochastically steady-state, which is about 16 h when run on 240 CPUs, and another 30 FTTs (48 h) for accumulating statistics.

Table 1
Computational parameters.

Property	Value
Particle density, $\rho_s(kg/m^3)$	2600
Particle size, $d_p(mm)$	2
Young's modulus (pa)	$2x10^8$
Coefficient of restitution	0.9
Coefficient of friction (particle-wall)	0.3
Coefficient of friction (particle-particle)	0.1
Fluid density, $\rho_f(kg/m^3)$	1163~1172
Fluid viscosity, $\eta_f(mpa \cdot s)$	13.9~14.2

3. Experimental measurement

3.1. Experimental set up

A schematic of the experimental pipe loop is shown in Fig. 2. The loop consists of a feed tank for mixture preparation, a pump with variable speed drive and a pipeline system. The pipeline is composed of sections of 44 mm I.D. PVC pipe and 2 sections of 44 mm I.D. transparent acrylic tubes with square sides for undistorted visualisation. The length of the horizontal pipe section is 6 m (as shown in Fig. 2). The pipe rig is operated as a closed circuit and slurry goes directly back to the feed tank after travelling through the pipeline system.

The system is equipped with MAGFLO MAG 6000 electromagnetic flow meters for measuring the mixture flowrate, U_m, and two sets of differential pressure transducers for measuring the pressure drop over pipe lengths of 1.5 m and 2 m, respectively. A temperature probe is installed in the vertical invert pipe for slurry temperature measurements. A Coriolis mass flow meter is used to estimate the slurry density and in-line concentration. An ITS p2000 Electrical Resistance Tomography (ERT) system is used to measure the solid concentration distribution in the pipe cross-section. An ERT ring is installed along the transparent acrylic horizontal tube with 16 electrodes for obtaining a tomogram of conductivity distribution. The reconstruction of electrical conductivity distribution and post-processing are handled in the EIDORS software package [62]. Measurements are logged and processed in a computerised data acquisition system at a frequency of 12 Hz. A qualitative view of the flow is also obtained through the transparent acrylic pipe section, where flow regime (e.g. settled bed, sliding bed, etc.) is easily determined.

3.2. Flow conditions

The Newtonian slurry was prepared using a Glycerol solution (65wt%) as the carrier fluid and glass beads added at different concentrations. The glass beads are monodisperse with a diameter $d_p = 2mm$ and density $\rho_p = 2600kg/m^3$. A typical test run starts with a low solid volume fraction, measurements are taken for one designed concentration over a range of velocities. Afterwards, the solid concentration is increased by adding more solids into the mixing tank and measurements are repeated at higher concentration. Slurry samples are collected both before and after each test for rheology measurements on the carrier fluid (solids removed) using a Haake Rheostress RS1 rheometer. Table 2 shows the range of suspension variables tested. The Re here is the bulk flow Reynolds number, which is defined based on the the carrier fluid density ρ_f and viscosity η_f, mixture flow rate U_m, and pipe diametero D.

4. Results

Two sets of representative experimental runs with flow regimes from sliding bed to partial suspension are selected for simulations.

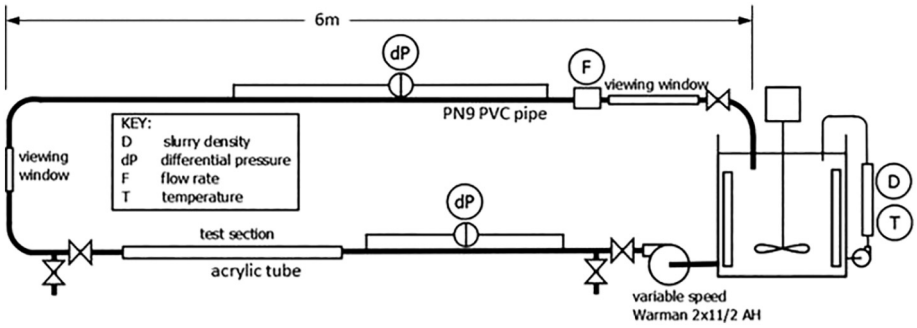

Fig. 2. Experimental pipe loop.

Table 2
Range of suspension variables tested.

Property	Value
Pipe diameter, $D(mm)$	44
Fluid density, $\rho_f(kg/m^3)$	1163~1172
Fluid viscosity, $\eta_f(mpa \cdot s)$	13.9~14.2
Solid density, $\rho_p(kg/m^3)$	2600
Particle size, $d_p(mm)$	2
In line concentration, C_v	0.15~0.22
Flow regime	sliding bed to partially suspended
Bulk flow *Re*	4000~10,000

A pipe section far away from the entrance where the flow has reached a statistically steady state is chosen as the flow domain. Flow conditions for the two sets of test runs are shown in Table 3. Test1 is conducted with nominal solid volume fraction of 15%. Afterwards, more solids are added to the pipe loop forming Test2 with a higher nominal solid volume fraction of 20%. The measured inline concentration C_v varies slightly from the designed concentration at different flow velocities because of the solids hold-up in a closed loop system, as shown in Table 3.

4.1. Qualitative view of the flow

Flow regimes from sliding bed to partial suspension are observed in the test runs. Fig. 3 shows a qualitative comparison of the flow between

Table 3
Flow conditions for simulation.

Property	Test1			Test2		
In line concentration, C_v	0.18	0.17	0.15	0.22	0.20	0.19
ERT integrated concentration, C_v	0.15 (−16.7%)	0.14 (−17.7%)	0.14 (−6.7%)	0.19 (−13.6%)	0.18 (−10.0%)	0.17 (−10.5%)
Pressure gradient per unit mass (m/s^2)	2.32	2.64	3.50	3.10	3.53	3.84
Bulk flow *Re*	6100	7600	10,200	6500	8000	9500
Mixture velocity, U_m (m/s)	1.66	2.10	2.77	1.76	2.18	2.56
Predicted Mixture velocity, U_m (m/s)	1.79	1.99	2.50	1.98	2.32	2.49
Difference	+7.7%	−5.2%	−9.8%	+12.5%	+6.4%	−2.7%

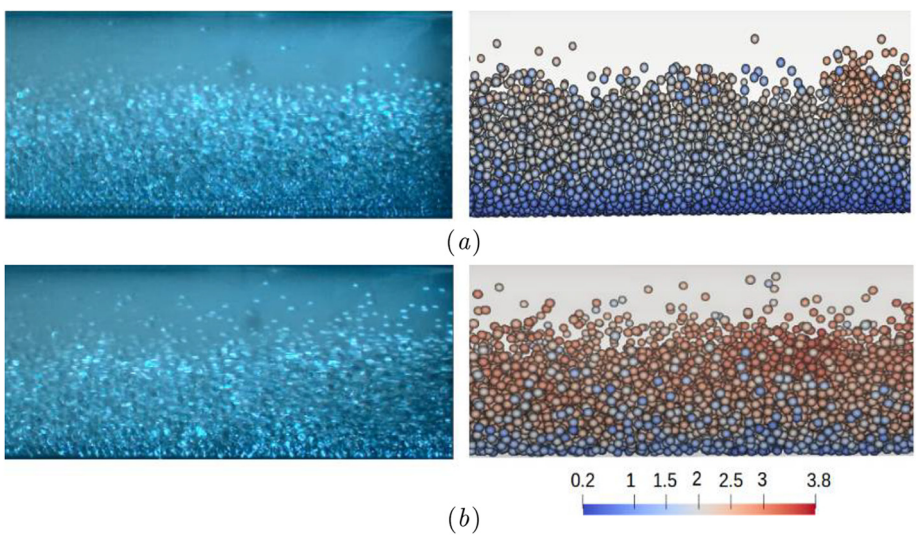

Fig. 3. Qualitative view of the pipe flow from experiment and simulation, where colour represents magnitude (m/s) of particle velocity (a) $Re = 6100$ (b) $Re = 10{,}200$.

the experiment and simulation for two typical flow conditions in Test1, which represents the formation of a sliding bed ($Re = 6100$) and partial suspension ($Re = 10{,}200$). For the flow with $Re = 6100$, the mixture velocity of 1.79 m/s is only slightly higher than the deposition limit 1.2 m/s calculated based on the Oroskar and Turian method [63], and particles tend to settle toward the bottom forming a bed along the pipe, with only a few saltating and being lifted in the upper section. The velocity of particles near the bed can be seen to be uniform (blue) and around 0.4 m/s. At higher mixture velocity 2.77 m/s, a flow regime transition from sliding bed to saltation mode occurs. Particles gradually lift off the bottom and form a dune structure, leading to a decreased thickness of the bed layer. This is quite clear in recorded videos, however more difficult to see in still images. With more particles now saltating, dunes disaggregate and a partial suspension is observed, as in the flow with $Re = 10{,}200$. The saltating particles have more intensive rotation and their velocities, which are indicated as red in Fig. 3b, are much higher than those located in the vicinity of the bottom. The predicted flows are qualitatively similar as those in the experiment with a predicted sliding bed shown in Fig. 3a and a partial suspension mode shown in Fig. 3b.

4.2. Mixture velocity and concentration profile

The mixture velocity results are shown in Table 3. The DNS-DEM predicted velocities are in good agreement and all within 10% of the experiment, except for the flow with $Re = 6500$ in Test2. The results indicate that the DNS-DEM model overestimates the mixture velocities at low *Re* while underestimates them at higher *Re*. The solid volume concentration profiles on the vertical centreline of the pipe are shown in Fig. 4. The concentration profiles reveal a stratified flow and display a similar pattern for all flow conditions. In the upper section of the pipe, the low solid volume fraction corresponds to the very few particles that are bouncing along the top of the bed. In the central region of the pipe, an approximate linear concentration distribution is observed. However, the model somewhat overestimates the concentration in the central region, especially for the flow with lower *Re*. This can be easily

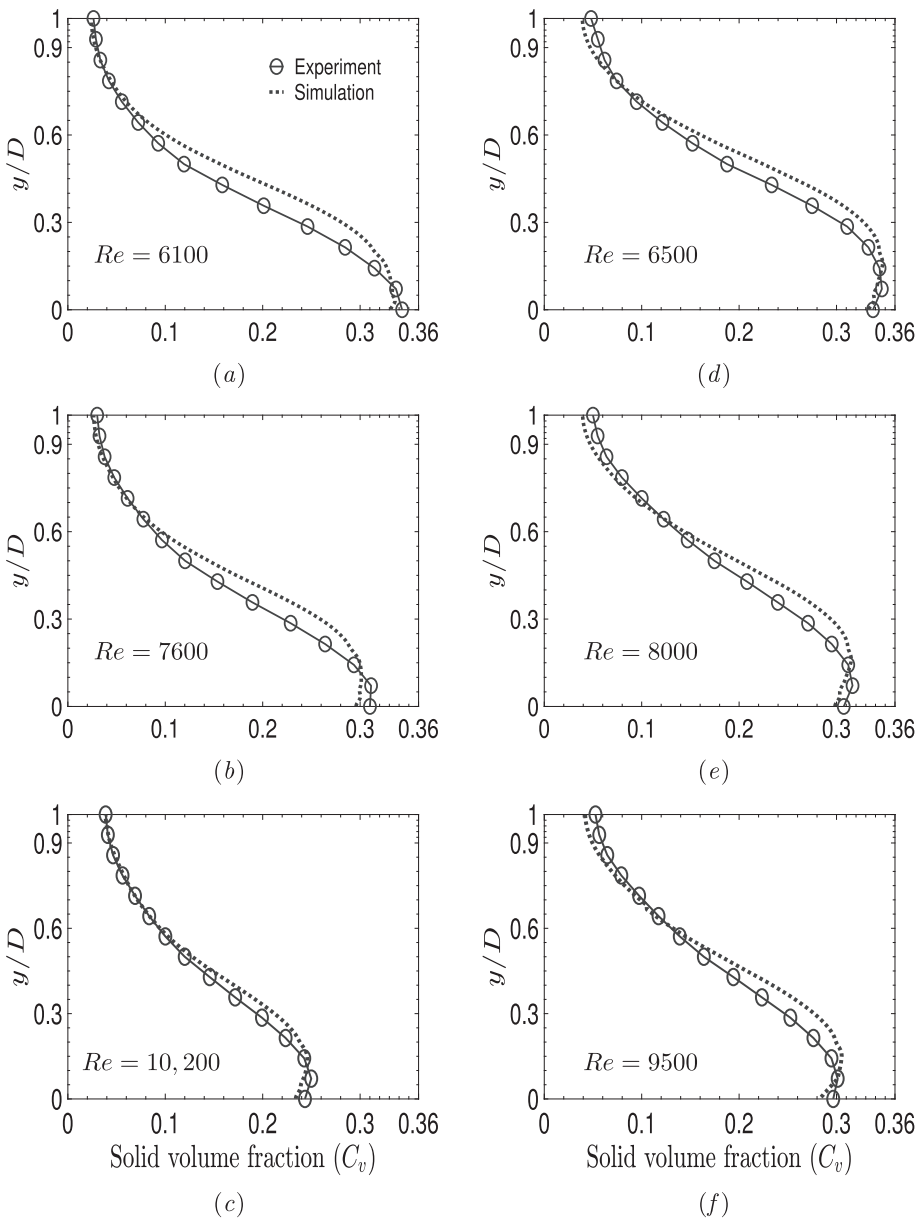

Fig. 4. Concentration profile in the centre line of a pipe cross-section: Test1 (a) $Re = 6100$ (b) $Re = 7600$ (c) $Re = 10{,}200$ Test2 (d) $Re = 6500$ (e) $Re = 8000$ (f) $Re = 9500$.

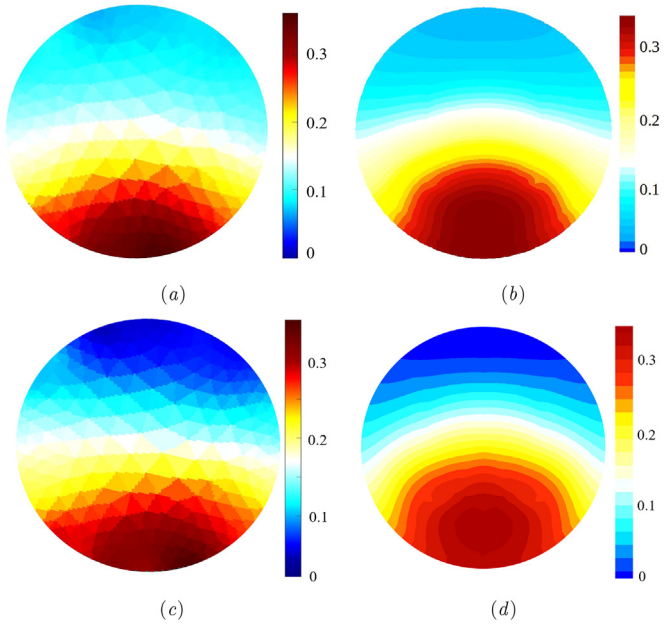

Fig. 5. 2D concentration distribution in the pipe cross-section for the flow with $Re = 6100$ (a) Experiment (b) Simulation and $Re = 8000$ (c) Experiment (d) Simulation.

seen in flows with $Re = 6100$ and $Re = 10{,}200$ in Test1 as shown in Fig. 4. In the lower section of the pipe, a slight underestimation of the concentration is seen and the concentration reaches its maximum near the pipe bottom. In Test1, the maximum concentration is approximately 0.35 for flow with $Re = 6100$ and decreases to 0.25 at $Re = 10{,}200$. The maximum concentration also increases with a higher nominal volume fraction in Test 2, and is around 0.30 for flow with $Re = 9500$.

The concentration profiles predicted are generally in good agreement with the experimental results and mostly less than 10% difference, particularly at the top & bottom where the measuring electrodes are close. As can be seen in Fig. 4, good agreement is always achieved at both the top & bottom for all the test runs. The relatively larger deviation in the central region of the pipe may be due to either measurement or model error. Fig. 5 shows the 2D concentration distribution in the pipe cross-section from ERT measurements and simulation for the flow with $Re = 6100$ in test1 and $Re = 8000$ in test2. ERT is a promising technique and has been applied in previous suspension studies [64,65] for visualisation of slurry flow, but it faces the challenges such as noise, low spatial resolution and the ill-posedness of the inverse problem in the image reconstruction [66]. In the experiment, the ERT ring has 16 electrodes placed around the circumference of the pipe. This sets the resolution for accurately capturing the conductivity distribution, which is limited near the centre of the reconstructed domains [67,68]. The reconstruction of electrical conductivity distribution and post-processing are handled in the EIDORS software package [62] with a finer mesh resolution of 428 elements in the pipe cross section, as shown in Fig. 5. The integrated solid concentration from ERT is also compared with the in-line concentration measured from Coriolis mass flow meter to indicate the estimated error from ERT in Table tab. flowcondition. The error indicates the ERT measurements underestimate the solids concentration than the actual flow, with the best agreement(-6.7%) found in the flow with $Re = 10{,}200$ and typically around 10% difference for flow in Test2. In the simulation, the DNS-DEM model applies the diffusion approach, which results in the solid volume fraction in the bed being diffused away from the pipe bottom to the central region, leading to an overestimation and larger discrepancy of concentration profile in the centre. The inherent limitation of the diffusion approach will decrease in the flow with no significant bed. Discrepancy in the concentration profiles are likely a result of both the ERT error and diffusion approach.

Future work should consider alternative DNS-DEM coupling methodologies without applying the diffusion. Both the porous cube method [50] and a conservative virtual volume fraction method [69] could possibly be adopted to deal with coarse particles in fine meshes. The difficulty associated with these methods is that the volume of a particle is distributed to its surrounding computational domain, searching for cells occupied by the particle can be difficult, particularly for those located on another processor. To implement these methods in the DNS-DEM solver, an algorithm for easy parallelization needs to be developed for efficient communication of particles to non-local cells.

Despite the known limitation of both the ERT & diffusion approach, the results obtained here are in good qualitative & reasonable quantitative agreement and are able to correctly distinguish different flow regimes. On this basis, we proceed to analyse the simulation results to obtain information of the flow that is not possible to obtain experimentally.

4.3. Mean flow velocity and fluctuations profiles

The simulated mean velocity profiles on the vertical centreline for both the fluid and particle phases are shown in Fig. 6, where lines represent the fluid phase and symbols represent the particle phase. The experimental data of mean fluid and particle velocity profile are not

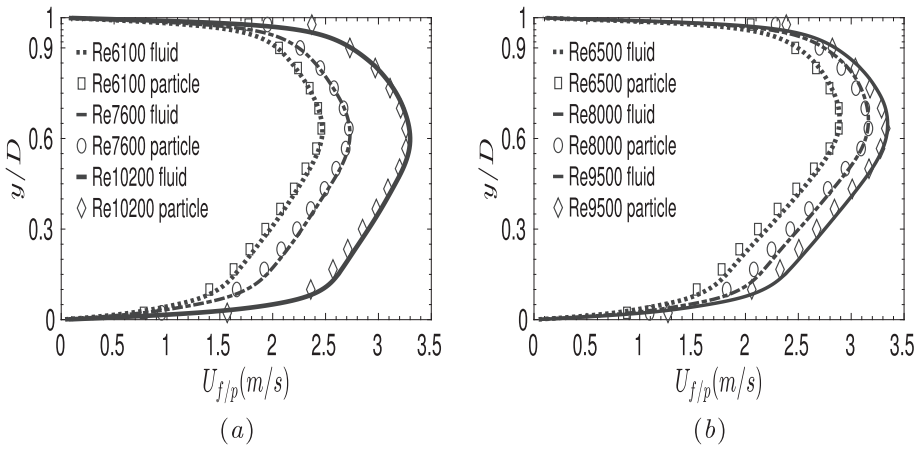

Fig. 6. Mean velocity profiles on a vertical centreline of the fluid and particle phase (a) Test1 (b) Test2.

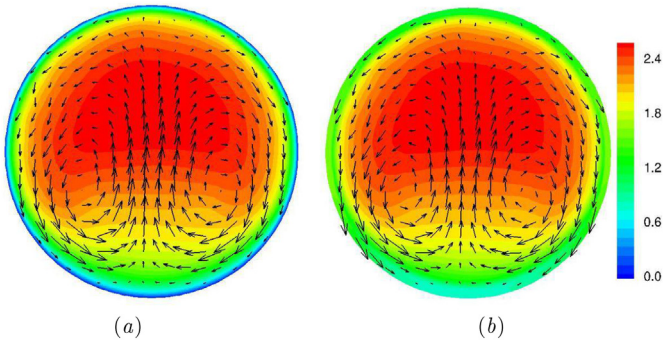

Fig. 7. Time-averaged cross-sectional vector field of the secondary flow velocity for the flow with $Re = 6100$ (a) fluid phase (b) particle phase.

available as they are very difficult to measure in any conditions other than dilute suspension flow. In dense suspension flow it is challenging to measure particle and fluid velocities reliably due to loss of measuring signal integrity caused by particle induced diffraction, refraction and obscuration. The simultaneous fluid-particle PIV method [70] which combines refractive index matched-particle image velocimetry (RIM-PIV) for fluid velocity measurement and particle tracking velocimetry (PTV) for the particle velocity statistics may be a viable option for suspension flow and has been applied in low concentration suspension flow [71], but its reliability in dense suspension flow remains unclear [72], and will always reach hard concentration limits where measurement is not viable. As can be seen in the figure, the mean particle phase flow are slightly slower than the fluid phase except in the near wall region. The fluid velocity at the wall is zero, namely the no-slip condition, while the particle phase has a relative tangential motion to the wall where it can slide and roll, resulting in a larger mean flow velocity than the fluid phase. The presence of coarse particles produces an asymmetric flow profile. This is more pronounced at higher concentration as shown in Fig. 6(b). The peak of the mean velocity shifts from its central position in single-phase flow to a higher location ($y/D \approx 0.6$).

Fig. 7 shows the time-averaged cross-sectional vector field of the secondary flow velocity under $Re = 6100$. The secondary flow

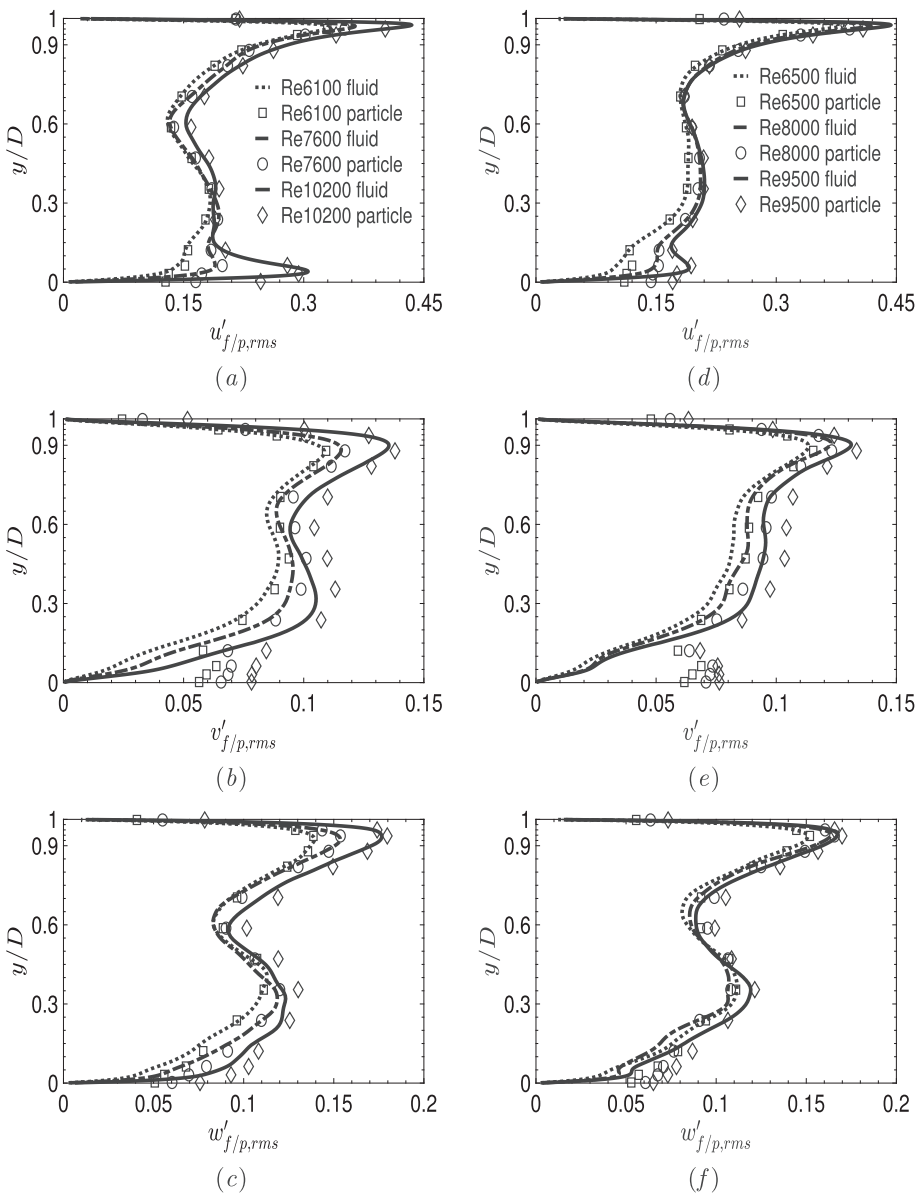

Fig. 8. The rms velocity fluctuations of the fluid and particle phase: Test1 (a) streamwise (b) wall-normal (c) spanwise Test2 (d) streamwise (e) wall-normal (f) spanwise.

structures for the fluid and particle phase are almost identical, and its magnitude is of the order of 2% of the bulk velocity. The mean cross-sectional flow takes the form of two rotating longitudinal vortices that lift fluid & particles vertically along the vertical centreline and back down outside. This secondary-flow pattern has previously been revealed in [73,74]. Belt et al. [73] conducted experimental study considering a simplified non-uniform distribution of particles ($d_p = 1mm$) kept at fixed positions in a pipe ($D = 50mm$) at a similar bulk flow $Re \approx 5000$. They found the direction of the secondary flow was determined by gradients in the radial and circumferential Reynolds stress caused by the inhomogeneous distribution of particles in the pipe cross-section. Their findings were later verified by Alletto and Breuer [74], who conducted numerical studies of particle-laden flow at mass loadings of 30% and 70%. The magnitude of secondary-flow predicted by Belt et al. was 7~9% of the bulk flow, whereas the value is significantly lower in this study (2% of the bulk flow). Our results are more consistent with Alletto and Breuer's findings (1~2% of the bulk flow). This may be likely due to a more homogeneous distribution of particles in the actual flow compared to the Belt et al.'s artificial distribution. Measurements of secondary flows is an involved task and often require a plurality of off-axis sensors [75,76]. For similar reasons such as loss of measuring signal integrity caused by particle induced diffraction, refraction and obscuration, it is an exceedingly difficult task to obtain meaningful measurements of velocity distributions at the dispersed phase concentrations.

The rms velocity fluctuations on the vertical centreline for both the fluid and particles phases are displayed in Fig. 8. The difference between the fluctuations in the upper and lower section of the pipe indicate significant turbulence damping by the particles, particularly in the streamwise direction. As an example, for $Re = 10{,}500$ in Test1, the near wall peak rms value of fluid streamwise fluctuation in the lower section is 0.31, which is around 30% lower than the peak value (0.44) in the upper section. Increasing the solid volume fraction further decreases the fluctuation level, as shown in Fig. 8(d) and the peak rms of streamwise fluctuation in the lower portion is only 0.19 for flow with a similar Re (9500) in Test2. The wall-normal and spanwise fluctuations are also damped but proportionally not as significantly as in the streamwise direction.

The particle fluctuations resemble the fluid phase fluctuation but usually with a higher fluctuation level in the cross-stream direction, especially in the central & lower bed layer region. Particle fluctuations do not vanish at the wall due to particle rotational and sliding motions. Unlike in the streamwise (Fig. 8(a) & (d)) and spanwise (Fig. 8(c) & (f)) direction where particles are mainly influenced by the drag force, the particle-particle/wall collision and gravity also affect the particle motion in the wall-normal direction. When a particle hits the wall, it will decelerate due to the imbalance between gravity and particle-wall collision; the particle will again accelerate as secondary flow and particle-wall collision drive the particle away from pipe wall. The local peak in the particle turbulence intensity at the height of approximately one particle diameter in the wall normal direction has also been noted in [6] where it is stated to be generated from particles entering and leaving the first layer of particles in the bed. Other studies have also compared the fluid & particle fluctuations in suspension flows [6,77–79]. Lashgari et al. [79] studied turbulent channel flow of a binary mixture of finite-sized ($d_p = 1/30 \sim 1/20$ channel height) neutrally buoyant particles at a similar $Re = 5600$ and solid volume fraction $C_v = 0.2$. They found a higher level of particle fluctuations in the cross-stream directions, but generally a lower streamwise fluctuation than that of the fluid phase away from the near-wall region. In contrast, Righetti & Romano [78] studied turbulent channel flow of dilute suspensions with medium size particles (0.1 ~ 0.2 mm) at Re close to 15,000 and found that the particle fluctuation in the streamwise direction was consistently larger than that of the fluid along the vertical centreline. Contrary to their findings, in this study the fluid and particle fluctuations in the streamwise direction are mostly the same except in the near wall region, while the biggest difference is found in the wall-normal (v_{rms}') direction that particle fluctuation are consistently larger than that of the fluid phase. Coarse particles are able to transfer fluctuation energy and

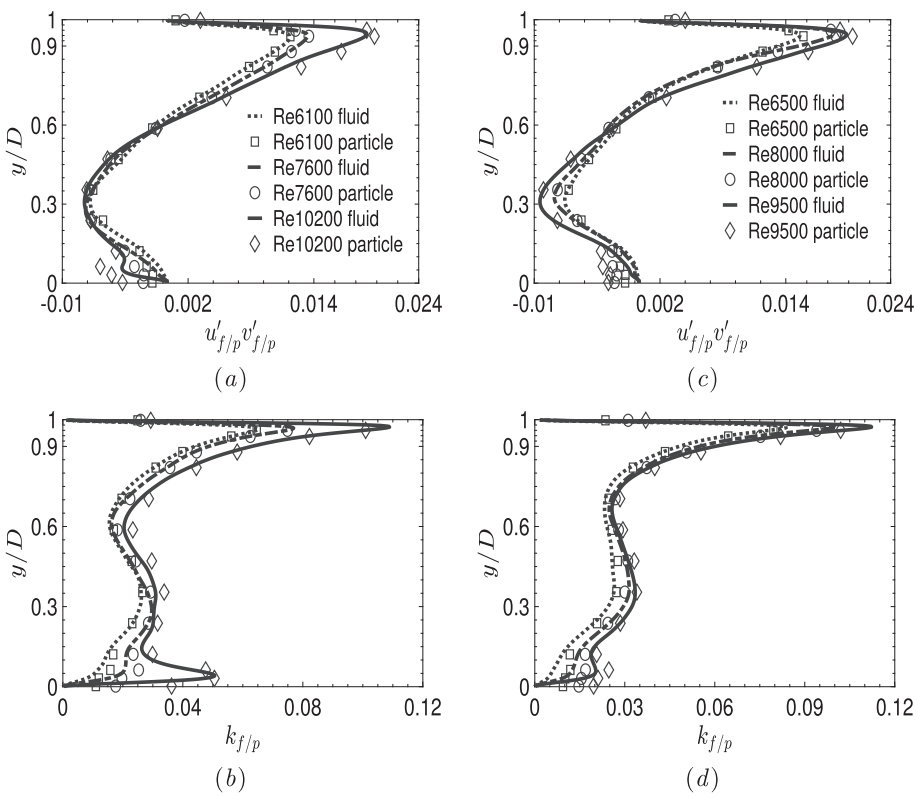

Fig. 9. Reynolds stress and turbulence kinetic energy profiles of the fluid and particle phase on a vertical centreline: Test1 (a) $u'v'$ (b) k; Test2 (c) $u'v'$ (d) k.

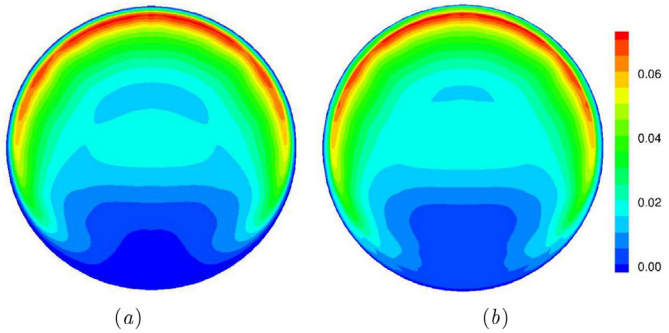

Fig. 10. Contours of the time-averaged turbulence kinetic energy in the pipe cross-section for the flow with $Re = 6100$ (a) fluid phase (b) particle phase.

momentum from other flow regions due to their inertia, and this local non-equilibrium state of the coarse particles can lead to higher fluctuation than the fluid phase [78]. In the near wall region, particles are lifted up by turbulent fluid ejections but respond slowly to the local velocity field owing to their inertia. As particles are driven by the fluid dynamics, they carry fluctuation energy and momentum from the near wall region to the buffer and outer region. This explains why the particle fluctuations in the outer region are consistently higher than the fluid phase.

The results of Reynolds stress and turbulence kinetic energy of both the fluid and particle phase on the vertical centreline are shown in Fig. 9. A reduction of the Reynolds stress peak value in the lower section also reveals turbulence damping from particles. The particle profile is similar to the fluid phase and a local maximum is observed close to the wall as well. From Fig. 9 (b) and (d), it can be seen the turbulence kinetic energy is significantly reduced in the lower portion of the pipe. For the flow with $Re = 10{,}500$ in Test1, the peak value of k_f reduces from 0.11 in the upper section to 0.05 in the lower section, and it further reduces to 0.02 as more solids are added (see similar $Re = 9500$ in Test2). Fig. 10 shows the contours of the turbulence kinetic energy in the pipe

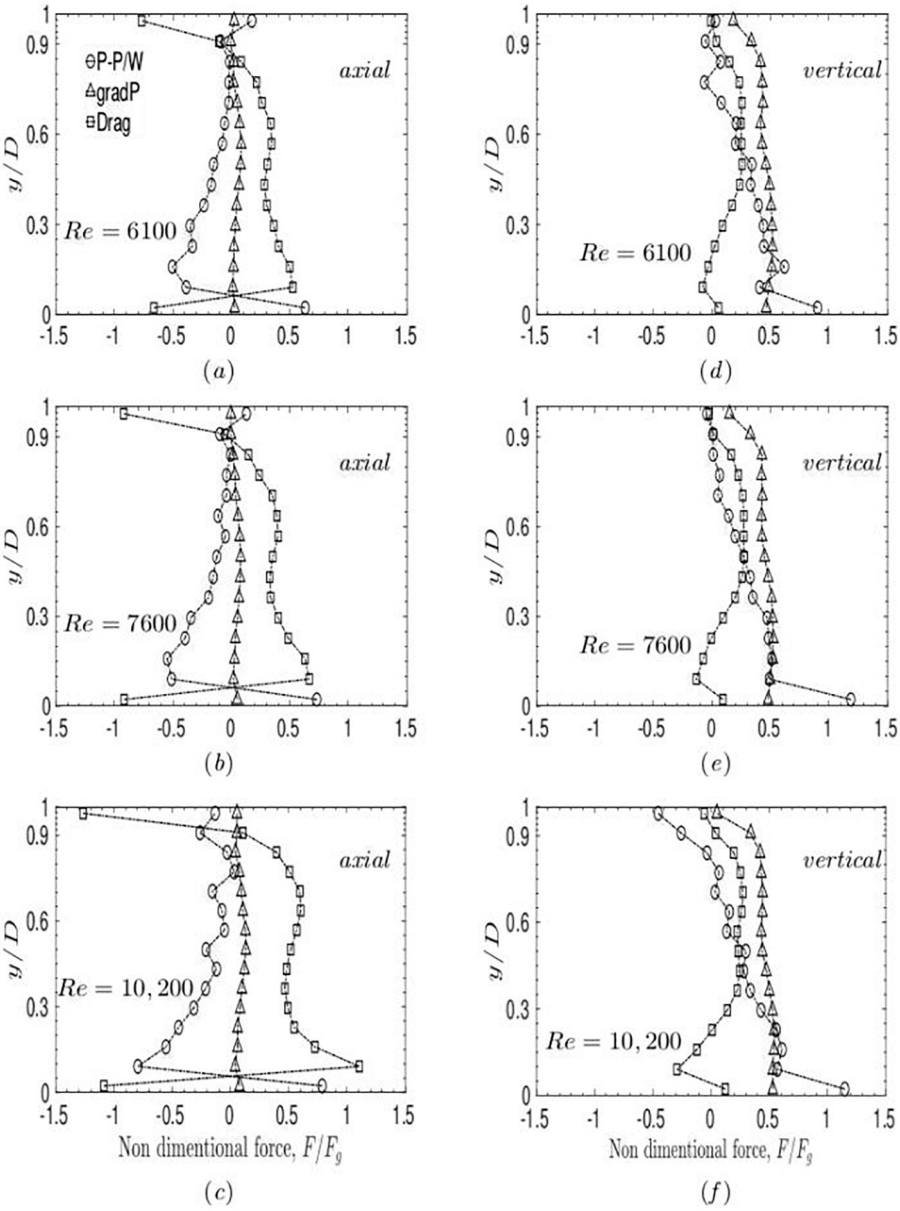

Fig. 11. Force distribution on particles on a vertical centreline: axial (a) $Re = 6100$ (b) $Re = 7600$ (c) $Re = 10{,}200$ vertical (d) $Re = 6100$ (e) $Re = 7600$ (f) $Re = 10{,}200$.

cross-section for the flow with $Re = 6100$. The contours for the fluid and particle phase are similar with large production of kinetic energy on the top and low kinetic energy at the bottom. A local minimum is also observed at a distance approximately a quarter of pipe diameter away from the top.

4.4. Distribution of forces on particles

The forces acting on individual particles are particle-particle and particle-wall collision forces (p-p/w), drag force, lift force, pressure gradient force, virtual mass force and viscous force. In order to understand the relative importance of these forces, they are averaged on a vertical slice of width $2d_p$ symmetric about the vertical centreline over the averaging period (10 FTTs) of the simulation. The distribution of forces acting on particles in both the axial and vertical direction are shown in Fig. 11. The forces shown are non-dimensionalised by the particle weight. Different from study in fluidised beds, where collective particle-particle collisions are zero for mono-dispersed particles [80], the sum of forces acting on particles are expected to be zero in the flow direction [22,81] if averaged over a sufficient amount of time and the number of particles is large enough. As can be seen from Fig. 11 (a)–(c), at most positions in the flow, p-p collisions are required to balance the drag force thus are not zero. Also seen in Fig. 11 (d) are some outliers such as at positions ($y/D \approx 0.15, 0.55, 0.85$), which are likely due to insufficient time averaging (10 FTTs). The force profiles in Test 2 are very similar to Test 1 and are not displayed.

The dominant forces on particles are the drag force, p-p/w collision and pressure gradient force. The lift force implemented as in [43] and Loth and Dorgan model [44], virtual mass and viscous force are $10^{-2} \sim 10^{-1}$ times as big as drag force and are not shown. It can be seen from Fig. 11 that in the axial direction, at positions near the bottom and top wall, the drag resists the particle motion and drag reaches a maximum. Particles near the bottom wall slow down and are lifted along the vertical centreline as shown in Fig. 7. As the velocity of fluid phase increases away from the wall, the drag force is now driving the particles in the flow direction above the lowest layer while p-p collisions resist the particle motion. The drag and p-p/w collisions generally increase at a higher *Re*, as can be seen from Fig. 11 (a) and (c). The pressure gradient force is trivial in driving the axial particle flow compared to drag and p-p/w collisions.

In the vertical direction, the pressure gradient force is significant in supporting the particles and displays a nearly uniform value except for positions near the top wall. The drag still plays a role but not as important as pressure gradient force and p-p/w collision. Similarly, the magnitude of p-p/w collision also increases at higher *Re*. The solid concentration in the lower section of the pipe is sufficiently high that particles compress against each other, while the wall resists the compression and supports the particles from the bottom. The resultant vertical p-p/w force in the lower section of the pipe is positive as shown in Fig. 11 (d)–(f). Above this lowest layer, the p-p collisions keep the particles suspended and support particles toward the centre. In the upper section of the pipe where the particle number is relatively low, particles are mainly supported by pressure gradient and drag force.

5. Conclusion

This paper presents a DNS-DEM model for investigating weakly turbulent ($4000 < Re < 10{,}000$) coarse particle suspension flow. Experiments in a pipe with solids volume fractions up to $\phi = 0.22$ were conducted for model validation. Suspension data including pressure drop, flow rate and concentration profile, as well as the visual observation of the flow were obtained at different flow regimes ranging from settled bed to suspended flow.

The predicted flows are qualitatively similar to experiments with the formation of a sliding bed (e.g. $Re = 6100$, $\phi = 0.18$) and transition from sliding bed to partial suspension (e.g., $Re = 10{,}200$, $\phi = 0.15$). The predicted mixture velocity and concentration profiles are in quite reasonable quantitative agreement with the experimental results, particularly under flow conditions where particles are suspended with a thin bed at the bottom. The concentration profiles predicted are mostly less than 10% difference and good agreements are always achieved at both the top & bottom in the pipe cross-section where the measuring electrodes are close. The maximum deviation is observed near the pipe centre for flows with a distinct sliding bed. The deviation may be a combined effect of the insufficient spatial resolution of the ERT in the experiment and the diffusion approach adopted in the coupling. Despite this limitation, it has little impact on the flow when there is no significant bed, which can be seen from the flow with $Re = 10200$ and $\phi = 0.15$. Future work may consider developing an alternative DNS-DEM coupling by adopting the porous cube or conservative virtual volume fraction method. An algorithm for easy parallelization of these methods needs to be developed for efficient searching of cells occupied by the particle, particularly for those located in different processors.

The mean flow profiles are significantly damped by the presence of coarse particles, particularly in the stream-swise direction. The time-averaged cross-sectional vector field of the secondary flow for the fluid & particle phase are almost identical, and the magnitude of the secondary flow is of the order of 2% of the bulk velocity. Experimental measurements of mean fluid velocity profile, particle velocity profile and secondary flow are not available and are difficult to measure. These measurements are needed and the reliability of potential techniques such as simultaneous fluidparticle PIV method needs to be verified, especially in dense suspension flow. The particle fluctuations resemble the fluid phase fluctuation but usually with a higher fluctuation level in the cross-stream direction. The biggest difference is found in the wall-normal flow direction, especially in the central & lower bed layer region. The force distribution reveals the particle-particle and particle-wall collision, the drag and pressure gradient force are dominating the particle motion in forming the resulted pattern. The impact of lift, virtual mass and viscous force is trivial in both the axial and vertical direction.

The results presented here demonstrate that DNS-DEM coupling is a promising approach for investigating weakly turbulent dense suspension flow, with most velocity and concentration profile predictions in quite good agreement with the experimental results. On this basis, this DNS-DEM modelling approach can be recommended and will form the basis of our future work on coarse-particle non-Newtonian suspension flow, an application that has significant interest in the disposal of mining waste streams and particles in these systems have been shown to be more fully suspended compared to an equivalent Newtonian suspension.

Declaration of Competing Interest

None.

Acknowledgements

The research is supported by Monash International Postgraduate Research Scholarship and Monash Graduate Scholarship, Monash University, Australia. The authors are also thankful for the funding and support from CSIRO Minerals, particularly Kosta Simic for his help on setting up the pipe loop and Keri Constanti-Carey for her rheological characterisation of the carrier fluids. Computations in this study are carried out with the assistance of resources and services from the National Computational Infrastructure (NCI), which is supported by the Australian Government via merit allocation scheme grant number D77. We gratefully acknowledge the resources and their support. The authors EZ, MR and SK also acknowledge support from the ARC Research Hub for Computational Particle Technology (IH1401001035) in undertaking this research.

References

[1] S. Akhshik, M. Behzad, M. Rajabi, CFD–DEM approach to investigate the effect of drill pipe rotation on cuttings transport behavior, J. Pet. Sci. Eng. 127 (2015) 229–244.
[2] L. Pullum, D.V. Boger, F. Sofra, Hydraulic mineral waste transport and storage, Annu. Rev. Fluid Mech. 58 (2018) 157–185.
[3] R.G. Gillies, C.A. Shook, J. Xu, Modelling heterogeneous slurry flows at high velocities, Can. J. Chem. Eng. 82 (2004) 1060–1065.
[4] R. Silva, F.A. Garcia, P.M. Faia, M.G. Rasteiro, Settling suspensions flow modelling: a review, Kona Powder 32 (2015) 41–56.
[5] P.J. Cullen, Food Mixing: Principles and Applications, John Wiley & Sons, 2009.
[6] F. Picano, W.P. Breugem, L. Brandt, Turbulent channel flow of dense suspensions of neutrally buoyant spheres, J. Fluid Mech. 764 (2015) 463–487.
[7] R.G. Gillies, Pipeline Flow of Coarse Particle Slurries, University of Saskatchewan Saskatoon, SK, 1993.
[8] R. Durand, E. Condolios, The Hydraulic Transport of Coal and Solid Materials in Pipes, National Coal Board, 1963.
[9] V. Matoušek, Research developments in pipeline transport of settling slurries, Powder Technol. 156 (2005) 43–51.
[10] M. Rasteiro, M. Figueiredo, H. Franco, Pressure drop for solid/liquid flow in pipes, Part. Sci. Technol. 11 (1993) 147–155.
[11] P. Doron, D. Barnea, A three-layer model for solid-liquid flow in horizontal pipes, Int. J. Muliph. Flow. 19 (1993) 1029–1043.
[12] M. Ishii, K. Mishima, Two-fluid model and hydrodynamic constitutive relations, Nucl. Eng. Des. 82 (1984) 107–126.
[13] G.V. Messa, S. Malavasi, Improvements in the numerical prediction of fully-suspended slurry flow in horizontal pipes, Powder Technol. 270 (2015) 358–367.
[14] K. Ekambara, R.S. Sanders, K. Nandakumar, J.H. Masliyah, Hydrodynamic simulation of horizontal slurry pipeline flow using ANSYS-CFX, Ind. Eng. Chem. Res. 48 (2009) 8159–8171.
[15] M. Eesa, M. Barigou, CFD investigation of the pipe transport of coarse solids in laminar power law fluids, Chem. Eng. Sci. 64 (2009) 322–333.
[16] M.K. Gopaliya, D. Kaushal, Modeling of sand-water slurry flow through horizontal pipe using CFD, J. Hydrol. Hydromech. 64 (2016) 261–272.
[17] G. Liu, Application of the two-fluid model with kinetic theory of granular flow in liquid–solid fluidized beds, Granularity in Materials Science 2018, p. 2.
[18] H. Zhu, Z. Zhou, R. Yang, A. Yu, Discrete particle simulation of particulate systems: theoretical developments, Chem. Eng. Sci. 62 (2007) 3378–3396.
[19] Y. Tsuji, T. Tanaka, T. Ishida, Lagrangian numerical simulation of plug flow of cohesionless particles in a horizontal pipe, Powder Technol. 71 (1992) 239–250.
[20] B. Xu, A. Yu, Numerical simulation of the gas-solid flow in a fluidized bed by combining discrete particle method with computational fluid dynamics, Chem. Eng. Sci. 52 (1997) 2785–2809.
[21] S. Kuang, M. Zhou, A. Yu, CFD–DEM modelling and simulation of pneumatic conveying: a review, Powder Technol. 365 (2020) 186–207.
[22] A. Uzi, A. Levy, Flow characteristics of coarse particles in horizontal hydraulic conveying, Powder Technol. 326 (2018) 302–321.
[23] R. Sun, H. Xiao, SediFoam: a general-purpose, open-source CFD–DEM solver for particle-laden flow with emphasis on sediment transport, Comput. Geosci. 89 (2016) 207–219.
[24] M. Zhou, S. Wang, S. Kuang, K. Luo, J. Fan, A. Yu, CFD-DEM modelling of hydraulic conveying of solid particles in a vertical pipe, Powder Technol. 354 (2019) 893–905.
[25] N. Gui, J.R. Fan, S. Chen, Numerical study of particle–particle collision in swirling jets: a DEM–DNS coupling simulation, Chem. Eng. Sci. 65 (2010) 3268–3278.
[26] Z. Qi, S. Kuang, A. Yu, Lattice boltzmann investigation of non-newtonian fluid flow through a packed bed of uniform spheres, Powder Technol. 343 (2019) 225–236.
[27] D. Nie, J. Lin, A fluctuating lattice-boltzmann model for direct numerical simulation of particle brownian motion, Particuology 7 (6) (2009) 501–506.
[28] S. Srinivasan, H.E. Van den Akker, O. Shardt, Shear thickening and history-dependent rheology of monodisperse suspensions with finite inertia via an immersed boundary lattice boltzmann method, Int. J. Multiph. Flow 125 (2020), 103205.
[29] I. Lashgari, F. Picano, W.-P. Breugem, L. Brandt, Laminar, turbulent, and inertial shear-thickening regimes in channel flow of neutrally buoyant particle suspensions, Phys. Rev. Lett. 113 (2014), 254502.
[30] W. Fornari, F. Picano, L. Brandt, The effect of polydispersity in a turbulent channel flow laden with finite-size particles, Eur. J. Mech. 67 (2018) 54–64.
[31] M.N. Ardekani, L. Brandt, Turbulence modulation in channel flow of finite-size spheroidal particles, J. Fluid Mech. 859 (2019) 887–901.
[32] T. Kempe, B. Vowinckel, J. Fröhlich, On the relevance of collision modeling for interface-resolving simulations of sediment transport in open channel flow, Int. J. Multiph. Flow 58 (2014) 214–235.
[33] P. Gnambode, P. Orlandi, M. Ould-Rouiss, X. Nicolas, Large-Eddy simulation of turbulent pipe flow of power-law fluids, Int. J. Heat Fluid Flow 54 (2015) 196–210.
[34] D. Mehta, A. Thota Radhakrishnan, J. van Lier, F. Clemens, A wall boundary condition for the simulation of a turbulent non-newtonian domestic slurry in pipes, Water 10 (2018) 124.
[35] R. Chhabra, J. Richardson, Hydraulic transport of coarse particles in viscous Newtonian and non-Newtonian media in a horizontal pipe, Chem. Eng. Res. Des. 63 (1985) 390–397.
[36] P. Vlasák, Z. Chára, J. Konfršt, Flow behaviour and structure of heterogeneous particles-water mixture in horizontal and inclined pipes, EPJ Web of Conferences, vol. 180, 2018, p. 02120.
[37] P.A. Cundall, O.D. Strack, A discrete numerical model for granular assemblies, Geotechnique 29 (1979) 47–65.
[38] C. Kloss, C. Goniva, A. Hager, S. Amberger, S. Pirker, Models, algorithms and validation for opensource dem and cfd–dem, Prog. Comput. Fluid Dyn. 12 (2012) 140–152.
[39] T.B. Anderson, R. Jackson, Fluid mechanical description of fluidized beds: equations of motion, Ind. Eng. Chem. Res. 6 (1967) 527–539.
[40] D. Gidaspow, Multiphase Flow and Fluidization: Continuum and Kinetic Theory Descriptions, Academic press, 1994.
[41] C.Y. Wen, Mechanics of fluidization, Chem. Eng. Prog. Symp. Ser. 62 (1966) 100–111.
[42] S. Ergun, Fluid flow through packed columns, Chem. Eng. Prog. 48 (1952) 89–94.
[43] D.A. Drew, Mathematical modeling of two-phase flow, Annu. Rev. Fluid Mech. 15 (1983) 261–291.
[44] E. Loth, A.J. Dorgan, An equation of motion for particles of finite Reynolds number and size, Environ. Fluid Mech. 9 (2) (2009) 187–206.
[45] P. Saffman, The lift on a small sphere in a slow shear flow, J. Fluid Mech. 22 (2) (1965) 385–400.
[46] R. Mei, An approximate expression for the shear lift force on a spherical particle at finite Reynolds number, Int. J. Multiph. Flow 18 (1) (1992) 145–147.
[47] Z. Zhou, S. Kuang, K. Chu, A. Yu, Discrete particle simulation of particle–fluid flow: model formulations and their applicability, J. Fluid Mech. 661 (2010) 482–510.
[48] Z. Peng, E. Doroodchi, C. Luo, B. Moghtaderi, Influence of void fraction calculation on fidelity of CFD-DEM simulation of gas-solid bubbling fluidized beds, AICHE J. 60 (6) (2014) 2000–2018.
[49] H. Zhu, A. Yu, Averaging method of granular materials, Phys. Rev. E 66 (2002), 021302.
[50] J. Link, L. Cuypers, N. Deen, J. Kuipers, Flow regimes in a spout–fluid bed: a combined experimental and simulation study, Chem. Eng. Sci. 60 (2005) 3425–3442.
[51] S. Kuang, K. Chu, A. Yu, Z. Zou, Y. Feng, Computational investigation of horizontal slug flow in pneumatic conveying, Ind. Eng. Chem. Res. 47 (2008) 470–480.
[52] S. Radl, B.C. Gonzales, C. Goniva, S. Pirker, State of the Art in Mapping Schemes for Dilute and Dense Euler-Lagrange Simulations, 2015.
[53] J. Capecelatro, O. Desjardins, Eulerian–Lagrangian modeling of turbulent liquid–solid slurries in horizontal pipes, Int. J. Multiph. Flow 55 (2013) 64–79.
[54] S. Pirker, D. Kahrimanovic, C. Goniva, Improving the applicability of discrete phase simulations by smoothening their exchange fields, Appl. Math. 35 (2011) 2479–2488.
[55] M. Rudman, H.M. Blackburn, Direct numerical simulation of turbulent non-newtonian flow using a spectral element method, Appl. Math. 30 (2006) 1229–1248.
[56] E. Zheng, M. Rudman, J. Singh, S. Kuang, Direct numerical simulation of turbulent non-newtonian flow using openfoam, Appl. Math. 72 (2019) 50–67.
[57] H.M. Blackburn, S.J. Sherwin, Formulation of a galerkin spectral element–fourier method for three-dimensional incompressible flows in cylindrical geometries, J. Comput. Phys. 197 (2) (2004) 759–778.
[58] C. Goniva, C. Kloss, N.G. Deen, J.A. Kuipers, S. Pirker, Influence of rolling friction on single spout fluidized bed simulation, Particuology 10 (2012) 582–591.
[59] S. Haren, Testing DNS Capability of OpenFOAM and STAR-CCM+, 2011.
[60] E. Komen, A. Shams, L. Camilo, B. Koren, Quasi-DNS capabilities of OpenFOAM for different mesh types, Comput. Fluids 96 (2014) 87–104.
[61] H.R. Norouzi, R. Zarghami, R. Sotudeh-Gharebagh, N. Mostoufi, Coupled CFD-DEM Modeling: Formulation, Implementation and Application to Multiphase Flows, John Wiley & Sons, 2016.
[62] A. Adler, A. Boyle, F. Braun, M.G. Crabb, B. Grychtol, W.R. Lionheart, H.F. Tregidgo, R. Yerworth, Eidors version 3.9, Elect. Imped. Tomogr. 21 (2017) 63.
[63] A.R. Oroskar, R.M. Turian, The critical velocity in pipeline flow of slurries, AICHE J. 26 (1980) 550–558.
[64] S.J. Stanley, G.T. Bolton, A review of recent electrical resistance tomography (ert) applications for wet particulate processing, Part. Part. Syst. Charact. 25 (3) (2008) 207–215.
[65] P. Faia, R. Silva, M.G. Rasteiro, F. Garcia, Electrical tomography: a review of configurations, and application to fibre flow suspensions characterisation, Appl. Sci. 10 (7) (2020) 2355.
[66] D. Holder, Electrical Impedance Tomography: Methods, History and Applications, CRC Press, 2004.
[67] S. Ren, F. Dong, C. Tan, High-precision electrical resistance tomography with external and internal electrode arrays, 2011 IEEE International Instrumentation and Measurement Technology Conference, IEEE 2011, pp. 1–6.
[68] R. Kotze, A. Adler, A. Sutherland, C. Deba, Evaluation of electrical resistance tomography imaging algorithms to monitor settling slurry pipe flow, Flow Meas. Instrum. 68 (2019), 101572.
[69] N. Gui, X. Yang, J. Tu, S. Jiang, A fine LES-DEM coupled simulation of gas-large particle motion in spouted bed using a conservative virtual volume fraction method, Powder Technol. 330 (2018) 174–189.
[70] S. Wiederseiner, N. Andreini, G. Epely-Chauvin, C. Ancey, Refractive-index and density matching in concentrated particle suspensions: a review, Exp. Fluids 50 (5) (2011) 1183–1206.
[71] G. Bellani, M.L. Byron, A.G. Collignon, C.R. Meyer, E.A. Variano, Shape effects on turbulent modulation by large nearly neutrally buoyant particles, J. Fluid Mech. 712 (2012) 41–60.
[72] M.L. Byron, E.A. Variano, Refractive-index-matched hydrogel materials for measuring flow-structure interactions, Exp. Fluids 54 (2) (2013), 1456.
[73] R. Belt, A. Daalmans, L. Portela, Experimental study of particle-driven secondary flow in turbulent pipe flows, J. Fluid Mech. 709 (2012) 1–36.
[74] M. Alletto, M. Breuer, Prediction of turbulent particle-laden flow in horizontal smooth and rough pipes inducing secondary flow, Int. J. Multiphas. Flow 55 (2013) 80–98.

[75] A. Chryss, L. Graham, K. Mohanarangnam, Slurry flow in self-formed channels on tailings beaches, Paste 2016: Proceedings of the 19th International Seminar on Paste and Thickened Tailings, 2016.
[76] A. Chryss, L. Graham, K. Mohanarangnam, Non-newtonian flow in small channels and their relevance to tailings beach, 20th International Conference on Hydrotransport, Melbourne, Australia 2017, pp. 213–224.
[77] D. Kaftori, G. Hetsroni, S. Banerjee, Particle behavior in the turbulent boundary layer. ii. Velocity and distribution profiles, Phys. Fluids 7 (1995) 1107–1121.
[78] M. Righetti, G.P. Romano, Particle–fluid interactions in a plane near-wall turbulent flow, J. Fluid Mech. 505 (2004) 93–121.
[79] I. Lashgari, F. Picano, P. Costa, W.-P. Breugem, L. Brandt, Turbulent channel flow of a dense binary mixture of rigid particles, J. Fluid Mech. 818 (2017) 623–645.
[80] Z. Peng, J.B. Joshi, B. Moghtaderi, M.S. Khan, G.M. Evans, E. Doroodchi, Segregation and dispersion of binary solids in liquid fluidised beds: a CFD-DEM study, Chem. Eng. Sci. 152 (2016) 65–83.
[81] S. Kuang, R. Zou, R. Pan, A. Yu, Gas–solid flow and energy dissipation in inclined pneumatic conveying, Ind. Eng. Chem. 51 (43) (2012) 14289–14302.

5.2 Validation with non-Newtonian suspension flows

5.2.1 Experimental measurement

The experimental pipe loop for non-Newtonian suspension flows is the same as in the Newtonian suspension experiments and details can be found in Appendix A. Similarly, measurements of pressure drop, mixture flow rates, concentration distribution from ERT, as well as qualitative view through the transparent acrylic pipe section are obtained. Coarse-particle suspension data can be found in Appendix B.

Table 5.1 Ranges of non-Newtonian suspension variables in the experiment

Property	Value
Pipe diameter, $D(mm)$	44
Fluid density, $\rho_f(kg/m^3)$	1000
Yield stress, $\tau_y(Pa)$	$0.01 \sim 0.33$
Flow index, n	$0.54 \sim 0.70$
Consistency, $k(pa \cdot s^n)$	$0.124 \sim 0.697$
Solid density, $\rho_p(kg/m^3)$	2600
Particle size, $d_p(mm)$	2 ± 0.2
In line concentration, C_v	$0.1 \sim 0.2$
Flow regime	sliding bed to partially suspended
Bulk flow Re_G	$6,000 \sim 15,000$

The non-Newtonian slurry is prepared using $0.1\%wt$ Carbopol (mixed with water and pH neutralised) solution as the carrier fluid and near mono-dispersed glass beads with diameter $d_p = 2mm$. Measurements are taken at different solids concentration over a range of velocities. Rheological measurements of the Carbopol solution (solids removed) are conducted both before and after each flow test using a Haake Rheostress RS1 rheometer. According to Singh et al. [121], high shear rate rheology is crucial in turbulent flow predictions using DNS and reduces discrepancy caused by both experimental measurements and choice of rheology models. Rheology measurements at shear rate $\dot{\gamma}$ up to $20,000$ (as shown in Fig 5.1) in a combined Couette and parallel plate geometries are conducted. The flow parameters are fitted with a Herschel-Bulkley (*HB*) model. The rheology measurements of the tests are presented in Appendix C. Ranges

of flow parameters tested are shown in Table 5.1. The bulk flow Re_G is expressed as $Re_G = \rho_f U_m D/\eta_w$, where U_m is the mixture flow rate, D is pipe diameter, ρ_f and η_w represent the carrier fluid density and mean wall viscosity, respectively.

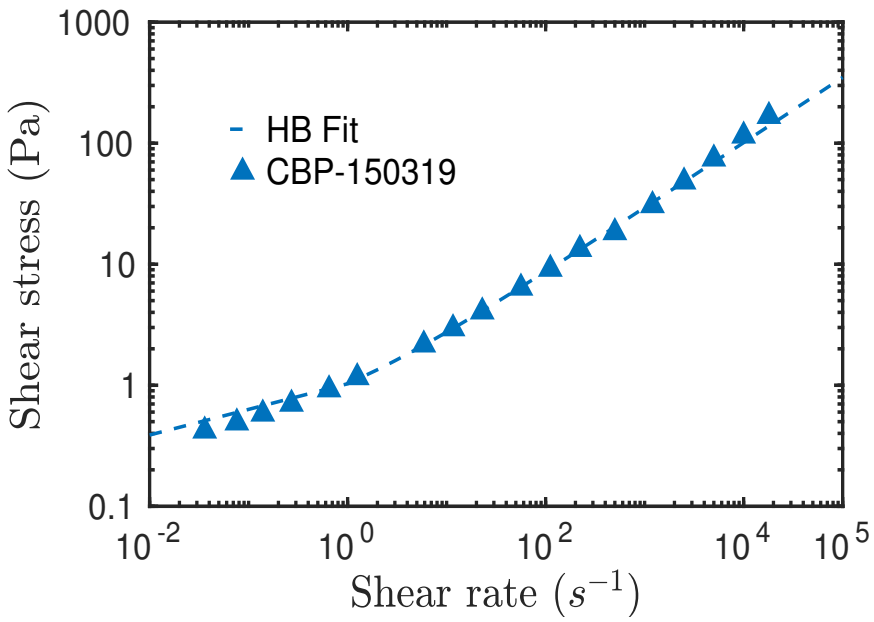

Fig. 5.1 High shear rate rheology measurement for the flow with $C_v = 0.1$

The flows shown in Table 5.1 are with a low yield stress that $\boldsymbol{\tau}_y < 1Pa$. Though the initially measured $\boldsymbol{\tau}_y$ of the Carbopol solution is $3.4\ Pa$ (with no solids added), it degrades to $2.3\ Pa$ after adding solids. As the flow circulates in the pipe, the Carbopol solution keeps degrading with time. The design of a weakly turbulent flow with a high yield stress can be difficult that the flow is likely to fall into a laminar regime due to the constraint of pump power capacity.

Another flow test has been attempted in getting a weakly turbulent flow with a higher yield stress. The non-Newtonian slurry is prepared using $0.2\%wt$ Carbopol (mixed with water) solution as the carrier fluid and $2\ mm$ mono-sized glass beads with a solid volume fraction of $C_v = 0.15$. The flow starts with a high viscosity ($\boldsymbol{\tau}_y = 6.91Pa$, $k = 3.62Pa \cdot s^n$ and $n = 0.46$). Water is then added gradually to adjust the viscosity down aiming to obtain a turbulent flow. However, the flow ends up in experiencing pipe blockage in the upper section of the pipe loop and fails to obtain desired turbulent flow data. Despite this, one set of laminar flow data with ERT measurements is obtained. The flow parameters are shown in Table 5.2.

Table 5.2 Flow parameters of the non-Newtonian suspension using $0.2\%wt$ Carbopol

Pipe diameter $D(mm)$	Solids concentration C_v	Particle diameter $d_p(mm)$	Mixture flow rate $\boldsymbol{U}_m(m/s)$	Yield stress $\boldsymbol{\tau}_y(Pa)$	Consistency $k(Pa \cdot s^n)$	Flow index n
44	0.15	2	1.64	3.03	1.7	0.49

5.2.2 Model validation

5.2.2.1 Qualitative view and mixture flow rates

Two representative sets of test runs are selected for discussion. For each set, same amount of solids are added but conveyed at different velocities. The first set is at in-line solids concentration 10%, while the second one is at a relatively higher in-line solids concentration $16 \sim 18\%$. The in-line solids concentration varies slightly when the flow velocity changes. Previously settled solids may get re-suspended as flow rate increases. The flow conditions of the two experimental sets are shown in Table 5.3.

Table 5.3 Flow conditions of the two representative experimental sets

Property	Test1 (CBP-150319)			Test2 (CBP-200319)		
In line concentration, C_v	0.1	0.1	0.1	0.18	0.16	0.16
Yield stress, $\boldsymbol{\tau}_y(Pa)$	0.33	0.23	0.16	0.08	0.04	0.01
Consistency, $k(Pa \cdot s^n)$	0.697	0.479	0.406	0.338	0.228	0.124
Flow index, n	0.54	0.58	0.59	0.60	0.64	0.70
Pressure gradient per unit mass (m/s^2)	3.9	4.6	5.2	4.2	4.5	4.9
Bulk flow Re_G	6,000	8,500	12,000	8,900	11,800	15,000
Mixture velocity, $\boldsymbol{U}_m$ (m/s)	2.85	3.19	3.67	2.59	2.99	3.20
Predicted mixture velocity, $\boldsymbol{U}_m$ (m/s)	2.73	3.11	3.40	2.47	2.71	2.96
Difference	-4.2%	-2.7%	-7.4%	-4.6%	-9.4%	-6.3%

A qualitative comparison between the experiment and DNS-DEM prediction is shown in Fig 5.2. The predicted flow looks qualitatively similar to the experiment with the formation of a bed for the flow ($Re_G = 8,900, C_v = 0.18$) and a heterogeneous pattern with partial suspension for the flow ($Re_G = 12,000, C_v = 0.1$). The experimental and predicted mixture velocity are shown in Table 5.3. The DNS-DEM model predicts the mixture flow rates well within 10% of the experiment. The best agreement is found for the flow ($Re_G = 8,500, C_v = 0.1$) with a deviation of -2.7%.

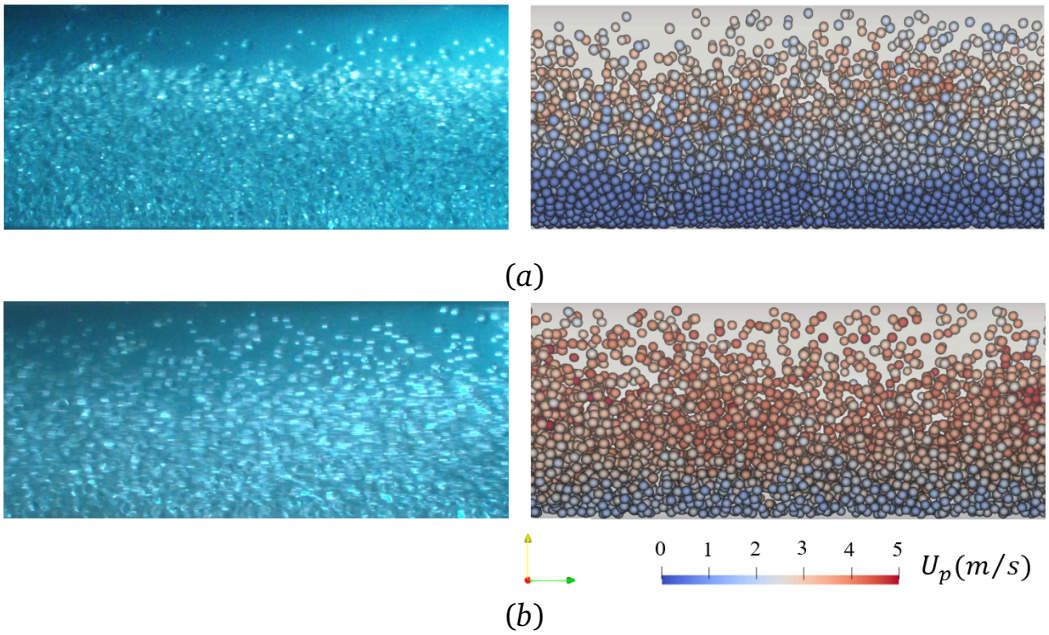

Fig. 5.2 Qualitative view of the pipe flow from experiment and DNS-DEM, colour contour represents velocity of particle phase (a) $Re_G = 8,900$, $C_v = 0.18$ (b) $Re_G = 12,000$, $C_v = 0.1$

Table 5.4 Flow parameters of non-Newtonian suspension from Pěník et al.[89]

Pipe diameter $D(mm)$	Solids concentration C_v	Particle diameter $d_p(mm)$	Mixture flow rate $\boldsymbol{U}_m(m/s)$	Yield stress $\tau_y(Pa)$	Consistency $k(Pa \cdot s^n)$	Flow index n
50	0.1	1.5	1.82∼4.76	0.81∼3.76	1.414∼2.643	0.479∼0.504

In addition to the experimental measurements mentioned above, DNS-DEM model predictions are also compared to mixture velocity measurements from Pěník et al. ([89] and personal communication), who conducted laminar and turbulent coarse particle ($0.57 \sim 1.5\ mm$) suspension flow in a Carbopol carrier in a $50\ mm$ pipe. The flow parameters of interest from their experiments are shown in Table 5.4. The flow in the turbulent regime from this set of data with bulk flow $Re_G = 5,000$ ($\boldsymbol{U}_m = 3.47m/s$) and $Re_G = 9,500$ ($\boldsymbol{U}_m = 4.76m/s$) are selected for comparison with DNS-DEM predictions. The predicted mixture velocities are also in very good agreement, which are $3.35\ m/s$ (-3.5%) and $4.52\ m/s$ (-5.0%), respectively.

5.2.2.2 Concentration profile

In the DNS-DEM coupling, the drag correlation for a packed bed in a *HB* fluid is needed. However, the correlation is unknown and it depends on fluid rheology, solids concentration and local shear rate. There have been a few studies working on single particle settling in both sheared [21, 88, 112, 114] and unsheared [8, 126, 133] shear-thinning fluids. On this basis, the following options offer alternatives for the unknown drag correlation:

- Approach 1: the Gidaspow drag model [44] in a Newtonian suspension is adopted, with a mere replacement of Newtonian viscosity with the *HB* viscosity;
- Approach 2: the Gidaspow drag model is adopted with the drag coefficient replaced by the correlation for single sphere settling in an unsheared yield-stress fluid [8, 126]. The effect of fluid volume fraction related to the contribution by neighbouring particles remains the same. The implementation is shown in equation 4.16.
- Approach 3: The local viscosity around a particle reduces when under shear. Similarly as in studies of particle settling under imposed shear [88, 114], the carrier viscosity and particle Reynolds number are defined based on the total shear rate $\dot{\gamma}_T$. The $\dot{\gamma}_T$ is defined as the vectorial sum of local shear rate $\dot{\gamma}$ and the shear from particle settling $|\boldsymbol{u}_f - \boldsymbol{u}_p|/d_p$, as shown in Eq. 5.1. The rest follows the same procedure as in Approach 2.

$$\dot{\gamma}_T = \sqrt{\dot{\gamma}^2 + (|\boldsymbol{u}_f - \boldsymbol{u}_p|/d_p)^2} \tag{5.1}$$

The predicted concentration profiles on the vertical centreline of the pipe cross-section for the flow ($Re_G = 6,000$) based on different approaches are shown in Fig 5.3. As can be seen, Approach 2 provides good agreement (the dotted line) with experimental results and much better agreement than a mere replacement of Newtonian viscosity with the *HB* viscosity (the red line). The Re_p in this case is around 50, it is likely the pressure drag is most important here thus the modification in Approach 3 (the blue line) produces little difference from Approach 2.

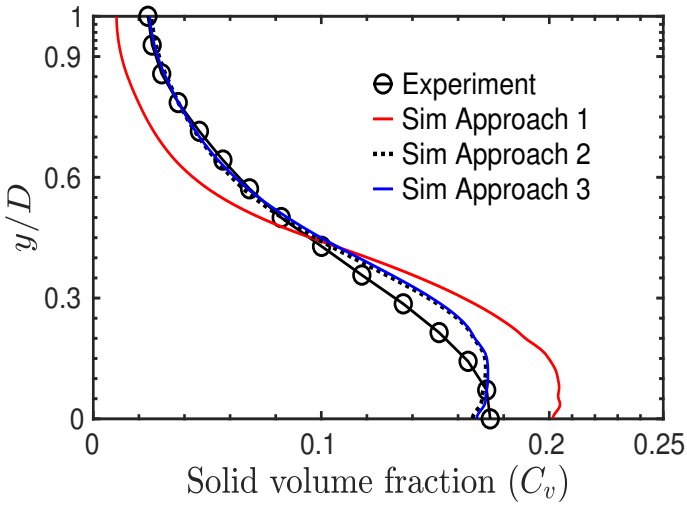

Fig. 5.3 Predicted concentration profile on the centreline of the pipe cross-section for the flow $Re_G = 6,000$ based on different drag correlations

Based on the modified drag correlation in Approach 2, the solid volume concentration profiles on the vertical centreline of the pipe cross-section for test sets $1\&2$ are shown in Fig 5.4. Generally the concentration profiles are in good agreement with the experimental measurements, particularly for the flow with $Re_G = 12,000$ and $C_v = 0.1$. The deviations are mostly within 10% and usually much less, except that in most of these flows we observe a slight underestimation of the solids concentration near the bottom wall and an overestimation in the region around $1/3$ height of the pipe.

Despite the uncertain accuracy of the drag correlation for a packed bed in a sheared *HB* fluid may cause somewhat discrepancy, the deviation is more likely caused by a combined effect of experimental error and modelling error due to the diffusion approach. The 2D concentration distribution in the pipe cross-section for the flow with $Re_G = 6,000$ from both the ERT and DNS-DEM prediction are shown in Fig 5.5. As discussed in section 5.1, ERT is a promising approach for concentration measurements but it has the limitation of low spatial resolution [58] in capturing the conductivity distribution, particularly in the central region. In addition, similarly as in the Newtonian suspension, the diffusion approach adopted in the DNS-DEM coupling may also cause the discrepancy as it diffuses away solid volume fraction from pipe bottom to the central region, though this effect would diminish as particles become more suspended, as demonstrated in the flow with $Re_G = 12,000$ and $C_v = 0.1$.

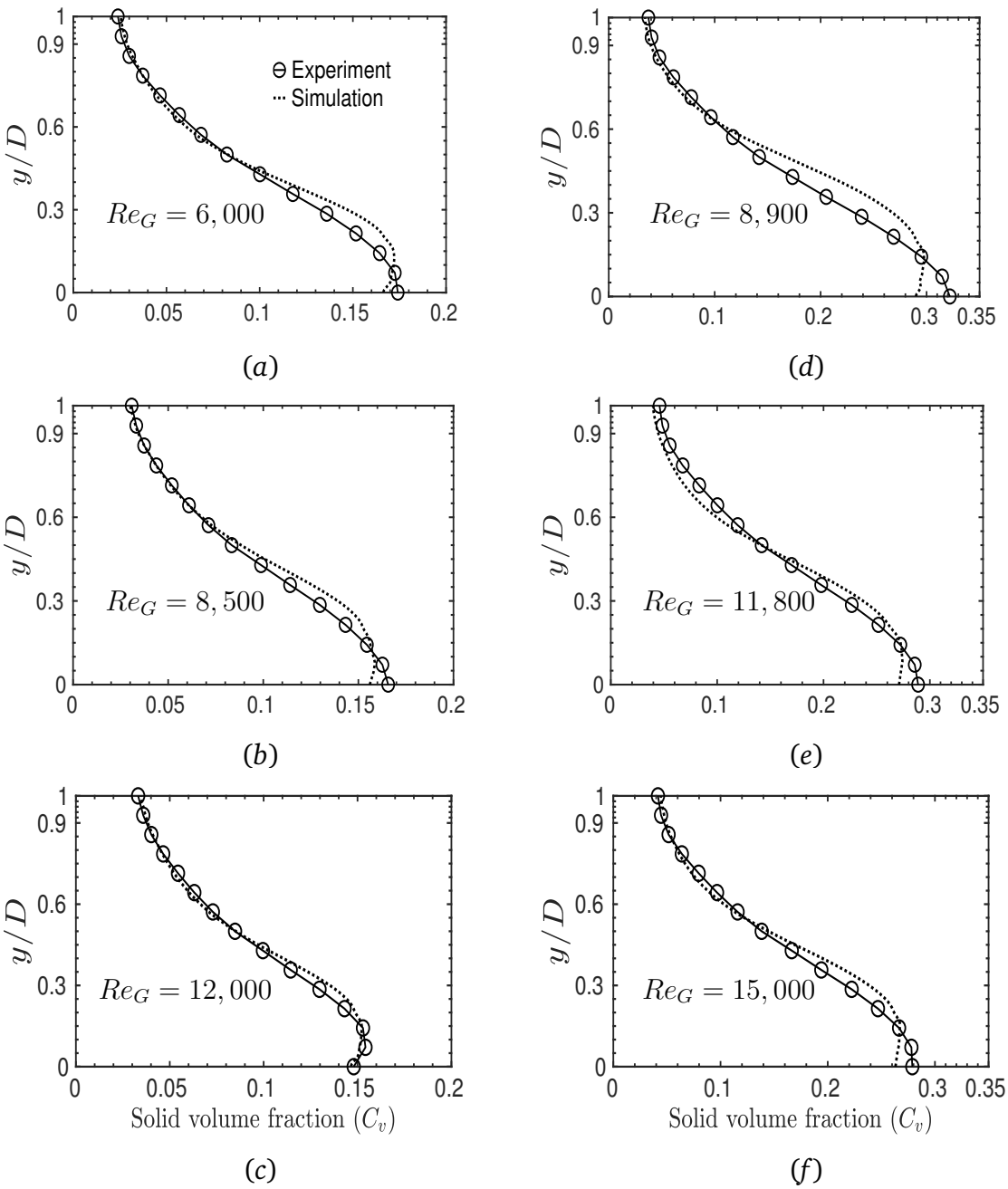

Fig. 5.4 Concentration profile on the centreline of the pipe cross-section: Test1 (a) $Re_G = 6,000$ (b) $Re_G = 8,500$ (c) $Re_G = 12,000$; Test2 (d) $Re_G = 8,900$ (e) $Re_G = 11,800$ (f) $Re_G = 15,000$

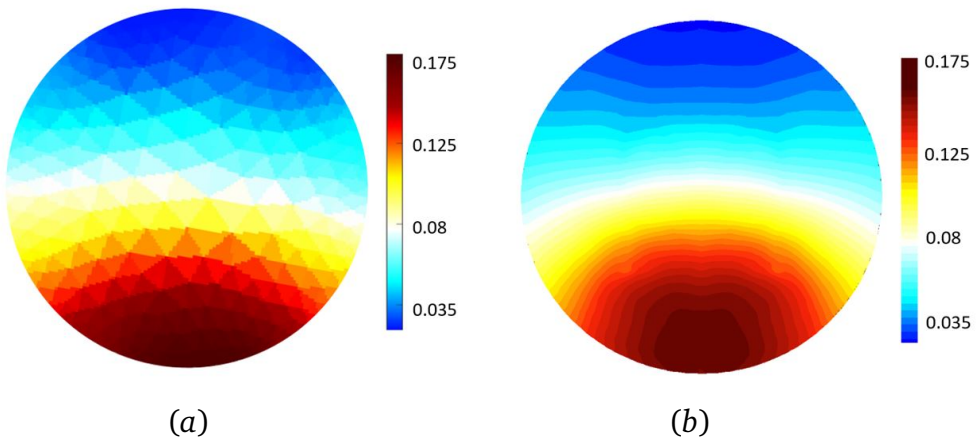

Fig. 5.5 2D concentration distribution in the pipe cross-section for the flow with $Re_G = 6000$ (a) Experiment (b) DNS-DEM

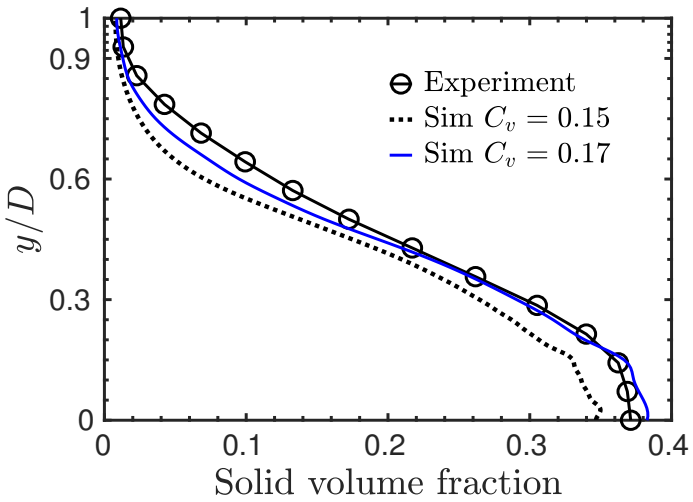

Fig. 5.6 Predicted concentration profile on the centreline of the pipe cross-section for the flow with $0.2\%wt$ Carbopol

Good agreement of the concentration profiles is achieved for the flow tests with a low yield stress ($\tau_y < 1Pa$). The DNS-DEM model prediction is also compared to the concentration profile of the flow with a higher yield stress ($\tau_y = 3.03Pa$) in Table 5.2. The results are shown in Fig 5.6. Since there is uncertainty in the density measurements from the Coriolis mass flow meter in this test, the in-line solids concentration in the DNS-DEM model was initially kept as the designed value of $C_v = 0.15$. As can be seen, the predicted concentration is consistently lower than the experimental measurement. This value $C_v = 0.15$ may be lower than the actual in-line solids concentration during the flow,

which could cause the discrepancy. Later based on the integrated concentration from ERT ($C_v = 0.17$), the predicted concentration profile displays much better agreement with the experimental measurement. The predicted mixture velocity is $1.71\ m/s$ ($+4.3\%$). The results demonstrate the feasibility of the modified drag correlation in predicting the flow with a higher yield stress.

5.2.3 Mean flow profile

The predicted mean velocity profiles on the vertical centreline of the pipe cross-section are shown in Fig 5.7. Experimental measurements of mean fluid and particle phase velocity profiles in dense suspensions are not possible with existing equipment, thus not available in this study. The velocity profiles of the flow with intermediate $Re_G = 8,500$ in test 1 and $Re_G = 11,800$ in test 2 are not shown for clarity as they closely align with the other two profiles.

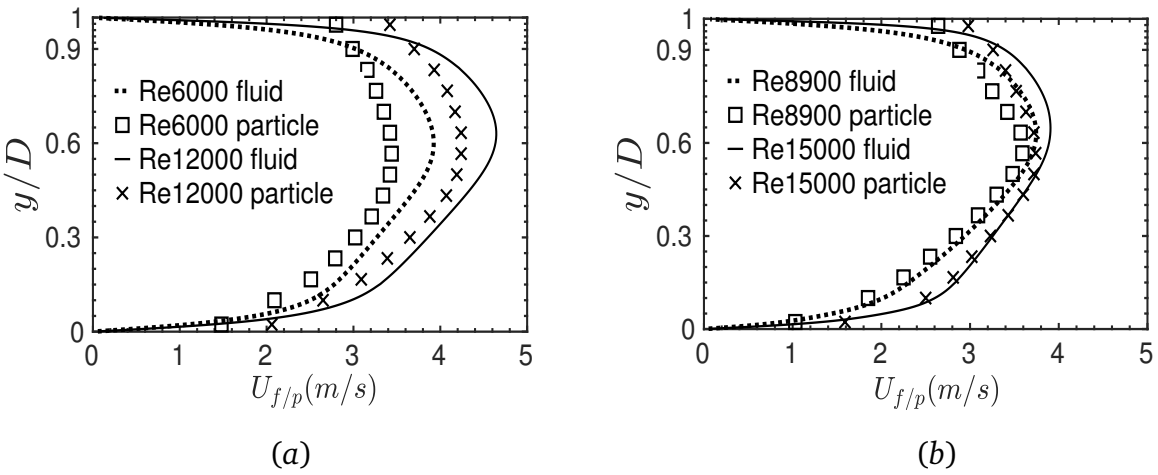

Fig. 5.7 Mean velocity profiles of the fluid and particle phases on the vertical centreline of the pipe cross-section (a) Test 1 (b) Test 2

The comparison of particle and fluid velocity profiles reveals how closely the particles follow the fluid flow. As can be seen from Fig 5.7, the velocity of the particle phase (represented with symbols) is generally lower compared to fluid phase (represented by lines), except for positions near the top & bottom wall. Near the wall, the particles can roll and slide thus the particle velocity is non-zero while no-slip boundary is applied for the fluid phase. The peak velocity for the particle phase is about 13% less than the fluid phase for the flow ($Re_G = 6,000$; $C_v = 0.1$) and 8% less for the flow ($Re_G = 12,000$;

$C_v = 0.1$). For flows with a higher concentration in test 2 ($C_v = 0.16 \sim 0.18$), there would be increased particle-particle interaction and turbulence modulation. The particle velocity profile moves closer to the fluid profile, particularly in the lower section of the pipe. An vertical asymmetry of the velocity around the horizontal centreline is produced with the presence of coarse particles, as can be seen in Fig 5.8. Higher solids concentration produces a bed layer at the bottom and further deviates the velocity profile from symmetry in the vertical direction.

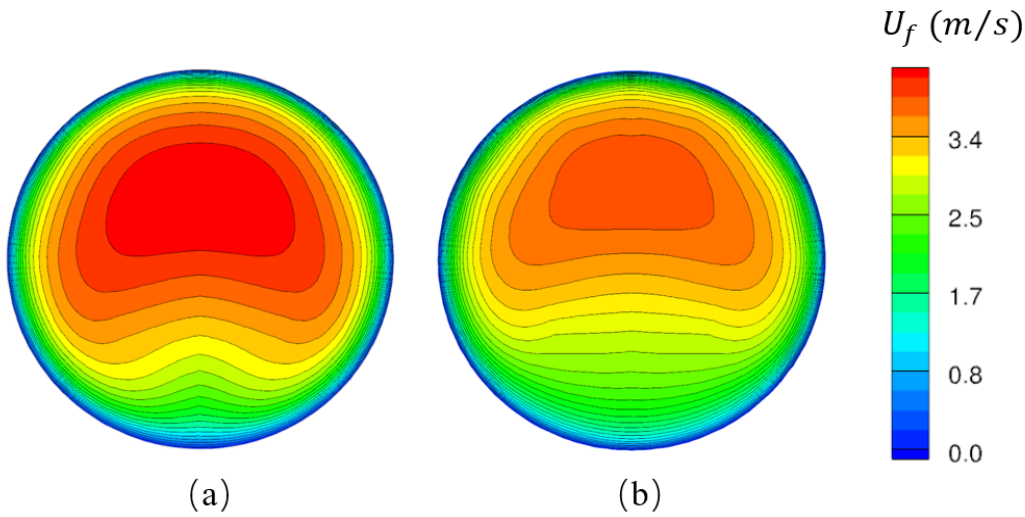

Fig. 5.8 Velocity contour of the fluid phase in the pipe cross-section for the flows (a) Test 1, $Re_G = 6,000$ (b) Test 2, $Re_G = 8,900$

The turbulent kinetic energy profiles on the vertical centreline of the pipe cross section are shown in Fig 5.9. Presence of coarse particles in the lower section of the pipe damps turbulence and causes significant reduction of turbulent kinetic energy, as can be seen from the flow with $Re_G = 15,000$ and $C_v = 0.16$. The near wall peak at top is 0.16 while it is only 0.06 at the bottom. The turbulent kinetic energy of the particle phase resembles the fluid phase but generally exhibits a slightly larger fluctuation, as can be seen in Fig 5.10. This is consistent with the findings in the previous turbulent Newtonian suspension paper in section 5.1. The particle fluctuations are found to be consistently higher than the fluid phase, particularly in the wall-normal direction. As stated in section 5.1, particle motion in the wall-normal direction is not only governed by particle-fluid interaction force, but also gravity and particle-particle/wall collision. As a particle hits the wall, it will decelerate and again accelerate to leave the wall driven by secondary

flow and particle-wall collisions. Compared to fine particles, coarse particles are more governed by their inertia and respond less rapidly to the local fluid field. As particles move along, they carry the momentum and fluctuation energy from the near wall domain to the central and outer domain due to their inertia [104], producing a consistently higher fluctuation than the fluid phase in the centreline of the pipe cross-section.

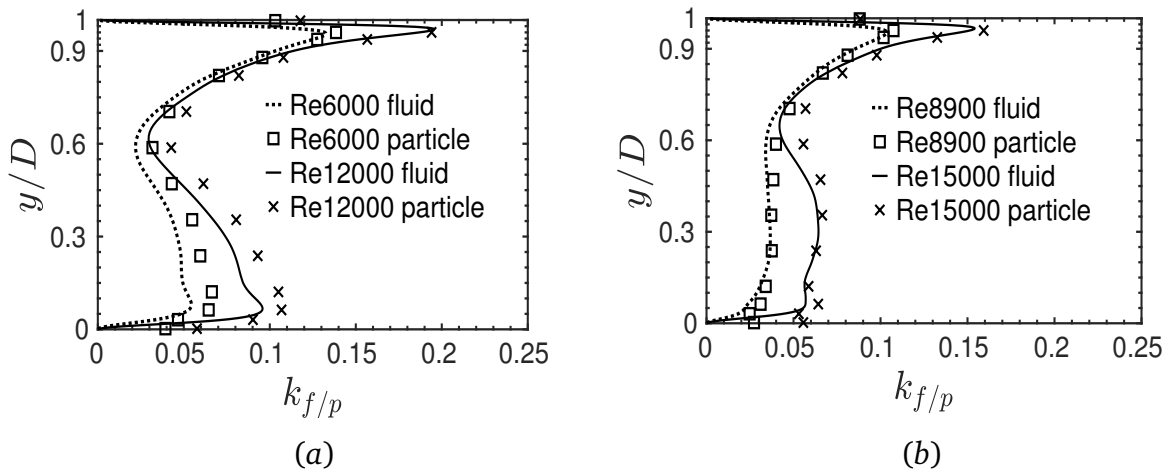

Fig. 5.9 Turbulence kinetic energy profiles of the fluid and particle phases on the vertical centreline of the pipe cross-section (a)Test1 (b) Test2

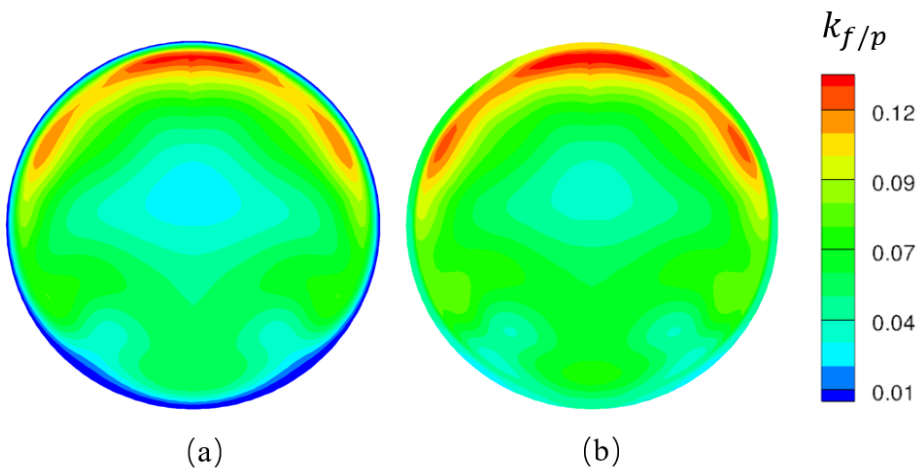

Fig. 5.10 Turbulence kinetic energy contour of the fluid and particle phases for the flow with $Re_G = 6,000$ and $C_v = 0.1$

5.3 Chapter summary

Coarse-particle Newtonian and non-Newtonian suspension experiments in a weakly turbulent ($4,000 < Re < 15,000$) flow regime have been designed & undertaken for validation of the DNS-DEM model. Suspension data including pressure drop, mixture flow rates and concentration profiles, as well as the visual observation of the flow are obtained at different flow regimes ranging from settled bed to suspended flow.

The predicted flows are generally in good qualitative and quantitative agreement with experimental measurements. The predicted mixture flow rates and concentration profiles are mostly less than 10% difference, particularly under flow conditions where particles are suspended with a small bed at the bottom. The maximum discrepancy in the concentration profile is observed near the pipe centre for flows with a distinct sliding bed. The deviation may result from a combined effect of the insufficient ERT resolution in the experiment and the diffusion approach in the DNS-DEM coupling. ERT has the limitation of low spatial resolution in capturing the conductivity distribution, especially near the centre of the reconstructed domain. The diffusion approach adopted in the DNS-DEM coupling may also cause the discrepancy as it diffuses away solid volume fraction from pipe bottom to the central region, though this effect would diminish as particles become more suspended.

To model particle-fluid interaction, the drag correlation for a sphere settling in a yield-stress fluid has been incorporated into the Gidaspow drag model. This modification provides better agreement with experimental results than a simple modification of replacing the Newtonian viscosity with the local *HB* viscosity in the drag. Despite the approximations, the predicted concentration profiles are generally in good agreement with experimental measurements in the non-Newtonian suspension.

Overall, the agreement with experimental measurements demonstrate that DNS-DEM model is a promising approach for investigating weakly turbulent non-Newtonian suspension flow with the extended drag model. On this basis, the validated DNS-DEM model will be applied to investigate how the carrier fluid rheology, solids properties and pipe size affects non-Newtonian suspension flow in a weakly turbulent flow regime.

6

Turbulent Coarse-Particle Non-Newtonian Suspension Flows

Understanding of the underpinning non-Newtonian suspension science is a necessity for successful application of high concentration suspensions. Currently there is no clear understanding on the flow regime transition in a turbulent non-Newtonian suspension. Investigation is needed to understand how flow regime is affected by the carrier fluid rheology and solids properties in order to select appropriate correlation for predicting the flow behaviour. It is also necessary to understand the relationship between pressure drop and carrier fluid & solid properties for transportation energy requirements. Flow characteristics of tailings suspensions can vary significantly between a small and large pipe. General rules for the scale-up are lacking and current suspension models have mostly been developed for the conventional suspensions with a Newtonian carrier. Understanding the similarity & difference between turbulent non-Newtonian and Newtonian suspensions would provide guidance on applying & modifying these conventional models. In this chapter, the validated DNS-DEM model is applied to investigate the effect of different flow parameters including the carrier fluid rheology (yield stress τ_y & flow index n), solids properties (particle size d_p & in-line concentration C_v) and pipe size D on the flow regime, pressure drop, velocity and concentration profiles in weakly turbulent

non-Newtonian suspension flows, in order to provide an extended understanding of high concentration suspensions. The simulation parameters in modelling different flow scenarios are firstly introduced, followed by a detailed discussion of the flow results in pipes of diameter 44, 100 and 200 mm, respectively.

6.1 Computational implementation and parameters

6.1.1 Computational implementation

Simulations are conducted in a horizontal periodic pipe with length $L = 4\pi D$ (D is the pipe diameter) and is the same domain as in Chapter 4 Section 4.3. Mesh independency study ($1.4 \sim 8$ million) for DNS of turbulent pipe flow can be found in Chapter 3 paper section 3.1. The structured hexahedral mesh in Chapter 6 is of size 6.1 million. The non-dimensional wall units r^+, $(R\theta)^+$ and z^+ in the near wall region are approximately 0.6, 5.7 and 9.5 respectively. Grid points in the axial direction (540 layers) are uniformly distributed. The CFD time step is 1e-4 and the DEM time step is 1e-6, which is approximately $1/10$ of the Rayleigh criteria. These mesh and time step sizes have previously been shown in Chapter 3 paper section 4.1 and in [108] to provide acceptable DNS results of wall-bounded flows.

6.1.2 Flow parameters

The complete set of parameter values is shown in Table 6.1 and 6.2. In order to compare with equivalent Newtonian suspensions found in previous studies [49, 118, 119], pipe diameters of $44, 100$ and $200mm$ are chosen. The ranges of the flow parameters are also chosen to allow comparison to previous non-Newtonian suspension studies [84, 96, 97, 129] and so that the simulations are in the range where DNS is feasible.

In a real suspension, the fine particles (usually $10 \sim 30\%$ by volume) combine with the conveying fluid (typically water) to form a non-Newtonian carrier, and the coarse particles are conveyed as coarse burden [96, 97]. The carrier fluid for all simulations is assumed to comprise 15% (v/v) rheologically active fine solids and 85% (v/v) water. The solids density is 2600 kg/m^3. On this basis, the carrier fluid density is 1240 kg/m^3. The shear-thinning rheology of the carrier fluid is chosen independently and described

using the Herschel-Bulkley (*HB*) model. Mono-sized particles with a ratio of particle diameter to pipe size $d_p/D = 1/22 \sim 1/10$ are used.

Table 6.1 Simulation parameters for the $44\ mm$ pipe

Sim No.	Solids concentration C_v	Yield stress $\tau_y(Pa)$	Consistency $k(Pa \cdot s^n)$	Flow index n	Particle size $d_p(mm)$	Pressure gradient $\partial P/\partial Z(KPa/m)$	Mixture flow rate $U_m(m/s)$	Bulk flow Re_G
No.1	0.1	5	0.378	0.59	2	6.5	3.54	17000
No.2	0.1	15	0.378	0.59	2	6.5	3.28	12000
No.3	0.1	25	0.378	0.59	2	6.5	2.72	7100
No.4	0.2	5	0.378	0.59	2	6.5	2.81	13600
No.5	0.3	5	0.378	0.59	2	6.5	1.89	9100
No.6	0.4	5	0.378	0.59	2	6.5	1.55	7500
No.7	0.1	5	0.378	0.55	2	4.5	2.89	18400
No.8	0.1	5	0.378	0.6	2	5.0	2.92	9900
No.9	0.1	5	0.378	0.8	2	9.5	2.88	1600
No.10	0.2	15	0.378	0.59	2	8.1	2.89	13300
No.11	0.2	N/A	0.0113	1	2	5.6	2.82	13600

Table 6.2 Simulation parameters for the 100 and $200\ mm$ pipes

Sim No.	Pipe Diameter $D(mm)$	Solids concentration C_v	Yield stress $\tau_y(Pa)$	Consistency $k(Pas^n)$	Flow index n	Particle Size $d_p/D(mm)$	Pressure gradient $\partial P/\partial Z(KPa/m)$	Mixture flow rate $U_m(m/s)$	Bulk flow Re_G
No.12	100	0.1	25	0.93	0.59	1/22(4.6)	3.5	2.89	5100
No.13	100	0.2	25	0.93	0.59	1/22(4.6)	5.0	2.90	8000
No.14	100	0.4	25	0.93	0.59	1/22(4.6)	11.2	2.95	17600
No.15	100	0.1	25	0.93	0.59	1/14(7)	3.5	2.99	5200
No.16	100	0.1	25	0.93	0.59	1/10(10)	3.1	2.90	4300
No.17	100	0.1	25	0.93	0.59	50%(7)+ 50%(4.6)	3.5	2.94	5200
No.18	100	0.2	15	0.93	0.59	1/22(4.6)	4.3	2.94	8300
No.19	100	0.2	15	0.70	0.59	1/22(4.6)	4.3	2.99	13600
No.20	200	0.2	15	1.17	0.59	1/22(9)	2.5	2.97	13000

Sim No.$1 \sim 6$ are conducted with a fixed pressure gradient,in order to simulate a pipe flow with a fixed pump power capacity. The pump efficiency is assumed to be uniform with changing rheology. Different from Sim No.$1 \sim 6$, Sim No.$7 \sim 20$ are conducted at an equivalent bulk flow velocity (approximately $2.9\ m/s$) by adjusting the pressure gradient. An initial value of the pressure gradient is estimated based on the Wilson-Thomas correlation [144] assuming a homogeneous flow, and the pressure gradient is then adjusted manually to obtain the desired bulk flow rate. This requires more computational resources and is about $2 \sim 3$ times as expensive as Sim No.$1 \sim 6$.

Pipe flow results in a $44mm$ pipe are presented in the next section, followed by results in larger pipes of diameter 100 and $200\ mm$, respectively. The effect of the carrier fluid rheology (yield stress τ_y & flow index n), solids properties (particle size d_p & in-line

concentration C_v) and pipe size D on the flow is revealed. Results are discussed in terms of the flow regime, velocity and concentration distribution, turbulence kinetic energy, secondary flow and force analysis on particles.

6.2 Flow in a $44\ mm$ pipe

6.2.1 Effect of yield stress

To investigate the effect of yield stress on the flow in a $44\ mm$ pipe, the following simulations are selected, as shown in Table 6.3. Flows with yield stress from 5 to 25 Pa and a fixed pressure gradient are conducted in Sim No.$1 \sim 3$. The in-line solids concentration in these flows is $C_v = 0.1$. Constant pressure gradient will result in lower bulk flow rate as yield stress increases. To consider the effect of yield stress $\boldsymbol{\tau}_y$ in flows at an equivalent bulk flow velocity, Sim No.4 and No.10 are conducted. The two flows are with yield stress $\boldsymbol{\tau}_y = 5Pa$ & $15\ Pa$ and in-line solids concentration $C_v = 0.2$. The pressure gradient in Sim No.10 is adjusted manually to obtain the desired flow rate as in Sim No.4.

Table 6.3 Simulation parameters for investigating the effect of yield stress $\boldsymbol{\tau}_y$

Sim No.	Solids concentration C_v	Yield stress $\boldsymbol{\tau}_y(Pa)$	Consistency $k(Pa \cdot s^n)$	Flow index n	Particle size $d_p(mm)$	Pressure gradient $\partial P/\partial Z(KPa/m)$	Mixture flow rate $U_m(m/s)$	Bulk flow Re_G
No.1	0.1	5	0.378	0.59	2	6.5	3.54	17000
No.2	0.1	15	0.378	0.59	2	6.5	3.28	12000
No.3	0.1	25	0.378	0.59	2	6.5	2.72	7100
No.4	0.2	5	0.378	0.59	2	6.5	2.81	13600
No.10	0.2	15	0.378	0.59	2	8.1	2.89	13300

6.2.1.1 Flow regime, concentration and velocity distribution

The qualitative view of the flow and instantaneous concentration contour for flows with different yield stress 5, 15 and 25 Pa and a fixed pressure gradient (Sim No.$1 \sim 3$) are shown in Fig 6.1. The flow regime shown is from a side view and concentration contour is on the centre plane. The pipe section is approximately $1/5$ of the simulated domain in the streamwise direction. As can be seen in Fig 6.1, heterogeneous flow and sliding beds are found in a turbulent regime. Visual observation shows that the coarse particles produce stratified flow in all the cases, and the flow does not become pseudo-homogeneous even with the presence of a sufficiently high yield stress ($25\ Pa$).

Instead, a loosely packed sliding bed starts to form when the yield stress reaches $25\ Pa$. For a pipe flow with a fixed pressure gradient, increasing the yield stress causes a more stratified flow. This is also seen from the concentration profile on the vertical centreline of the pipe cross-section shown in Fig 6.2(a) that the flow with higher yield stress $25\ Pa$ produces a more stratified concentration profile compared with the $5\ Pa$ case.

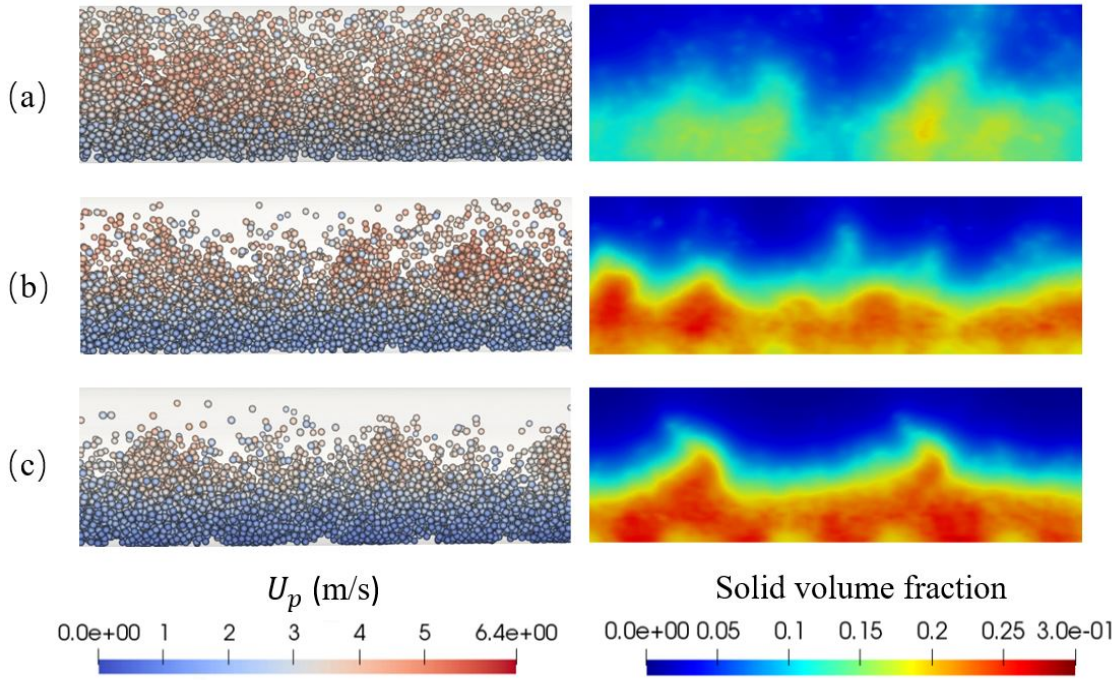

Fig. 6.1 Qualitative view of the flow and instantaneous concentration contour for flows with different yield stress and a fixed pressure gradient (a) $5\ Pa$ (b) $15\ Pa$ (c) $25\ Pa$. Only $1/5$ of the axial extent of the domain is shown

For a pipe flow with a fixed pressure gradient, increasing the yield stress leads to a reduced bulk flow velocity (as shown in Fig 6.2 (b)), indicating a higher pressure gradient is required for a fixed mass transport. The mixture flow rates for the flow at ($25\ Pa$) is 23% less than the flow at ($5\ Pa$). The delivered solids concentration C_{vd} calculated based on the mean fluid and particle velocity also deceases with increasing yield stress. The ratio of delivered solids concentration to in-line concentration C_{vd}/C_v is 0.92, 0.89 and 0.75 for the yield stress at $5\ Pa$, $15\ Pa$ and $25\ Pa$, respectively.

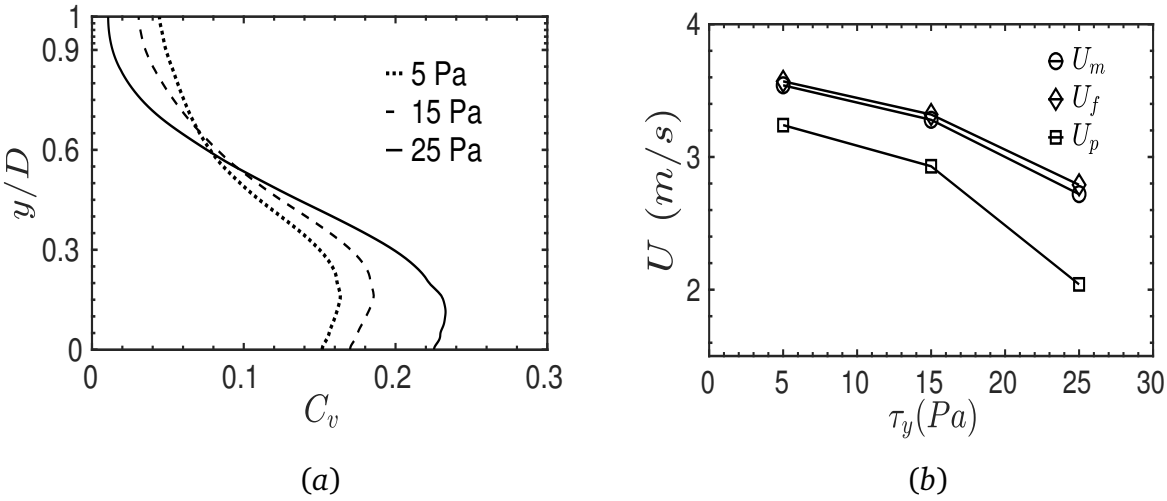

Fig. 6.2 Flows with different yield stress and a fixed pressure gradient (a) concentration profile on the vertical centreline of the pipe cross-section (b) the mean bulk flow, fluid and particle velocity

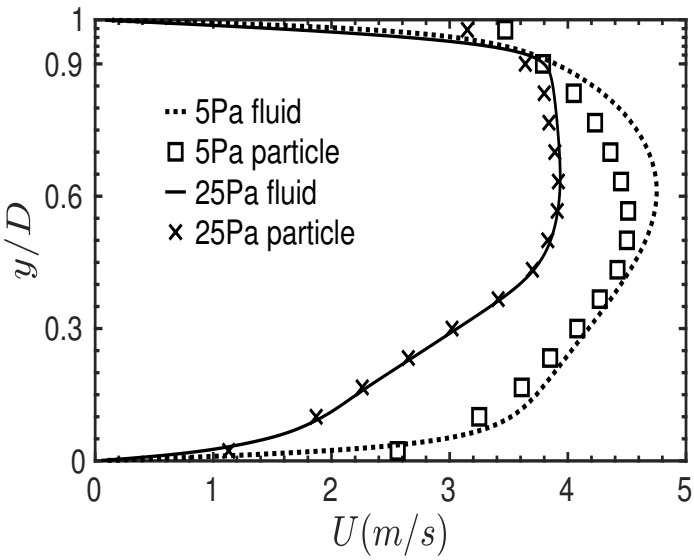

Fig. 6.3 Mean velocity profiles on the vertical centreline of the pipe cross-section for the flows with different yield stress and a fixed pressure gradient

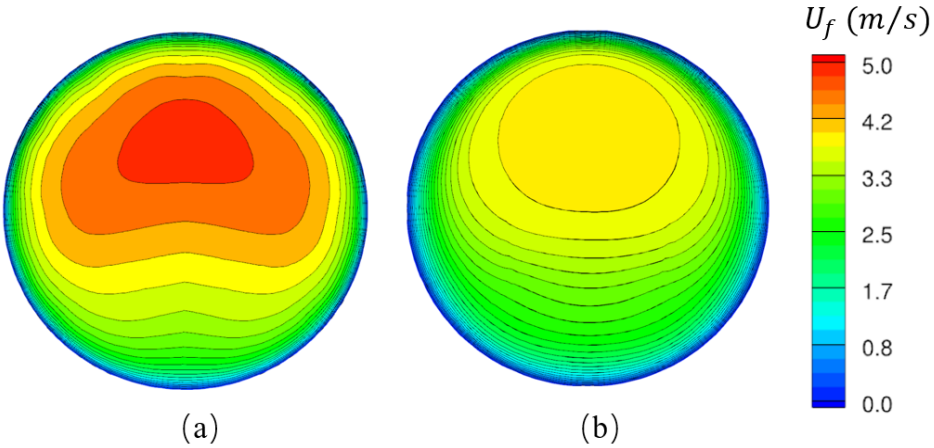

Fig. 6.4 Velocity contour of the fluid phase in the pipe cross-section for flows with different yield stress and a fixed pressure gradient (a) 5 Pa (b) 25 Pa

The mean velocity profiles on the vertical centreline for the flow with $\tau_y = 5Pa$ and $25Pa$ are shown in Fig 6.3 and fluid velocity contours in the cross-section are shown in Fig 6.4. The velocity profiles for the flow with $\tau_y = 15Pa$ are closely aligned with the other two thus are not shown for clarity. The velocity profile becomes more flattened and the maximum value decreases with increasing yield stress. The particle phase generally follows the fluid flow but with slightly lower velocity in the upper section of the pipe. With increasing yield stress, the fluid and particle velocity profiles approach each other and further deviate from vertical symmetry. The core of the flow (where the maximum velocity lies) also moves further upwards from the pipe centre (as shown in Fig 6.4) along with higher solids concentration at the pipe bottom.

6.2.1.2 Force analysis on particles and turbulent kinetic energy

Particles in turbulent suspension flows are supported by two mechanisms, namely particle interaction with turbulent eddies and particle-particle interaction through inertial contacts [46]. The vertical force balance on the centreline for the flows with yield stress 5 & 25 Pa is shown in Fig 6.5. Forces are non-dimensionalised with the gravity force. It is found that the major forces supporting the particles are the drag force, particle-particle/wall collisions (P-P/W) and pressure gradient force. The lift, virtual mass and viscous forces are negligible in supporting the particles thus are not shown.

P-P/W near the wall is big and forces with a magnitude larger than 1.5 (e.g., P-P/W at the wall in Fig 6.5(a)) are not shown for clarity.

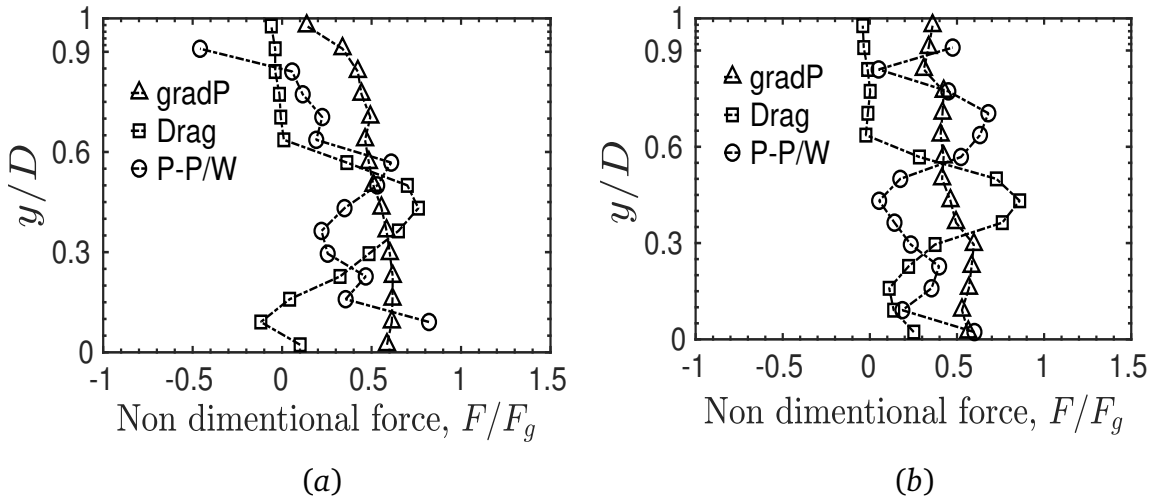

Fig. 6.5 The vertical force balance on the centreline of the pipe cross-section for the flows (a) 5 Pa (b) 25 Pa

As can be seen in Fig 6.5, the presence of the viscous core region contributes to the dominant drag force on particles in the central region with correspondingly lower particle-particle collisions. It is known that the apparent viscosity of a shear-thinning fluid reaches its maximum at the pipe centre and minimum at the pipe wall for laminar and on average for turbulent flows [20]. Studies used to assume the highly viscous core region combined with the yield stress can be beneficial to support coarse particles near the pipe centre and prevent them settling [20, 70]. However, a consensus has been reached that coarse particles settling can occur in a laminar non-Newtonian suspension flow, as revealed in studies such as Cooke [22], Thomas et al. [129] and Talmon & Mastbergen [127]. Yield stress is no longer available to support the particles when they are under shear [6, 95] because the local viscosity around a particle reduces. Unlike in a laminar flow, particles will interact with turbulent eddies in a turbulent suspension. The question remains as to how effective turbulent re-suspension is, and how the combined effect of turbulence and yield stress would support particle suspension in a turbulent non-Newtonian suspension.

Traditionally, turbulent non-Newtonian suspensions have been treated as if they are homogeneous when pipeline design has been undertaken [96]. The assumption is established on a cursory comparison of the particle Stokes number based on the

characteristic sheared settling velocity and the characteristic eddy velocity [97]. On this basis, particles are assumed to be efficiently suspended and sustained due to the presence of high viscosity and turbulent mixing. However, turbulent support on particles is effective only when the eddy's scale and velocity exceed the particle size and fall velocity. Turbulent kinetic energy contours for the particle and fluid phases for the flow with $\tau_y = 5Pa$ are shown in Fig 6.6. As can be seen, turbulence in the lower section is significantly damped with the presence of particles, and thus becomes less effective in counteracting the particle weight. Meanwhile, for a flow with a fixed pressure gradient, increasing the yield stress leads to reduced bulk flow velocity, as revealed in Fig 6.2. This results in significantly reduced turbulence intensity, as shown in Fig 6.7. The peak value of the turbulent kinetic energy in the upper section for the flow ($25\ Pa$) is 85% less than the corresponding value in the flow ($5\ Pa$). The instantaneous velocity contours in the pipe cross-section for flows with $\tau_y = 5Pa$ & $25Pa$ are shown in Fig 6.8. The flow is less turbulent and getting close to laminar when the $\tau_y = 25Pa$. In this case, the presence of high yield stress causes a strong damping of the turbulence that leads to the collapse of turbulent support and a more stratified flow is observed in the flow with $\tau_y = 25Pa$.

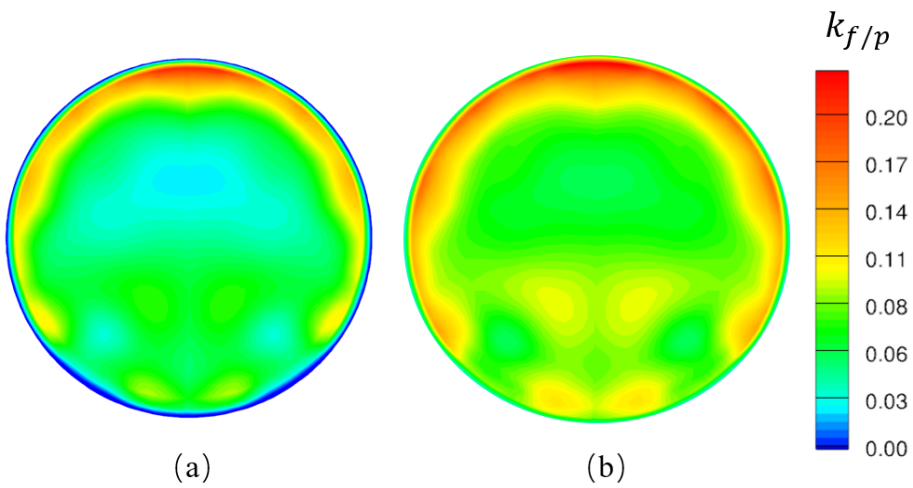

Fig. 6.6 Turbulent kinetic energy contours in the pipe cross-section for the flow with $\tau_y = 5Pa$ (a) fluid phase (b) particle phase

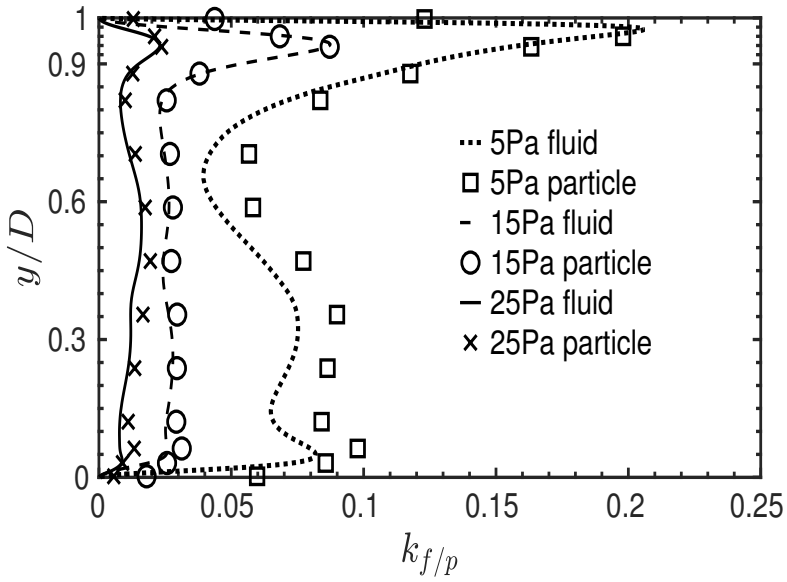

Fig. 6.7 Mean turbulent kinetic energy profiles on the vertical centreline of the pipe cross-section for flows with different yield stress and a fixed pressure gradient

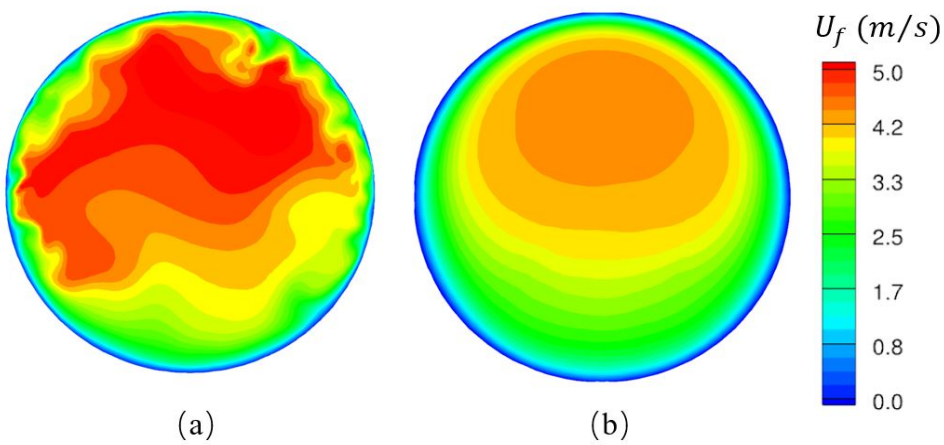

Fig. 6.8 Instantaneous velocity contour of the fluid phase in the pipe cross-section for flows with different yield stress and a fixed pressure gradient (a) 5 Pa (b) 25 Pa

The above simulations are conducted with a fixed pressure gradient, however, the effect of changes in yield stress at the same bulk flow rate is of interest, clearly the pressure gradient will be different. Sim No.4 and 10 are conducted with different yield stresses (5 and 15 Pa) but at an equivalent bulk flow velocity 2.8 m/s and $Re_G \approx 13,000$. These are undertaken with $C_v = 0.2$ and do not fit the same sequence as Sim No. $1 \sim 3$. Effect of in-line solids concentration on the flow will be revealed later in Sec 6.2.3. The corresponding concentration profiles are shown in Fig 6.9. The results indicate that

particles are only slightly more suspended for the flow ($15\ Pa$) compared to the flow ($5\ Pa$) at an equivalent bulk flow velocity and very similar Re_G, 13300 vs 13500.

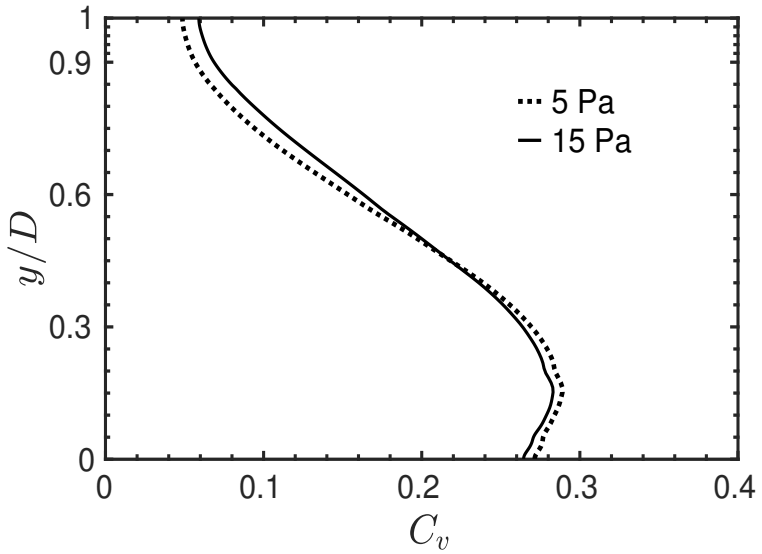

Fig. 6.9 Concentration profiles on the vertical centreline of the pipe cross-section for flows with different yield stress and an equivalent bulk flow velocity

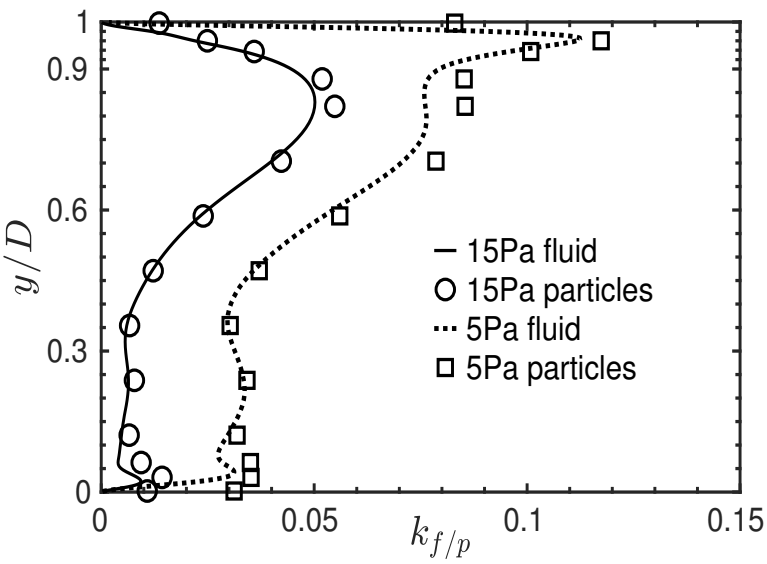

Fig. 6.10 Mean turbulent kinetic energy profiles on the vertical centreline of the pipe cross-section for flows with different yield stress and an equivalent bulk flow velocity

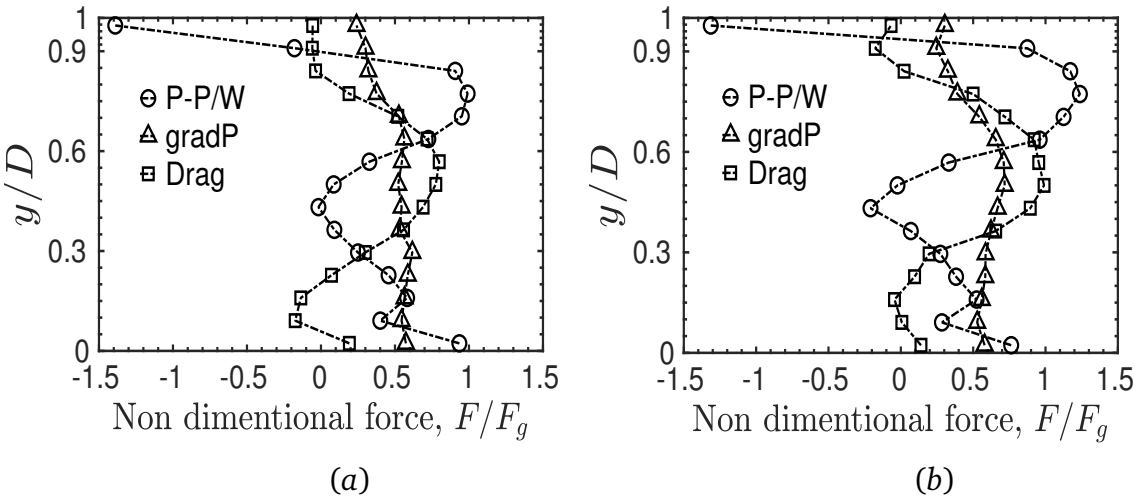

Fig. 6.11 The vertical force balance on the centreline of the pipe cross-section for the flows (a) Sim No.4, $\tau_y = 5Pa$ (b) Sim No.10, $\tau_y = 15Pa$

The corresponding mean turbulent kinetic energy profiles and force analysis on particles in the two flows are shown in Fig 6.10 and Fig 6.11 respectively. Similarly to Fig 6.7, a stronger damping of turbulence is observed in the flow with a higher yield stress ($15\ Pa$). The peak value of the turbulent kinetic energy in the upper section for the flow with $15\ Pa$ is about half of the corresponding value in the flow with $5\ Pa$. However, there is a stronger coupling between the fluid and particles in the highly viscous core region in the $15\ Pa$ case, as revealed by the larger magnitude of drag shown in Fig 6.11(b). The maximum drag is close to 1 in the $15\ Pa$ case and 0.78 in the $5\ Pa$ case. The stronger coupling combined with the weaker turbulence contributes to marginally improved solids suspension in the flow with a higher yield stress. Meanwhile, this beneficial effect is at the cost of a higher pressure drop by 27%. In summary, higher yield stress leads to more stratification in a flow with a constant pressure gradient, but slightly improved particle suspension at an equivalent bulk flow rate.

6.2.1.3 Secondary flow

For all the flows, a secondary flow of two rotating cells is observed in the pipe cross-section, as shown in Fig 6.12.

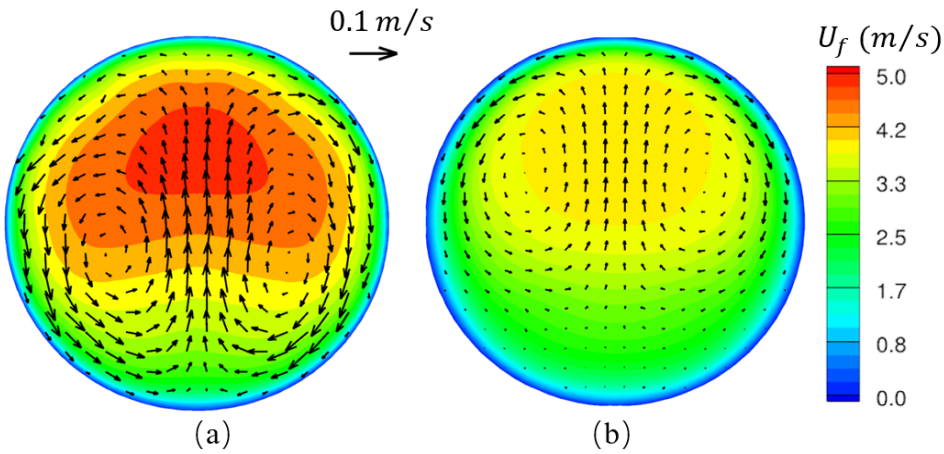

Fig. 6.12 Time-averaged cross-sectional vector field of the secondary flow for the case with a constant pressure gradient (a) $5\ Pa$ (b) $25\ Pa$

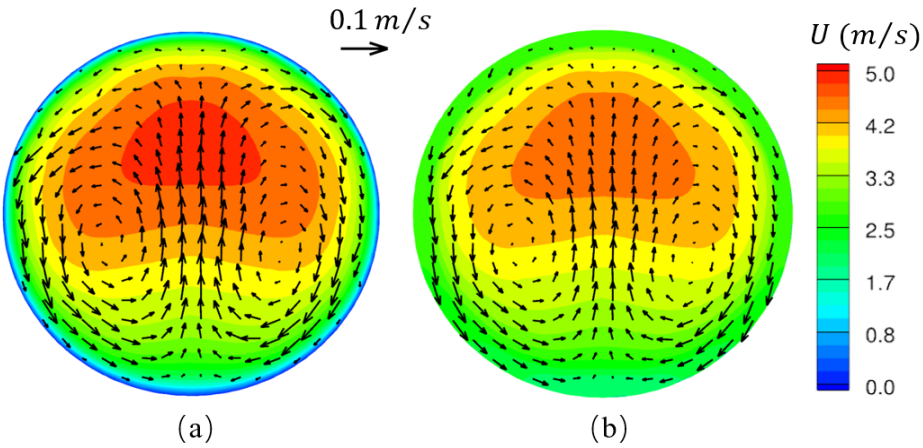

Fig. 6.13 Example time-averaged cross-sectional vector field of the secondary flow for $\tau_y = 5Pa$ (Sim No. 1) (a) fluid phase (b) particle phase.

The two symmetric rotating longitudinal vortices lift fluid & particles vertically along the centreline and back down outside. The magnitude of the secondary flow (based on the maximum vector) is 2, 1.5 and 1.1% of the mean bulk flow rate in the 5, 15 and 25 Pa case with a constant pressure gradient. The mean secondary flow pattern of the fluid and particle phase for the 5 Pa case (Sim No. 1) is shown in Fig 6.13. The two patterns are very similar, except that the particle phase has a larger velocity magnitude near the wall as it can roll and slide, while slightly smaller value in the inner domain. The secondary flow pattern moves upward when τ_y increases as shown in Fig 6.12 (b). The secondary flow for cases with different τ_y and fixed bulk flow rate is shown in Fig 6.14. The flow patterns are close to each other. The magnitude is 1.8 % in the 5 Pa case and about 10 % higher than that in the 15 Pa case.

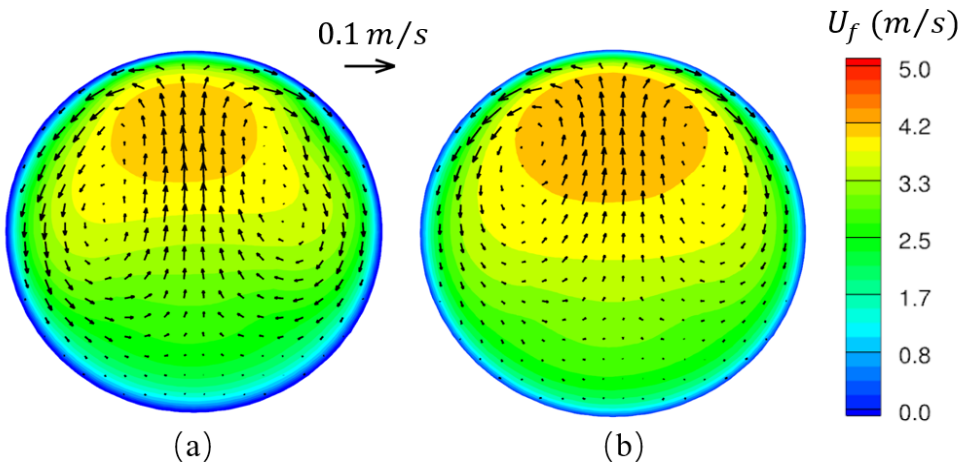

Fig. 6.14 Time-averaged cross-sectional vector field of the secondary flow for the case with same bulk flow rate (a) $5\ Pa$ (b) $15\ Pa$

6.2.2 Effect of flow index

The flow index n represents the degree of shear-thinning and is a measure of the extent of deviation from Newtonian rheology. The more shear-thinning (lower n) the carrier fluid, the further it deviates from the Newtonian rheology. To investigate the effect of flow index on the flow in a $44\ mm$ pipe, the following simulations are selected, as shown in Table 6.4. Flow indices n from 0.55 to 0.8 at an equivalent bulk flow velocity are conducted. This approach allows investigating the effect of n at flow rates in the order of meters per second ($2.9\ m/s$) as commonly found in tailings transportation. Both k and τ_y are fixed thus the mean wall viscosity and Re_G are different in these simulations. The lower limit $n = 0.55$ is chosen so that the flow falls into the weakly turbulent regime and is feasible with current DNS resolution. Similarly, the effect of flow index on the non-Newtonian suspension behaviour is discussed in terms of flow regime, concentration & velocity distribution, turbulent kinetic energy and secondary flow.

Table 6.4 Simulation parameters for investigating the effect of flow index n

Sim No.	Solids concentration C_v	Yield stress $\tau_y(Pa)$	Consistency $k(Pas^n)$	Flow index n	Particle size $d_p(mm)$	Pressure gradient $\partial P/\partial Z(KPa/m)$	Mixture flow rate $U_m(m/s)$	Bulk flow Re_G
No.7	0.1	5	0.378	0.55	2	4.5	2.89	18400
No.8	0.1	5	0.378	0.6	2	5.0	2.92	9900
No.9	0.1	5	0.378	0.8	2	9.5	2.88	1600

6.2.2.1 Flow regime and concentration distribution

The qualitative view of the flow (side view) and instantaneous concentration contour (on the centre plane) for flows with different n at an equivalent bulk flow velocity are shown in Fig 6.15.

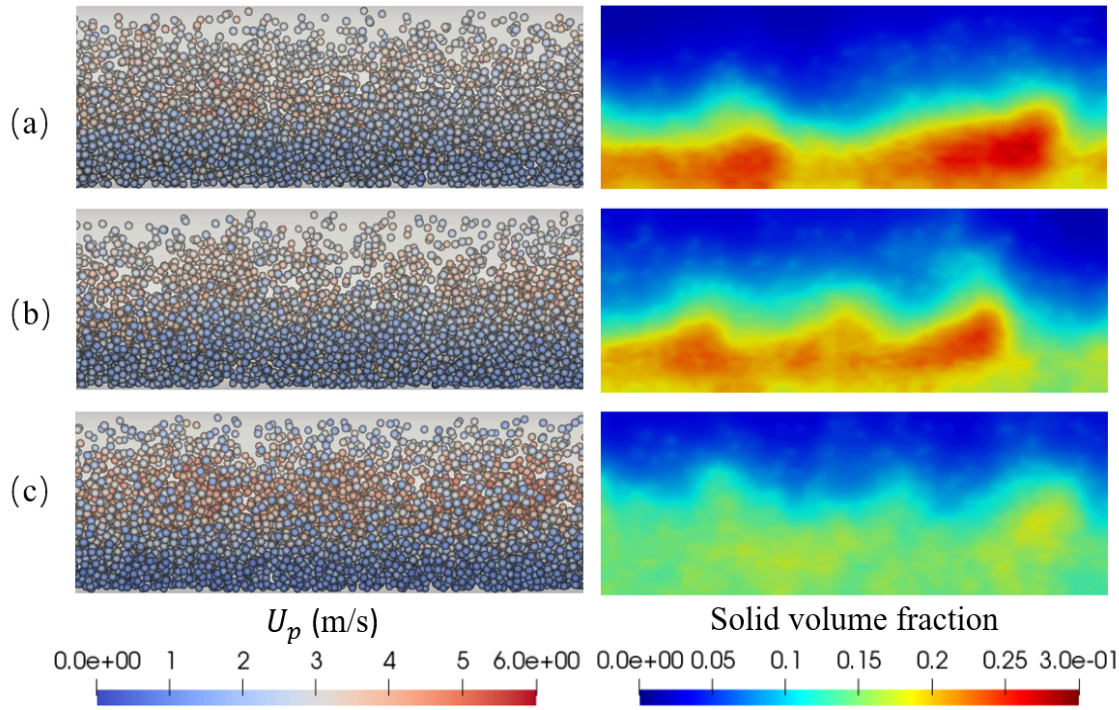

Fig. 6.15 Qualitative view of the flow and instantaneous concentration contour for flows with different flow index (a) 0.55 (b) 0.6 (c) 0.8. Only $1/5$ of the axial extent of the domain is shown

As can be seen, the flow becomes more stratified as the carrier fluid becomes more shear-thinning (lower n). This is also revealed in the concentration profiles shown in Fig 6.16 (a). The profile becomes more uniform with n increased from 0.55 to 0.8. The ratio of delivered solids concentration to in-line concentration C_{vd}/C_v also increases and is 0.90, 0.91 and 0.93 for n at 0.55, 0.6 and 0.8, respectively.

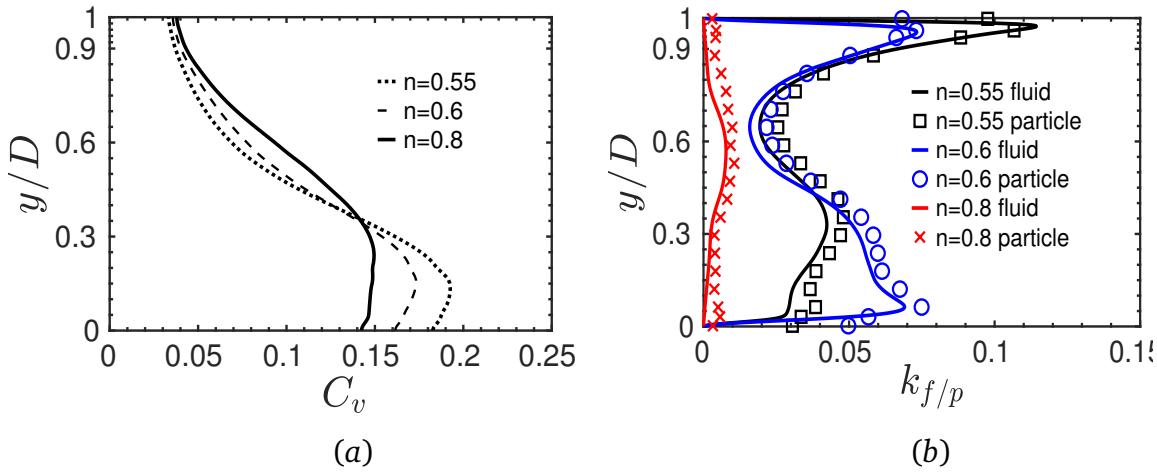

Fig. 6.16 Profiles on the vertical centreline of the pipe cross-section for flows with different flow index (a) Concentration (b) Turbulent kinetic energy

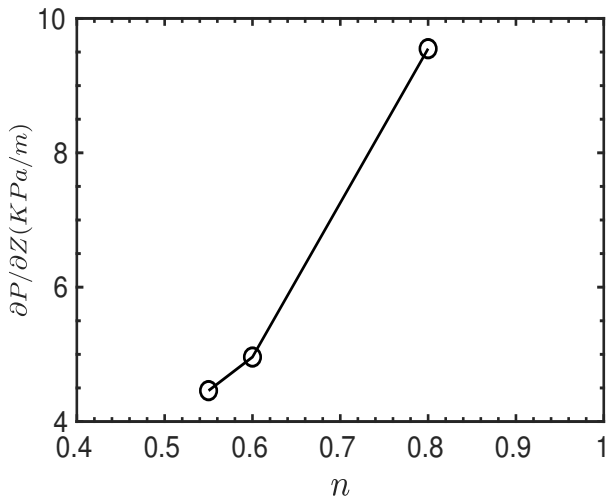

Fig. 6.17 Pressure drop for flows with different flow index

With fixed k and τ_y, the mean wall viscosity η_w increases with increasing n for flows at an equivalent bulk flow rate. The η_w increases from 0.009 to 0.098 $Pa \cdot s$ as n increases from 0.55 to 0.8. This simultaneously results in a change from turbulent to laminar flow with Re_G drops from $18,400$ to $1,600$. The corresponding turbulent kinetic energy profiles on the centreline in the pipe cross section are shown in Fig 6.16 (b). The peak value of the turbulent kinetic energy for the flow ($n = 0.8$) is 90% less than the corresponding value in the flow ($n = 0.55$). However, the combined effect of weaker turbulence and much higher viscosity leads to a more uniform solids distribution for the case with $n = 0.8$. The finding is consistent with the results in a flow with a higher yield

stress at an equivalent bulk flow rate, as discussed in Sec 6.2.1.2. The pressure drop for flows with different flow index at an equivalent bulk flow rate is shown in Fig 6.17. Despite a flow is more stratified as the carrier becomes more shear-thinning, it requires less pressure drop. A 53% reduction in pressure drop is observed as n decreases from 0.8 to 0.55.

6.2.2.2 Velocity distribution and secondary flow

The velocity profiles and contours for flows with different flow index at an equivalent bulk flow rate are shown in Fig 6.18 and Fig 6.19, respectively.

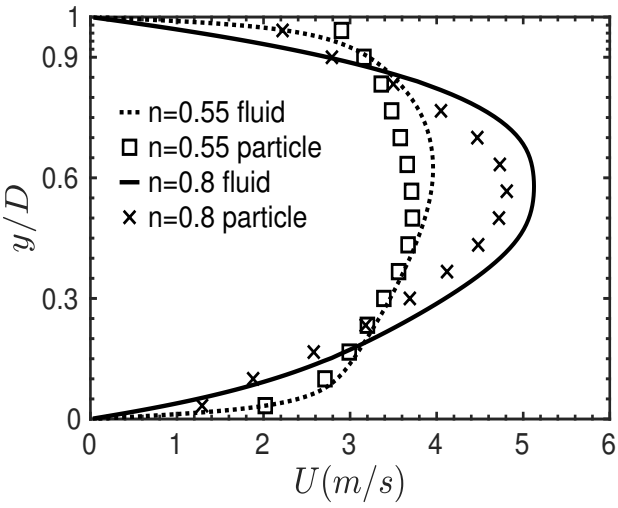

Fig. 6.18 Mean velocity profiles on the vertical centreline of the pipe cross-section for the flows with different flow index

The results show a change from a turbulent to laminar velocity profile, with a flattening of the profile as n decreases. Results are similar to Eesa and Barigou's findings [33] for coarse particles in a power-law fluid that enhanced shear thinning results in a blunter solid and fluid velocity profile. A secondary flow of two rotating cells is also observed in the pipe cross-section, as shown in Fig 6.20. The two symmetric rotating longitudinal vortices lift fluid & particles vertically along the centreline and back down outside. However, the magnitude is quite different. Note the different vector scale in Fig 6.20 (a) and (b). The flow with $n = 0.55$ has a much larger magnitude of secondary flow than the case with $n = 0.8$. The two rotating cells also move upward as n increases.

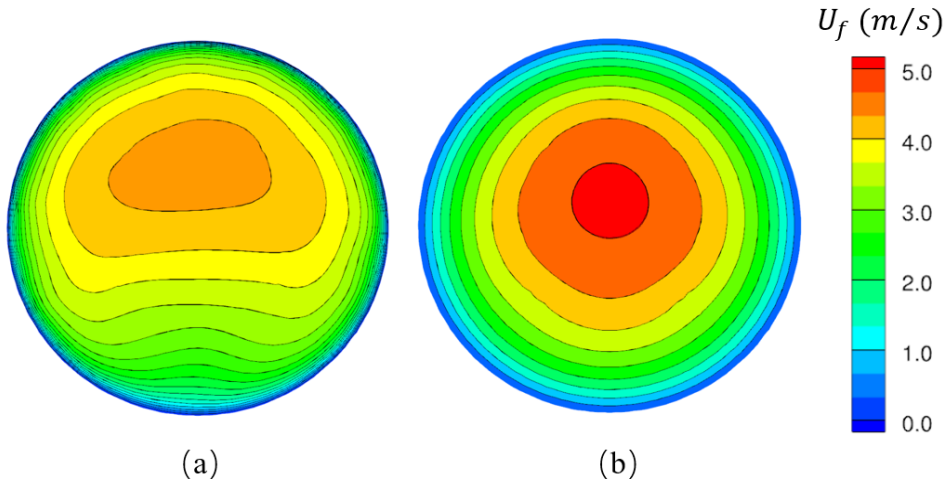

Fig. 6.19 Velocity contour of the fluid phase in the pipe cross-section for flows with different flow index (a) 0.55 (b) 0.8

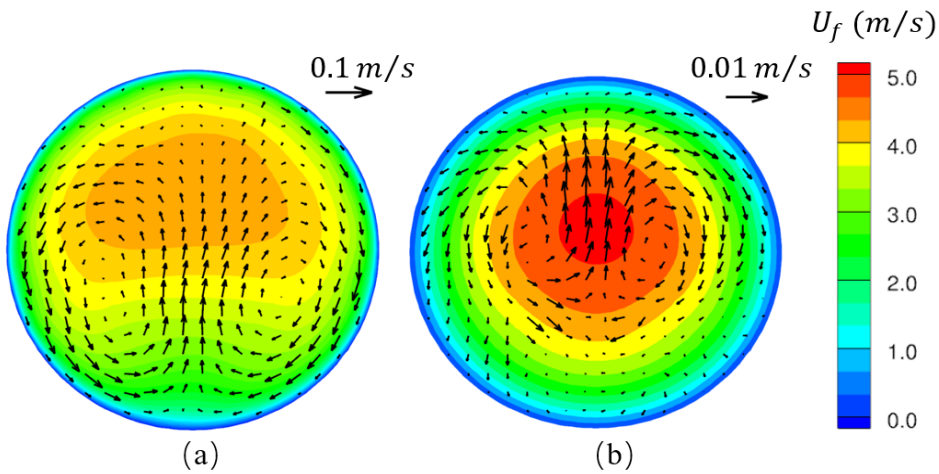

Fig. 6.20 Time-averaged cross-sectional vector field of the secondary flow velocity for the flows with different flow index (a) 0.55 (b) 0.8 (note vector scale is different)

In summary, for flows with different flow index at an equivalent bulk flow rate, a more shear-thinning carrier leads to a more stratified flow but requires less pressure drop. This indicates in an actual suspension flow, as the flow becomes more shear-thinning, less power from the pump is required but the delivered concentration also decreases.

6.2.3 Effect of in-line solids concentration

To investigate the effect of in-line solids concentration on the flow in a $44\ mm$ pipe, the following simulations are selected, as shown in Table 6.5. The concentration is varied

from 0.1 to 0.4 with a fixed pressure gradient in Sim No.$1, 4, 5$ and 6. A concentration of 0.4 is very high ($\sim 64\%$ by mass) and is rarely used in conventional tailings. However, this is the kind of concentration desired for stable tailings disposal and it could be more feasible in non-Newtonian suspensions [96]. Effect of in-line solids concentration on the non-Newtonian suspension behaviour is discussed in terms of flow regime, concentration & velocity distribution, force analysis on particles and secondary flow.

Table 6.5 Simulation parameters for investigating the effect of in-line solids concentration in a $44\ mm$ pipe

Sim No.	Solids concentration C_v	Yield stress $\tau_y(Pa)$	Consistency $k(Pa \cdot s^n)$	Flow index n	Particle size $d_p(mm)$	Pressure gradient $\partial P/\partial Z(KPa/m)$	Mixture flow rate $U_m(m/s)$	Bulk flow Re_G
No.1	0.1	5	0.378	0.59	2	6.5	3.54	17000
No.4	0.2	5	0.378	0.59	2	6.5	2.81	13600
No.5	0.3	5	0.378	0.59	2	6.5	1.89	9100
No.6	0.4	5	0.378	0.59	2	6.5	1.55	7500

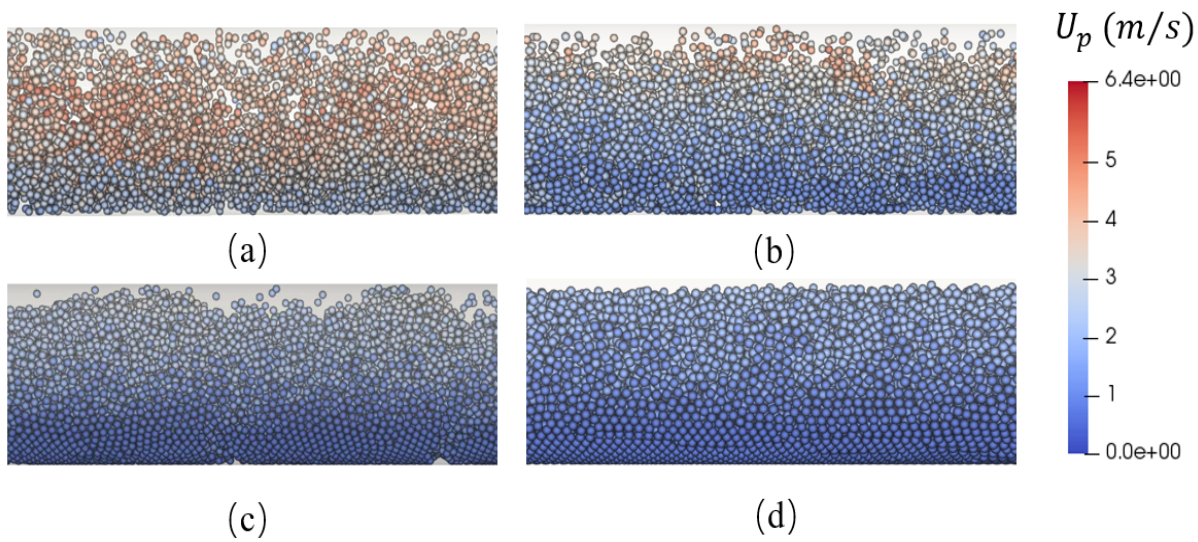

Fig. 6.21 Qualitative view of the flows with different in-line solids concentration and a fixed pressure gradient, where colour represents the magnitude of particle velocity (a) $C_v = 0.1$ (b) $C_v = 0.2$ (c) $C_v = 0.3$ and (d) $C_v = 0.4$. (Note only $1/5$ of full domain is shown)

6.2.3.1 Flow regime, concentration and velocity distribution

The qualitative view of the flow (side view) and instantaneous concentration contour (on the centre plane) for the flows with different in-line solids concentration and a fixed pressure gradient are shown in Fig 6.21 and Fig 6.22, respectively. As can be seen, all

the flows display stratification. For the flow with the lowest in-line solids concentration ($C_v = 0.1$), particle suspension and saltation are the two major modes of transport. With more solids added, a moving bed is found in the flow with in-line solids concentration of $C_v = 0.4$.

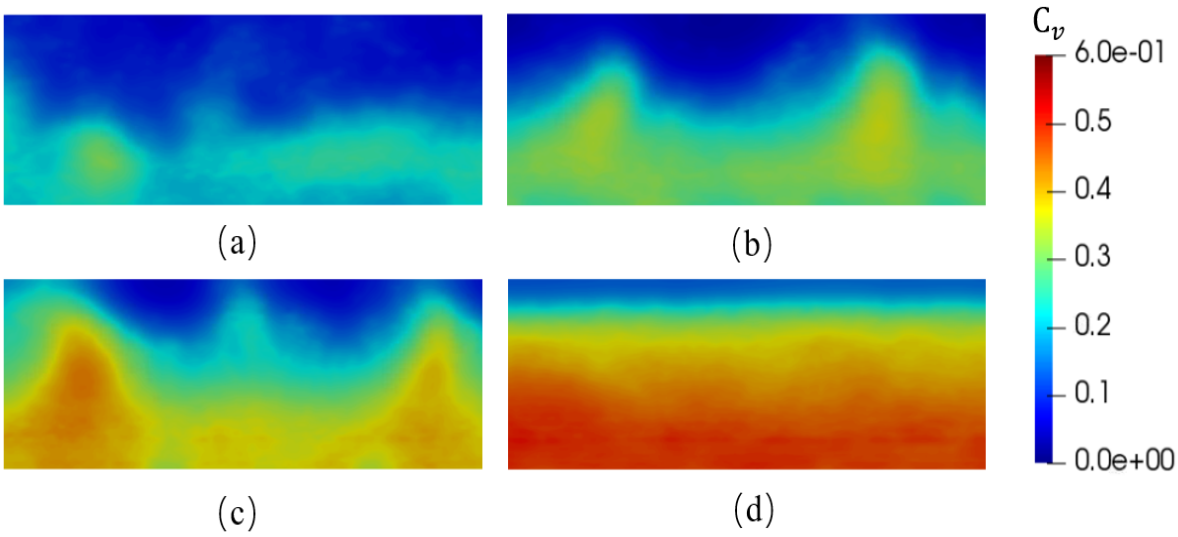

Fig. 6.22 Instantaneous concentration contour for the flows with different in-line solids concentration and a fixed pressure gradient (a) $C_v = 0.1$ (b) $C_v = 0.2$ (c) $C_v = 0.3$ and (d) $C_v = 0.4$

The concentration profiles on the vertical centreline over the pipe cross-section are shown in Fig 6.23. A close to linear concentration distribution is found from the top to the position of approximately $y/D = 0.2$ for $C_v = 0.2$ & 0.3. The concentration reaches a maximum at the bottom of the pipe and increases with higher in-line solids concentration. For the flow with $C_v = 0.1$ & 0.2, the maximum value lies just above the pipe invert. For $C_v = 0.3$ & 0.4, a nearly constant concentration is found near the bottom due to the existence of the bed. Despite a moving bed forming at the bottom, it's not as densely packed as the concentration value at the bottom is around 0.5 for the flow with $C_v = 0.4$. Effective solids transportation is observed from the bottom to the position around $y/D = 0.7$, with a sharp decrease of concentration from the position $y/D = 0.7$ to the upper wall.

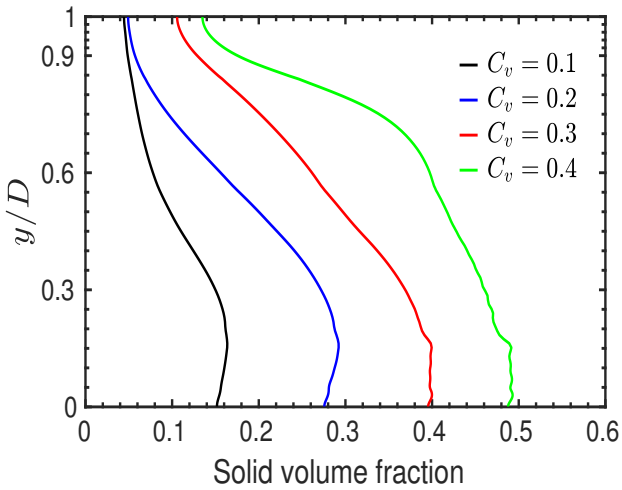

Fig. 6.23 Concentration profiles on the vertical centreline of the pipe cross-section for the flows with different in-line solids concentration and a fixed pressure gradient

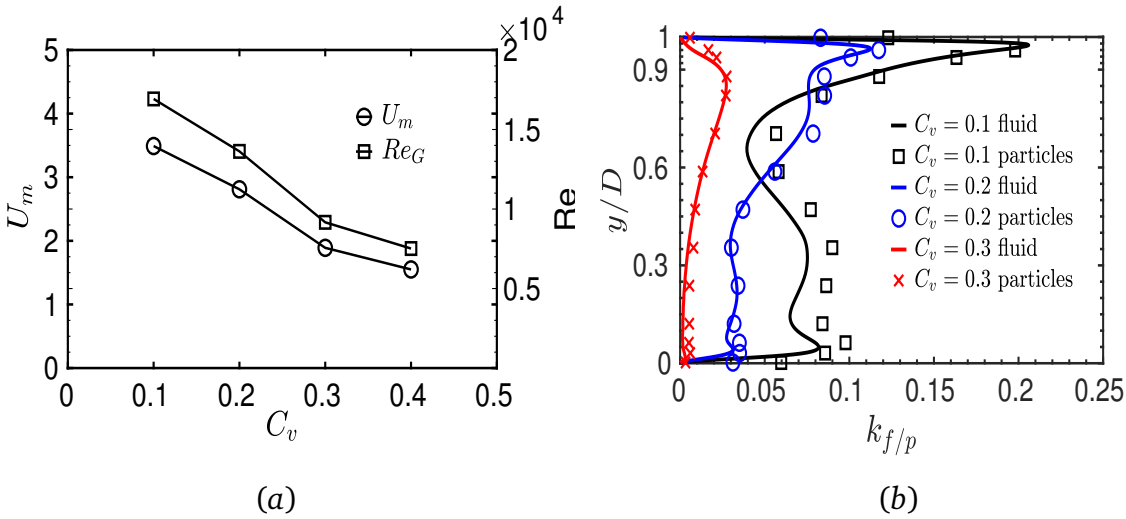

Fig. 6.24 Flow with different in-line solids concentration and a fixed pressure gradient (a) Mean bulk flow velocity and Re_G (b) Turbulent kinetic energy profile on the vertical centreline

With higher in-line concentration, the mean bulk flow velocity reduces, as shown in Fig 6.24 (a), with a 55% reduction when increasing C_v from 0.1 to 0.4. The bulk flow Re_G follows the same trend as the mean bulk flow velocity since the mean wall viscosity is the same in these flows. It is also expected the turbulence will be strongly damped with increasing solids, and this is the case as shown in Fig 6.24 (b). The turbulent kinetic energy is close to zero for the case with $C_v = 0.4$ and is thus not shown. The peak value of the turbulent kinetic energy in the upper section for the flow ($C_v = 0.3$) is 85%

less than the corresponding value in the flow ($C_v = 0.1$). The instantaneous velocity contours in the pipe cross-section (shown in Fig 6.25) also indicate a less turbulent flow with increasing solids concentration. Turbulence in the lower part of the pipe is damped with the presence of concentrated coarse particles and it becomes ineffective in re-suspending the settled particles. Increasing the concentration leads to significantly reduced turbulence intensity (as shown in Fig 6.24 (b)) such that turbulent support collapses completely leading to further stratification.

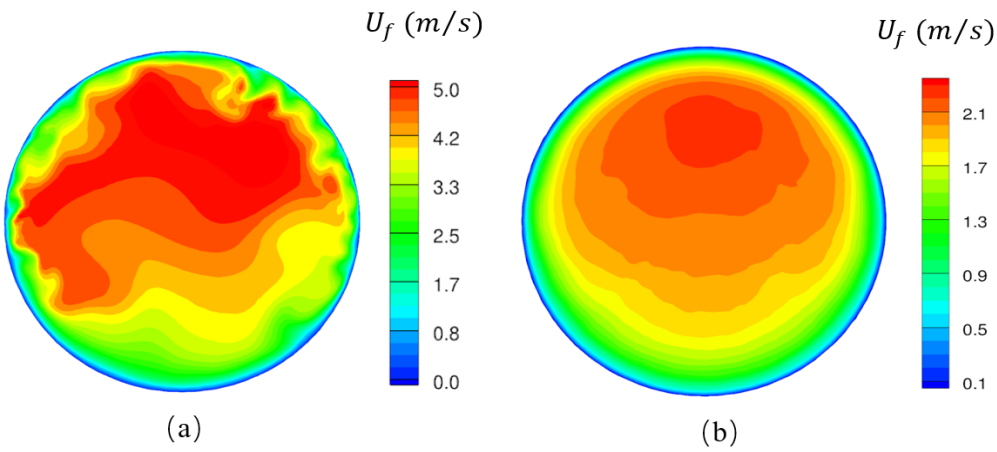

Fig. 6.25 Instantaneous velocity contour of the fluid phase in the pipe cross-section for flows with different in-line solids concentration and a fixed pressure gradient (a) $C_v = 0.1$ (b) $C_v = 0.4$

The corresponding mean velocity profiles on the vertical centreline and fluid velocity cross-sectional contours are shown in Fig 6.26 and 6.27, respectively. A general vertical asymmetry of the velocity profile around the horizontal centreline is found. In addition, there is a gradual flattening of the velocity profile with increasing solids concentration. At higher concentration, there is less room for particles to settle and velocity profiles become less asymmetric. The particle phase generally follows the fluid for $C_v = 0.1$ but with slight lower velocity magnitude in the upper section of the pipe where concentration is lower. At higher concentrations ($C_v = 0.3$ and 0.4), particle-particle collisions are significant, and the two profiles are almost identical to each other.

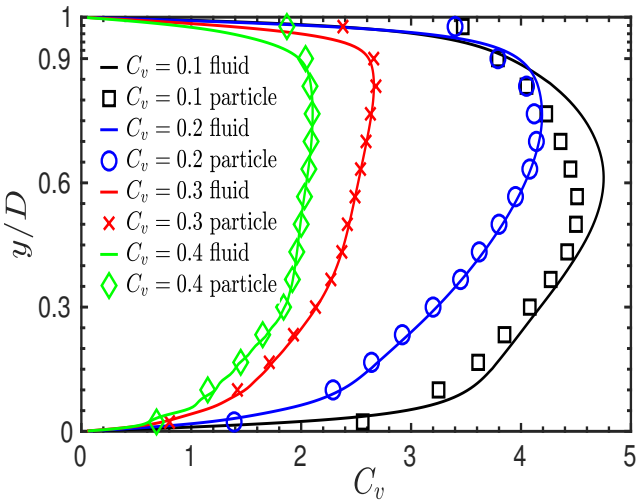

Fig. 6.26 Mean velocity profiles on the vertical centreline of the pipe cross-section for the flows with different in-line solids concentration and a fixed pressure gradient

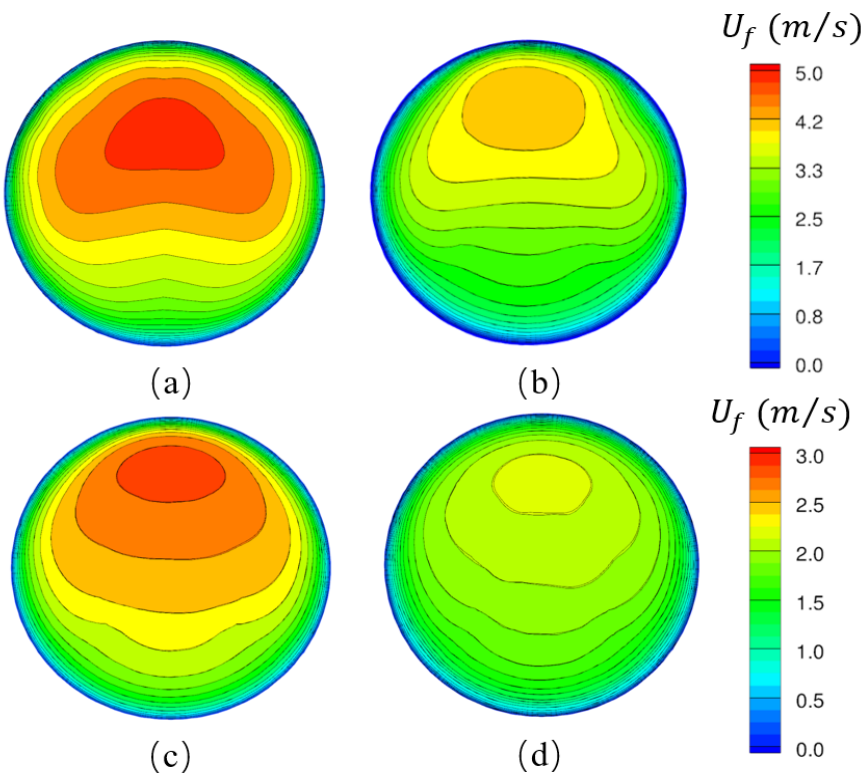

Fig. 6.27 Velocity contour of the fluid phase for the flows with different in-line solids concentration (a) $C_v = 0.1$ (b) $C_v = 0.2$ (c) $C_v = 0.3$ and (d) $C_v = 0.4$. Note the smaller velocity scale in (c) and (d) as to show more details

6.2.3.2 Force analysis on particles and secondary flow

To reveal how particles are suspended at different in-line solids concentration in a turbulent non-Newtonian suspension, a vertical force analysis on the particle phase on the vertical centreline is shown in Fig 6.28.

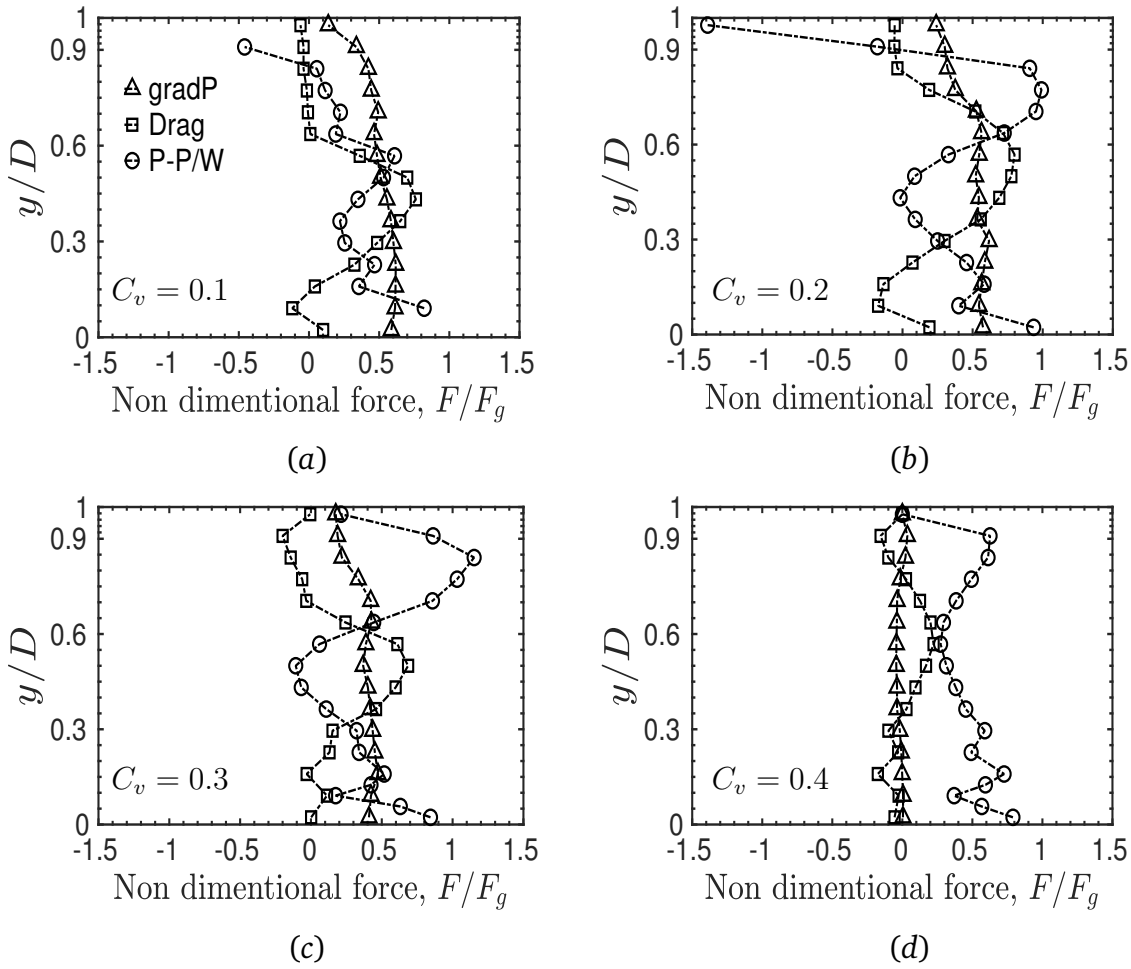

Fig. 6.28 Vertical force analysis on the particle phase on the vertical centreline for the flows with different in-line solids concentration and a fixed pressure gradient (a) $C_v = 0.1$ (b) $C_v = 0.2$ (c) $C_v = 0.3$ and (d) $C_v = 0.4$

Forces shown are non-dimensionalised with the gravity force. Particle-particle/wall collisions (P-P/W) near the wall are big and forces with a magnitude larger than 1.5 are not shown for clarity (e.g., P-P/W in Fig 6.28 (a)). As can be seen, the presence of the viscous core region contributes to the dominant drag force on particles in the central region and the pressure gradient force has a nearly uniform distribution on the vertical centreline. In the lower section, the resultant p-p/w collision is positive and

supports particles towards the centre. Particle-particle collision is correspondingly lower in the highly viscous core region. In the upper section, particle-particle collision becomes stronger due to the higher turbulence intensity there. At high concentration ($C_v = 0.4$), particle-particle collision becomes dominant on the vertical centreline, as shown in Fig 6.28 (d).

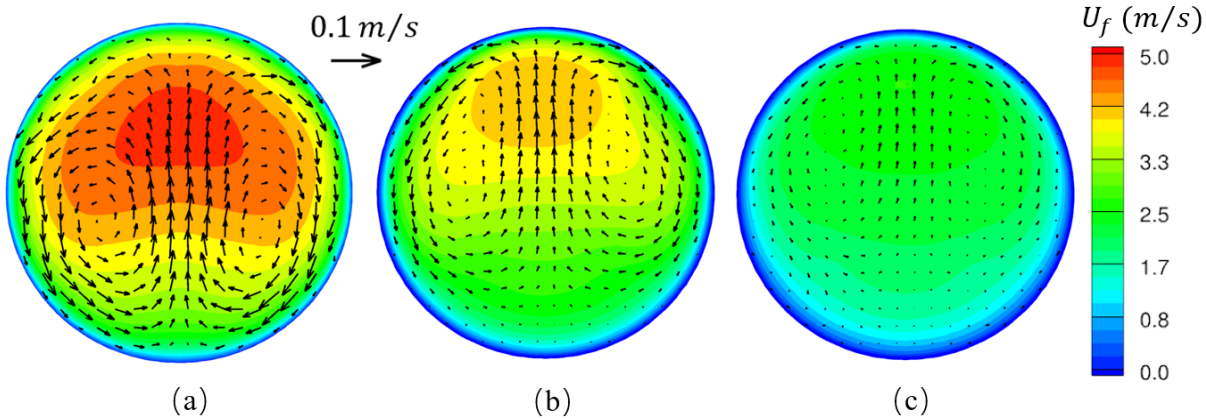

Fig. 6.29 Time-averaged cross-sectional vector field of the secondary flow velocity for the flows with different in-line solids concentration and a fixed pressure gradient (a) $C_v = 0.1$ (b) $C_v = 0.2$ and (c) $C_v = 0.3$

The secondary flow for different in-line solids concentration (and a fixed pressure gradient) is shown in Fig 6.29. The magnitude of the secondary flow (based on the maximum vector) is 2, 1.8 and 1.2% of the mean bulk flow rate for C_v from 0.1 to 0.3. The secondary flow pattern completely disappears in the flow with high concentration ($C_v = 0.4$), thus is not shown in Fig 6.29. The secondary flow shows a similar pattern with two symmetric rotating longitudinal vortices lifting fluid & particles vertically along the centreline and back down outside. The pattern also moves upward for higher C_v as more particles settle in the lower section.

6.2.4 Comparison with equivalent Newtonian suspensions

The turbulent non-Newtonian suspensions investigated so far exhibit similar heterogeneous flow as observed in a Newtonian suspension. To reveal the similarity and difference with an equivalent Newtonian suspension, the following simulations are conducted, as shown in Table 6.6. Sim No.11 is a Newtonian suspension with an equivalent mean wall viscosity and bulk flow Re to Sim No.10.

Table 6.6 Simulation parameters for investigating equivalent Newtonian and non-Newtonian suspensions in a $44\ mm$ pipe

Sim No.	Solids concentration C_v	Yield stress $\tau_y(Pa)$	Consistency $k(Pa \cdot s^n)$	Flow index n	Particle size $d_p(mm)$	Pressure gradient $\partial P/\partial Z(KPa/m)$	Mixture flow rate $U_m(m/s)$	Bulk flow Re_G
No.10	0.2	15	0.378	0.59	2	8.1	2.89	13300
No.11	0.2	N/A	0.0113	1	2	5.6	2.82	13600

The concentration profiles of the Newtonian and non-Newtonian suspensions are shown in Fig 6.30. As can be seen, particles in a non-Newtonian suspension are only slightly more uniformly distributed compared to an equivalent Newtonian suspension. The difference is minor except near lower pipe wall.

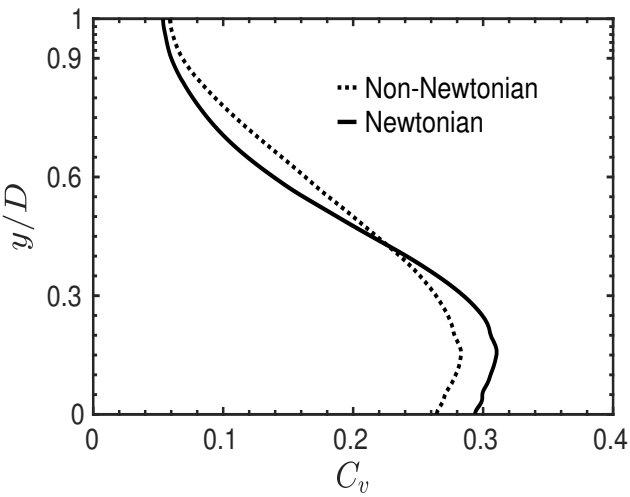

Fig. 6.30 Concentration profiles on the vertical centreline of the pipe cross-section for the Newtonian and non-Newtonian flow

The presence of the highly viscous carrier fluid causes reduced turbulence intensities in a non-Newtonian flow, as shown in Fig 6.31(a). A 60% reduction of the turbulent kinetic energy is observed when comparing the peak values in the upper section. However, the coupling between the carrier fluid and suspended particles becomes stronger. This is revealed from the drag force analysis on particles shown in Fig 6.31(b). The drag force is dominant in the highly viscous region and has a largest magnitude around 1. This beneficial effect is not present in a Newtonian suspension. In a Newtonian suspension, particles are more supported by the pressure gradient force and particle-particle collisions on the vertical centreline, as discussed in Chapter 5 paper Section 4.4. The drag is not as significant as in a non-Newtonian suspension. Despite the slightly improved solids suspension on the vertical centreline, the delivered concentration in

these two flows are almost identical, with the ratio of delivered concentration to in-line solids concentration $C_{vd}/C_v = 0.95$. Meanwhile, a non-Newtonian flow requires higher pressure gradient to obtain the same mixture flow rates as in a Newtonian suspension. The pressure drop in Sim No.10 is 45% higher in order to obtain the same mixture flow rates as in Sim No.11.

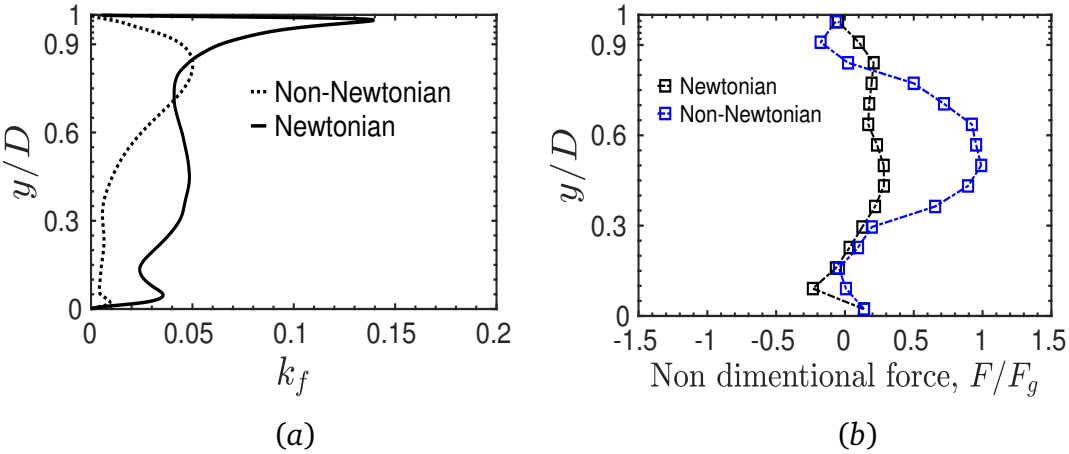

Fig. 6.31 Profiles on the vertical centreline of the pipe cross-section (a) Turbulent kinetic energy (b) Vertical drag force on the particle phase

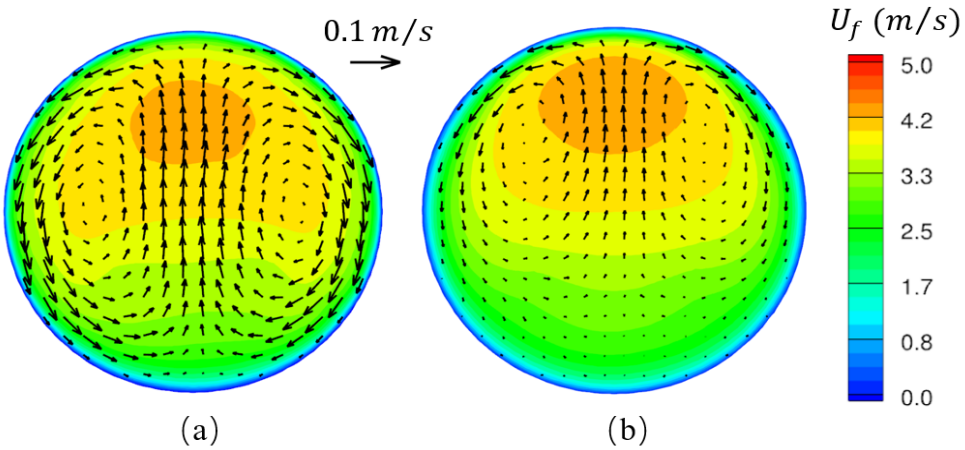

Fig. 6.32 Time-averaged cross-sectional vector field of the secondary flow velocity for the flow (a) Newtonian (b) non-Newtonian

Secondary flow is observed in both Newtonian and non-Newtonian suspensions, as shown in Fig 6.32. The Newtonian secondary flow has a larger magnitude (2.7 % of the mean bulk flow rate, based on the maximum vector) than the non-Newtonian case (1.6 %), and the two rotating cells cover the entire pipe cross-section. While in

the non-Newtonian flow with $\tau_y = 15Pa$, the secondary flow only appears in the upper section.

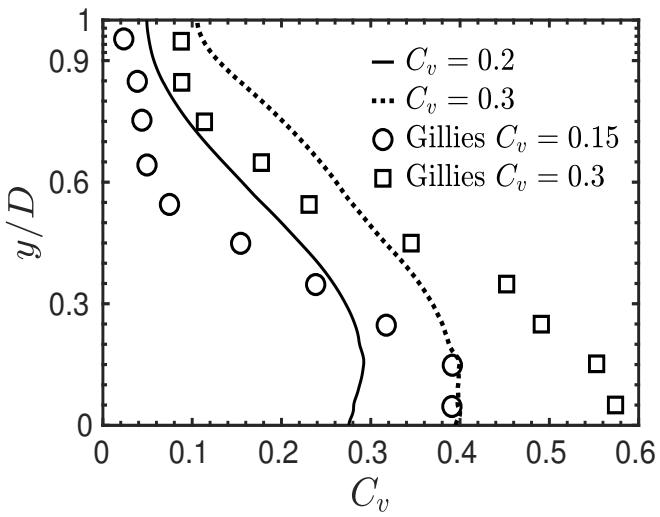

Fig. 6.33 Comparison of concentration profiles with a traditional water-sand slurry from Gillies [49] at a similar pipe & particle scale and bulk flow velocity

A comparison of a non-Newtonian suspension with a traditional water-sand slurry from Gillies [49] conducted at a similar pipe & particle scale and bulk flow velocity is also considered (Pipe D: $53\ mm$; particle size d_p: $2.4\ mm$; C_v 0.15 & U_m $3.1\ m/s$ and C_v 0.3 & U_m $1.8\ m/s$). The water-sand slurry concentration profiles are compared with those from Sim No.$4 \sim 5$, as shown in Fig 6.33. Note that in this comparison, the water-sand slurry in [49] has a much lower viscosity, where the Re is in the scale of $O(10^5)$ and Re_p ($\sim$300) is about 10 times bigger than that in Sim No.$4 \sim 5$. The results indicate the non-Newtonian flow has a better suspension at lower Re compared to a traditional water-sand slurry at a similar pipe & particle scale. As can be seen in Fig 6.33, the maximum concentration at the bottom is 0.4 for the flow (Sim No. 5, $C_v = 0.3$). There is no "packed" bed observed, while the maximum concentration reaches 0.6 for the water-sand slurry with $C_v = 0.3$. The ratio of delivered concentration to in-line solids concentration C_{vd}/C_v in the water-sand slurries are 0.81 and 0.77, which are lower than 0.95 and 1.00 in Sim No.$4 \sim 5$, respectively.

The above results suggest the non-Newtonian suspension doesn't show much improvement in solids suspension compared to an equivalent Newtonian suspension with the same mean wall viscosity, but has a better suspension at lower Re compared to

a traditional water-sand slurry at a similar pipe & particle scale. Meanwhile, it would definitely be more appropriate to assume a heterogeneous flow or a sliding bed rather than a pseudo-homogeneous flow in designing a turbulent non-Newtonian suspension at these Re. The comparison to an equivalent Newtonian suspension suggests when modifying existing Newtonian empirical correlations & layer models for description of non-Newtonian suspension behaviour, the local non-Newtonian rheology should be incorporated into these models to reflect the weaker turbulence and stronger coupling between the carrier and particles. The degree of packing in the stratified bed reduces compared to a Newtonian equivalent. A lower value of the empirical features in layer models such as the mean lower layer concentration should be considered.

6.3 Flow in pipes of diameter 100 & 200 mm

A pipe diameter of $44\ mm$ is a small scale lab pipe and real applications have larger diameters. To reveal the non-Newtonian suspension flow at a larger pipe scale, flows are also considered in pipes of diameter 100 & $200\ mm$. Flow in a larger pipe requires less pressure gradient, thus a high yield stress flow is feasible. Yield stresses of 15 and $25\ Pa$ are considered in a large pipe to reveal the impact of high yield stress in a non-Newtonian suspension flow. The carrier fluid rheology and solids properties are varied at an equivalent bulk flow velocity (approximately $2.9\ m/s$). These diameters and parameters are chosen as they are commonly used in previous tailings studies [49, 84, 97, 119]. Since the DNS-DEM model has only been validated in a small scale lab pipe ($44\ mm$), results for flow in a large pipe presented in this section are illustrative of how the change of solids in-line concentration C_v, yield stress τ_y and particle size d_p would affect the flow behaviour. This section only presents results in a large pipe. Effect of pipe size on the flow will be covered later in Sec 6.4.

6.3.1 Effect of in-line solids concentration

To investigate the effect of in-line solids concentration C_v on the flow at an equivalent bulk flow velocity, $C_v = 0.1$, 0.2 and 0.4 are conducted in Sim No.$12 \sim 14$. Solids used are mono-sized particles with diameter of $d_p = 4.6mm$, which is the same d_p/D ratio as in a $44\ mm$ pipe for $2\ mm$ particles. Clearly this is a bigger particle size and will change

the results. Effect of particle size on transport characteristics will be covered later in Sec 6.3.3.

Table 6.7 Simulation parameters for investing the effect of in-line solids concentration in a $100\ mm$ pipe

Sim No.	Pipe Diameter $D(mm)$	Solids concentration C_v	Yield stress $\tau_y(Pa)$	Consistency $k(Pa \cdot s^n)$	Flow index n	Particle Size $d_p/D(mm)$	Pressure gradient $\partial P/\partial Z(KPa/m)$	Mixture flow rate $U_m(m/s)$	Bulk flow Re_G
No.12	100	0.1	25	0.93	0.59	1/22(4.6)	3.5	2.89	5100
No.13	100	0.2	25	0.93	0.59	1/22(4.6)	5.0	2.90	8000
No.14	100	0.4	25	0.93	0.59	1/22(4.6)	11.2	2.95	17600

6.3.1.1 Flow regime and concentration distribution

The qualitative view of the flow (side view) and instantaneous solid volume fraction (on the centre plane) for the flows with different in-line solids concentration in the $100\ mm$ pipe are shown in Fig 6.34.

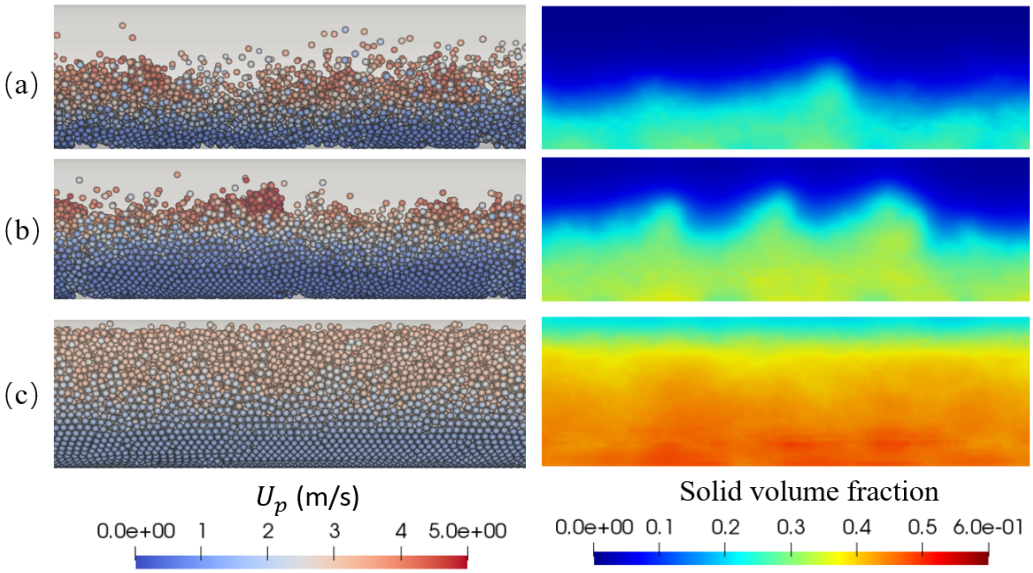

Fig. 6.34 Qualitative view of the flow and instantaneous solid volume fraction for flows with different in-line solids concentration in a $100\ mm$ pipe (a) $C_v = 0.1$ (b) $C_v = 0.2$ and (c) $C_v = 0.4$

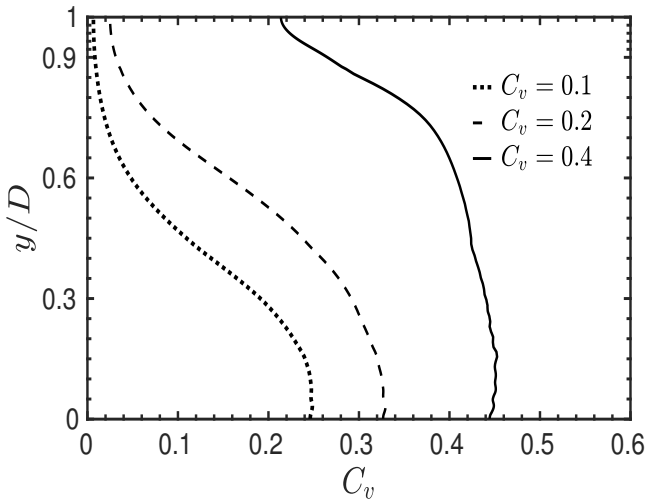

Fig. 6.35 Concentration profile on the vertical centreline of the pipe cross-section for flows with different in-line solids concentration in a $100\ mm$ pipe

Similarly to a $44\ mm$ pipe, the flow transits from partial suspension with saltation at a low concentration to a moving sliding bed at a high concentration. Particle dune and surge formations are observed in the flow at a lower concentration. At the highest concentration ($C_v = 0.4$), particles occupy the entire pipe with less room to move around. The concentration profiles on the vertical centreline of a pipe cross-section for these flows are shown in Fig 6.35. The concentration profiles all indicate a stratified flow pattern. For the flow with $C_v = 0.4$, the concentration profile becomes nearly uniform with a small gradient from the bottom to the position around $y/D = 0.7$, while a sudden increase of the gradient is observed in the upper section. The concentration near the upper wall reduces to a value of approximately 0.21. The maximum value of around 0.45 in the lower portion indicates a loosely packed moving bed at the bottom.

6.3.1.2 Velocity distribution

The mean velocity profiles on the vertical centreline of the pipe cross-section and fluid velocity contours for the flows with different in-line solids concentration in the $100\ mm$ pipe are shown in Fig 6.36 and Fig 6.37, respectively.

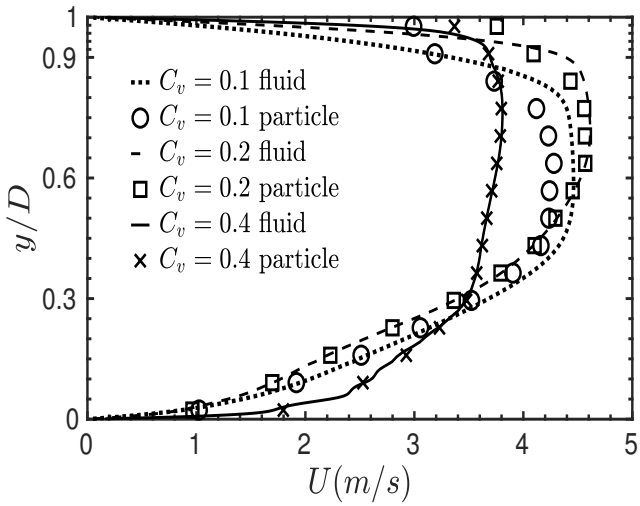

Fig. 6.36 Mean velocity profiles on the vertical centreline of the pipe cross-section for the flows with different in-line solids concentration in a $100\ mm$ pipe

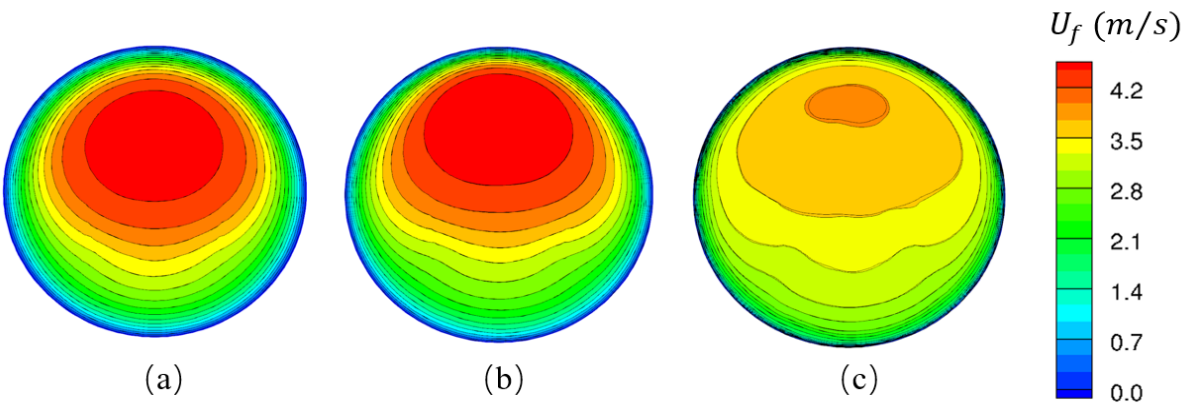

Fig. 6.37 Velocity contour of the fluid phase in the pipe cross-section for the flows with different in-line solids concentration in a $100\ mm$ pipe (a) $C_v = 0.1$ (b) $C_v = 0.2$ and (c) $C_v = 0.4$

The profile also becomes less asymmetric for the flow with a high concentration ($C_v = 0.4$). Although the flows here have an equivalent mixture flow rate, the maximum fluid and particle velocity reduces for increasing C_v. Meanwhile, the near wall bed layer in the flow with $C_v = 0.4$ moves at a velocity around $1.8\ m/s$, which is much higher than that in the flow with a lower concentration. The core of the flow (where the maximum velocity lies) moves further upwards from the pipe centre with increasing C_v.

6.3.1.3 Pressure drop

The pressure drop for flows with different in-line solids concentration in a $100\ mm$ pipe is shown in Fig 6.38. The predicted pressure drops are 3.5, 5.0 and $11.2\ KPa/m$ for the flows with in-line solids concentration $C_v = 0.1$, 0.2 and 0.4, respectively.

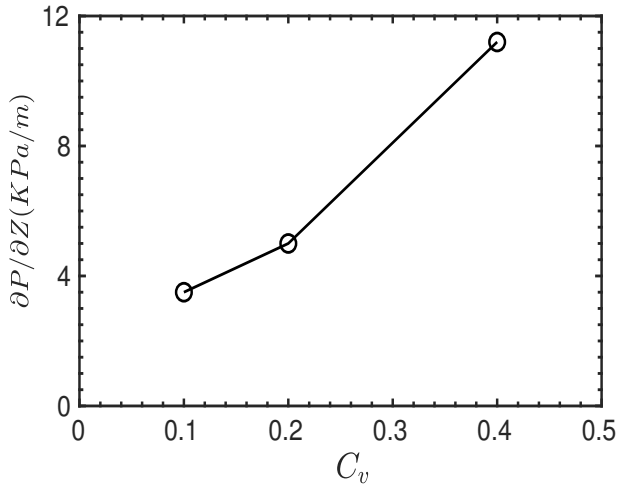

Fig. 6.38 Pressure drop for flows with different in-line solids concentration in a $100\ mm$ pipe

As expected, higher pressure gradient is needed to maintain the same mixture flow rate with increasing solids concentration. High concentration transportation at the same velocity requires an increased pressure drop for two reasons. Firstly an increased mass needs to be transported; secondly a higher friction loss is caused by the particle-wall collisions. In conditions where turbulent diffusion is ineffective in re-suspending the particles, the solids load settles on the pipe invert. This necessitates an extra pressure gradient in the flow direction to keep the bed in motion. As can be seen in Fig 6.38, a steep rise in the pressure drop is found when increasing C_v from 0.2 to 0.4. The pressure drop for the flow with in-line solids concentration $C_v = 0.4$ is about twice that of the flow with $C_v = 0.2$. Further discussion on pressure drop is covered in section 6.4, where flows in pipes of different diameters are compared.

Despite increasing C_v requiring higher pressure gradient, the ratio of delivered solids volume fraction to in-line concentration C_{vd}/C_v increases and is 0.66, 0.84 and 1.00 for $C_v = 0.1$, 0.2 and 0.4, respectively. The energy consumption per unit mass of solids transported per unit pipe length, i.e., $SEC\ (J/kg \cdot m)$ is defined as [143]

$$SEC = \frac{\partial P/\partial Z}{C_{vd} \cdot \rho_s} \tag{6.1}$$

The SEC is 20.4, 11.5 and 10.7 $J/kg \cdot m$ for $C_v = 0.1$, 0.2 and 0.4, respectively. The SEC in the flow ($C_v = 0.4$) is only half as in $C_v = 0.1$. Although in-line concentration of 0.4 ($\sim 64\%$ by mass of coarse particles) requires much higher power for transportation and is not used in traditional transport operations, results in Sec 6.3.1 indicate going to an ultra high concentration is feasible and more energy efficient in highly viscous non-Newtonian suspension where solids concentration approaches the packing conditions of the suspension. Effective solids suspension is observed in most positions ($y/D < 0.7$) in the flow with $C_v = 0.4$. The coarse particles occupy the entire pipe during the flow, despite stratification is observed, the bed is not as densely packed. The flow mechanism is different from that described in previous Newtonian two and three-layer models. A new modelling approach would be needed for ultra high concentration suspensions and a lower value of the packing concentration in the bed should be considered.

6.3.2 Effect of yield stress

To reveal the effect of yield stress on the non-Newtonian suspension flow in a 100 mm pipe, the following two simulations are selected, as shown in Table 6.8. Sim No.13 and 18 are flows with yield stress $\tau_y = 15Pa$ and $25Pa$, respectively.

Table 6.8 Simulation parameters for investigating the effect of $\boldsymbol{\tau_y}$ in a 100 mm pipe

Sim No.	Pipe Diameter $D(mm)$	Solids concentration C_v	Yield stress $\boldsymbol{\tau_y}(Pa)$	Consistency $k(Pas^n)$	Flow index n	Particle Size $d_p/D(mm)$	Pressure gradient $\partial P/\partial Z(KPa/m)$	Mixture flow rate $U_m(m/s)$	Bulk flow Re_G
No.13	100	0.2	25	0.93	0.59	1/22(4.6)	5.0	2.90	8000
No.18	100	0.2	15	0.93	0.59	1/22(4.6)	4.3	2.94	8300

The concentration and velocity profiles on the vertical centreline of the pipe cross section for the above simulations are shown in Fig 6.39 and Fig 6.40, respectively. It can be seen the concentration and velocity profiles with $\tau_y = 25Pa$ are almost identical to those with $\tau_y = 15Pa$. The presence of a higher yield stress doesn't produce a more uniform distribution in a large pipe. High yield stress is found to be ineffective here in supporting the particles during a suspension flow, while requiring a higher pressure gradient. As can be seen in Table 6.8, pressure drop in the flow with $\tau_y = 25Pa$ is

approximately 16% higher compared to the flow with $\tau_y = 15Pa$. Most of the findings here are in agreement with the results presented in section 6.2.1, where the effect of yield stress on the turbulent non-Newtonian suspension flow has been discussed in a 44 mm pipe. The details are not repeated for brevity.

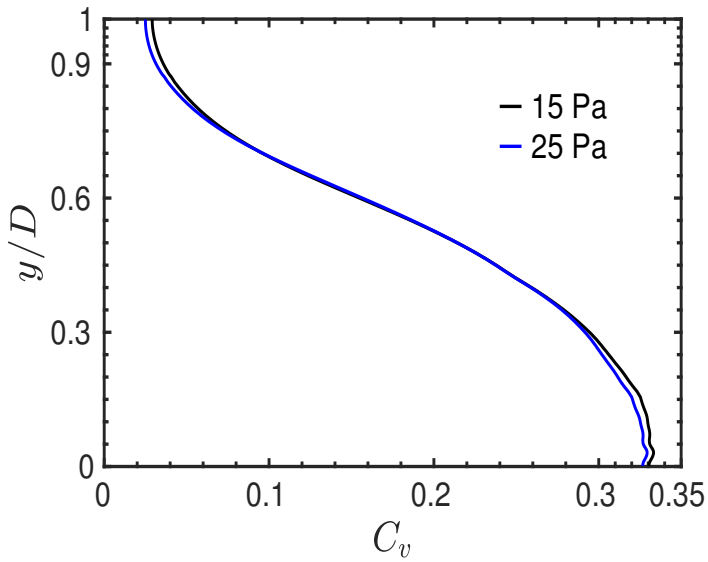

Fig. 6.39 Concentration profiles on the vertical centreline of the pipe cross-section for flows with different yield stress in a 100 mm pipe

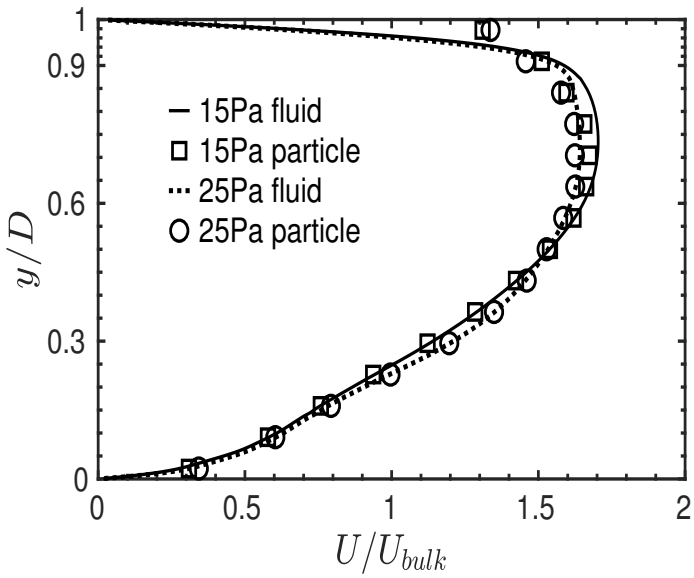

Fig. 6.40 Velocity profile on the vertical centreline of the pipe cross-section for flows with different yield stress in a 100 mm pipe (normalised by the mean bulk flow velocity)

6.3.3 Effect of particle size

Tailings suspension often occurs with a broad size distribution. Due to the intensive computational efforts required in DND-DEM, it is not possible to model a flow with a wide size distribution that includes small particles. To include particles with $d_p \approx 1mm$ will require $O(10^6)$ particles in a $100\ mm$ pipe. This is currently beyond the computational resources. The following simulations are selected to investigate the effect of particle size in the $100\ mm$ pipe, as shown in Table 6.9. Mono-sized particles are used. Simulations are conducted by varying the ratio of particle size to pipe diameter in the range of $1/22 \sim 1/10$ at an in-line concentration $C_v = 0.1$. A flow consisting of particles of two different coarse sizes, $d_p = 4.6mm$ (50% v/v) and $d_p = 7mm$ (50% v/v) is also conducted in Sim No.17.

Table 6.9 Simulation parameters for investigating the effect of d_p in a $100\ mm$ pipe

Sim No.	Pipe Diameter $D(mm)$	Solids concentration C_v	Yield stress $\tau_y(Pa)$	Consistency $k(Pa \cdot s^n)$	Flow index n	Particle Size $d_p/D(mm)$	Pressure gradient $\partial P/\partial Z(KPa/m)$	Mixture flow rate $U_m(m/s)$	Bulk flow Re_G
No.12	100	0.1	25	0.93	0.59	1/22(4.6)	3.5	2.89	5100
No.15	100	0.1	25	0.93	0.59	1/14(7)	3.5	2.99	5200
No.16	100	0.1	25	0.93	0.59	1/10(10)	3.1	2.90	4300
No.17	100	0.1	25	0.93	0.59	50%(7)+ 50%(4.6)	3.5	2.94	5200

6.3.3.1 Flow regime and concentration distribution

The qualitative view of the flow (side view) and instantaneous concentration contours (on the centre plane) for the flows with different particle sizes in a $100\ mm$ pipe are shown in Fig 6.41 and Fig 6.42, respectively. Although it seems reasonable to presume that particles would settle more easily with increasing particle size, it is found that larger particles are more mobile in this case while smaller particles form a loose bed at the bottom, as can be seen by comparing Fig 6.41 (a) and (c). The flow with a larger particle size has a more uniform distribution as revealed from the concentration profiles in Fig 6.43. The ratio of delivered solids volume fraction to in-line concentration C_{vd}/C_v is 0.66, 0.80 and 0.85 for $d_p = 4.6$, 7 and $10\ mm$, respectively.

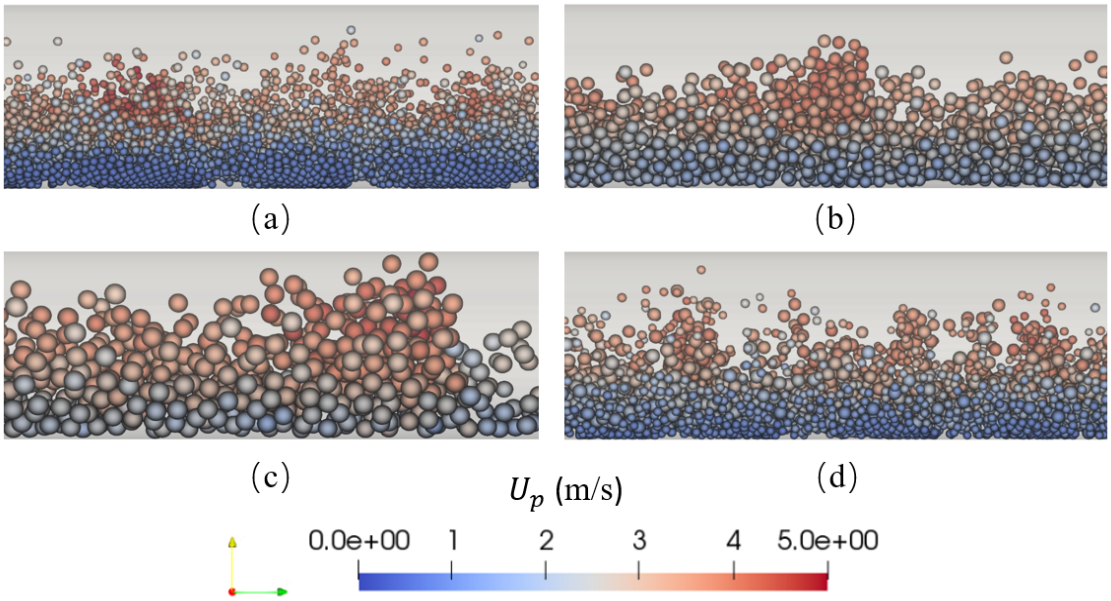

Fig. 6.41 Qualitative view of the flow with different particle sizes (a) $d_p = 4.6mm$ (b) $d_p = 7mm$ (c) $d_p = 10mm$ and (d) $d_p = 4.6mm$ & $7mm$

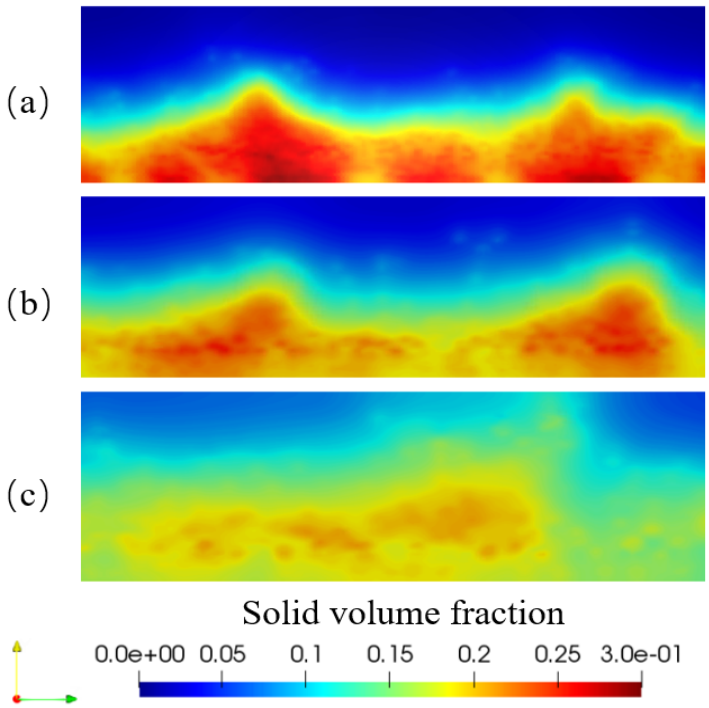

Fig. 6.42 Instantaneous concentration contours on the centre plane for flows with different particle sizes (a) $d_p = 4.6mm$ (b) $d_p = 7mm$ and (c) $d_p = 10mm$

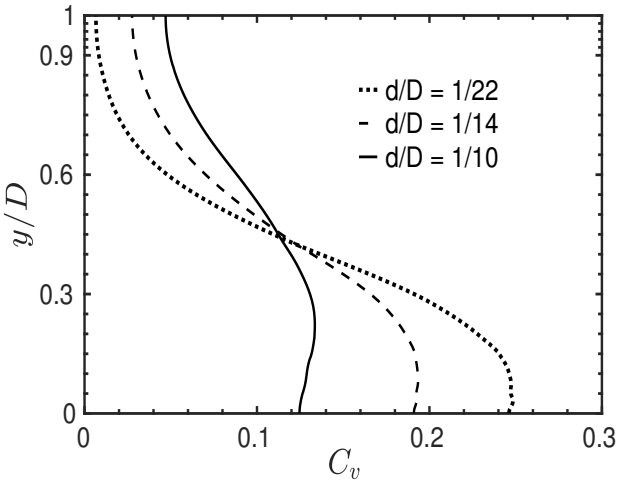

Fig. 6.43 Concentration profile on the vertical centreline of the pipe cross section for flows with different particle sizes

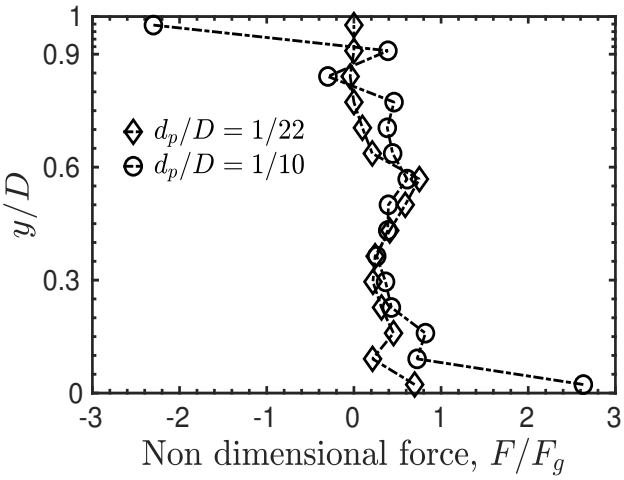

Fig. 6.44 Vertical comparison of the particle-particle/wall collision (P-P/W) on the vertical centreline for flows with different particle sizes

For flows with a constant in-line solids concentration, the particle number density decreases with increasing particle size. An intensive bouncing from the bottom wall and inter-particle collisions, plus an increasing collisions with the upper wall are observed for the flow with $d_p = 10mm$. Although this is not obvious from the still image, it is clearly seen in the animation. It is also revealed from the vertical force comparison of particle-particle/wall collision (P-P/W) on the vertical centreline, as shown in Fig 6.44. The flow with $d/D = 1/10$ has a larger P-P/W in most positions, and with a significantly higher value near the wall than $d/D = 1/22$. Smaller particles at the bottom also collide

with the wall but are subject to compression from the upper layers of particles and are less free to move due to the higher particle number density. Significant particle saltation and suspension is only observed above the bed for smaller particles, with the dune formation as seen in Fig 6.42.

Previous studies also investigate the effect of particle size on the concentration distribution in a suspension flow. Among them, Gillies [49] conducted water-sand slurry flow with in-line solids concentration of 0.15 & 0.30 in a $53\ mm$ pipe. Similarly to this study, a more uniform distribution was observed for $2.4\ mm$ sand than $0.55\ mm$ sand at flow rates of both $1.8\ m/s$ and $3.1\ m/s$. Contrary to the findings here, Eesa and Barigou [33] investigated pipe transport of coarse particles ($2 \sim 9\ mm$) in a laminar power-law fluid based on the Two-Fluid Model (TFM). Particle settling was more pronounced in their study for a flow with larger particles. The difference may arise from the treatment of the solids stress term in TFM, which is based on empirical constitutive correlations and inter-particle collisions are modelled, not captured as they are here. A consensus has not been reached on the effect of coarse particle size & size distribution in non-Newtonian carriers and further studies are needed in this area.

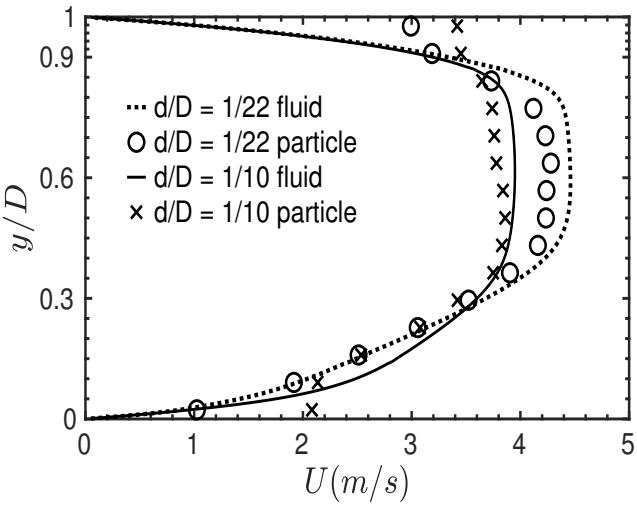

Fig. 6.45 Velocity profiles on the vertical centreline of the pipe cross section for flows with different particle sizes

6.3.3.2 Velocity distribution

The velocity profiles on the vertical centreline of the pipe cross-section and fluid velocity contours for flows with different particle sizes are shown in Fig 6.45 and Fig 6.46,

respectively. The velocity profile for the flow with the intermediate particle size $d_p = 7mm$ lies between the other two, and is thus not shown for clarity.

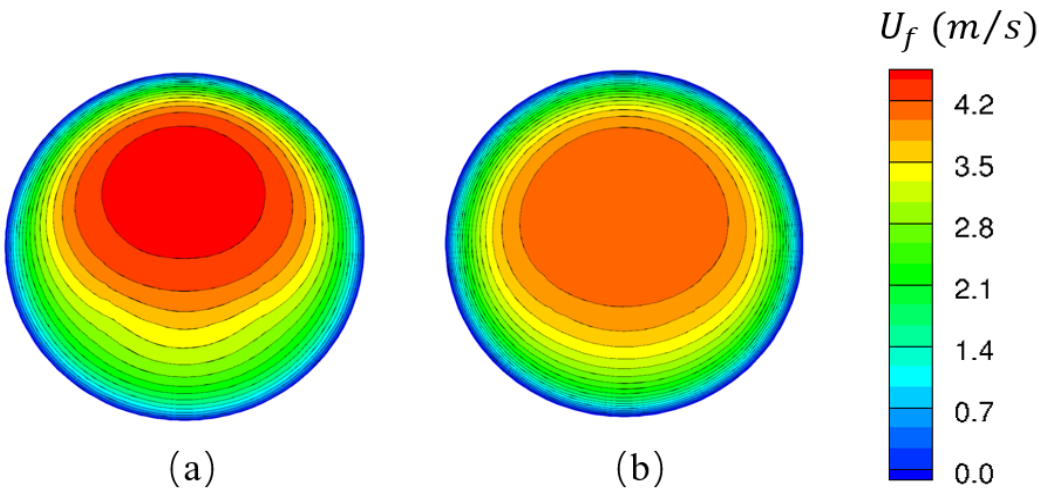

Fig. 6.46 Velocity contour for flows with different particle sizes (a) $d_p = 4.6mm$ (b) $d_p = 10mm$

With increasing particle diameter, the profile asymmetry decreases and the particles are more uniformly distributed. A blunting of the velocity profile in the central region is found. The velocity contour becomes more symmetric for the flow with $d_p = 10mm$ and the area of the core flow region increases compared to that with $d_p = 4.6mm$. The maximum velocity also reduces for the flow with $d_p = 10mm$ but the position of maximum velocity appears to be independent of the particle size, and lies slightly above the centreline. Simultaneously, particles with $d_p = 10mm$ travel faster at both the upper and lower wall compared to those with $d_p = 4.6mm$ and have significant velocity ($2m/s$) near the wall, suggesting that friction is playing less of a role as d_p increases.

6.3.3.3 Pressure drop

The pressure drop for flows with different particle sizes is shown in Fig 6.47. As can be seen in Fig 6.47, the particle size has a minor effect on the pressure drop for the ranges investigated ($4.6 \sim 10mm$). The pressure drop for the flow with $d_p = 4.6mm$ is about the same as for that with $d_p = 7mm$, while the flow with $d_p = 10mm$ shows a 11% pressure drop reduction.

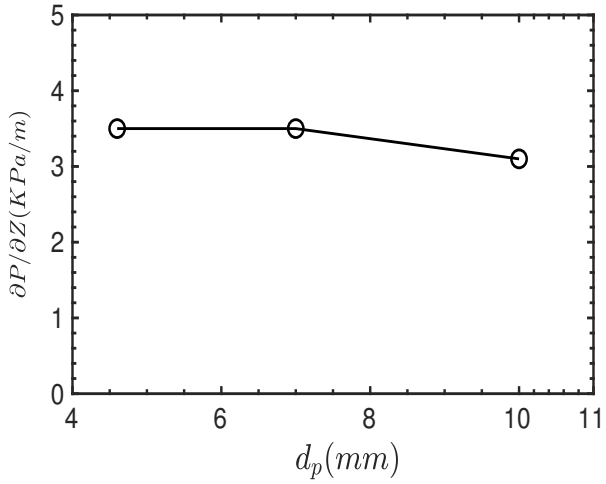

Fig. 6.47 Pressure drop for flows with different particle sizes

For a suspension flow, pressure drop arises from counteracting the fluid-wall, fluid-particle, particle-wall and particle-particle friction. These types of friction are all dependent on the contact surface area. For a pipe flow with a constant in-line solids concentration, increasing the particles size reduces the particle number density and total surface area of particles. There is therefore less friction for a flow with larger particles. Simultaneously, less particles settling at the bottom also reduces the particle-wall friction. Hence a reduced pressure drop is observed for flow with $d_p = 10mm$.

In summary, results in Sec 6.3.3 indicate in a turbulent coarse-particle suspension, the pressure drop is not very sensitive to the coarse-particle size over this range of d_p but flow with coarser particles has a higher delivered concentration (given the same feed concentration). However, how coarse particles (in the mm range) affect the concentration distribution hasn't reached a consensus. Further studies are needed in this area particularly for suspension flows with a wider size distribution.

6.4 Effect of pipe size

Simulations in pipes of diameter 44, 100 and 200 mm, respectively (Sim No. 10, 19 and 20) are selected to investigate the effect of pipe size on the flow, as shown in Table 6.10. Note that the particle sizes are different here. To use $d_p = 2mm$ in larger pipes is infeasible as particle number of $O(10^6)$ is required. Simulations are conducted by fixing the ratio of particle diameter to pipe size $d_p/D = 1/22$. In addition, the consistency

k also needs to be adjusted for different pipe size to ensure the flow lies in a weakly turbulent regime. The k is adjusted so all the flows have an equivalent bulk flow Re_G.

Table 6.10 Simulation parameters for investigating the effect of pipe size

Sim No.	Pipe Diameter $D(mm)$	Solids concentration C_v	Yield stress $\tau_y(Pa)$	Consistency $k(Pa \cdot s^n)$	Flow index n	Particle Size $d_p/D(mm)$	Pressure gradient $\partial P/\partial Z(KPa/m)$	Mixture flow rate $U_m(m/s)$	Bulk flow Re_G
No.10	44	0.2	15	0.378	0.59	1/22 (2)	8.1	2.89	13300
No.19	100	0.2	15	0.70	0.59	1/22 (4.6)	4.3	2.99	13600
No.20	200	0.2	15	1.17	0.59	1/22 (9)	2.5	2.97	13000

6.4.1 Flow regime and concentration distribution

The qualitative view of the flow (side view) and instantaneous concentration contour (on the centre plane) for flows with different pipe sizes are shown in Fig 6.48.

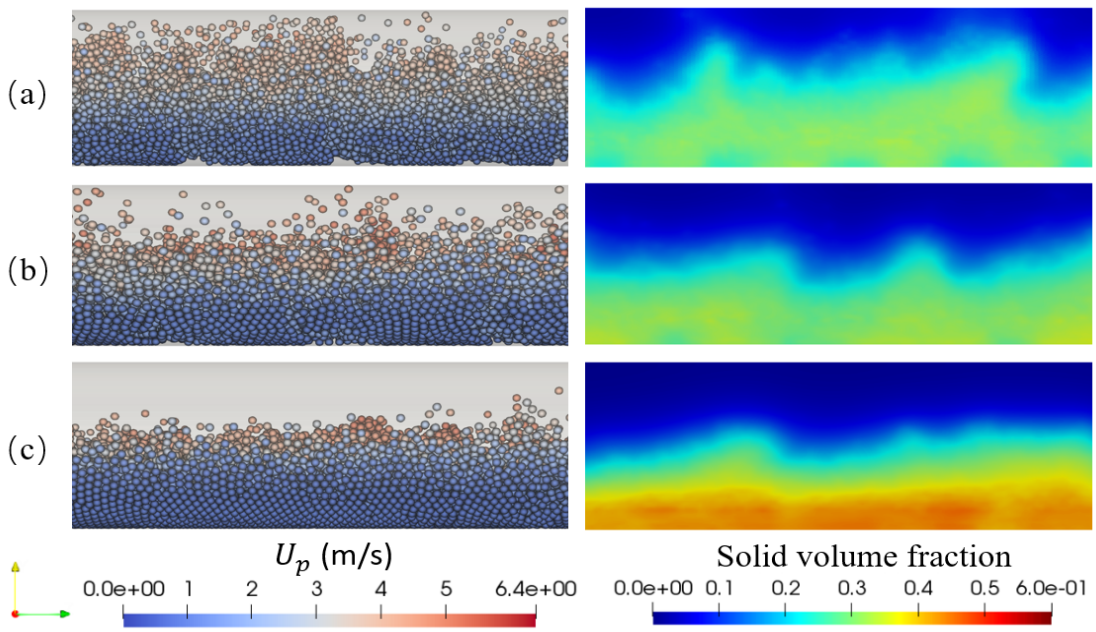

Fig. 6.48 Qualitative view of the flow and instantaneous concentration contour for flows with different pipe sizes (a) $44\ mm$ (b) $100\ mm$ and (c) $200\ mm$

Particles are more suspended in a small pipe while they settle more easily in a large pipe. A moving bed is observed in the flow of pipe diameter $200\ mm$. The corresponding concentration profiles are shown in Fig 6.49. To consider the effect of particle size on the flow in pipes of different diameters, an additional simulation with $d_p = 4.6mm$ in a $44\ mm$ pipe is conducted and compared with the flow in a $100\ mm$ pipe. The concentration profile is shown as in the red line in Fig 6.49. Consistent with the

findings in section 6.3.3, larger particles are more uniformly distributed for a flow with a constant in-line solids concentration. The results confirm that particles with the same size ($d_p = 4.6mm$) settle more easily in a $100mm$ pipe than in a $44mm$ pipe. Meanwhile, the ratio of delivered concentration to in-line concentration C_{vd}/C_v is 0.93, 0.90 and 0.76 for the pipe diameter $D = 44$, 100 and 200 mm, respectively.

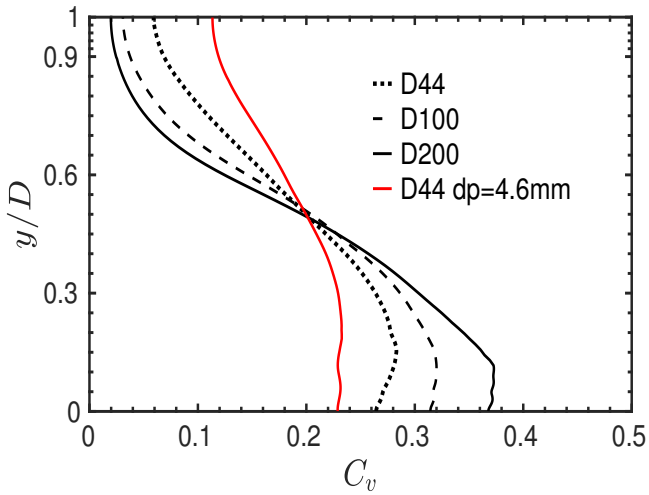

Fig. 6.49 Concentration profile on the vertical centreline of the pipe cross-section for flows with different pipe sizes and $d_p/D = 1/22$, except the red line where $d_p/D = 1/10$

6.4.2 Velocity distribution

The velocity profiles on the vertical centreline in the pipe-cross section for flows with different pipe sizes are shown in Fig 6.50. In the lower part of the pipe, the near wall velocity decreases with increasing pipe size. The lowest value is found in the flow with the largest pipe diameter (200 mm). As can be seen, the fluid velocity gradient near the top and bottom wall is much steeper in a small pipe. The suspended load above the bed layers in a small pipe also moves faster due to the sharper increase in velocity. In most of the central and upper regions, the velocity is higher in a large pipe because more particles have settled and damp of the flow in the upper part is less.

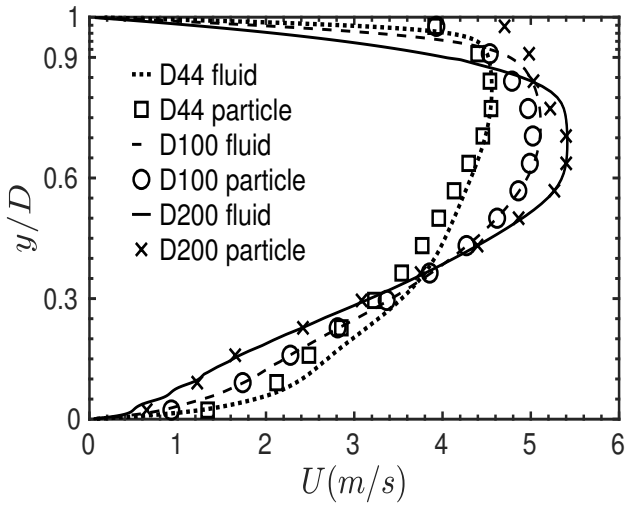

Fig. 6.50 Velocity profile on the vertical centreline in the pipe cross section for flows with different pipe sizes

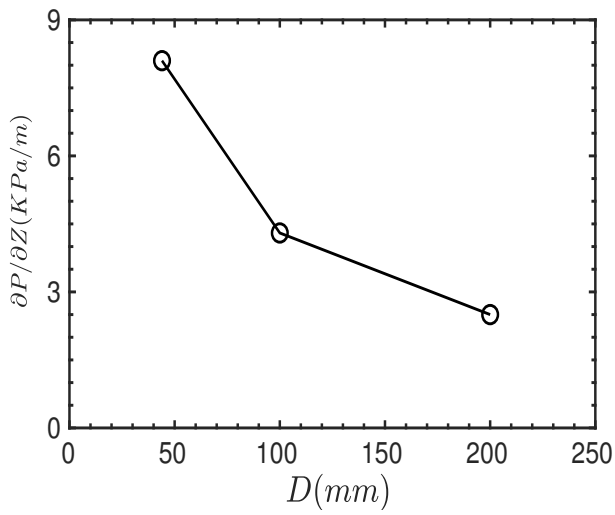

Fig. 6.51 Pressure drop for flows with different pipe sizes

6.4.3 Pressure drop

The pressure drop for flows with different pipe sizes is shown in Fig 6.51. As expected, the pressure drop decreases with increasing pipe diameter. The pressure drop reduces by 47% and 89% when increasing pipe diameter from 44 to 100 and 200 mm, respectively. Before running the simulation, an estimation of the pressure drop based on the Wilson-Thomas correlation [144] assuming a pseudo-homogeneous flow was made. The estimated values for these flows are 6.4, 3.3 and 1.9 KPa/m, respectively. These values are approximately 21%, 23% and 24% lower than those predicted by DNS-DEM as shown in Table 6.10. The difference is likely caused by the presence of the stratified bed layers

which are not considered in the Wilson-Thomas correlation. Particles concentrated at the bottom also increase particle-wall friction leading to higher pressure drop. This suggests it would be more appropriate to use a layer model to predict the pressure drop.

A non-Newtonian two-layer model [98, 107] has been found to work well in a laminar suspension flow. Subsequently a more advanced multi-component model [97] has been developed for both laminar and turbulent non-Newtonian suspensions, which includes a very fine fraction contributing to the viscosity of the carrier fluid, a homogeneously suspended fine fraction, a heterogeneous component and a settled bed of coarse particles. The total pressure gradient comprises the contribution from these components is calculated as in Eq.2.2. The model has been found to predict the pressure drop within the order of $10 \sim 15\%$ for various tested suspensions including a bimodal suspension of glass ballotini, a sand suspension conveyed in carbopol and tailings suspension in pipes of 100 and $150\ mm$ [97]. However, it is stated in [97] solids in most of these tested suspensions are small and don't fall into the stratified fraction ($d_p > 0.015D$). The prediction from the third component $\frac{dp}{dx}|_s$ needs further validation.

The solids in the simulations here are of $d_p/D = 1/22$, which fall into the stratified fraction. The calculation of pressure drop based on the multi-component model follows the same procedure as in [97]. The fine fraction X_e is 15%, and the other solids contribute to the stratified fraction X_s (85%). The estimated pressure drops based on the multi-component model are 9.6, 5.0 and $2.9\ KPa/m$, respectively. The values are higher than the predictions from DNS-DEM with deviations of 18.5%, 16.3% and 16.0%, respectively. The pressure drop estimations based on different models for flow with different pipe sizes are shown in Table 6.11 and Fig 6.52. A comparison of the pressure drop for one of the experimental flows in Sec 5.2 (Test 2, $C_v = 0.18$) is also shown. The multi-component model shows a better prediction (except Sec 5.2 Test 2) than the Wilson-Thomas correlation when comparing to values from DNS-DEM, as the pressure drop from the stratified load is also considered. In the multi-component model, an empirical value of $k_1 = 1.65$ accounting for the enhanced non-Newtonian effects is used. This empirical value may overestimate the pressure drop contribution from the non-Newtonian carrier, particularly when the carrier is less viscous (e.g., $\tau_y = 0.08Pa$, $k = 0.338Pa \cdot s^n$ and $n = 0.6$ in Sec 5.2 Test 2). A value of $k_1 \approx 1.4$ is found to fit well

with the DNS-DEM predictions for Sim No. 10, 18 & 19 and a lower value of $k_1 \approx 1.2$ for the Test 2.

Table 6.11 Pressure drop estimation based on different models for flows with different pipe sizes

Sim No.	Pipe Diameter $D(mm)$	DNS-DEM KPa/m	Multi-Component Model [97] KPa/m	Wilson-Thomas Correlation [144] KPa/m	Experiment KPa/m
No.10	44	8.1	9.6 (+19%)	6.4 (-21%)	N/A
No.18	100	4.3	5.0 (+16%)	3.3 (-23%)	N/A
No.19	200	2.5	2.9 (+16%)	1.9 (-24%)	N/A
Sec 5.2 Test 2	44	4.4 (+5%)	5.5 (+30%)	3.6 (-14%)	4.2

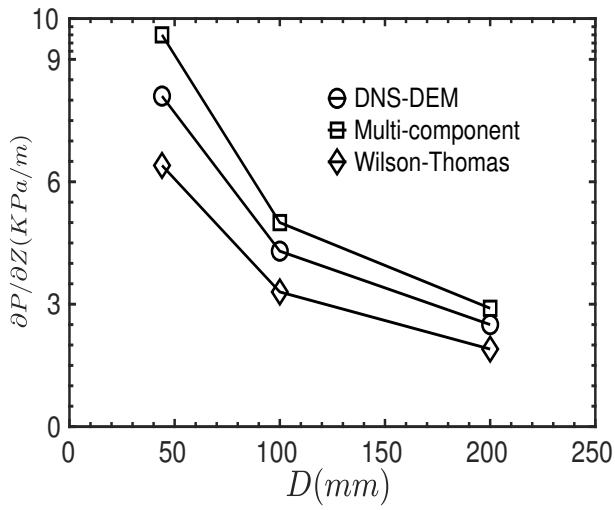

Fig. 6.52 Pressure drop estimation based on different models

To make the multi-component model [97] more accurate for pressure drop analysis, a larger database considering experimental and simulation data with different fractions of solids, particularly with solids falling in the stratified fraction is needed. Experimental data with coarse stratified solids in large pipes can also be used for additional validation of the DNS-DEM model. General trends for the empirical constants k_1, k_2 and k_3 with varied carrier rheology and solids properties need to be established. For scale-up, large pipe loops also need to be equipped with instrumentation for detecting the stratified flow so the model can be properly calibrated.

6.5 Chapter summary

The DNS-DEM model has been applied to investigate weakly turbulent coarse-particle non-Newtonian suspension flows. In particular how the carrier fluid rheology support particle suspensions, and how the interaction of turbulent eddies, yield stress and particle-particle interaction act together to produce different phenomenon compared to an equivalent Newtonian suspension have been considered. The conclusions and future work from this chapter are as follows:

- **Interaction of turbulent eddies, yield stress and coarse particles**

  The flows all displayed stratification and particles were able to settle in the weakly turbulent regime considered here. The flow did not become pseudo-homogeneous even in the presence of a sufficiently high yield stress ($25\ Pa$). Turbulence in the lower portion of the pipe was damped with the presence of concentrated particles and thus became ineffective in re-suspending the particles. Meanwhile, for a flow with a fixed pressure gradient, increasing the yield stress led to significantly reduced bulk velocity and turbulence intensity such that turbulent support could collapse completely leading to further stratification. However, results from pipe flows with different yield stresses and an equivalent bulk flow velocity indicated that higher yield stress did very slightly improve particle suspensions but at the cost of a higher pressure drop. A relatively stronger coupling between the fluid and particles was found for a higher yield stress, however this beneficial effect was compromised by the presence of weaker turbulence. The combined effect contributed to only slightly improved solids suspension in the flow with a higher yield stress.

- **Turbulent non-Newtonian vs Newtonian suspension**

  Heterogeneous flow and a sliding bed were present in a weakly turbulent non-Newtonian suspension, but the details and extent of the flow were different to those in Newtonian suspensions. The degree of packing in the stratified bed reduced compared to a Newtonian equivalent with the same mean wall viscosity. A non-Newtonian flow also displayed a better suspension at lower Re compared to a traditional water-sand slurry at a similar pipe & particle scale. However,

higher pressure gradient was required to obtain the same mixture flow rates as in a Newtonian suspension. A major difference between a Newtonian and non-Newtonian suspension was found in the force analysis on particles. The drag force was observed to be dominant in the central region in a non-Newtonian flow while particles in a Newtonian suspension were supported more by pressure gradient force and particle-particle collisions.

- **Flow regime, velocity and concentration distribution**

  The flow displayed stratification with a transition from particle suspension and saltation to a moving bed with increasing in-line solids concentration. For a pipe flow with a fixed pressure gradient, increasing the yield stress caused a more stratified flow. Meanwhile, particles were more suspended in a small pipe but settled more easily in a large pipe. The velocity profiles were generally asymmetrical about the horizontal centreline due to particle settling toward the lower part of the pipe. There was a gradual flattening of the velocity profile with increasing τ_y, decreasing n and higher solids concentration, and the core of the flow (where the maximum velocity lies) moved further upwards from the pipe centre. The particle phase generally followed the fluid but with a slightly lower velocity magnitude in the flow with a lower concentration ($C_v \leq 0.2$). At a higher concentration ($C_v = 0.3$ and 0.4), particle-particle collisions were significant and the two profiles approached each other more closely.

- **Secondary flow and force analysis on particles**

  For most flows, a time-mean secondary flow of two rotating cells was observed. The two symmetric rotating longitudinal vortices lifted fluid & particles vertically along the centreline and back down on the outside. The magnitude of the secondary flow was small at about $1 \sim 2\%$ of the mean bulk flow velocity. The secondary flow pattern moved upward with increasing τ_y and C_v. Particles were supported by both turbulent diffusion and inter-particle collisions. The major forces supporting the particles were the drag force, particle-particle/wall collisions and pressure gradient force. The presence of the viscous core region contributed to the dominant drag force on particles in the central region with correspondingly lower particle-particle collisions. At a very high concentration ($C_v = 0.4$), particle-particle collision

became dominant on the vertical centreline and improved solids suspension, but reduced turbulence to a very low level.

- **Pressure drop**

  The model predicted an increase in pressure drop with increasing yield stress, flow index or in-line solids concentration, and a decrease in pressure drop with increasing pipe diameter or particle diameter. Comparing to values from the DNS-DEM model, the multi-component model [97] showed a better prediction of the pressure drop than the Wilson-Thomas correlation [144], because the pressure drop from the stratified load was also considered in [97]. To make the multi-component model feasible for pressure drop analysis, general trends for the empirical constants k_1, k_2 and k_3 with a range of carrier rheology and solids properties need to be established.

- **Implications to real tailings suspension**

  Results in this study reveal it would be more appropriate to assume a heterogeneous flow or a sliding bed rather than a pseudo-homogeneous flow in designing a turbulent coarse-particle non-Newtonian suspension. For a real suspension, as the carrier degrades with lower yield stress or becomes more shear-thinning, less energy is required to pump the slurry but delivered concentration also decreases. The head loss is not sensitive to the coarse-particle size but flow with coarser particles would have a higher delivered concentration (given the same feed concentration). The comparison to an equivalent Newtonian suspension suggests when modifying existing Newtonian empirical correlations & layer models for description of non-Newtonian suspension behaviour, the local non-Newtonian rheology should be incorporated into these models to reflect the weaker turbulence and stronger coupling between the carrier and particles. The degree of packing in the stratified bed is different to a Newtonian equivalent. The extent of stratification is also different in small and large pipes. These differences should be accounted for in developing non-Newtonian versions of layer models.

  Although in-line concentration of 0.4 ($\sim 64\%$ by mass of coarse particles) requires much higher power for transportation and is not used in traditional transport operations, results here indicate going to an ultra high concentration is feasible

and more energy efficient in highly viscous non-Newtonian suspension where solids concentration approaches the packing conditions of the suspension. Effective solids suspension is observed in most positions in the flow with $C_v = 0.4$. At a very high concentration, particle-particle collision becomes dominant (at least on the vertical centreline) and improves solids suspension. The coarse particles occupy the entire pipe during the flow, despite stratification, the bed is not as densely packed. The flow mechanisms at ultra high concentrations are different from that described in two and three-layer models. A new modelling approach is needed for ultra high concentration suspensions and new criteria need to be established for the maximum packing concentration in the bed.

- **Limitation of the model and future work**

  The results for flows with high yield stress in this study require additional validation since the DNS-DEM model has only been validated in flows with $\tau_y < 5Pa$. It should be noted that drag correlations for particle bed in a shear-thinning fluid, particularly in a sheared flow are still unknown. In the DNS-DEM coupling, the drag correlation for particle bed in a Newtonian fluid is extended to the *HB* fluid as in Eq. 4.16. Though the model has captured the general trend of the effect of flow parameters in a non-Newtonian suspension, the extent of solids distribution and difference may vary from the results shown in this chapter. Drag correlations for a single sphere and particle clouds of different volume fractions in a sheared pseudo-plastic fluids should be investigated.

  The DNS-DEM model works in a weakly turbulent flow regime due to the DNS requirements of high resolution. The first step in this process has now been taken with the model developed in this thesis. Future work should develop suitable SGS models for LES of shear-thinning flow and adopt a similar coupling framework of LES-DEM to investigate turbulent non-Newtonian suspension at a higher Reynolds number. These models would be able to quantify the effect of different flow parameters on the suspension flow behaviour under a wide range of operating conditions.

7

Conclusion and Future Work

The interaction between non-Newtonian carrier and coarse particles in high concentration suspensions is still poorly understood, particularly in the transitional and turbulent flow regimes. This project presents a DNS-DEM model for investigating weakly turbulent coarse-particle non-Newtonian suspension flows. Turbulent Newtonian and non-Newtonian suspension experiments in a pipe were conducted for model validation. Suspension data including pressure drop, mixture flow rates and concentration profiles, as well as the visual observation of the flow were obtained for different flow regimes ranging from settled bed to suspended flow. The validated DNS-DEM model was subsequently applied to investigate turbulent non-Newtonian suspension behaviour. The effect of carrier fluid rheology (yield stress τ_y & flow index n), solids properties (particle size d_p & in-line concentration C_v) and pipe size on flow regime, pressure drop, velocity and concentration distribution in a turbulent non-Newtonian suspension flow were carried out to provide an extended understanding of high concentration suspensions. Corresponding responses to questions posed at the end of Chapter 2 are included in the conclusion.

7.1 Conclusion

7.1.1 DNS of shear-thinning non-Newtonian turbulence

In response to $Q1$, a flexible DNS approach for modelling the turbulent flow of shear-thinning non-Newtonian fluids was presented utilising the widely used open source CFD library OpenFOAM. Despite the lower second order discretisation schemes used in OpenFOAM, DNS results of Newtonian fluids predicted by OpenFOAM corresponded very well with the DNS reference (computed using a spectral element code, *Semtex*) and experimental data. The maximum error observed was 4.1% when predicting the mean velocity and turbulence intensities, and was usually less than 2% for turbulence statistics. For a shear-thinning fluid, OpenFOAM predicted the flow to be a little more transitional than the equivalent results from *Semtex*, with lower radial and azimuthal turbulence intensities and higher axial intensity. Despite this, the first and second order turbulence statistics differed by at most 16%, and usually much less. The discrepancy between the codes decreased as the Reynolds number increased, with a maximum difference of 10% for $Re_G = 7,500$. The results demonstrated that while OpenFOAM did not provide identical results to a high accuracy SEM-Fourier code for DNS of a non-Newtonian shear-thinning fluid, the results were quite reasonable with mean flow velocity and viscosity profiles being predicted to be almost the same. Even though there were discrepancies in the second order turbulence statistics, these were not large and would likely not affect predictions in this thesis where engineering accuracy is the desired outcome.

7.1.2 Newtonian suspensions and model validation

In response to $Q2$ & 4, a DNS-DEM model was developed for coarse-particle suspension flow via the Open Source package CFDEM, which coupled OpenFOAM and LIGGGHTS. The model was validated with weakly turbulent ($4,000 < Re < 15,000$) coarse-particle Newtonian suspension flow experiment. The predicted flows were qualitatively similar to experiments with the formation of a sliding bed (e.g. $Re = 6,100, C_v = 0.18$) and transition from sliding bed to partial suspension (e.g. $Re = 10,200, C_v = 0.15$). The predicted mixture velocity magnitude and concentration profiles were also in quite good quantitative agreement with the experimental results, particularly under flow conditions where particles were suspended with a small bed at the bottom. The concentration

profiles predicted were mostly less than 10% difference to ERT measurements and good agreement was always achieved at both the top & bottom in the pipe cross-section where the measuring electrodes were close. The maximum deviation was observed near the pipe centre for flows with a distinct sliding bed. The deviation may be due to the insufficient spatial resolution of the ERT in the experiment, especially near the centre of the reconstructed domain. Another possible reason was that part of the solid volume fraction in the bed had been diffused from the pipe bottom toward the central region due to the diffusion approach adopted in the DNS-DEM coupling (in response to $Q3$). Despite this inherent limitation of the diffusion method, it had little impact on the flow when there was no significant bed. The mean turbulence intensities were significantly damped by the presence of coarse particles, particularly in the streamwise direction. The mean flow of the particle phase resembled the fluid phase but generally had a higher fluctuation level due to their inertia. The force distribution revealed the particle-particle and particle-wall collision, the drag and pressure gradient force dominated the particle motion in forming the resulting distribution. The impact of lift, virtual mass and viscous force was negligible in both the axial and vertical direction.

7.1.3 Non-Newtonian suspensions and model validation

In contrast to a Newtonian suspension, the drag correlation for a packed bed in a Herschel-Bulkley (*HB*) fluid is unavailable, particularly for particles in a sheared *HB* flow. In the DNS-DEM coupling, the drag correlation for a sphere settling in a yield-stress fluid was incorporated into the Ergun and Wen-Yu drag model, while the effect of fluid volume fraction remained the same. This modification provided better agreement with experimental results than a simple modification of replacing Newtonian viscosity with the *HB* viscosity in the drag term. Despite the unknown drag correlation, as well as discrepancy caused from ERT measurements and diffusion approach, the predicted mixture flow rates and concentration profiles were all in good agreement with the extended drag model and mostly less than 10% difference. The results demonstrated the DNS-DEM model also worked well for non-Newtonian suspension flows with the extended drag model and was a promising development for investigating non-Newtonian suspension behaviour.

7.1.4 DNS-DEM investigation of non-Newtonian Suspensions

All the flows displayed some level of stratification and particles were able to settle in the weakly turbulent regime. The flow did not become pseudo-homogeneous even with the presence of a sufficiently high yield stress ($25\ Pa$). Turbulence in the lower portion of the pipe was damped with the presence of concentrated particles thus became ineffective in re-suspending the particles. Meanwhile, for flows with a fixed pressure gradient, increasing the yield stress led to significantly reduced turbulence intensity that resulted in collapse of turbulent support and a more stratified flow was observed. Results from pipe flows with different magnitude of yield stress but an equivalent bulk flow velocity indicated that higher yield stress did marginally improve particle suspensions but at the cost of a higher pressure drop. In response to $Q5$ & 6, for a flow with a higher yield stress, there was a relatively stronger coupling between the carrier fluid and particles. However, higher yield stress simultaneously led to further damping of the turbulence. The combined effect contributed to only slight improvement of solids suspension. The degree of packing in the stratified bed reduced compared to a Newtonian equivalent with the same mean wall viscosity. However, higher pressure gradient was required to obtain the same mixture flow rates as in a Newtonian suspension.

The DNS-DEM model predicted an increase in pressure drop with increasing yield stress, flow index or in-line solids concentration, and a decrease in pressure drop with increasing pipe diameter or particle diameter. The flow changed from a partial suspension and saltation to a moving bed with increasing in-line solids concentration. Meanwhile, particles were more suspended in a small pipe while they settled more easily in a large pipe. The velocity profiles were generally asymmetrical about the centreline due to particle settling in the lower portion. There was a gradual flattening of the velocity profile with increasing τ_y, increasing solids concentration or decreasing n, and the core of the flow (where the maximum velocity lies) moved further above the pipe centre. The presence of the viscous core region contributed to the dominance of drag force on particles in the central region with correspondingly lower particle-particle collisions. At a very high concentration ($C_v = 0.4$), particle-particle collision became dominant on the vertical centreline and consequently improved solids suspension. For most of the flows, a secondary flow of two symmetric rotating longitudinal vortices

was observed in a pipe cross-section, which lifted fluid & particles vertically along the centreline and back down outside.

7.1.5 Contribution

The DNS-DEM model developed in this thesis provides an ability to investigate high concentration coarse solids non-Newtonian suspensions in complex geometries. Results from this model presented here provide an extended understanding of the complex interaction between the non-Newtonian carrier and particle transport in high concentration suspensions occurring in a weakly turbulent regime. Compared to an experimental approach, the DNS-DEM model is able to quantify the effect of different flow parameters on the suspension flow behaviour under a wide range of operating conditions. By comparing the similarity and difference with equivalent Newtonian suspensions, such knowledge can be used to provide guidance on modifying existing empirical Newtonian correlations & stratified layer models and enable prediction of the non-Newtonian suspension behaviour with improved certainty and accuracy. Experimental data obtained in this project has contributed to filling the data gap in the weakly turbulent flow regime and is valuable for validation of other suspension models as well. This general-purpose DNS-DEM approach could also be adopted in applications with more complex geometries such as pumps, pipe bends, mixing vessels, and other process equipment.

7.2 Future work

Due to the intensive computation efforts required in DNS, the DNS-DEM studies are limited to mono-sized coarse particles in transitional and weakly turbulent ($Re < 15,000$) flow regimes. However, real tailings suspensions typically involve a broad size distribution, with existence of finer particles than those in this study. Real particles are non-spherical with irregular shapes as well. In addition, tailings suspension can occur in much more complex geometries such as in pipe fittings and inclined pipes. To extend this study to real tailings suspensions, the following recommendations are made:

- Future work could adopt a similar coupling framework as in the DNS-DEM and consider RANS/LES-DEM studies of turbulent non-Newtonian suspension at higher Reynolds number. The RANS/LES-DEM would be less computational intensive and

allow simulating flow cases with a much wider particle size distribution. To develop the non-Newtonian RANS/LES-DEM model, understanding of transition and turbulence in shear-thinning fluids is needed for deriving suitable wall functions for RANS and SGS model for LES.

- Non-sphericity of particles is a crucial factor in fluid-particle interaction but has often been neglected in CFD simulations. The OpenFOAM-CFDEM-LIGGHTS coupling framework is now feasible for non-spherical particles simulation with its superquadric shape particles module. Effect of the particle shapes on the flow regime transition, pressure drop and concentration distribution in non-Newtonian suspension should be investigated.

- OpenFOAM can reliably accommodate complex geometries using the finite volume approach with unstructured meshes. Future work could adopt the coupling framework and look at applications in geometries such as pipe bends and inclined pipes. Studies on the effect of inclination on pressure drop and concentration distribution in non-Newtonian suspensions are recommended. Results could be compared with predictions from current non-Newtonian layer models to test their accuracy.

In addition to these, the following aspects are worth consideration for further improvement of the DNS-DEM model:

- In the DNS-DEM coupling, the drag correlation for a packed bed in a Newtonian fluid was extended to *HB* fluid in this study. As mentioned previously, the drag correlation for a packed bed in a *HB* fluid is unavailable, particularly for particles in a sheared flow. Drag correlations for a single sphere as well as particle clouds of different volume fractions in a sheared power-law and *HB* fluids need to be investigated to develop more robust drag relationships. These could be derived through an immersed boundary method. These drag correlations, once available can be implemented into the force models in the CFD-DEM coupling method within the CFDEM framework.

- The DNS-DEM model applies the diffusion approach to deal with the presence of coarse particles in fine meshes, which is based on the theory that each particle influences the surrounding fluid over a small but non-zero distance. This suggests

that part of the solid volume fraction in the bed has been diffused out from the pipe bottom to the central region, leading to an overestimation of concentration in the centre. Future work may consider an alternative DNS-DEM coupling framework without applying the diffusion. The two-grid formulation [29] and big spherical cell [68] approach could possibly be adopted to deal with coarse particles in fine meshes. The difficulty associated with these methods is that searching for cells occupied by the multi-grid or big sphere can be difficult, particularly for those located in another processor. To implement these methods in the CFD-DEM solver, an algorithm for easy parallelization needs to be developed.

- In validating the DNS-DEM model, experimental measurements of mean fluid velocity profile, particle velocity profile and secondary flow were not available in this study and are difficult to measure. In dense suspension flow, it is challenging to measure particle and fluid velocities reliably due to loss of measuring signal integrity caused by particle induced diffraction, refraction and obscuration. These measurements are needed for further validation of the model and the reliability of potential techniques such as simultaneous fluid-particle PIV method, which combines refractive index matched-particle image velocimetry (RIM-PIV) for fluid velocity measurement and particle tracking velocimetry (PTV) for the particle velocity statistics needs to be verified for dense suspension flow.

References

[1] Adler, A., Boyle, A., Braun, F., Crabb, M. G., Grychtol, B., Lionheart, W. R., Tregidgo, H. F., and Yerworth, R. (2017). Eidors version 3.9. *Electrical Impedance Tomography*, 21:63.

[2] Aidun, C. K. and Clausen, J. R. (2010). Lattice-Boltzmann method for complex flows. *Annu. Rev. Fluid Mech.*, 42:439–472.

[3] Akhshik, S., Behzad, M., and Rajabi, M. (2015). CFD–DEM approach to investigate the effect of drill pipe rotation on cuttings transport behavior. *J. Petrol. Sci. Eng.*, 127:229–244.

[4] Alghalibi, D., Lashgari, I., Brandt, L., and Hormozi, S. (2018). Interface-resolved simulations of particle suspensions in Newtonian, shear-thinning and shear-thickening carrier fluids. *J. Fluid Mech.*, 852:329–357.

[5] Anderson, T. B. and Jackson, R. (1967). Fluid mechanical description of fluidized beds: Equations of motion. *Ind. Eng. Chem. Res*, 6:527–539.

[6] Arabi, A. S. and Sanders, R. S. (2016). Particle terminal settling velocities in non-Newtonian viscoplastic fluids. *Can. J. Chem. Eng.*, 94:1092–1101.

[7] Ardekani, M. N. and Brandt, L. (2019). Turbulence modulation in channel flow of finite-size spheroidal particles. *J. Fluid Mech.*, 859:887–901.

[8] Atapattu, D., Chhabra, R., and Uhlherr, P. (1995). Creeping sphere motion in Herschel-Bulkley fluids: flow field and drag. *J. Non-Newton. Fluid*, 59(2-3):245–265.

[9] Barigou, M., Fairhurst, P., Fryer, P., and Pain, J. (2003). Concentric flow regime of solid–liquid food suspensions: theory and experiment. *Chem. Eng. Sci.*, 58:1671–1686.

[10] Bartosik, A. (2010). Simulation of turbulent flow of a fine dispersive slurry. *Chem. Process Eng.*, 31(1):67–80.

[11] Bartosik, A. (2011). Mathematical modelling of slurry flow with medium solid particles. In *2nd International Conference on Mathematical Models for Engineering Science, Np*, pages 124–129.

[12] Benslimane, A., Bekkour, K., François, P., and Bechir, H. (2016). Laminar and turbulent pipe flow of bentonite suspensions. *J. Petrol. Sci. Eng.*, 139:85–93.

[13] Blackburn, H. M. and Sherwin, S. J. (2004). Formulation of a Galerkin spectral element–Fourier method for three-dimensional incompressible flows in cylindrical geometries. *J. Comput. Phys.*, 197(2):759–778.

[14] Blight, G. (2009). *Geotechnical engineering for mine waste storage facilities*. CRC Press.

[15] Buckingham, E. (1921). On plastic flow through capillary tubes. In *Proc. Am. Soc. Testing Materials*, pages 1154–1156.

[16] Capecelatro, J. and Desjardins, O. (2013). Eulerian–Lagrangian modeling of turbulent liquid–solid slurries in horizontal pipes. *Int. J. Multiph. Flow*, 55:64–79.

[17] Charles, M. and Charles, R. (1971). *Hydraulic transport of bulky materials*. Advances in Solid-Liquid Flow in Pipes and its Application.

[18] Chen, H., Xiao, Y., Liu, Y., and Shi, Y. (2017). Effect of young's modulus on dem results regarding transverse mixing of particles within a rotating drum. *Powder Technol.*, 318:507–517.

[19] Chhabra, R. and Richardson, J. (1985). Hydraulic transport of coarse particles in viscous Newtonian and non-Newtonian media in a horizontal pipe. *Chem. Eng. Res. Des.*, 63:390–397.

[20] Chhabra, R. P. and Richardson, J. F. (1999). *Non-Newtonian flow in the process industries: fundamentals and engineering applications*. Butterworth-Heinemann.

[21] Childs, L., Hogg, A., and Pritchard, D. (2016). Dynamic settling of particles in shear flows of shear-thinning fluids. *J. Non-Newton. Fluid*, 238:158–169.

[22] Cooke, R. (2002). Laminar flow settling: the potential for unexpected problems. In *British Hydromechanics Research Group 15th International Conference on Slurry Handling and Pipeline Transport HYDROTRANSPORT*, volume 15, pages 121–133.

[23] Courant, R., Friedrichs, K., and Lewy, H. (1967). On the partial difference equations of mathematical physics. *IBM J. Res. Dev.*, 11(2):215–234.

[24] Crowe, C., Troutt, T., and Chung, J. (1996). Numerical models for two-phase turbulent flows. *Annu. Rev. Fluid Mech.*, 28:11–43.

[25] Cullen, P. J. (2009). *Food mixing: principles and applications*. John Wiley & Sons.

[26] Cundall, P. A. and Strack, O. D. (1979). A discrete numerical model for granular assemblies. *Geotechnique*, 29:47–65.

[27] De Angelis, E., Casciola, C., and Piva, R. (2002). DNS of wall turbulence: dilute polymers and self-sustaining mechanisms. *Comput. Fluids*, 31(4-7):495–507.

[28] de Gennes, P. G. (1999). Granular matter: a tentative view. *Rev. Mod. Phys.*, 71:S374.

[29] Deb, S. and Tafti, D. K. (2013). A novel two-grid formulation for fluid–particle systems using the discrete element method. *Powder technol.*, 246:601–616.

[30] Doron, P. and Barnea, D. (1993). A three-layer model for solid-liquid flow in horizontal pipes. *Int. J. Multiph. Flow*, 19(6):1029–1043.

[31] Duckworth, R., Pullum, L., Addie, G., and Lockyear, C. (1986). Pipeline transport of coarse materials in a non-Newtonian carrier fluid. In *Hydrotransport 10 : 10th International Conference on the Hydraulic Transport of Solids in Pipes*.

[32] Eesa, M. and Barigou, M. (2008). Horizontal laminar flow of coarse nearly-neutrally buoyant particles in non-Newtonian conveying fluids: CFD and PEPT experiments compared. *Int. J. Multiph. Flow*, 34:997–1007.

[33] Eesa, M. and Barigou, M. (2009). CFD investigation of the pipe transport of coarse solids in laminar power-law fluids. *Chem. Eng. Sci.*, 64:322–333.

[34] Ekambara, K., Sanders, R. S., Nandakumar, K., and Masliyah, J. H. (2009). Hydrodynamic simulation of horizontal slurry pipeline flow using ANSYS-CFX. *Ind. Eng. Chem. Res.*, 48:8159–8171.

[35] Ergun, S. (1952). Fluid flow through packed columns. *Chem. Eng. Prog.*, 48:89–94.

[36] Escudier, M. and Presti, F. (1996). Pipe flow of a thixotropic liquid. *J. Non-Newton. Fluid*, 62(2-3):291–306.

[37] Escudier, M., Presti, F., and Smith, S. (1999). Drag reduction in the turbulent pipe flow of polymers. *J. Non-Newton. Fluid*, 81(3):197–213.

[38] Fairhurst, P., Barigou, M., Fryer, P., Pain, J., and Parker, D. (2001). Using positron emission particle tracking (PEPT) to study nearly neutrally buoyant particles in high solid fraction pipe flow. *Int. J. Multiph. Flow*, 27(11):1881–1901.

[39] Fornari, W., Picano, F., and Brandt, L. (2018). The effect of polydispersity in a turbulent channel flow laden with finite-size particles. *Eur. J. Mech.*, 67:54–64.

[40] Ge, W. and Li, J. (2003). Macro-scale phenomena reproduced in microscopic systemspseudo-particle modeling of fluidization. *Chem. Eng. Sci.*, 58(8):1565–1585.

[41] Ge, W., Wang, L., Xu, J., Chen, F., Zhou, G., Lu, L., Chang, Q., and Li, J. (2017). Discrete simulation of granular and particle-fluid flows: from fundamental study to engineering application. *Rev. Chem. Eng.*, 33(6):551–623.

[42] Germano, M., Piomelli, U., Moin, P., and Cabot, W. H. (1991). A dynamic subgrid-scale eddy viscosity model. *Phys. Fluids A: Fluid Dyn.*, 3(7):1760–1765.

[43] Ghosh, T. and Shook, C. (1990). Transport of coarse particles in power-law fluids. In *Freight Pipelines: Proceedings of the 6th International Symposium on Freight Pipelines*. Taylor & Francis.

[44] Gidaspow, D. (1994). *Multiphase flow and fluidization: continuum and kinetic theory descriptions*. Academic press.

[45] Giguere, R., Fradette, L., Mignon, D., and Tanguy, P. (2008). Characterization of slurry flow regime transitions by ert. *Chem. Eng. Res. Des.*, 86:989–996.

[46] Gillies, R. and Shook, C. (1994). Concentration distributions of sand slurries in horizontal pipe flow. *Particul. Sci. Technol.*, 12:45–69.

[47] Gillies, R., Shook, C., and Wilson, K. (1991). An improved two-layer model for horizontal slurry pipeline flow. *Can. J. Chem. Eng.*, 69(1):173–178.

[48] Gillies, R., Sun, R., Sanders, R., and Schaan, J. (2007). Lowered expectations: the impact of yield stress on sand transport in laminar, non-Newtonian slurry flows. *J. S. Afr. I. Min. Metall.*, 107(6):351–357.

[49] Gillies, R. G. (1993). *Pipeline flow of coarse particle slurries*. University of Saskatchewan Saskatoon, SK.

[50] Gillies, R. G., Shook, C. A., and Xu, J. (2004). Modelling heterogeneous slurry flows at high velocities. *Can. J. Chem. Eng.*, 82:1060–1065.

[51] Gnambode, P., Orlandi, P., Ould-Rouiss, M., and Nicolas, X. (2015). Large-eddy simulation of turbulent pipe flow of power-law fluids. *Int. J. Heat Fluid Fl.*, 54:196–210.

[52] Goniva, C., Kloss, C., Deen, N. G., Kuipers, J. A., and Pirker, S. (2012). Influence of rolling friction on single spout fluidized bed simulation. *Particuology*, 10:582–591.

[53] Gopaliya, M. K. and Kaushal, D. (2016). Modeling of sand-water slurry flow through horizontal pipe using CFD. *J. Hydrol. Hydromech.*, 64:261–272.

[54] Gradeck, M., Fagla, B., Baravian, C., and Lebouché, M. (2005). Experimental thermomechanic study of Newtonian and non-Newtonian suspension flows. *Int. J. Heat Mass Tran.*, 48:3469–3477.

[55] Gui, N., Fan, J. R., and Chen, S. (2010). Numerical study of particle–particle collision in swirling jets: A DEM–DNS coupling simulation. *Chem. Eng. Sci.*, 65:3268–3278.

[56] Hallbom, D. J. (2008). *Pipe flow of homogeneous slurry*. PhD thesis, University of British Columbia.

[57] Hill, K. B. and Shook, C. A. (1998). Pipeline transport of coarse particles by water and by fluids with yield stresses. *Particul. Sci. Technol.*, 16(2):163–183.

[58] Holder, D. (2004). *Electrical impedance tomography: methods, history and applications*. CRC Press.

[59] Hsu, T.-J., Jenkins, J. T., and Liu, P. L.-F. (2003). On two-phase sediment transport: Dilute flow. *J. Geophys. Res. Oceans*, 108(C3).

[60] Hughmark, G. A. (1977). Turbulence properties in the core of pipe flow. *Ind. Eng. Chem.*, 16(2):307–308.

[61] Ishii, M. and Mishima, K. (1984). Two-Fluid model and hydrodynamic constitutive relations. *Nucl. Eng. Des.*, 82:107–126.

[62] Jha, S. K. and Bombardelli, F. A. (2009). Two-phase modeling of turbulence in dilute sediment-laden, open-channel flows. *Environ. Fluid Mech.*, 9(2):237.

[63] Jones, H. and Boger, D. V. (2012). Sustainability and waste management in the resource industries. *Ind. Eng. Chem.*, 51:10057–10065.

[64] Kempe, T., Vowinckel, B., and Fröhlich, J. (2014). On the relevance of collision modeling for interface-resolving simulations of sediment transport in open channel flow. *Int. J. Multiph. Flow*, 58:214–235.

[65] Kloss, C., Goniva, C., Hager, A., Amberger, S., and Pirker, S. (2012). Models, algorithms and validation for opensource DEM and CFD–DEM. *Prog. Comput. Fluid Dy.*, 12:140–152.

[66] Komen, E., Shams, A., Camilo, L., and Koren, B. (2014). Quasi-DNS capabilities of OpenFOAM for different mesh types. *Comput Fluids*, 96:87–104.

[67] Krampa-Morlu, F., Bergstrom, D., Bugg, J., Sanders, R., and Schaan, J. (2004). Numerical simulation of dense coarse particle slurry flows in a vertical pipe. In *5th International Conference on Multiphase flow, ICMF*, volume 4.

[68] Kuang, S., Chu, K., Yu, A., Zou, Z., and Feng, Y. (2008). Computational investigation of horizontal slug flow in pneumatic conveying. *Ind. Eng. Chem.*, 47:470–480.

[69] Kuang, S., Zhou, M., and Yu, A. (2020). CFD-DEM modelling and simulation of pneumatic conveying: A review. *Powder Technol.*, 365:186–207.

[70] Lali, A., Khare, A., Joshi, J., and Nigam, K. (1989). Behaviour of solid particles in viscous non-Newtonian solutions: settling velocity, wall effects and bed expansion in solid-liquid fluidized beds. *Powder Technol.*, 57:39–50.

[71] Lashgari, I., Picano, F., Breugem, W.-P., and Brandt, L. (2014). Laminar, turbulent, and inertial shear-thickening regimes in channel flow of neutrally buoyant particle suspensions. *Phys. Rev. Lett.*, 113:254502.

[72] Li, J., Ge, W., Wang, W., Yang, N., Liu, X., Wang, L., He, X., Wang, X., Wang, J., and Kwauk, M. (2013). *From multiscale modeling to meso-science*. Springer.

[73] Li, X. and Zhao, J. (2018). Dam-break of mixtures consisting of non-Newtonian liquids and granular particles. *Powder Technol.*, 338:493–505.

[74] Lilly, D. K. (1992). A proposed modification of the germano subgrid-scale closure method. *Phys. Fluids A: Fluid Dyn.*, 4(3):633–635.

[75] Link, J., Cuypers, L., Deen, N., and Kuipers, J. (2005). Flow regimes in a spout–fluid bed: A combined experimental and simulation study. *Chem. Eng. Sci.*, 60:3425–3442.

[76] Liu, G. (2018). Application of the Two-Fluid model with kinetic theory of granular flow in liquid–solid fluidized beds. *Granularity in Materials Science*, pages 2–24.

[77] Loth, E. and Dorgan, A. J. (2009). An equation of motion for particles of finite Reynolds number and size. *Environ. Fluid Mech.*, 9(2):187–206.

[78] Malin, M. (1997). Turbulent pipe flow of power-law fluids. *Int. Commun. Heat Mass*, 24(7):977–988.

[79] Matousek, V. (1999). *Flow mechanism of sand-water mixtures in pipelines.* PhD thesis, Technische Universiteit Delft.

[80] Mehta, D., Thota Radhakrishnan, A. K., Van Lier, J., and Clemens, F. (2018). A wall boundary condition for the simulation of a turbulent non-Newtonian domestic slurry in pipes. *Water*, 10(2):124.

[81] Mei, R. (1992). An approximate expression for the shear lift force on a spherical particle at finite Reynolds number. *Int. J. Multiph. Flow*, 18(1):145–147.

[82] Messa, G. V. and Malavasi, S. (2015). Improvements in the numerical prediction of fully-suspended slurry flow in horizontal pipes. *Powder Technol.*, 270:358–367.

[83] Mikula, R. (2012). Advances in oil sands tailings handling: building the base for reclamation. *Restoration and Reclamation of Boreal Ecosystems: Attaining Sustainable Development*, pages 103–22.

[84] Mishra, S., Chandra, H., and Arora, A. (2012). Solid liquid non-Newtonian fluid flow in pipe: a review. *Acta Mech. Slovaca.*, 16:62–73.

[85] Nie, D. and Lin, J. (2015). Behavior of three circular particles in a confined power-law fluid under shear. *J. Non-Newton. Fluid*, 221:76–94.

[86] Norouzi, H. R., Zarghami, R., Sotudeh-Gharebagh, R., and Mostoufi, N. (2016). *Coupled CFD-DEM modeling: formulation, implementation and application to multiphase flows*. John Wiley & Sons.

[87] Ohta, T. and Miyashita, M. (2014). DNS and LES with an extended Smagorinsky model for wall turbulence in non-Newtonian viscous fluids. *J. Non-Newton. Fluid*, 206:29–39.

[88] Ovarlez, G., Bertrand, F., Coussot, P., and Chateau, X. (2012). Shear-induced sedimentation in yield stress fluids. *J. Non-Newton. Fluid*, 177:19–28.

[89] Pěník, V., Kesely, M., and Matoušek, V. (2016). Coarse particle support in turbulent flow of visco-plastic carrier. In *EPJ Web of Conferences*, volume 114. EDP Sciences.

[90] Picano, F., Breugem, W. P., and Brandt, L. (2015). Turbulent channel flow of dense suspensions of neutrally buoyant spheres. *J. Fluid Mech.*, 764:463–487.

[91] Pinho, F. and Whitelaw, J. (1990). Flow of non-Newtonian fluids in a pipe. *J. Non-Newton. Fluid*, 34(2):129–144.

[92] Pinto, T. S., Junior, D. M., Slatter, P., and Leal Filho, L. (2014). Modelling the critical velocity for heterogeneous flow of mineral slurries. *Int. J. Multiph. Flow*, 65:31–37.

[93] Pirker, S., Kahrimanovic, D., and Goniva, C. (2011). Improving the applicability of discrete phase simulations by smoothening their exchange fields. *Appl. Math.*, 35:2479–2488.

[94] Plimpton, S. (1993). Fast parallel algorithms for short-range molecular dynamics. Technical report, Sandia National Labs., Albuquerque, NM, United States.

[95] Pullum, L. (2009). Settling of coarse particles in visco-plastic fluids during pipeline transport. In *6th International Conference for Conveying and Handling of Particulate Solids, Brisbane Convention & Exhibition Centre, Queensland, Australia*.

[96] Pullum, L., Boger, D. V., and Sofra, F. (2018). Hydraulic mineral waste transport and storage. *Annu. Rev. Fluid Mech.*, 58:157–185.

[97] Pullum, L., Chryss, A., Graham, L., Matoušek, V., and Pěník, V. (2015). Modelling turbulent transport of solids in non-Newtonian carrier fluids applicable to tailings disposal. In *12th International conference on Transport and Sedimentation of Solid Particles, Delft, Netherlands*, pages 22–25.

[98] Pullum, L., Graham, L., and Slatter, P. (2004). A non-Newtonian two-layer model and its application to high density hydrotransport. In *Proc. of Hydrotransport*, volume 16, pages 579–593.

[99] Qi, Z., Kuang, S., Qiu, T., and Yu, A. (2020). Lattice-Boltzmann investigation on fluid flows through packed beds: Interaction between fluid rheology and bed properties. *Powder technol.*, 369:248–260.

[100] Qi, Z., Kuang, S., and Yu, A. (2019). Lattice-Boltzmann investigation of non-Newtonian fluid flow through a packed bed of uniform spheres. *Powder technol.*, 343:225–236.

[101] Radl, S., Gonzales, B. C., Goniva, C., and Pirker, S. (2015). State of the art in mapping schemes for dilute and dense Euler-Lagrange simulations. In *SINTEF Proceedings*. SINTEF Academic Press.

[102] Rasteiro, M., Figueiredo, M., and Franco, H. (1993). Pressure drop for solid/liquid flow in pipes. *Particul. Sci. Technol.*, 11:147–155.

[103] Rasti, E., Talebi, F., and Mazaheri, K. (2017). A DNS investigation of drag reduction phenomenon in turbulent flow of a viscoelastic fluid. *J. Solid Fluid Mech.*, 7(1):255–274.

[104] Righetti, M. and Romano, G. P. (2004). Particle–fluid interactions in a plane near-wall turbulent flow. *J. Fluid Mech.*, 505:93–121.

[105] Ro, K. and Ryou, H. (2012). Development of the modified $k - \epsilon$ turbulence model of power-law fluid for engineering applications. *Sci. China Technol. Sci.*, 55(1):276–284.

[106] Roco, M. and Shook, C. (1984). Model for turbulent slurry flow. *Journal of pipelines*, 4(1):3–13.

[107] Rojas, M. R. and Saez, A. E. (2012). Two-layer model for horizontal pipe flow of Newtonian and non-Newtonian settling dense slurries. *Ind. Eng. Chem. Res.*, 51(20):7095–7103.

[108] Rudman, M. and Blackburn, H. M. (2006). Direct numerical simulation of turbulent non-Newtonian flow using a spectral element method. *Appl. Math. Model.*, 30(11):1229–1248.

[109] Rudman, M., Blackburn, H. M., Graham, L. J., and Pullum, L. (2004). Turbulent pipe flow of shear-thinning fluids. *J. Non-Newton. Fluid*, 118(1):33–48.

[110] Saffman, P. (1965). The lift on a small sphere in a slow shear flow. *J. Fluid Mech.*, 22(2):385–400.

[111] Sanders, R., Sun, R., Gillies, R., McKibben, M., Litzenberger, C., and Shook, C. (2004). Deposition velocities for particles of intermediate size in turbulent flow. In *Hydrotransport*, volume 16, pages 429–442.

[112] Sarabian, M., Rosti, M. E., Brandt, L., and Hormozi, S. (2020). Numerical simulations of a sphere settling in simple shear flows of yield stress fluids. *J. Fluid Mech.*, 896:A17.

[113] Sawko, R. (2012). *Mathematical and computational methods of non-Newtonian, multiphase flows*. PhD thesis, Cranfield University.

[114] Sethuraman, L. (2020). *Particle settling in sheared non-Newtonian fluids*. PhD thesis, Monash University.

[115] Shah, S. N. and Lord, D. L. (1991). Critical velocity correlations for slurry transport with non-Newtonian fluids. *AIChE J.*, 37:863–870.

[116] Shirgaonkar, A. A., MacIver, M. A., and Patankar, N. A. (2009). A new mathematical formulation and fast algorithm for fully resolved simulation of self-propulsion. *J. Comput. Phys.*, 228(7):2366–2390.

[117] Shook, C. A., Gillies, R. G., and Sanders, R. S. S. (2002). *Pipeline hydrotransport: With applications in the oil sand industry*. SRC Pipe Flow Technology Centre.

[118] Shook, C. A. and Roco, M. C. (2015). *Slurry flow: principles and practice*. Elsevier.

[119] Silva, R., Garcia, F. A., Faia, P. M., and Rasteiro, M. G. (2015). Settling suspensions flow modelling: a review. *Kona Powder and Particle Journal*, 32:41–56.

[120] Singh, J., Rudman, M., and Blackburn, H. (2017). The influence of shear-dependent rheology on turbulent pipe flow. *J. Fluid Mech.*, 822:848–879.

[121] Singh, J., Rudman, M., Blackburn, H. M., Chryss, A., Pullum, L., and Graham, L. J. (2016). The importance of rheology characterization in predicting turbulent pipe flow of generalized Newtonian fluids. *J. Non-Newton. Fluid*, 232:11–21.

[122] Smith, K., Davidson, M., and Lawson, N. (2000). Dispersion of neutrally buoyant solids falling vertically into stationary liquid and horizontal channel flow. *Comput Fluids*, 29(4):369–384.

[123] Smuts, E. M. (2015). *A methodology for coupled CFD-DEM modeling of particulate suspension rheology*. PhD thesis, University of Cape Town.

[124] Summer, R., McKibben, M., and Shook, C. (1990). Concentration and velocity distributions in turbulent vertical slurry flows. *Ecoulements Solide-Liquide*, 2(2):33–42.

[125] Sun, R. and Xiao, H. (2016). SediFoam: A general-purpose, open-source CFD–DEM solver for particle-laden flow with emphasis on sediment transport. *Comput. Geosci.*, 89:207–219.

[126] Tabuteau, H., Coussot, P., and de Bruyn, J. R. (2007). Drag force on a sphere in steady motion through a yield-stress fluid. *J. Rheol.*, 51(1):125–137.

[127] Talmon, A. and Mastbergen, D. (2004). Solids transport by drilling fluids: Concentrated bentonite-sand-slurries. In *Proceedings of the 12th International Conference on Transport and Sedimentation of Solid Particles, Institute of Hydrodynamics, Academy of Sciences of the Czech Republic, Prague*, pages 641–649.

[128] Thévenin, D., Behrendt, F., Maas, U., Przywara, B., and Warnatz, J. (1996). Development of a parallel direct simulation code to investigate reactive flows. *Comput. Fluids*, 25(5):485–496.

[129] Thomas, A., Pullum, L., and Wilson, K. (2004). Stabilised laminar slurry flow: review, trends and prognosis. In *Proc. 16th Int. Conf. Hydraulic Transport of Solids: HYDROTRANSPORT*, volume 16, pages 701–716.

[130] Thomas, A. and Wilson, K. (1987). New analysis of non-Newtonian turbulent flowndashyield-power-law fluids. *Can. J. Chem. Eng.*, 65(2):335–338.

[131] Toghraie, D., Esfahani, N. N., Zarringhalam, M., Shirani, N., and Rostami, S. (2020). Blood flow analysis inside different arteries using non-Newtonian Sisko model for application in biomedical engineering. *Comput, Meth. Prog. Bio.*, 190:105338.

[132] Treinen, J. M. (2017). *Modelling transport and deposition of coarse particles in viscoplastic tailings beach flows*. PhD thesis, University of Colorado at Boulder.

[133] Tripathi, A., Chhabra, R. P., and Sundararajan, T. (1994). Power law fluid flow over spheroidal particles. *Ind. Eng. Chem.*, 33(2):403–410.

[134] Tsuji, Y., Tanaka, T., and Ishida, T. (1992). Lagrangian numerical simulation of plug flow of cohesionless particles in a horizontal pipe. *Powder Technol.*, 71:239–250.

[135] Tsukahara, T., Ishigami, T., Yu, B., and Kawaguchi, Y. (2011). DNS study on viscoelastic effect in drag-reduced turbulent channel flow. *J. Turbul.*, 12(13):1–25.

[136] Uzi, A. and Levy, A. (2018). Flow characteristics of coarse particles in horizontal hydraulic conveying. *Powder Technol.*, 326:302–321.

[137] Wang, L., Wu, C., and Ge, W. (2017). Effect of particle clusters on mass transfer between gas and particles in gas-solid flows. *Powder Technol.*, 319:221–227.

[138] Wang, L., Zhang, B., Wang, X., Ge, W., and Li, J. (2013). Lattice-Boltzmann based discrete simulation for gas-solid fluidization. *Chem. Eng. Sci.*, 101:228–239.

[139] Wen, C. and Yu, Y. (1966). Mechanics of fluidization. In *Chem. Eng. Prog. Symp. Ser.*, volume 62, pages 100–111.

[140] Wilson, K. (1976). A unified physically-based analysis of solid-liquid pipeline flow. In *Proc. Hydrotransport*, volume 4, pages 1–16. BHRA Cranfield, UK.

[141] Wilson, K. and Horsley, R. (2004). Calculating fall velocities in non-Newtonian (and Newtonian) fluids: a new view. In *Proc. Hydrotransport*, volume 16, pages 37–46.

[142] Wilson, K., Horsley, R., Kealy, T., Reizes, J., and Horsley, M. (2003). Direct prediction of fall velocities in non-Newtonian materials. *Int. J. Miner. Pprocess.*, 71(1-4):17–30.

[143] Wilson, K. C., Addie, G. R., Sellgren, A., and Clift, R. (2006). *Slurry transport using centrifugal pumps*. Springer Science & Business Media.

[144] Wilson, K. C. and Thomas, A. D. (1985). A new analysis of the turbulent flow of non-Newtonian fluids. *Can. J. Chem. Eng.*, 63(4):539–546.

[145] WISE (2016). *Chronology of major tailings dam failures*. WISE Uranium Project.

[146] Wu, B. (2011). CFD investigation of turbulence models for mechanical agitation of non-Newtonian fluids in anaerobic digesters. *Water Res.*, 45(5):2082–2094.

[147] Xu, B. and Yu, A. (1997). Numerical simulation of the gas-solid flow in a fluidized bed by combining discrete particle method with computational fluid dynamics. *Chem. Eng. Sci.*, 52:2785–2809.

[148] Yu, Z. and Fan, L.-S. (2010). Lattice-Boltzmann method for simulating particle–fluid interactions. *Particuology*, 8(6):539–543.

[149] Zheng, E., Rudman, M., Kuang, S., and Chryss, A. (2020). Turbulent coarse-particle suspension flow: measurement and modelling. *Powder Technol.*, 373:647–659.

[150] Zhou, M., Wang, S., Kuang, S., Luo, K., Fan, J., and Yu, A. (2019). CFD-DEM modelling of hydraulic conveying of solid particles in a vertical pipe. *Powder Technol.*, 354:893–905.

[151] Zhou, Z., Kuang, S., Chu, K., and Yu, A. (2010). Discrete particle simulation of particle–fluid flow: model formulations and their applicability. *J. Fluid Mech.*, 661:482–510.

[152] Zhu, H. and Yu, A. (2002). Averaging method of granular materials. *Phys. Rev. E.*, 66:021302.

[153] Zhu, H., Zhou, Z., Yang, R., and Yu, A. (2007). Discrete particle simulation of particulate systems: theoretical developments. *Chem. Eng. Sci.*, 62:3378–3396.

A

Experimental Procedure

A.1 Pipe loop

The pipeline is composed of sections of $44\ mm$ I.D. PVC pipe and 2 sections of transparent acrylic tubes with square sides for undistorted visualisation. The length of the horizontal pipe section is $6\ m$ (as shown in Fig A.1). The pipe rig is operated as a closed circuit and slurry goes directly back to the feed tank after travelling through the pipeline system. The pipe loop contains the following components:

- Two MAGFLO MAG 6000 electromagnetic flow meters for measuring the mixture flowrate, U_m, based on the voltage induced by flow through a magnetic field
- Two sets of differential pressure transducers for measuring the pressure drop over pipe lengths of $1.5\ m$ and $2\ m$, respectively
- An ITS p2000 Electrical Resistance Tomography (ERT) system for measuring the solid concentration distribution in the pipe cross-section. An ERT ring is installed along the transparent acrylic horizontal tube with 16 electrodes for obtaining a tomogram of conductivity distribution
- A Coriolis mass flow meter for estimating the slurry density and in-line concentration. The Coriolis mass flow meter measures the mass flow rate based on the

phase shift (proportional to the mass flow momentum change) caused by the tube vibration or twist as flow passes through

- Transparent acrylic tubes for visual inspection of the flow, where flow regime (e.g. settled bed, sliding bed, etc.) is easily determined
- A temperature probe installed in the vertical invert pipe for slurry temperature measurements
- A feed tank for mixture preparation. The tank is of diameter $900\ mm$ and volume $800\ L$.
- A centrifugal pump with variable speed drive.

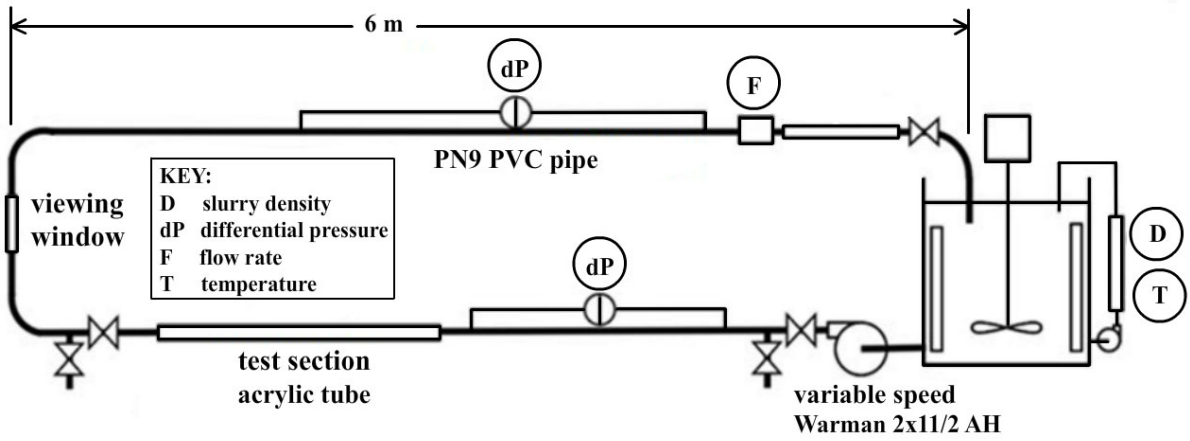

Fig. A.1 Experimental pipe loop

A.2 Flow conditions and test procedures

The Newtonian slurry is prepared using a Glycerol solution ($65wt\%$) as the carrier fluid and glass beads added at different concentrations ($15\% \sim 22\% v/v$). The glass beads are mono-dispersed with a diameter $d_p = 2 \pm 0.2\ mm$ and density $\rho_p = 2600 kg/m^3$. The non-Newtonian slurry is prepared using $0.1\% wt$ Carbopol (mixed with water and pH neutralised) solution as the carrier fluid and mono-dispersed glass beads of the same size ($10\% \sim 20\% v/v$). The experimental procedure is as follows:

- Clean the pipe loop with water. This ensures the pipe loop is not contaminated from previous carriers.

- Add the required amount of carrier (Glycerol or Carbopol solution) in the tank. For the Carbopol solution, water is firstly added into the tank. The Carbopol is then added with the stirrer running on low. The stirrer is left on for a few hours to mix the solution. Sodium hydroxide is added to neutralise the Carbopol solution (pH = 7.0).

- A typical test run starts with a low solid volume fraction, measurements are taken for one designed concentration over a range of velocities. Measurements are logged and processed in a computerised data acquisition system at a frequency of $12\ Hz$. The collected data includes the time, logging interval, pressure drop, volumetric flow rate, mass flow rate and temperature. Afterwards, the solid concentration is increased by adding more solids into the mixing tank and measurements are repeated at higher concentration.

- For each test, the ITS P2000 takes 200 frames of the voltage measurements at an injection current $1\ mA$ and frequency $9600\ Hz$. The data is post-processed in the EIDORS software package [1] to reconstruct the conductivity distribution. Video measurements are taken simultaneously during ERT measurements.

- Slurry samples are collected both before and after each test for rheology measurements on the carrier fluid (solids removed) using a Haake Rheostress RS1 rheometer. Rheology measurements for the Carbopol solution at shear rate $\dot{\gamma}$ up to $20,000$ in a combined Couette and parallel plate geometries are conducted. The rheology measurements of the tests are presented in Appendix C.

B

Coarse-Particle Suspension Data

B.1 Test series: Newtonian-Glyc-120219

B.1.1 Glycerol solution $65\%wt$, glass beads $C_v = 0.18$

Table B.1 Suspension flow parameters

Property	Value
Pipe diameter, $D(mm)$	44
Fluid density, $\rho_f(kg/m^3)$	1163
Fluid viscosity, $\eta_f(mpa \cdot s)$	13.9
Temperature, $T(^\circ C)$	15
Solid density, $\rho_p(kg/m^3)$	2600
Particle size, $d_p(mm)$	2 ± 0.2
In line concentration, C_v	0.18
ERT integrated concentration, C_v	0.15
Mixture velocity, $\boldsymbol{U}_m$ (m/s)	1.66
Bulk flow Re	$6,100$
Pressure gradient per unit mass (m/s^2)	2.32

Table B.2 Concentration on the vertical centreline and chord-averaged concentration

Centreline		Chord average	
y/D	C_v	y/D	C_v
1.00	0.026	1.00	0.026
0.93	0.029	0.93	0.028
0.86	0.033	0.87	0.029
0.79	0.042	0.80	0.033
0.71	0.055	0.73	0.039
0.64	0.072	0.67	0.049
0.57	0.093	0.60	0.063
0.50	0.119	0.53	0.090
0.43	0.159	0.47	0.120
0.36	0.201	0.40	0.178
0.29	0.246	0.33	0.222
0.21	0.285	0.27	0.277
0.14	0.315	0.20	0.310
0.07	0.337	0.13	0.337
0.00	0.343	0.07	0.344
N/A	N/A	0.00	0.342

B.1.2 Glycerol solution $65\%wt$, glass beads $C_v = 0.17$

Table B.3 Suspension flow parameters

Property	Value
Pipe diameter, $D(mm)$	44
Fluid density, $\rho_f(kg/m^3)$	1163
Fluid viscosity, $\eta_f(mpa \cdot s)$	14.2
Temperature, $T(°C)$	15
Solid density, $\rho_p(kg/m^3)$	2600
Particle size, $d_p(mm)$	2 ± 0.2
In line concentration, C_v	0.17
ERT integrated concentration, C_v	0.14
Mixture velocity, $\boldsymbol{U}_m$ (m/s)	2.1
Bulk flow Re	$7,600$
Pressure gradient per unit mass (m/s^2)	2.64

Table B.4 Concentration on the vertical centreline and chord-averaged concentration

Centreline		Chord average	
y/D	C_v	y/D	C_v
1.00	0.030	1.00	0.030
0.93	0.033	0.93	0.031
0.86	0.038	0.87	0.032
0.79	0.048	0.80	0.036
0.71	0.061	0.73	0.042
0.64	0.078	0.67	0.055
0.57	0.097	0.60	0.069
0.50	0.120	0.53	0.095
0.43	0.154	0.47	0.120
0.36	0.190	0.40	0.163
0.29	0.229	0.33	0.198
0.21	0.264	0.27	0.248
0.14	0.294	0.20	0.277
0.07	0.311	0.13	0.304
0.00	0.310	0.07	0.316
N/A	N/A	0.00	0.315

B.1.3 Glycerol solution $65\%wt$, glass beads $C_v = 0.15$

Table B.5 Suspension flow parameters

Property	Value
Pipe diameter, $D(mm)$	44
Fluid density, $\rho_f(kg/m^3)$	1163
Fluid viscosity, $\eta_f(mpa \cdot s)$	13.9
Temperature, $T(°C)$	15
Solid density, $\rho_p(kg/m^3)$	2600
Particle size, $d_p(mm)$	2 ± 0.2
In line concentration, C_v	0.15
ERT integrated concentration, C_v	0.14
Mixture velocity, $\boldsymbol{U}_m$ (m/s)	2.77
Bulk flow Re	$10,200$
Pressure gradient per unit mass (m/s^2)	3.5

Table B.6 Concentration on the vertical centreline and chord-averaged concentration

Centreline		Chord average	
y/D	C_v	y/D	C_v
1.00	0.038	1.00	0.038
0.93	0.041	0.93	0.039
0.86	0.046	0.87	0.040
0.79	0.055	0.80	0.045
0.71	0.068	0.73	0.051
0.64	0.082	0.67	0.064
0.57	0.099	0.60	0.077
0.50	0.118	0.53	0.101
0.43	0.144	0.47	0.122
0.36	0.170	0.40	0.155
0.29	0.197	0.33	0.179
0.21	0.222	0.27	0.212
0.14	0.241	0.20	0.233
0.07	0.249	0.13	0.253
0.00	0.244	0.07	0.257
N/A	N/A	0.00	0.245

B.2 Test series: Newtonian-Glyc-210219

B.2.1 Glycerol solution $65\%wt$, glass beads $C_v = 0.22$

Table B.7 Suspension flow parameters

Property	Value
Pipe diameter, $D(mm)$	44
Fluid density, $\rho_f(kg/m^3)$	1163
Fluid viscosity, $\eta_f(mpa \cdot s)$	13.9
Temperature, $T(^\circ C)$	15
Solid density, $\rho_p(kg/m^3)$	2600
Particle size, $d_p(mm)$	2 ± 0.2
In line concentration, C_v	0.22
ERT integrated concentration, C_v	0.19
Mixture velocity, $\boldsymbol{U}_m$ (m/s)	1.76
Bulk flow Re	$6,500$
Pressure gradient per unit mass (m/s^2)	3.1

Table B.8 Concentration on the vertical centreline and chord-averaged concentration

Centreline		Chord average	
y/D	C_v	y/D	C_v
1.00	0.048	1.00	0.048
0.93	0.055	0.93	0.057
0.86	0.062	0.87	0.058
0.79	0.074	0.80	0.065
0.71	0.095	0.73	0.075
0.64	0.121	0.67	0.090
0.57	0.152	0.60	0.114
0.50	0.188	0.53	0.158
0.43	0.233	0.47	0.195
0.36	0.275	0.40	0.256
0.29	0.311	0.33	0.293
0.21	0.333	0.27	0.330
0.14	0.344	0.20	0.347
0.07	0.347	0.13	0.355
0.00	0.337	0.07	0.354
N/A	N/A	0.00	0.336

B.2.2 Glycerol solution $65\%wt$, glass beads $C_v = 0.20$

Table B.9 Suspension flow parameters

Property	Value
Pipe diameter, $D(mm)$	44
Fluid density, $\rho_f(kg/m^3)$	1163
Fluid viscosity, $\eta_f(mpa \cdot s)$	13.9
Temperature, $T(°C)$	15
Solid density, $\rho_p(kg/m^3)$	2600
Particle size, $d_p(mm)$	2 ± 0.2
In line concentration, C_v	0.2
ERT integrated concentration, C_v	0.18
Mixture velocity, $\boldsymbol{U}_m$ (m/s)	2.18
Bulk flow Re	$8,000$
Pressure gradient per unit mass (m/s^2)	3.53

Table B.10 Concentration on the vertical centreline and chord-averaged concentration

Centreline		Chord average	
y/D	C_v	y/D	C_v
1.00	0.050	1.00	0.050
0.93	0.055	0.93	0.053
0.86	0.064	0.87	0.055
0.79	0.080	0.80	0.063
0.71	0.100	0.73	0.075
0.64	0.123	0.67	0.096
0.57	0.147	0.60	0.118
0.50	0.175	0.53	0.154
0.43	0.208	0.47	0.183
0.36	0.240	0.40	0.224
0.29	0.271	0.33	0.252
0.21	0.295	0.27	0.289
0.14	0.312	0.20	0.306
0.07	0.317	0.13	0.321
0.00	0.307	0.07	0.324
N/A	N/A	0.00	0.309

B.2.3 Glycerol solution $65\%wt$, glass beads $C_v = 0.19$

Table B.11 Suspension flow parameters

Property	Value
Pipe diameter, $D(mm)$	44
Fluid density, $\rho_f(kg/m^3)$	1163
Fluid viscosity, $\eta_f(mpa \cdot s)$	13.9
Temperature, $T(°C)$	15
Solid density, $\rho_p(kg/m^3)$	2600
Particle size, $d_p(mm)$	2 ± 0.2
In line concentration, C_v	0.19
ERT integrated concentration, C_v	0.17
Mixture velocity, $\boldsymbol{U}_m$ (m/s)	2.56
Bulk flow Re	$9,500$
Pressure gradient per unit mass (m/s^2)	3.84

Table B.12 Concentration on the vertical centreline and chord-averaged concentration

Centreline		Chord average	
y/D	C_v	y/D	C_v
1.00	0.053	1.00	0.052
0.93	0.056	0.93	0.054
0.86	0.065	0.87	0.056
0.79	0.079	0.80	0.064
0.71	0.097	0.73	0.075
0.64	0.117	0.67	0.094
0.57	0.139	0.60	0.114
0.50	0.164	0.53	0.146
0.43	0.194	0.47	0.172
0.36	0.223	0.40	0.211
0.29	0.253	0.33	0.237
0.21	0.276	0.27	0.271
0.14	0.294	0.20	0.289
0.07	0.301	0.13	0.304
0.00	0.297	0.07	0.307
N/A	N/A	0.00	0.298

B.3 Test series: CBP-150319

B.3.1 Carbopol solution $0.1\%wt$, glass beads $C_v = 0.10$

Table B.13 Suspension flow parameters

Property	Value
Pipe diameter, $D(mm)$	44
Fluid density, $\rho_f(kg/m^3)$	1000
Yield stress, $\tau_y(Pa)$	0.33
Flow index, n	0.54
Consistency, $k(pa \cdot s^n)$	0.697
Solid density, $\rho_p(kg/m^3)$	2600
Particle size, $d_p(mm)$	2 ± 0.2
In line concentration, C_v	0.1
ERT integrated concentration, C_v	0.09
Mixture velocity, $\boldsymbol{U}_m$ (m/s)	2.85
Bulk flow Re_G	$6,000$
Pressure gradient per unit mass (m/s^2)	3.9

Table B.14 Concentration on the vertical centreline and chord-averaged concentration

Centreline		Chord average	
y/D	C_v	y/D	C_v
1.00	0.023	1.00	0.023
0.93	0.025	0.93	0.024
0.86	0.029	0.87	0.026
0.79	0.037	0.80	0.028
0.71	0.046	0.73	0.033
0.64	0.056	0.67	0.043
0.57	0.068	0.60	0.053
0.50	0.082	0.53	0.070
0.43	0.100	0.47	0.086
0.36	0.118	0.40	0.110
0.29	0.137	0.33	0.127
0.21	0.152	0.27	0.148
0.14	0.165	0.20	0.161
0.07	0.174	0.13	0.172
0.00	0.175	0.07	0.176
N/A	N/A	0.00	0.175

B.3.2 Carbopol solution $0.1\%wt$, glass beads $C_v = 0.10$

Table B.15 Suspension flow parameters

Property	Value
Pipe diameter, $D(mm)$	44
Fluid density, $\rho_f(kg/m^3)$	1000
Yield stress, $\tau_y(Pa)$	0.23
Flow index, n	0.58
Consistency, $k(pa \cdot s^n)$	0.479
Solid density, $\rho_p(kg/m^3)$	2600
Particle size, $d_p(mm)$	2 ± 0.2
In line concentration, C_v	0.1
ERT integrated concentration, C_v	0.09
Mixture velocity, $\boldsymbol{U}_m$ (m/s)	3.19
Bulk flow Re_G	$8,500$
Pressure gradient per unit mass (m/s^2)	4.6

Table B.16 Concentration on the vertical centreline and chord-averaged concentration

Centreline		Chord average	
y/D	C_v	y/D	C_v
1.00	0.031	1.00	0.031
0.93	0.033	0.93	0.033
0.86	0.037	0.87	0.035
0.79	0.044	0.80	0.037
0.71	0.052	0.73	0.041
0.64	0.061	0.67	0.049
0.57	0.071	0.60	0.058
0.50	0.083	0.53	0.073
0.43	0.099	0.47	0.086
0.36	0.114	0.40	0.107
0.29	0.130	0.33	0.122
0.21	0.143	0.27	0.140
0.14	0.155	0.20	0.150
0.07	0.163	0.13	0.159
0.00	0.166	0.07	0.163
N/A	N/A	0.00	0.166

B.3.3 Carbopol solution $0.1\%wt$, glass beads $C_v = 0.10$

Table B.17 Suspension flow parameters

Property	Value
Pipe diameter, $D(mm)$	44
Fluid density, $\rho_f(kg/m^3)$	1000
Yield stress, $\tau_y(Pa)$	0.16
Flow index, n	0.59
Consistency, $k(pa \cdot s^n)$	0.406
Solid density, $\rho_p(kg/m^3)$	2600
Particle size, $d_p(mm)$	2 ± 0.2
In line concentration, C_v	0.1
ERT integrated concentration, C_v	0.09
Mixture velocity, $\boldsymbol{U}_m$ (m/s)	3.67
Bulk flow Re_G	$12,000$
Pressure gradient per unit mass (m/s^2)	5.2

Table B.18 Concentration on the vertical centreline and chord-averaged concentration

Centreline		Chord average	
y/D	C_v	y/D	C_v
1.00	0.033	1.00	0.033
0.93	0.036	0.93	0.036
0.86	0.040	0.87	0.038
0.79	0.047	0.80	0.040
0.71	0.054	0.73	0.043
0.64	0.063	0.67	0.052
0.57	0.073	0.60	0.060
0.50	0.085	0.53	0.074
0.43	0.100	0.47	0.087
0.36	0.114	0.40	0.107
0.29	0.130	0.33	0.121
0.21	0.143	0.27	0.138
0.14	0.153	0.20	0.150
0.07	0.154	0.13	0.162
0.00	0.148	0.07	0.161
N/A	N/A	0.00	0.149

B.4 Test series: CBP-200319

B.4.1 Carbopol solution $0.1\%wt$, glass beads $C_v = 0.18$

Table B.19 Suspension flow parameters

Property	Value
Pipe diameter, $D(mm)$	44
Fluid density, $\rho_f(kg/m^3)$	1000
Yield stress, $\tau_y(Pa)$	0.08
Flow index, n	0.60
Consistency, $k(pa \cdot s^n)$	0.338
Solid density, $\rho_p(kg/m^3)$	2600
Particle size, $d_p(mm)$	2 ± 0.2
In line concentration, C_v	0.18
ERT integrated concentration, C_v	0.15
Mixture velocity, $\boldsymbol{U}_m$ (m/s)	2.59
Bulk flow Re_G	$8,900$
Pressure gradient per unit mass (m/s^2)	4.2

Table B.20 Concentration on the vertical centreline and chord-averaged concentration

Centreline		Chord average	
y/D	C_v	y/D	C_v
1.00	0.037	1.00	0.037
0.93	0.040	0.93	0.038
0.86	0.048	0.87	0.040
0.79	0.061	0.80	0.047
0.71	0.078	0.73	0.055
0.64	0.096	0.67	0.073
0.57	0.117	0.60	0.091
0.50	0.142	0.53	0.120
0.43	0.173	0.47	0.147
0.36	0.205	0.40	0.189
0.29	0.239	0.33	0.220
0.21	0.269	0.27	0.259
0.14	0.295	0.20	0.283
0.07	0.315	0.13	0.304
0.00	0.322	0.07	0.315
N/A	N/A	0.00	0.320

B.4.2 Carbopol solution $0.1\%wt$, glass beads $C_v = 0.16$

Table B.21 Suspension flow parameters

Property	Value
Pipe diameter, $D(mm)$	44
Fluid density, $\rho_f(kg/m^3)$	1000
Yield stress, $\tau_y(Pa)$	0.04
Flow index, n	0.64
Consistency, $k(pa \cdot s^n)$	0.228
Solid density, $\rho_p(kg/m^3)$	2600
Particle size, $d_p(mm)$	2 ± 0.2
In line concentration, C_v	0.16
ERT integrated concentration, C_v	0.15
Mixture velocity, $\boldsymbol{U}_m$ (m/s)	2.99
Bulk flow Re_G	$11,800$
Pressure gradient per unit mass (m/s^2)	4.5

Table B.22 Concentration on the vertical centreline and chord-averaged concentration

Centreline		Chord average	
y/D	C_v	y/D	C_v
1.00	0.046	1.00	0.046
0.93	0.049	0.93	0.047
0.86	0.055	0.87	0.048
0.79	0.068	0.80	0.054
0.71	0.083	0.73	0.062
0.64	0.100	0.67	0.079
0.57	0.119	0.60	0.095
0.50	0.142	0.53	0.123
0.43	0.170	0.47	0.147
0.36	0.198	0.40	0.185
0.29	0.227	0.33	0.212
0.21	0.252	0.27	0.244
0.14	0.272	0.20	0.264
0.07	0.286	0.13	0.282
0.00	0.289	0.07	0.288
N/A	N/A	0.00	0.289

B.4.3 Carbopol solution $0.1\%wt$, glass beads $C_v = 0.16$

Table B.23 Suspension flow parameters

Property	Value
Pipe diameter, $D(mm)$	44
Fluid density, $\rho_f(kg/m^3)$	1000
Yield stress, $\tau_y(Pa)$	0.01
Flow index, n	0.7
Consistency, $k(pa \cdot s^n)$	0.124
Solid density, $\rho_p(kg/m^3)$	2600
Particle size, $d_p(mm)$	2 ± 0.2
In line concentration, C_v	0.16
ERT integrated concentration, C_v	0.15
Mixture velocity, $\boldsymbol{U}_m$ (m/s)	3.2
Bulk flow Re_G	$15,000$
Pressure gradient per unit mass (m/s^2)	4.9

Table B.24 Concentration on the vertical centreline and chord-averaged concentration

Centreline		Chord average	
y/D	C_v	y/D	C_v
1.00	0.042	1.00	0.042
0.93	0.045	0.93	0.043
0.86	0.052	0.87	0.045
0.79	0.064	0.80	0.050
0.71	0.080	0.73	0.059
0.64	0.097	0.67	0.075
0.57	0.116	0.60	0.092
0.50	0.138	0.53	0.120
0.43	0.166	0.47	0.144
0.36	0.194	0.40	0.182
0.29	0.222	0.33	0.208
0.21	0.247	0.27	0.240
0.14	0.267	0.20	0.259
0.07	0.278	0.13	0.277
0.00	0.279	0.07	0.282
N/A	N/A	0.00	0.279

C

Rheology Measurement

C.1 Test series: CBP-150319-Pre

- Combined Couette and parallel plate test (Pre-test)

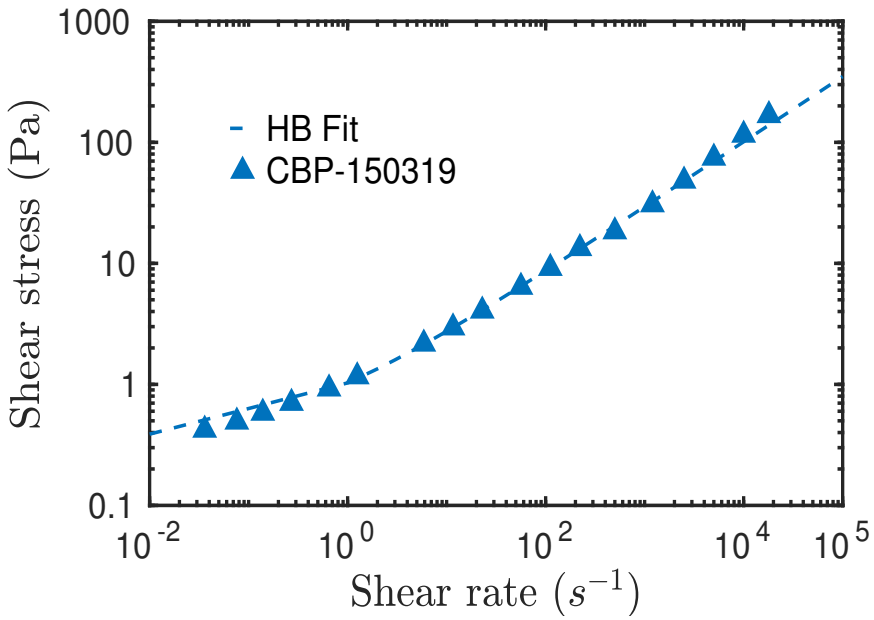

Fig. C.1 High shear rate rheology measurement for the flow with $C_v = 0.1$ ($\tau_y = 0.33Pa$, $k = 0.697Pa \cdot s^n$, $n = 0.54$)

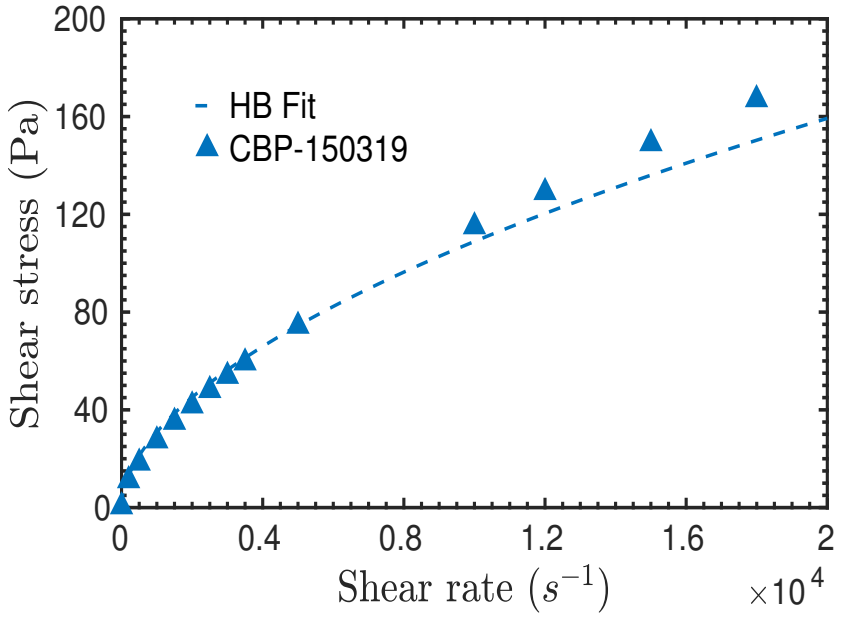

Fig. C.2 High shear rate rheology measurement for the flow with $C_v = 0.1$ ($\tau_y = 0.33Pa$, $k = 0.685Pa \cdot s^n$, $n = 0.55$)

C.2 Test series: CBP-150319-Post

- Combined Couette and parallel plate test (Post-test, $Re_G \approx 6,000$)

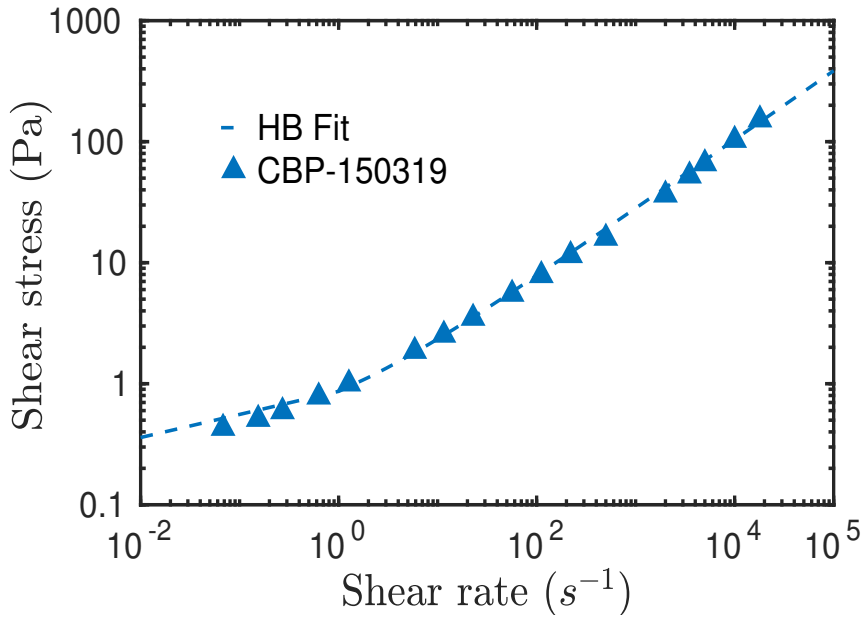

Fig. C.3 High shear rate rheology measurement for the flow with $C_v = 0.1$ ($\tau_y = 0.32Pa$, $k = 0.544Pa \cdot s^n$, $n = 0.57$)

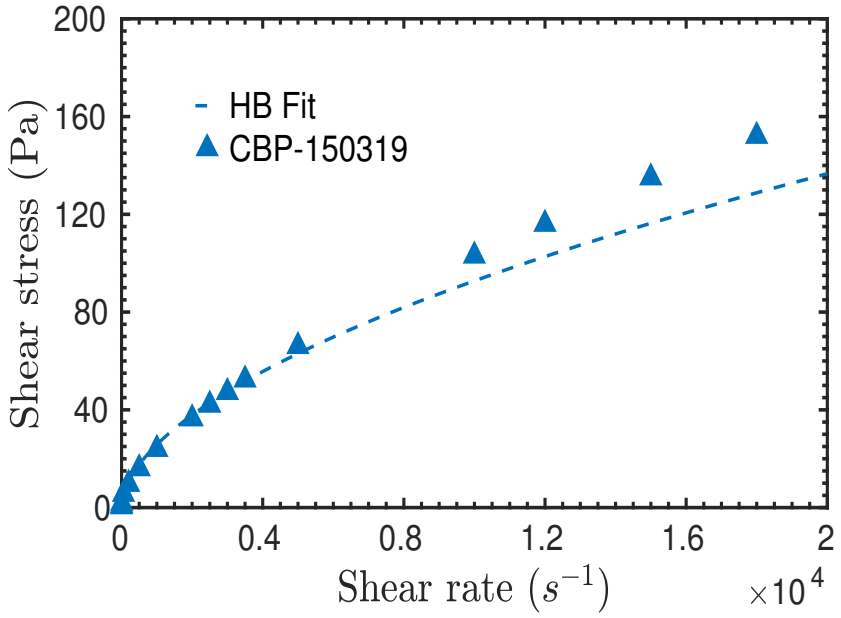

Fig. C.4 High shear rate rheology measurement for the flow with $C_v = 0.1$ ($\tau_y = 0.32Pa$, $k = 0.532Pa \cdot s^n$, $n = 0.56$)

C.3 Test series: CBP-200319-Pre

- Combined Couette and parallel plate test (Pre-test)

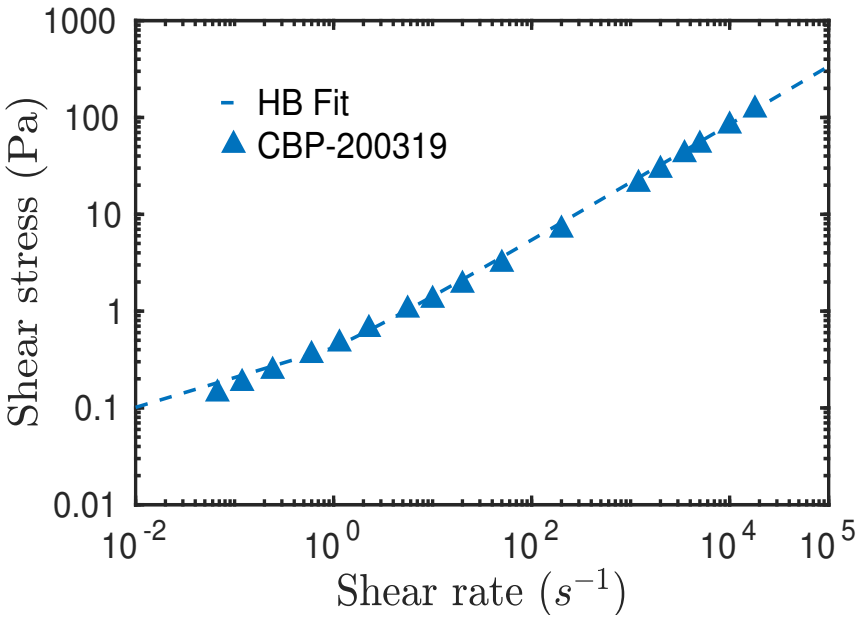

Fig. C.5 High shear rate rheology measurement for the flow with $C_v = 0.1$ ($\tau_y = 0.08Pa$, $k = 0.338Pa \cdot s^n$, $n = 0.6$)

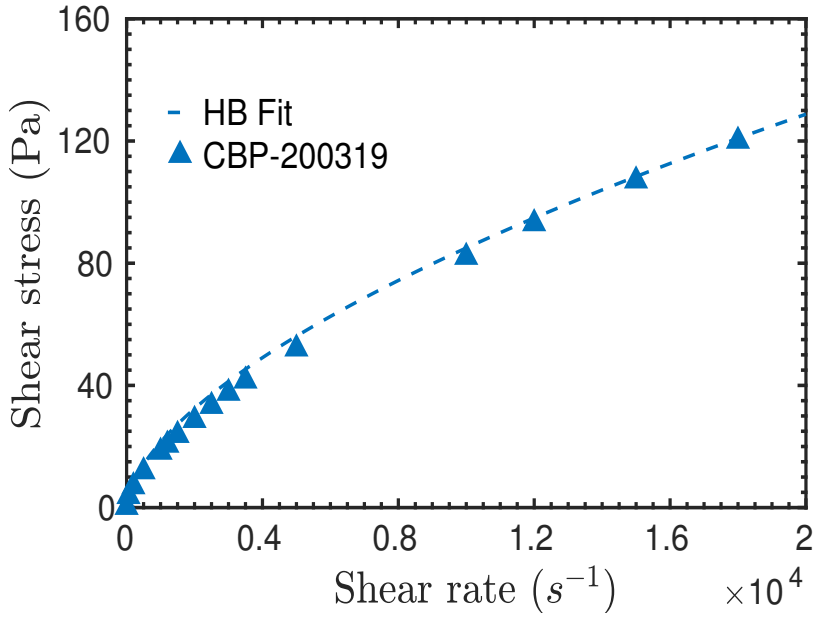

Fig. C.6 High shear rate rheology measurement for the flow with $C_v = 0.1$ ($\tau_y = 0.084Pa$, $k = 0.338Pa \cdot s^n$, $n = 0.6$)

C.4 Test series: CBP-200319-Post

- Combined Couette and parallel plate test (Post-test)

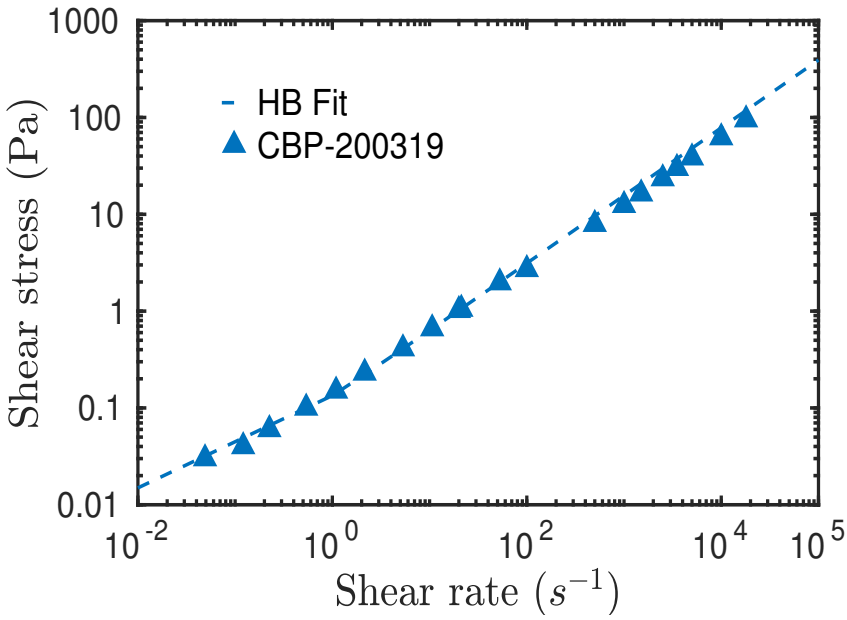

Fig. C.7 High shear rate rheology measurement for the flow with $C_v = 0.1$ ($\tau_y = 0.01Pa$, $k = 0.124Pa \cdot s^n$, $n = 0.7$)

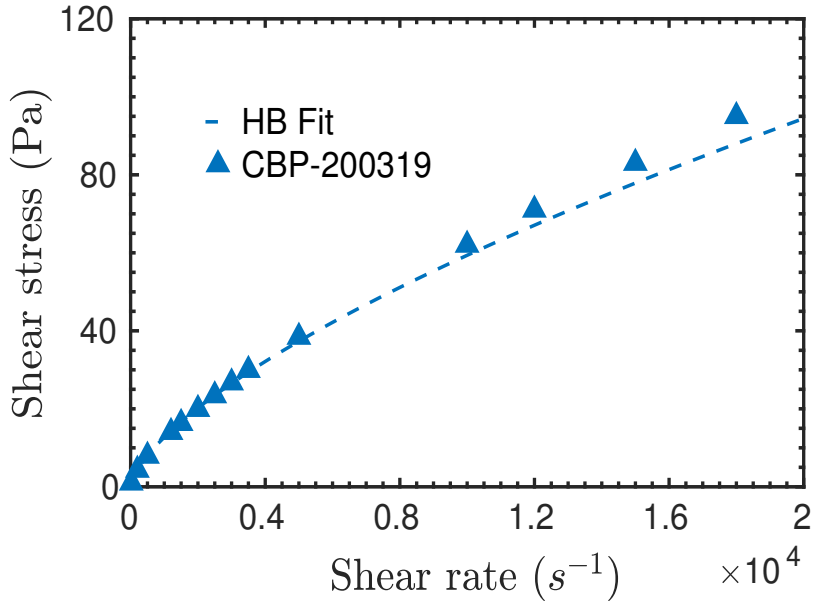

Fig. C.8 High shear rate rheology measurement for the flow with $C_v = 0.1$ ($\tau_y = 0.014Pa$, $k = 0.124Pa \cdot s^n$, $n = 0.67$)